TECHNICAL UNIVERSITY OF MUNICH

# Investigating molecules at surfaces - from preparative mass spectrometry of large biomolecules to complex desorption kinetics

Dissertation

*Karolina Angela Stoiber*

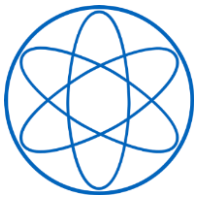

TUM Department of Physics

*Chair of Molecular Nanoscience &*

*Chemical Physics of Interfaces*

# TECHNICAL UNIVERSITY OF MUNICH

## Department of Physics


# Investigating molecules at surfaces - from preparative mass spectrometry of large biomolecules to complex desorption kinetics


*Karolina Angela Stoiber*


Vollständiger Abdruck der von der Fakultät für Physik der Technischen Universität München zur Erlangung des akademischen Grades eines

**Doktors der Naturwissenschaften (Dr. rer. nat.)**

genehmigten Dissertation.

| | | |
|---|---|---|
| Vorsitzende: | | Prof. Dr. Karen Alim |
| Prüfer der Dissertation: | 1. | Prof. Dr. Johannes V. Barth |
| | 2. | Prof. Dr. Ulrich Heiz |


Die Dissertation wurde am 12. April 2021 bei der Technischen Universität München eingereicht und durch die Fakultät für Physik am 10. Mai 2021 angenommen.

*Für meinen Papa*

# Abstract

Functional and complex organic and biomolecules are becoming increasingly relevant in surface and nanoscience. They can be used as building blocks for sophisticated nano-architectures. The analysis of these molecules requires a well-defined environment. Experiments such as characterizing desorption kinetics, adsorption and assembly behaviours, structural and electronic properties of molecules are frequently performed on single-crystal metal supports in ultra-high vacuum (UHV).

Large and fragile soluble biomolecules are prone to decomposition using classical thermal evaporation methods for deposition. In this thesis, a home-built electrospray-controlled ion beam deposition (ES-CIBD) system, a very gentle and structure-preserving technique, is evaluated by processing representatives of three different groups of biomolecules - the polyamine spermine (200 Da), the protein insulin (5.7 kDa) and the circular dsDNA pUC19 (1.7 MDa).

After the analyte molecules are ionized and transferred into UHV, the ion beam is analysed and filtered by a digital quadrupole mass spectrometer (dQMS). In this way, an adsorbate layer without impurities, residual gas or ion fragments is generated. Positive and negative spray modes are applied during the ESI process and different conformations of the molecules are tested, introduced by variation of pH, ionic strength or by enzymatic manipulation. Analysis of corresponding mass spectra revealed details about charging behaviour and charge states as well as geometric differences of the analyte molecules. Structural properties such as conformation and conformational change, topography and adsorption properties are investigated by scanning tunnelling microscopy (STM). The findings are evaluated by careful analysis including length and width measurements as well as the behaviour of self-assembled structures.

Another approach to analyse surface processes is temperature programmed desorption (TPD). Sophisticated analyses and simulations reveal desorption kinetics such as ortho-ortho coupling for two phenol derivates (bisphenol A -BPA and diethylstilbestrol – DES) and the cyclodehydrogenation of various species of metallo-tetraphenylporphyrins. Such *on-surface* reactions involve desorption of molecular hydrogen. The measured desorption rates are simulated using Polanyi-Wigner-equation-based models. Accompanying X-ray photoelectron spectroscopy (XPS) and STM measurements support the findings by TPD analysis.

# Zusammenfassung

Funktionelle, komplexe organische und Bio-Moleküle werden immer relevanter im Bereich der Nanowissenschaften und können als Bausteine für anspruchsvolle Nano-Architekturen verwendet werden. Da die Analyse dieser Moleküle eine wohldefinierte Umgebung erfordert, werden Experimente zur Charakterisierung der Desorptionskinetik, des Adsorptions- und Assemblierungsverhaltens, der strukturellen und elektronischen Eigenschaften von Molekülen häufig auf einkristallinen Metallsubstraten im Ultrahochvakuum (UHV) durchgeführt.

Große und fragile Biomoleküle sind anfällig für Zersetzung, wenn sie mithilfe von klassischen thermischen Verdampfungsmethoden deponiert werden.

In dieser Arbeit wird eine selbstgebaute Elektrosprayquelle mit kontrollierter Ionenstrahldeposition (ES-CIBD), eine sehr schonende und strukturerhaltende Technik, anhand der Prozessierung von Vertretern dreier verschiedener Gruppen von Biomolekülen - dem Polyamin Spermin (200 Da), dem Protein Insulin (5.7 kDa) und der zirkulären dsDNA pUC19 (1.7 MDa) - evaluiert.

Nachdem die Moleküle ionisiert und ins UHV überführt wurden, wird der Ionenstrahl mit einem digitalen Quadrupol-Massenspektrometer (dQMS) analysiert und gefiltert. Auf diese Weise wird eine Adsorbatschicht ohne Verunreinigungen, Restgasmoleküle oder Ionenfragmente erzeugt. Während des ESI-Prozesses werden positive und negative Sprühmodi angewendet. Verschiedene Konformationen der DNA-Moleküle werden getestet, die durch Variation des pH-Wertes, der Ionenstärke oder durch enzymatische Manipulation herbeigeführt wurden. Die Analyse der entsprechenden Massenspektren gibt Aufschluss über Ladungsverhalten und Ladungszustände sowie geometrische Unterschiede der Moleküle. Strukturelle Eigenschaften der Konformation und Konformationsänderung, Topographie und Adsorptionseigenschaften werden mittels Rastertunnelmikroskopie (STM) untersucht. Die Ergebnisse werden durch sorgfältige Analysen mit Längen- und Breitenmessungen sowie des Verhaltens von selbstassemblierenden Strukturen ausgewertet.

Ein weiterer Ansatz zur Analyse von Oberflächenprozessen ist die temperaturprogrammierte Desorption (TPD). Ausgefeilte Analysen und Simulationen zeigen Desorptionskinetiken wie die ortho-ortho-Kopplung für zwei Phenolderivate (Bisphenol A -BPA und Diethylstilbestrol - DES) und die Cyclodehydrogenierung verschiedener Spezies von

Metallo-Porphyrinen. Solche *On-Surface* Reaktionen beinhalten die Desorption von molekularem Wasserstoff. Die gemessenen Desorptionsraten werden mit auf Polanyi-Wigner-Gleichungen basierenden Modellen simuliert. Begleitende Röntgenphotoelektronenspektroskopie (XPS) und STM-Messungen unterstützen die Ergebnisse der TPD Analyse.

# Contents

**Abstract** ..... i

**Zusammenfassung** ..... iii

**1 Introduction** ..... 1

**Part A| Characterization of different biomolecules using ES-CIBD** ..... 5

**2 Fundamentals and theory** ..... 7

2.1 Principles of electrospray ionization (ESI) ..... 7

2.1.1 Electrospray modes ..... 8

2.1.2 Coulomb fission ..... 10

2.1.3 Ion generation ..... 10

2.2 Working principle of ion guides ..... 14

2.3 Deposition of charged particles ..... 19

2.4 Scanning tunnelling microscopy ..... 20

2.4.1 Electron tunnelling ..... 20

2.4.2 The Tersoff-Hamann model ..... 24

2.4.3 STM operation modes ..... 24

2.5 Ultraviolet-visible spectroscopy ..... 25

2.6 Biomolecules ..... 26

2.6.1 Deoxyribonucleic acid ..... 26

2.6.2 Proteins ..... 29

2.6.3 Polyamines ..... 30

**3 Electrospray-controlled ion beam deposition (ES- CIBD)** ..... 31

3.1 ESI source ..... 31

3.2 ES-CIBD system ..... 32

3.3 Set-up: ES-CIBD and STM ..... 34

**4 Characterization of charge states and adsorption for biomolecules following different ionization models** ..... 37

4.1 Mass spectrometric analysis and deposition of Insulin ..... 37

4.1.1 Sample preparation, experimental flow and analytical methods ..... 39
4.1.2 Results and Discussion ..... 40
4.2 Mass spectrometric analysis and deposition of Spermine ..... 44
4.2.1 Sample preparation, experimental flow and analytical methods ..... 45
4.2.2 Results and Discussion ..... 46
4.3 Mass spectrometric analysis and deposition of pUC19 DNA ..... 51
4.3.1 Sample preparation, experimental flow and analytical methods ..... 54
4.3.2 Mass spectrum and analysis of pristine DNA (base spectrum) ..... 56
4.3.3 Impact of modified topology on mass spectrometric parameters ..... 60
4.3.4 Investigation of DNA structure on metal surfaces ..... 65
4.4 Conclusion ..... 85

**Part B| Analysis of thermal programmed desorption measurements on organic molecules ..... 89**

**5 TPD-Fundamentals and theory ..... 91**
5.1 Adsorption processes and scattering ..... 91
5.1.1 Possible processes on the surface ..... 91
5.1.2 Layer growth ..... 92
5.2 Influence of coverage and precursor ..... 93
5.3 Desorption from monolayer ..... 95
5.3.1 Polanyi – Wigner equation ..... 95
5.3.2 Transition state theory and microscopic reversibility ..... 98
5.3.3 Desorption from multilayer-equilibrium on the surface ..... 99
5.3.4 Order in the first monolayer ..... 100

**6 Experimental methods and analysis ..... 103**
6.1 Ultra-high vacuum and surface science ..... 103
6.2 Temperature-Programmed Desorption ..... 104
6.2.1 Measurement of desorption rate ..... 104
6.2.2 Conventional analysis of kinetic parameters ..... 105
6.2.3 Analytical simulation of desorption spectra ..... 109
6.2.4 Monte-Carlo Simulation of a first order desorption process ..... 112
6.3 X-ray photoelectron spectroscopy ..... 115

**7 Instrumentation ..... 117**

**8 Desorption kinetics of the dehydrogenation of Bisphenol A and Diethylstilbestrol ..... 121**
8.1 Experimental procedures ..... 122
8.2 Modelling of the TPD spectra ..... 124
8.3 Results and Discussion ..... 125
8.4 Conclusion ..... 131

**9 Desorption kinetics associated to cyclodehydrogenation reaction of metallo-tetraphenyl porphyrins ..... 133**
9.1 Experimental procedures ..... 135
9.2 Low-energy electron diffraction (LEED) ..... 137
9.3 X-ray photoelectron spectroscopy (XPS) and multilayer desorption ..... 137
9.4 Temperature programmed desorption (TPD) ..... 142
9.4.1 Monolayers of 2H-TPP, Ru-TPP, Ti-TPP and TiO-TPP ..... 142
9.4.2 Sub-monolayers of 2H-TPP and Ru-TPP ..... 147
9.4.3 Saturated monolayers of 2H-TPP and Ru-TPP – The section model .. 148
9.4.4 Saturated monolayer of 2H-TPP and Ru-TPP – The coherent model . 152
9.5 Conclusion ..... 164

**10 Conclusion and Outlook ..... 167**

**Appendix A ..... 171**

**Appendix B ..... 175**

**Bibliography ..... 191**

**Acknowledgements ..... 213**

# 1 Introduction

An important aspect of surface and nano science is to investigate atoms and molecules of the nanometre scale and to understand chemical and physical phenomena on surfaces or interfaces. Layer-ordering and self-assembly on surfaces are consequences of the properties of the adsorbed molecules and may lead to macroscopic effects. On-surface processes are often very complicated. To understand the investigated systems, models and absolute control of their structure and composition are required. Thus, surface science experiments are mainly performed in an ultra-high vacuum (UHV) environment in order to provide model conditions and reduce surface contaminations [1]. Investigation and analysis of surfaces involve both, chemical and physical techniques. Experimental methods like X-ray photoelectron spectroscopy (XPS), low-energy electron diffraction (LEED) and thermal desorption spectroscopy (TPD) rely on the detection of electrons or ions which are emitted from the surface. Scanning probe techniques such as atomic force microscopy [2] and scanning tunnelling microscopy (STM) [3] give real space information of the surfaces with atomic precision.

One of the main goals of surface science is to guide the fabrication of electronic devices which get smaller and better in terms of performance. The bottom-up approach [4] uses interaction of single atoms and molecules triggering self-assembly and thus, employing functional, nanostructured materials. The exact control of size, shape and composition on an atomic level allows for downscaling and engineering of nano architectures for a multitude of purposes. Self-assembled monolayers (SAMs) of deliberately tailored organic compounds may provide well-defined chemical and structural properties and provide versatile surface functionalization. Thus, bottom-up surface nanofabrication is an alternative for the widely used top-down designs [4] as it is in principle more precise and controllable. This method is employed in various fields such as energy conversion [5–7], light emission [8, 9], molecular machines [10, 11], catalysis [12–17], chemical sensors [18, 19], molecular electronics [20, 21], quantum computing [22, 23], spintronics and information storage [24–26]. Moreover, interfaces and surfaces play an important role in biological processes and their understanding, for example the biological response to a material with effects on biocompatibility, synthesis of complex biological surfaces, tissue engineering, molecular and bio-recognition [27, 28]. This allows for tissue growth and fabrication of biosensors and medical implants. Most of the research is still focusing on fundamentals in physics, chemistry and electronics by investigating

model systems. A well-defined and clean substrate like a single crystal surface is required in order to support self-assembly processes of extended nanostructures made from small building blocks [29]. Moreover, a precisely controlled deposition of particles in UHV is mandatory to limit detrimental effects and impurities introduced by sample preparation and surrounding atmosphere.

This thesis focuses on the ionization, deposition and adsorption properties of different biomolecules as well as the desorption and reaction kinetics of organic molecules. The investigations include common UHV techniques such as electrospray-controlled ion beam deposition (ES-CIBD), STM, XPS and TPD. The most common technique for UHV deposition of organic species is based on thermal evaporation by organic molecular beam epitaxy (OMBE). However, the sublimation of molecules in vacuum is limited since thermo-labile, reactive and large particles tend to fragmentation or unwanted reactions before the evaporation temperature is reached [30]. An alternative is the pulse injection technique, which injects dissolved molecules into vacuum resulting in a simultaneous deposition of solvent and analyte species. In some cases, gentle thermal treatment (annealing) may desorb the solvent particles from the surface without affecting the analyte molecules [30]. An alternative approach to expand the range of investigable molecules has its origin in mass spectrometry (MS) which uses the ionization and gas phase capabilities of the technology. The basic design of a mass spectrometer consists of an ion source, transfer ion guides, a mass-to-charge selective device and a detector [31]. Since the early 20$^{th}$ century, different ionization techniques have been developed for various purposes: electron impact ionization, chemical ionization, field ionization and fast atom bombardment which expose the molecules to harsh conditions [32]. In the 1980s, matrix-assisted laser desorption ionization (MALDI) and electrospray ionization (ESI) were invented allowing for soft ionization of large and thermally sensitive analyte molecules with high ionization and transfer efficiencies [33]. In 1989, Fenn et al. demonstrated the transfer of large biomolecules into gas phase for the first time [34]. In 2002, John Fenn and Koichi Tanaka were awarded the Nobel Prize for the electrospray principle [35]. With ESI, a nearly unrestricted range of analyte species is accessible, provided that the analyte can be solved in a “sprayable” solvent, and a virtually unlimited mass range, currently up to $300$ MDa [36, 37]. Consequently, ESI became one of the most widely used ionization techniques. In addition to analytical MS, a new technique, the preparative MS is developed [38, 39]. The detector is replaced by a processing stage, which extracts ions from the spectrometer. This allows for subsequent deposition of a $m/z$-filtered, thus purified ion beam on a sample surface. Therefore, the

spectrometer gives access to information about the analyte molecules. Different conformations or polymerization can change the charge states of the analyte species and thus, may cause shifts in the $m/z$-spectra. Furthermore, the kinetic energy of the ions can be precisely controlled during the landing process [40]. The integrity of the deponent species can be preserved by a landing process with low kinetic energies (soft-landing) [40–43], whereas increasing the landing energy explicitly may lead to unique structural and chemical modifications (reactive landing) [44]. As it was proven by analytical and preparative MS, ionization techniques such as ESI outperform the standard UHV deposition methods especially with reactive, fragile or large chemical and biological molecules like saccharides [45], proteins [46, 47] and DNA [48]. Preparative MS requires high ion beam intensities to cover the surface with about a monolayer (e.g., $2-3$ spermine molecules per nm$^2$) of analyte molecule in about an hour.

In this work, a home-built electrospray-controlled ion beam deposition (ES-CIBD) system [49] was used to investigate several biomolecules of different sizes and structural properties: the polyamine spermine, the protein insulin and the circular DNA pUC19. The investigation of these molecules includes mass spectrometry experiments in combination with scanning tunnelling microscopy (STM) to analyse ionization behaviour, charging properties including integrity and purity of the molecules and structural details of the adsorbate species on the surfaces of Ag(111) and Cu(111).

In the second part of this work, a different approach of the investigation of surface reactions after deposition is discussed. While heating the surface, the desorbing species are detected by time-resolved mass spectrometry. This technique is called thermal programmed desorption (TPD). In the beginning, it only served as cleaning procedure. In 1933, Taylor and Langmuir performed the first experiments applying the TPD technique to estimate kinetic parameters of an adsorbate system [50]. The desorption process is driven by vibrational excitations and may involve the interaction of the adsorbate species with each other. In addition to details about potentials between substrate and adsorbate, diffusion and phase changes affect the ordering of particles on the surface. In principle, TPD can give information about all these processes. As surface chemistry tends to be complex rather than simple, the best outcome is obtained by combining different methods such as TPD, XPS and STM.

In this work, two intricate on-surface reactions are investigated by analysing and simulating the desorption kinetics. A Cu(111) crystal serves as template for the promotion of highly selective, surface-assisted hydroxyl-directed covalent coupling

reactions. The nature of the substrate plays an important role in the sequential reaction steps [51]. A detailed analysis of TPD experiments in combination with XPS and STM provides information about the chemical and structural evolution of the adsorbed phenol derivatives (Bisphenol A and Diethylstilbestrol) from self-assembled monolayers to branched molecular chains. Furthermore, the cyclodehydrogenation (CDH) reaction of various metallo- porphyrins on Ag(111) is addressed. A sophisticated analysis of TP-XPS and TPD measurements reveals reaction kinetics of the flattening of 2H-TPP and Ru-TPP.

# Part A

## Characterization of different biomolecules using ES-CIBD

# 2 Fundamentals and theory

In this chapter, basic theoretical principles of the electrospray-controlled ion beam deposition (ES-CIBD) process are described. The first step towards a successful deposition is the generation of charged species in an ion source. Subsequently, the ions are transferred to a mass spectrometer by different ion guides from ambient pressure to UHV to separate neutral particles from the ions. In the mass spectrometer, the ions are selected and $m/z$-filtered according to their mass-to-charge ratio. The last step is the landing process which depends on the kinetic energy of the ions. Low energies lead to a soft landing of intact molecules while high energies can trigger impact-driven decomposition and chemical reactions. The subsequent investigation of the particles on the surface is performed by scanning tunnelling microscopy. Ultraviolet-visible spectroscopy (UV-Vis) is used to determine the concentration of molecules in the analyte solution which is used for the ES-CIBD. Furthermore, structural details about certain biomolecules, which are used for the experiments, are provided.

## 2.1 Principles of electrospray ionization (ESI)

For more than 50 years, the ionization of non-volatile and large molecules in gas phase has been of interest especially for mass spectrometry and applications in vacuum and surface science. Different techniques as electron impact ionization, fast atom bombardment, matrix-assisted laser desorption (MALDI) and electrospray ionization (ESI) were established [52, 53]. Inventing and developing electrospray ionization introduced mass spectrometry to the field of biochemistry as large, fragile and thermo- labile organic and biological molecules like proteins can be ionized and thus, detected [35, 54]. Because of a high amount of accessible analyte molecules of a broad mass range [33, 34], this technique is used in preparative and analytical mass spectrometry and is getting more common in surface science [38, 39].

A schematic of an ESI source is depicted in Figure 2.1. A vessel, typically a syringe, is connected to the emitter and supplies an analyte solution with dissolved molecules. The emitter is a small capillary made from fused silica or metal. A high voltage (HV) source supplies a defined potential to the analyte which generates a strong electric field towards a counter electrode. Thus, the charge carriers accumulate on the surface of the liquid and the solution forms an elliptical shape at the tip of the emitter. This results in

an electrostatic force between emitter and counter electrode. Depending on the applied voltage, the ions can be ionized in two different spray modes resulting in positive or negative ions. At a critical voltage, the shape changes to a so-called Taylor cone which ejects a spray of small charged droplets [55]. Due to alternating steps of steady solvent evaporation and Coulomb fission, these droplets eventually disintegrate to pure analyte ions.

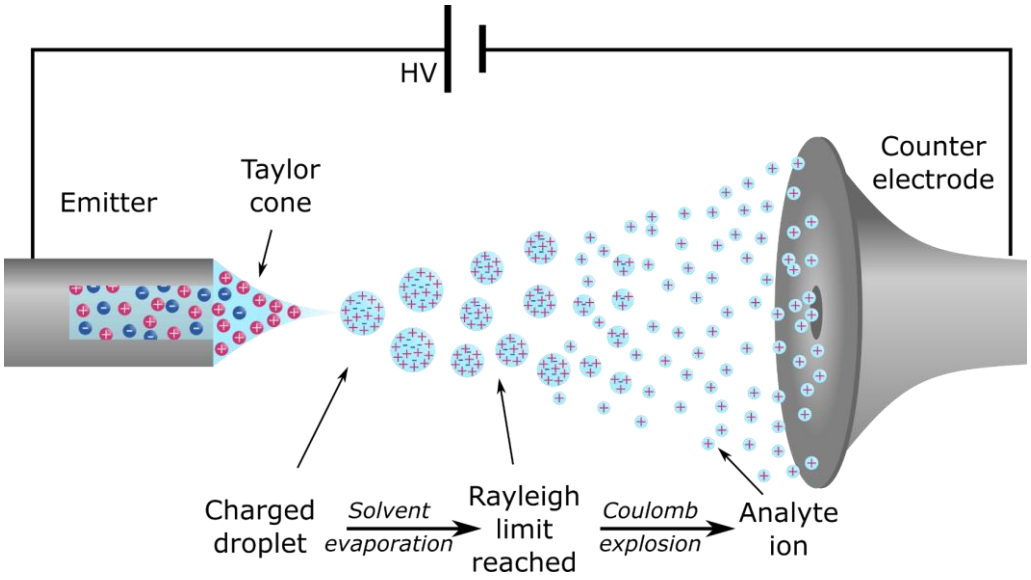


***Figure 2.1*** *Depiction of the ESI process. A strong electric field between emitter (filled with analyte solution) and counter electrode is generating charged droplets at the tip of the emitter. Because of solvent evaporation and Coulomb explosion, the droplets are shrinking and disintegrate to pure analyte ions.*

### 2.1.1 Electrospray modes

Different forces act on the Taylor cone at the tip of the emitter such as electric, gravitational and capillary forces. Depending on their ratio, different regimes and behaviours of the spray can be found. In the electro-hydrodynamic (EHD) regime, which is used in practical applications, the electric forces are of the same order of magnitude as or larger than the capillary forces whereas gravitational force is negligible. The different spray modes depend on various parameters as composition and physical properties of the analyte solution, geometry and electrical conductivity of the emitter, composition and physical properties of the surrounding sheath gas and applied potentials [56, 57]. Applying low potentials, the EHD modes are periodic with periodically changing cones and emitted currents [58, 59]. A large drop is detaching from the emitter which results in a single current pulse per period (electro dripping,

Figure 2.2a). In spindle and intermittent cone-jet mode, a fine spray of charged droplets is emitted. This electrospray is interrupted by the detachment of a fragment or the change of the periodicity and the shape of the cone (Figure 2.2b). Applying potentials in the medium range, the EHD modes are steady due to high and continuous ion current. Figure 2.2c shows the cone-jet mode with a Taylor cone [55]. The profile and length of the cone strongly depend on flow rate and properties of the analyte such as electrical conductivity or surface tension [60, 61]. High current modes as the oscillating and the multiple-jet mode are depicted in Figure 2.2d, e. Due to the applied potentials, the jet can get unstable and starts oscillating by losing its symmetry and shifting laterally. Further increasing the potential, the jet splits up and the ions originate from multiple cones at the tip of the emitter [62].

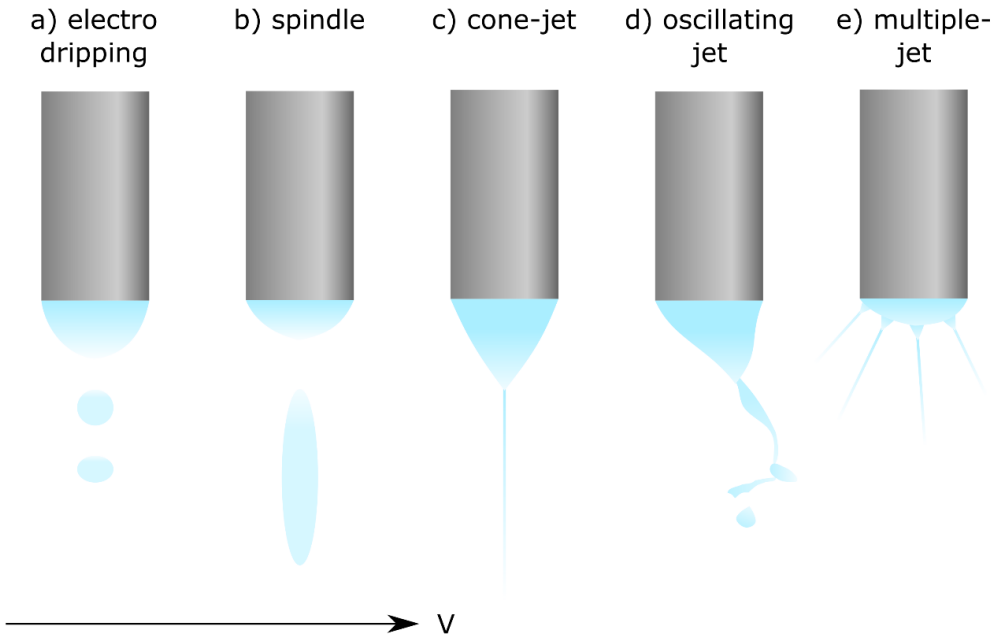


***Figure 2.2*** *Schematic depiction of electrospray modes. a) electro dripping, b) spindle, c) cone-jet d) oscillating and e) multiple-jet modes.*

Additionally, different spray parameters influence the shape of the cone, the formation and detaching of charged droplets [63–67]. A stable spray mode depends on the applied potential on the emitter, the pumping speed of the syringe, composition of the analyte solution and on surrounding gases. A stable spray mode can be identified by the shape of the cone and generated by varying the parameters.

### 2.1.2 Coulomb fission

When the highly charged droplets are accelerated towards the counter electrode, the neutral solvent molecules in the analyte solution start evaporating. While the droplets shrink, they can only hold a distinct maximum number of positive or negative charge. This critical charge $q_R$ is called Rayleigh limit and depends on the size and the surface tension $\gamma$ of the droplets:

$$q_R = 8\pi \cdot \sqrt{\varepsilon_0 \cdot \gamma \cdot r^3} \tag{2.1}$$

With the vacuum permittivity $\varepsilon_0$ and the radius of the droplet $r$ [68]. For $q = q_R$, the surface tension is equal to the Coulomb repulsion. If $q \geq q_R$, the droplets become unstable and are sensitive to small perturbations. The charged droplets split in order to increase their surface area (Coulomb fission) [69, 70]. After a few cycles of Coulomb fission and solvent evaporation, the size of the droplets decreases from some µm to few nm [71]. Translating the calculation of the Rayleigh limit based on the diameter of a spherical water droplet (standard conditions) into a function of molecular mass, it can be concluded that objects up to approximately $600$ Da are capable to carry a single charge. Modification of this calculations is required for other shapes of objects and composition of solvent (exemplary calculated for cylindrical shapes of DNA in Section 4.3.2).

### 2.1.3 Ion generation

The process of the formation of gas phase ions from small charged droplets can be described with three theoretical models [71]: the ion evaporation model (IEM) for molecules with low molecular weight, the charge residue model (CRM) for large, globular analytes and the chain ejection model (CEM) for long and chain-like molecules. The charge of the ions in solution originates from (de)protonation by e.g., shifting the $pH$ with acidic or basic components, additions of charged molecules, dissociation of a salt- like compound and as an adverse effect by electrolytic oxidation or reduction [72, 73].

**Ion evaporation model (IEM)**

The IEM describes the formation of gas phase ions from solvated ions usually with a low molecular weight. A schematic of the process is shown in Figure 2.3a. When the

large parent droplet (blue) starts shrinking due to solvent evaporation, the charged ion (red) is diffusing towards the surface. Because of electric forces on the ion within the parent droplet, surface protrusions start to occur when reaching the Rayleigh limit. To restore the stability of the parent droplet, a small droplet with one dissolved ion is ejected [74, 75]. This process is similar to the Coulomb fission for small droplets in the nanometre regime [76]. By the evaporation of neutral water molecules, the droplet starts shrinking and repeats the process of the IEM when reaching a critical charge. As depicted in Figure 2.4a, a molecular dynamics (MD) simulation by Ahadi et al. [77] shows $11$ $NH_4^+$ ions dissolved in $1500$ MeOH molecules forming a large droplet. Initially, the $NH_4^+$ ions are not located on the surface of the droplet. A position on the surface, as predicted by Gauss' law, is energetically unfavourable since the ammonium ions are dissolved in a polar medium. Thus, the ions could prefer to be distributed within the droplet and diffuse towards the surface induced by the dipole moment of the methanol molecules [77]. Then, the droplet features a protrusion consisting of a single $NH_4^+$ ion encapsulated by MeOH molecules. After detaching, a new small droplet with one ammonium ion surrounded by $13$ methanol molecules is formed. The large droplet can relax to its initial shape due to restored stability.

This theory was established on very small objects like sodium or ammonium cations with a diameter of about $0.1$ nm. Kebarle and Verkerk initially set an upper and lower limit for the size of droplets at about $10$ nm for IEM and CRM, respectively [78]. However, recent MD simulations on larger objects like the proteins ubiquitin and cytochrome c (with masses between $8$ and $12$ kDa) also revealed behaviours which can be ascribed to the IEM, dependent on assumed droplet sizes in combination with their charge states in solution. While proteins in small droplets ($r = 3$ nm) always ionize according to the CRM (see below), highly charged cations ($6^+$ or $8^+$) in droplets of almost twice the size ($r = 5.5$ nm) culminate in formation of gaseous ions at $\frac{1}{4}$ to $\frac{1}{3}$ of all events following an IEM process [79]. For this comparison, the model charges are not proportional to the surface of a particular droplet, which limits the meaning of the outcome.

The IEM process seems similar to the CEM (see below), however, the molecule inside the droplet remains globular in contrast to elongated unfolded structures observed with CEM processes.

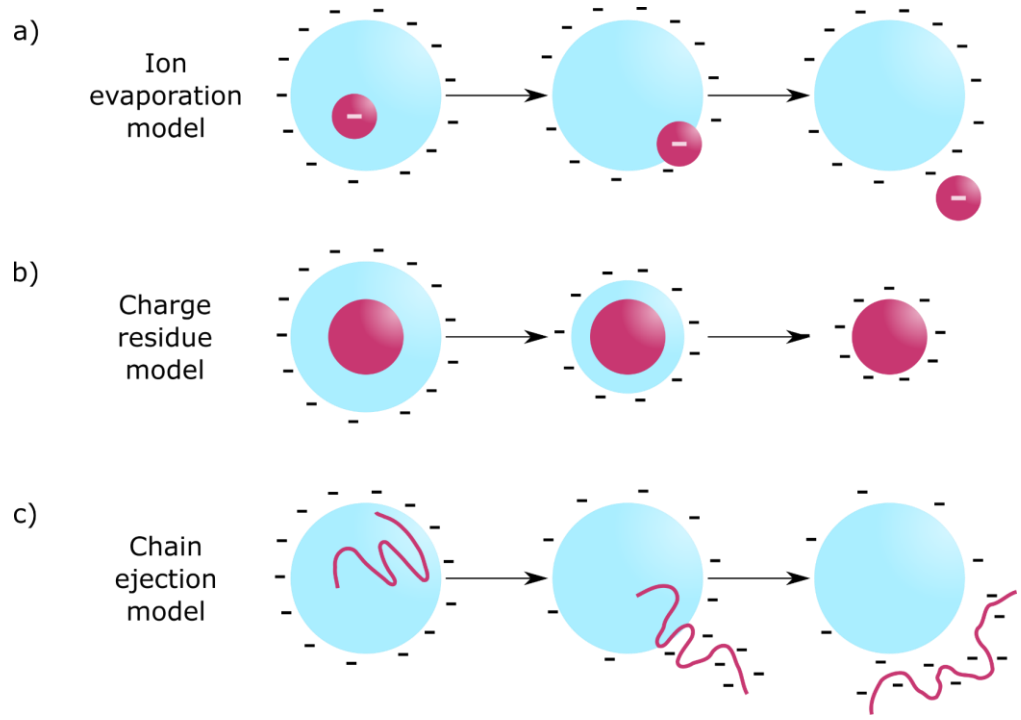


***Figure 2.3*** *Depiction of a) ion evaporation model (IEM), b) charge residue model (CRM) and c) chain ejection model (CEM) with the solvent droplet in blue and the corresponding negative ion in magenta. a) The droplet is shrinking while the solvent is evaporating. A small protrusion is formed and the ion is ejected restoring the stability of the droplet. b) The droplet shrinks because the solvent is evaporating. Small charged droplets of solvent are ejected accompanied by Coulomb fission processes until the final transmission of surface charge to drying analyte molecules. In the end, only the charged analyte molecule remains. c) The chain-like molecule inside the droplet is unfolding and diffusing towards the surface. Subsequently, it is ejected and charged incrementally (adapted from [71] with modifications).*

**Charge residue model (CRM)**

The ionization process of large, globular analyte molecules can be described with the CRM. For example, most folded proteins have a globular conformation in aqueous solutions with the hydrophobic parts to the centre and the hydrophilic parts exposed to the surrounding water environment [80]. In Figure 2.3b, the process is illustrated. The analyte molecule (red) is in the centre of a large droplet (blue) which is charged close to the Rayleigh limit. The solvation shell around the molecule is small. The charge carriers in the solution influence the chemistry and mass of the resulting ion. The analyte molecule is charged as soon as the last solvent molecule of the shell evaporated [78, 81–83]. As a result, the globular proteins stay in a native conformation charged close to the Rayleigh limit of a comparable solvent droplet [84]. A MD simulation (Figure 2.4b) shows a water droplet with a diameter of $3$ nm containing the folded protein ubiquitin and $16$ $Na^+$ ions. Due to evaporation of neutral solvent molecules, the droplet starts

shrinking. In consequence, the charge accumulates on the surface resulting in an imbalance of surface charge and surface tension. Local electrical disturbances lead to ejection of small charged droplets similar to the IEM process until the entire droplet oscillates at the Rayleigh limit ensuing global fission into smaller charged droplets. This iterative process results eventually in a final stage with the analyte molecule surrounded by a thin, however, charged solvent shell. Upon further evaporation, the solvent shell transmits its surface charges to the drying analyte molecule. Finally, the remaining ubiquitin is charged by six residual $Na^+$ ions.

**Chain ejection model (CEM)**

The ionization process of disordered, chain-like molecules, like DNA, unfolded proteins or polymer chains, can be described by the CEM (Figure 2.3c). A chain-like molecule in globular conformation (red) is starting to unfold within a droplet (blue) which is charged close to the Rayleigh limit. Then, the unfolded molecular chain diffuses towards the surface. Finally, it is stepwise charged and ejected from the droplet into gas phase until it is completely detached [85, 86]. Figure 2.4c depicts a MD simulation of a coarse-grained model consisting of $27$ backbone (brown) and $26$ side chain beads (positive: blue, negative: green). The polymer is located close to the centre of a water droplet with four additional $NH_4^+$ ions. When the chain is ejected, small amounts of solvent molecules attach to the hydrophilic side groups. Finally, the strongly elongated chain is detached from the droplet [85].

An ion, following the CEM, often carries a high number of charges. The charges are transferred to the molecule during the incremental ejection process which is driven by a combination of electrostatic repulsion and hydrophobicity. A presumed charge equilibration between the droplet and its protruding polypeptide tail is accounted for the high protonation rate and the very fast process for the often high intensities observed in respective mass spectra [87].

In summary, ions produced by the CRM process stick most time during the ionization process in the droplet centre. They are charged by the final collapse of the charged solvent shell resulting in a surface charge close to the Rayleigh limit of a comparable water droplet. In an IEM process, molecules continuously diffuse towards the surface of the droplet at which they are ejected while acquiring the local charges of the surface segment. Ions emerging from a CEM process also diffuse to the surface. As the elongated species are ejected progressively, they can carry more charges than a globular molecule of the same mass.

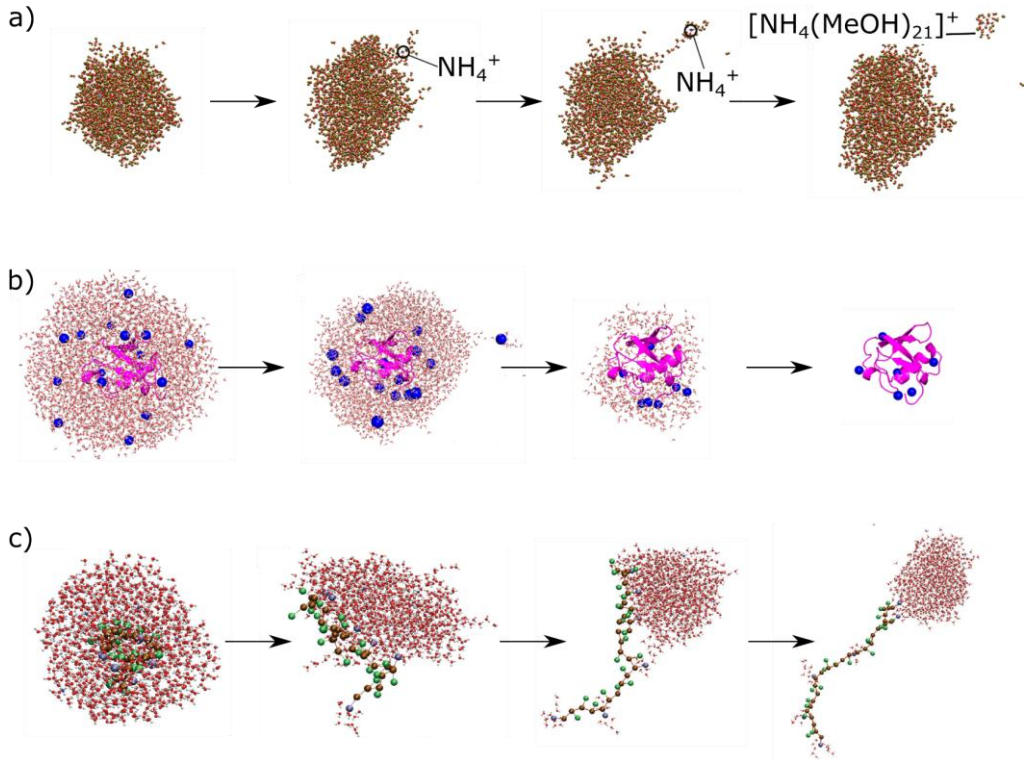


***Figure 2.4*** *MD simulation of a) IEM, b) CRM and c) CEM. a) hydrogen (white), oxygen (red), nitrogen (blue) and methyl groups (ochre). From [74] with modifications. b) hydrogen (white), oxygen (red), sodium (blue) and the folded protein (magenta). From [84] with modifications. c) hydrogen (white), oxygen (red), nitrogen (blue), neutral backbone of the chain (brown), positive side chain (large blue), negative side chain (orange). From [85] with modifications.*

## 2.2 Working principle of ion guides

After generating ions in the ion source, they can be transferred from ambient pressure to UHV using ion optics. There are DC ion guides with static electric fields such as electrostatic lenses [88, 89] and RF driven ion guides [90] such as stacked ring ion guides and linear multipole ion guides. The RF field which is generated between the electrodes of the RF ion guides, is trapping the ions inside the ion guide [49]. Here, only principles of RF driven ion guides are described.

**Stacked ring ion guide**

A stacked ring ion guide or funnel can be operated at high pressures. The trajectory of the ions inside the ion guide is along the axis of the stacked ring electrodes. The inscribed radius of the electrodes is shrinking from inlet to outlet which defines the diameter of the ion beam (Figure 2.5a). Neighbouring electrodes are supplied with RF signals which are shifted by $180°$ in phase. Additionally, a DC gradient, which is realized

by an array of resistors, can be applied along the axis of the ion guide. In a high pressure regime, the ions scatter with residual gas atoms and thus, tend to follow the gas flow towards the vacuum pump[1]. Because of the RF field in $xy$-direction and the adjustable DC potential along the $z$-axis, the ions are trapped inside the funnel and a driving force is generated in order to accelerate the ions towards the outlet, respectively.

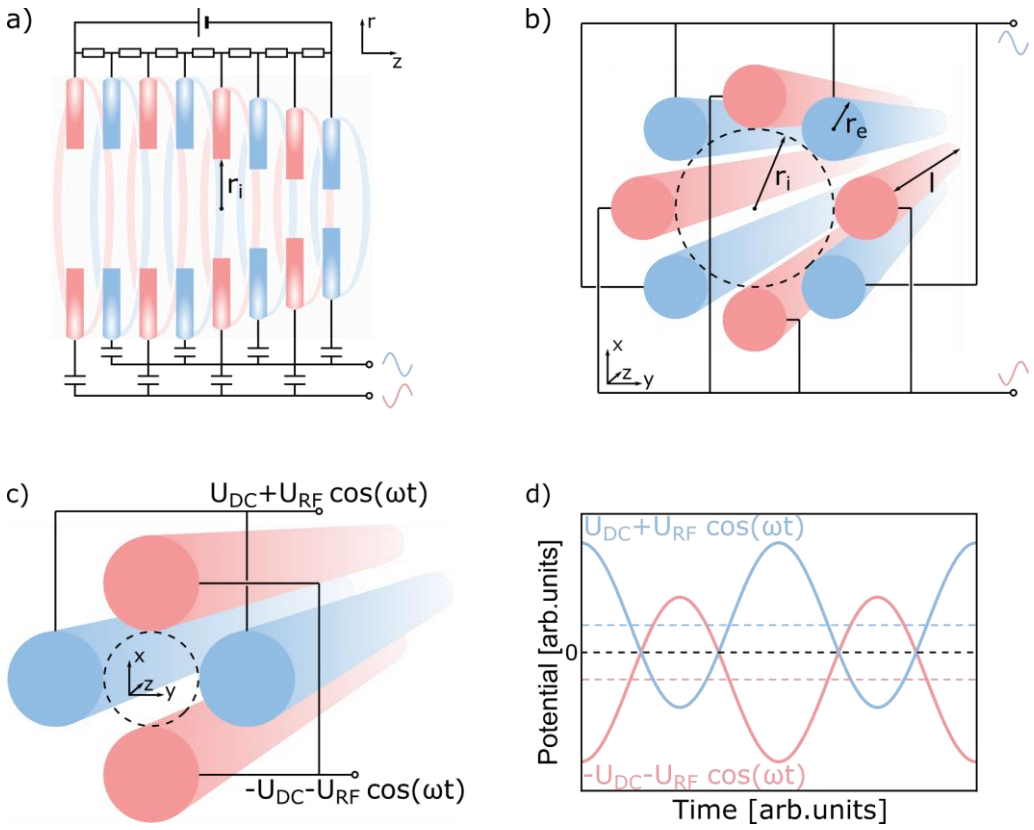


***Figure 2.5*** *Schematics of electrode arrays and electrical supplies. a) a stacked ring ion guide, b) a linear multipole ion guide with eight electrodes and c) a linear QMS. The blue and red electrodes indicate the different RF signals which are shifted by* $180°$ *in phase.* $r_i$ *is the inscribed radius,* $r_e$ *is the radius of the electrodes and* $l$ *is the length of the ion guide. d) The graph shows the applied RF signals with superimposed DC potentials to operate a QMS (adapted from [49] and [91] with modifications).*

**Linear multipole ion guide**

A linear multipole consists typically of an even number of cylindrical electrodes, which are arranged circular around a central axis, equidistantly (Figure 2.5b). An oscillating field is generated by applying RF potentials (sinusoidal or rectangular) on the electrodes which are shifted by $180°$ in phase at neighbouring electrodes. This creates a two-dimensional trapping potential around the central axis to guide ions along a desired

[1] Depends on pressure

path. With suitable potentials and dimensions of the electrodes, certain charged particles can have stable trajectories when they are located in the inscribed radius[2] of the ion guide. In contrast to the stacked-ring ion guide, a multipole ion guide has no continuous potential gradient in $z$-direction and is suitable for low pressures.

**Linear quadrupole mass spectrometer (QMS)**

The linear quadrupole has two electrode pairs and is a special case of a linear multipole. Developed in the 1950s by Paul and Steinwedel [92, 93], the QMS is used especially for mass spectrometry and ion filtering [32, 94–96]. In contrast to a multipole ion guide, only a small $m/z$-range of ion should be transmitted. In 1989, Prof. Dr. Wolfgang Paul was awarded the noble price for the development of the ion trap technique.

Four rods with a specific geometry[3] are used as electrodes to generate the quadrupole field (Figure 2.5c). A ratio of electrode radius to inscribed radius in the range of $\frac{r_e}{r_i} \approx 1.14 - 1.16$ is suitable for operation. Neighbouring rods are supplied with alternating electrical signals shifted by $180°$ in phase. The signal consists typically of a sinusoidal RF signal with an amplitude $U_{RF}$ and a superimposed DC potential $U_{DC}$ (Figure 2.5d). The resolving DC is the potential between the two rod pairs. Using theoretical calculations, stable trajectories of the ions inside the quadrupole can be estimated.

Considering a particle with mass $m$ and charge $q$ in an external electro-magnetic field with $\vec{E}(\vec{r},t)$ and $\vec{B}(\vec{r},t)$, the equation of motion can be written as [90]:

$$m\ddot{\vec{r}} = q\vec{E}(\vec{r},t) + q\dot{\vec{r}} \times \vec{B}(\vec{r},t). \tag{2.2}$$

Neglecting the finite length of the rods ($z = \infty$), Equation 2.2 can be separated into $x$- and $y$- direction [32]. In dimensionless form, the equation yields

$$\frac{d^2x}{d\tau^2} + (a_x + 2q_x \cos 2\tau)x = 0$$
$$\frac{d^2y}{d\tau^2} + (a_y + 2q_y \cos 2\tau)y = 0 \tag{2.3}$$

with $\tau = \frac{\omega t}{2}$. The parameters $a$ and $q$ are defined as

[2] Radius of the largest circle inside the ion guide that does not touch the electrodes.

[3] They can be circular or hyperbolic.

$$a_x = -a_y = \frac{4qU_{DC}}{mr_i^2\omega^2}$$
$$q_x = -q_y = \frac{2qU_{RF}}{mr_i^2\omega^2} \quad (2.4)$$

with the frequency $\omega$. The ion motion can result in a stable ion trajectory for a given set of $U_{DC}$, $U_{RF}$ and $\omega$. This causes ions of a certain $m/z$-range to be able to pass the quadrupole. As shown in Figure 2.6, the apices of the stability regions of ions with different mass-to-charge ratio (grey) can be connected by a straight line (black) with the slope $\frac{a}{q} \propto \frac{U_{DC}}{U_{RF}}$.

A mass-resolved scan is performed by simultaneously ramping up $RF$ and $DC$ amplitudes along a pre-defined curve. This curve is typically a straight line with a small offset to lower DC potentials and a lower slope compared to the line of apices. As only a small range of $m/z$- ratios allow for a stable trajectory for each set of potentials on the scan line, the resulting transmitted ion current can be directly attributed to a certain $m/z$-ratio and a spectrum can be recorded. However, there is always a conflict between transmission efficiency and resolution. A scan line close to the apices of the stability region results in a high resolution, but might lead to a low transmission. A second way of scanning is the $RF$-only mode. Here, the scan line follows the $U_{RF}$-axis without an superimposed DC potential. As the stability diagrams of each mass has an intersection with the $U_{RF}$-axis, each $m/z$-ratio has a critical RF amplitude $U_{RF,critical}$ without stable trajectory for $U_{RF} > U_{RF,critical}$. For low RF amplitudes, the signal is resulting from all intensities of mass-to-charge ratios with $U_{RF} < U_{RF,critical}$. Ramping up the amplitude, the intensity drops significantly when $U_{RF} > U_{RF,critical}$ of a charged particle in the ion beam. The power supply of a QMS with sinusoidal $RF$ signal consists of a resonant $LC$ circuit with a constant frequency $\omega$ and adjustable voltages.

In comparison to regular sinusoidal RF driven QMS, the stability diagram of a rectangular RF is compressed in $q$-direction. Thus, the apex of the stability region shifts to a lower RF amplitude with a nearly constant DC offset (dimensionless amplitude $q = 0.55$, DC offset between RF phases $a = 0.23$) [97–99]. Moreover, a rectangular RF driven QMS allows for variable frequencies and thus, can be used for a nearly unlimited mass range.

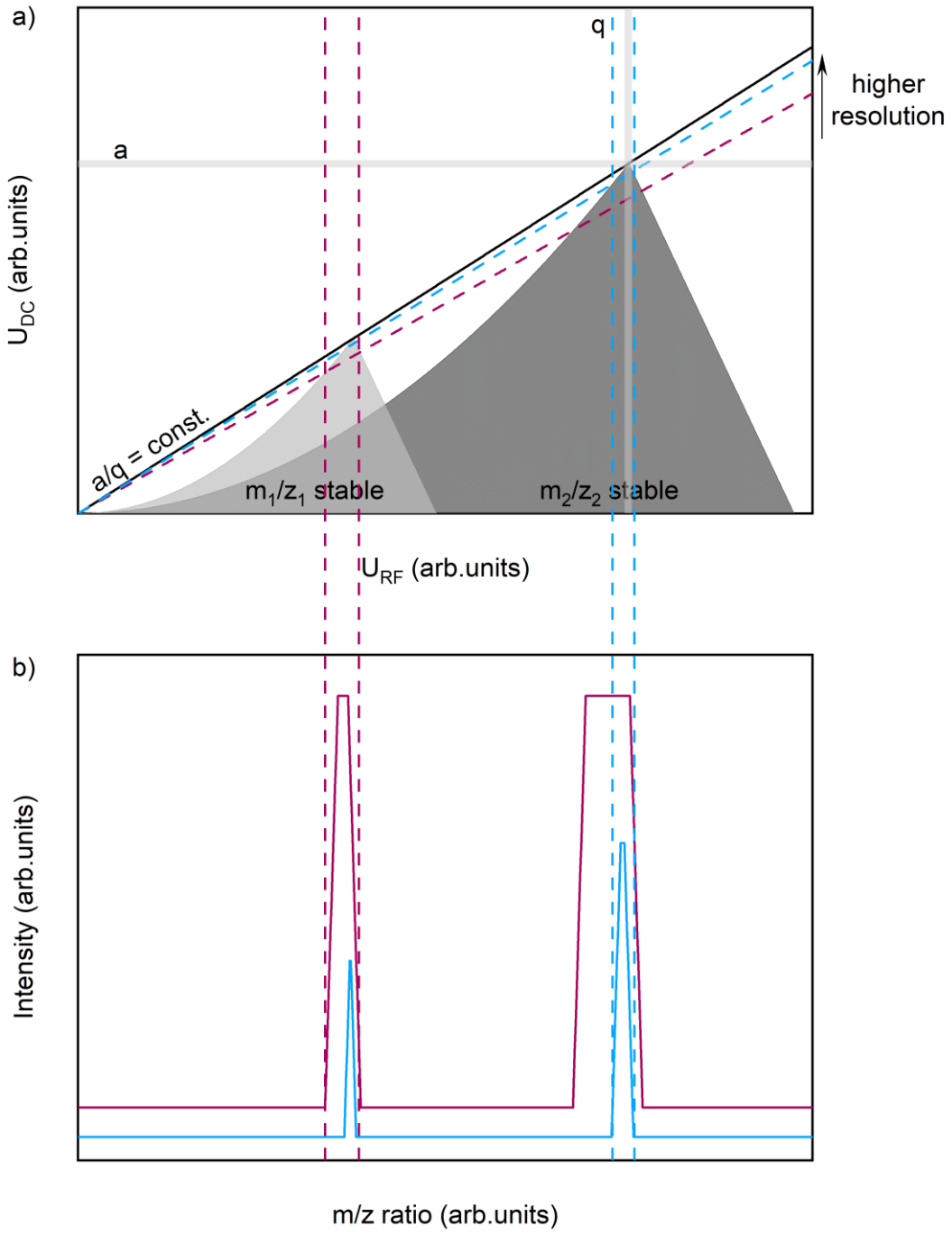


***Figure 2.6*** *a) Stability diagram of a QMS. The regions of two mass-to-charge ratios with stable trajectories in $x$- and $y$-direction are depicted in grey. Two scan lines with different resolving DC and b) the resulting mass spectra are plotted in blue (high resolution) and red (low resolution). Adapted from [49] with modifications.*

## 2.3 Deposition of charged particles

The successful landing of charged particles on solid surfaces in UHV is the last step of the ES-CIBD process. The different processes of deposition can be divided into four groups by the kinetic energy of the ions [44, 100–102]:

| Soft landing | | Reactive landing | |
|---|---|---|---|
| Thermal range | Hyperthermal range | Low energy range | High energy range |
| $< 1\ \mathrm{eV}/z$ | $1 - 100\ \mathrm{eV}/z$ | $0.1 - 100\ \mathrm{keV}/z$ | $> 100\ \mathrm{keV}/z$ |

***Table 2.1*** *Temperature ranges of soft and reactive landing.*

The so-called soft landing is defined as the deposition without chemical decomposition and thus, with preserving structural and chemical integrity [41]. In contrast, the reactive landing uses high landing energies to intentionally decompose molecules on the surface as typical energies of chemical bonds are $\leq 10\ \mathrm{eV}/z$. This allows for manipulation of conformation and reformation of bonds. Energies above $100\ \mathrm{eV}$ are used for ion implantation, Rutherford backscattering or sputtering [44]. Additional to the landing energy, the structure of the molecule and the surface have an influence on physical and chemical properties of the deposition, as energy transfer by electronic and vibrational excitation, charge transfer and reactions [44, 100]. Hard surfaces could already decompose landing molecules at low kinetic energies, while soft surfaces, such as organic brush-like structures or some self-assembling monolayers (SAMs) [41, 103] are established to cushion impact. Small ions are rigid and thus, they are prone to decomposition at high energetic states. In contrast, large ions allow for high landing energies as they have a high degree of freedom [46, 100, 104–106]. Large molecules tend to have a higher charge and an increasing $m/z$-ratio[4] than small particles (see Section 2.1). Thus, a maximum kinetic energy per charge of an ion is a better criterion than an absolute value. The landing energy of the ions is defined by the electrical potential applied to the target surface which requires an electrically conducting or semi- conducting substrate material. The charge which is introduced by deposited particles is directly neutralized or induces a mirror charge and thus, leads to a current

[4] Not proportional! The mass is proportional to $r^3$ and the charge depends on the surface and thus, is proportional to $r^2$

on the sample. This current is proportional to the ion beam intensity. Non-conductive surfaces, however, lead to charge accumulation and thus, uncontrollable changes of the potential and undefined landing energies [103, 104, 107–110]. Soft-landing and reactive- landing experiments have already been performed with proteins, oligomers, peptides and carbohydrates [45, 47, 106, 107, 111–116].

## 2.4 Scanning tunnelling microscopy

Scanning tunnelling microscopy (STM) is a surface sensitive technique that scans the surface in order to measure its properties. Furthermore, it allows for the investigation of deposited molecules in UHV. It was invented by Binning and Rohrer in 1983 [117] for which they were awarded the noble prize in 1986 [118]. During operation, a sharp, conductive tip (shown in Figure 2.7) is close to the surface. By applying a bias voltage, a current is induced between tip and sample surface based on the tunnelling effect. The current sensitively depends on the distance between tip and surface and, thus, gives information about the structure of the surface.

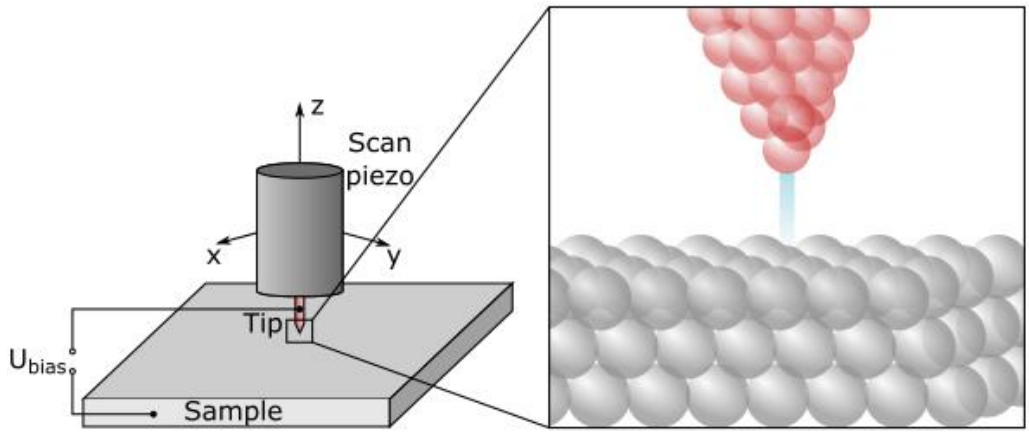


***Figure 2.7*** *Principle of STM. A tip attached to a piezo-tube is scanning the surface of a crystal. The zoom-in shows the tip close to the surface which results in a tunnelling current. Adapted from [119] with modifications.*

### 2.4.1 Electron tunnelling

The tunnelling effect is a quantum mechanical phenomenon which was first observed in the early 20$^{th}$ century [120]. In classical physics, an electron cannot propagate through a potential barrier $V(\vec{r})$ which is higher than its own kinetic energy $E$. In quantum

mechanics, an electron can be described by a wave function $\psi(\vec{r},t)$ which is defined by the Schrödinger equation

$$-\frac{\hbar^2}{2m}\nabla^2\psi(\vec{r},t)+V(\vec{r},t)\psi(\vec{r},t)=\frac{\mathrm{d}}{\mathrm{d}t}\psi(\vec{r},t) \tag{2.5}$$

with the reduced Planck constant $\hbar=\frac{h}{2\pi}$ and the mass of the electron $m$. Restricting the Schrödinger equation to time-independent and one-dimensional case, leads to

$$-\frac{\hbar^2}{2m}\frac{\mathrm{d}^2}{\mathrm{d}z^2}\psi(z)+V(z)\psi(z)=E\psi(z). \tag{2.6}$$

As shown in Figure 2.8a, a potential landscape of an electron propagating in positive $z$- direction leads to the solution of Equation 2.6 which is given by

$$\psi(z)=\begin{cases}\psi_0\exp\left(i\frac{\sqrt{2m(E-V_0)}}{\hbar}z\right), & z<0\\ \psi_0\exp\left(-\frac{\sqrt{2m(V_1-E)}}{\hbar}z\right), & 0\le z\le z_0\\ \psi_0\exp\left(-i\frac{\sqrt{2m(E-V_0)}}{\hbar}z\right), & z>z_0.\end{cases} \tag{2.7}$$

In the first ($z<0$) and in the third region ($z>z_0$), the electron energy $E$ is higher than the potential $V$. The electron can propagate in positive and negative $z$-direction if $z<0$ and has a non-vanishing probability to be observed if $z>z_0$. The solution of the Schrödinger equation in the second region ($0\le z\le z_0$) can be found using the first derivative (cf. Figure 2.8b) and the continuity of the wave function $\psi(z)$. The probability $P$ to find an electron inside a barrier with the height $V_1$ and the width $z_0$ can be calculated by

$$P=|\psi(z_0)|^2=|\psi_0|^2\exp\left(-2z_0\frac{\sqrt{2m(V_1-E)}}{\hbar}\right). \tag{2.8}$$

In theory for STM, the first and third regions represent tip and sample and the second region can be identified with the vacuum barrier between tip and sample, as shown in Figure 2.8c.

Applying a bias voltage $eU$ which is much smaller than the work function $\phi = -E_F$[5], electrons with energies $E_F - eU < E < E_F$ contribute to a net tunnelling current

$$I \approx I_0 \exp\left(-2z_0 \frac{\sqrt{2m\phi}}{\hbar}\right). \tag{2.9}$$

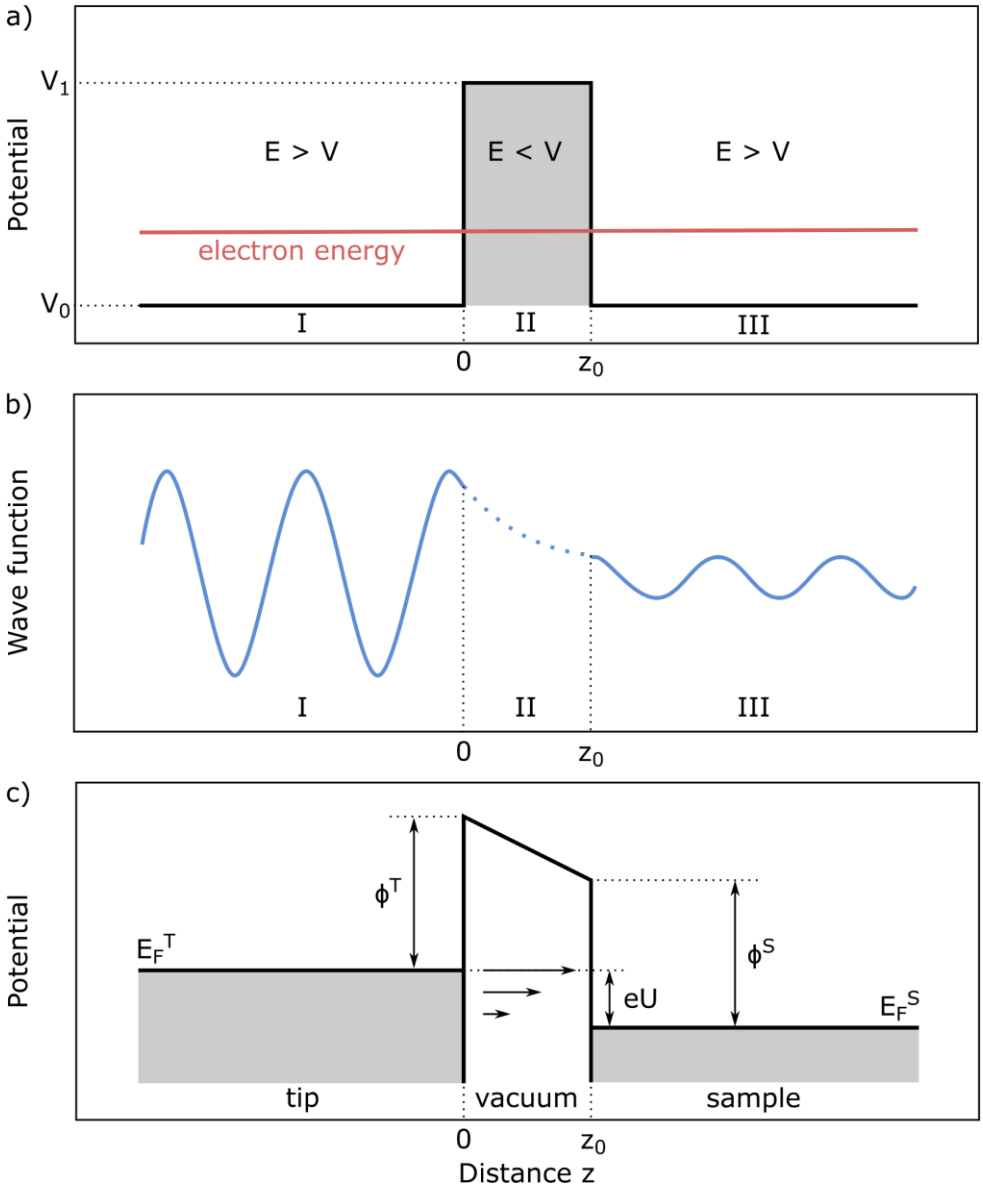


***Figure 2.8*** *Schematic depiction of a) Electron tunnelling through a potential barrier. b) Wave function with exponential decay. c) Electron tunnelling with applied bias voltage $U$. At low temperatures and small voltages, only electrons with Fermi energy contribute to the tunnelling current. Adapted from [119] with modifications.*

[5] For simplification, work function of tip and sample are assumed to be equal ($\phi = \phi^{Tip} = \phi^{Sample}$).

Without applying a bias voltage, the electrons can tunnel from tip to sample and vice versa due to thermal activation. The tunnelling junction is treated as in Bardeen's approach [121] with restrictions according to Tersoff and Hamann [122]. It suggests that tip and sample have different wave functions $\psi_T$ and $\psi_S$ and that a matrix element describes the overlap of the two wave functions at a separating surface. The transition probability $T$ is defined by

$$T = \frac{2\pi}{\hbar} |M_{ST}|^2 \delta(E_S - E_T) \tag{2.10}$$

with $M_{ST} = \langle \psi_S | \mathcal{H} | \psi_T \rangle$, the matrix element for an Hamiltonian $\mathcal{H}$ which is generally unknown. Thus, the tunnelling current can be written as

$$I = \frac{2\pi e^2}{\hbar} U \sum_{T,S} f(E_T)[1 - f(E_S + eU)] |M_{ST}|^2 \delta(E_T - E_S) \tag{2.11}$$

with the Fermi function $f(E)$. The sum includes only electrons which are tunnelling from occupied states of the tip to unoccupied states of the sample (cf. Pauli exclusion principle). For elastic tunnelling, which includes energy conversation, the $\delta$-function has only states with the same energy. For low temperatures and small voltages, the Fermi function becomes step-like which results in a tunnelling current

$$I = \frac{2\pi e^2}{\hbar} U \sum_{T,S} |M_{ST}|^2 \delta(E_T - E_F) \delta(E_S - E_F). \tag{2.12}$$

As the $\delta$-function implies, only electrons with states close to Fermi energy contribute to the tunnelling current. Bardeen proposed that $|M_{ST}|$ can be treated as a constant as it does not change significantly around the Fermi level. Assuming constant tip parameters as radius $R$, work function $\phi$ and density of states (DOS) $\rho_T(E_F)$, the current is proportional to the convolution of DOS of tip and sample:

$$I \propto \sum_{T,S} \rho_S(E_T - E_F) \rho_T(E_S - E_F). \tag{2.13}$$

Thus, the tunnelling current strongly depends on the distance between tip and sample surface. This makes STM a suitable technique to measure electronic and topographic properties of the surface at the atomic scale [121–124].

### 2.4.2 The Tersoff-Hamann model

Tersoff and Hamann [121, 125] suggest a simple model to define the local DOS of the tip and the tunnelling matrix element. Assuming a spherical potential of a defined radius $R$, it is modelled as an atomically sharp tip with an apex consisting of a single atom. According to the Tersoff-Hamann model, the tunnelling matrix element $|M_{ST}|$ can be calculated by

$$M_{ST} = \frac{2\pi\hbar}{m}\sqrt{\Omega_T R \exp(\kappa R)\,\psi_S(\overrightarrow{r_0})} \tag{2.14}$$

$\Omega_T$ is the volume of the tip, $\kappa = \frac{\sqrt{2m(V_1-E)}}{\hbar}$ is the decay constant and $\overrightarrow{r_0}$ is the position of the apex centre. The model treats the local DOS of the tip as constant, sets the temperature of the junction to zero and disregards inelastic tunnelling. This results in a tunnelling current which depends on the DOS of the sample and the decay constant:

$$I = \frac{32\pi^3 e^2 U \phi^2(E_F) R^2}{\hbar\kappa^4}\exp(2\kappa R)\rho_T(E_F)\sum_S \rho_S(E_T - E_F). \tag{2.15}$$

This model is a very simplified interpretation of the electronic structure of the tip, but very valuable for the interpretation of STM images or simulations.

### 2.4.3 STM operation modes

STM provides two different operation modes. The constant-current mode keeps the tunnelling current constant with a feedback loop. During a measurement, the current is continuously measured and compared to a setpoint value. Amplifying the current and converting the difference between current and setpoint to a voltage, the $z$-piezo is moved to the correct the height of the tip. The tip is retracted if the measured current is larger than the setpoint and vice versa. In this way, the tip follows the corrugation of the surface as it is shown in Figure 2.9a. Therefore, the information of the image depends on the topography and on the local DOS of the sample.

Measuring in the constant height modes, the tip height remains constant while the current is the measurement signal as it can be seen in Figure 2.9b. This operation mode requires flat surfaces, absence of thermal drift and vibrational damping which makes its application difficult.

STM measurements allow for real space imaging with atomic resolution. The topographic maps show orientation, assemblies, size and electronic information of the species on the surface. In this thesis, the STM is used to identify and analyse molecules which are deposited by ES-CIBD.

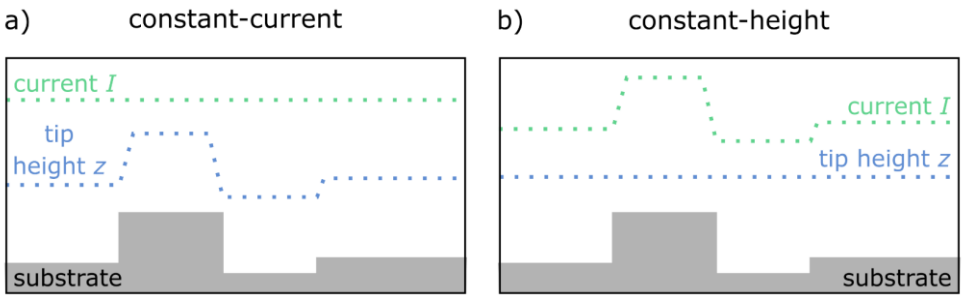


***Figure 2.9*** *Depiction of STM operation modes. a) The tip height is varied in the constant- current mode. b) In the constant-height mode, the current is measured. Adapted from [119][119] with modifications.*

## 2.5 Ultraviolet-visible spectroscopy

Ultraviolet-visible spectroscopy (UV-Vis) is an absorption spectroscopic technique which uses ultraviolet and visible light. Molecules are able to absorb energy for excitation of these electrons to higher molecular orbitals. The more easily the electrons get excited, the longer is the wavelength of light that can be absorbed. UV-Vis can be used for quantitative determination of analytes such as biological macromolecules.
Using the Beer-Lambert law, the concentration $c$ of an absorbing species in solution can be measured [126, 127]:

$$A = \log\left(\frac{I_0}{I}\right) = \varepsilon \cdot c \cdot L \tag{2.16}$$

With the measured absorbance $A$, the intensity of the incident light at a distinct wavelength $I_0$, the transmitted intensity $I$, the path length through the sample $L$ and the extinction coefficient $\varepsilon$.
The sample analyte is typically placed in transparent cuvettes with a length of $1\,\mathrm{cm}$ made from fused silica or quartz glass. The spectrophotometer consists of a light source (Deuterium arc lamp for UV, Tungsten filament for Vis), a holder for the sample, a diffraction grating and a photomultiplier as detector. First, a cuvette filled with the solvent and without the analyte molecule is measured [128] as a reference. Subtracting

the reference measurement from the absorbance signal of the sample molecules gives access to the concentration of the analyte according to Equation 2.16.

## 2.6 Biomolecules

Biomolecules are essential organic compounds exerting numerous functions in living organisms such as metabolism, cell division and development, regulation, as carrier of information and as structuring elements. Biological molecules mainly constitute from the four key groups, nucleic acids, lipids, (poly)peptides and carbohydrates. All these compounds mainly consist of oxygen, carbon, hydrogen and nitrogen, in addition to further elements such as phosphorus, sulphur and various metals. The composition is characteristic and determines the function of single molecules and in combination with partners.

### 2.6.1 Deoxyribonucleic acid

Deoxyribonucleic acid (DNA), as representative of nucleic acids group, carries the information for proteins besides some additional regulatory properties. DNA is built from two parallel strands consisting of repetitive nucleotide building blocks, which assemble into long, string-like twisted macromolecules called (double)helix (Figure 2.11). Basically, two kinds of molecular interaction drive this structure: alternating covalently- bound phosphate-ribose (monosaccharide sugar) units are building the backbone. Nucleobases of purine type (adenine A, guanine G), linked to the ribose perpendicular to the axis of the helix, connect to an opposite nucleobase of pyrimidine type (thymine T, cytosine C), which is bound to a second backbone strand, by $2$ or $3$ hydrogen bonds (Figure 2.10, Figure 2.11). The interaction of A with T or C with G, called Watson-Crick pairing [129], constitutes the characteristic three-dimensional structure of the most common form of DNA[6].

Because of the threefold hydrogen bonding, the cytosine/guanine base pair has a higher binding energy than the thymine/adenine base pair with only two hydrogen bonds. The specific nucleobase composition of a certain DNA sequence results in a characteristic temperature at which the hydrogen bonds break leading to a disassembly of the double

[6] There exist other pairing types than Watson-Crick resulting in different 3D structures such as quadruplexes [130–132].

strand into two single strands (melting) and in turn, at cooling its re-assembly. This sequence-dependent feature is used to control specific amplification of DNA in the procedure of PCR [133]. Melting of double strand DNA was applied in some of the ESI experiments to generate single strand species (see Chapter 4.2).

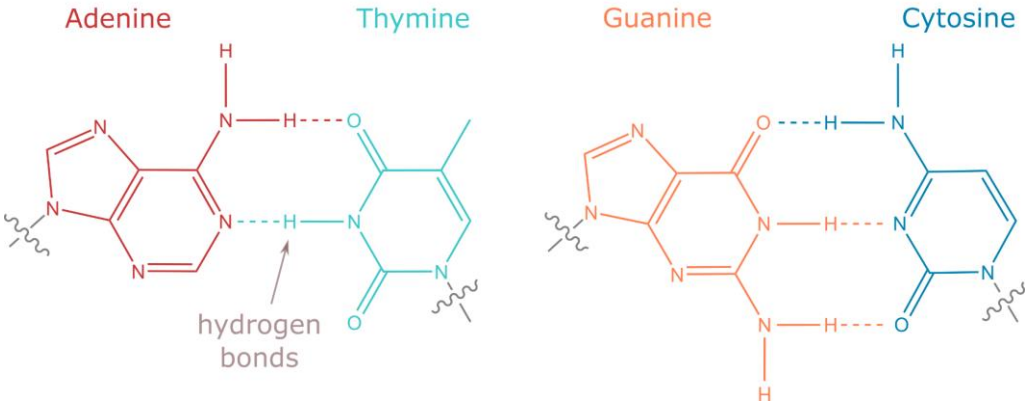


***Figure 2.10*** *WCBP for adenine/thymine and guanine/cytosine[7].*

In physiological environment, two antiparallel polynucleotide strands coiling around each other form a right-handed double helix (B-form, [134]). Because of the helical structure and because the strands are not symmetrically located with respect to each other, the two grooves between the strands are unequally sized. Besides the B-Form, other DNA helix forms exist with different geometries such as direction of rotation, diameters, axial rise etc. (see Table 2.2). In drying experiments, conversion of B-Form DNA to A-form DNA could be observed [135].

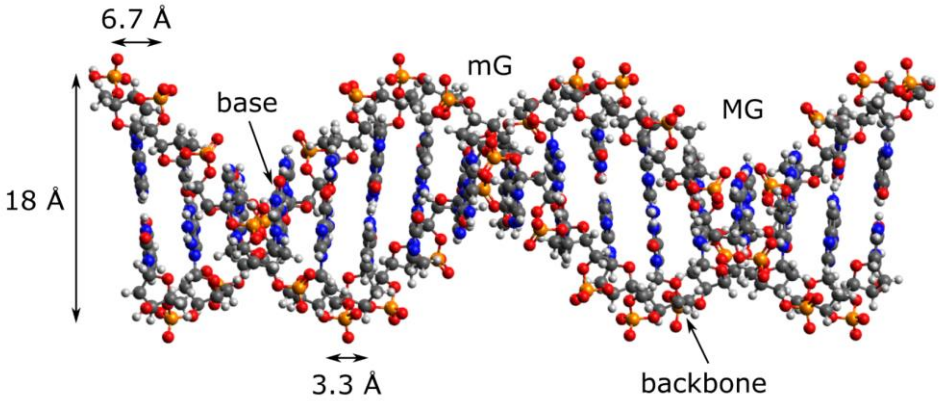


***Figure 2.11*** *Structure of a double-strand DNA in B-form (modelled with [136]).*

[7] ChemDraw, PerkinElmer Instruments

| | | B-form | A-form | Z-form |
|---|---|---|---|---|
| **Orientation** | | right | right | left |
| **Diameter** | | 2.0 nm | 2.6 nm | 1.8 nm |
| **Bp per turn** | | 10 | 11 | 12 |
| **Distance between bp** | | 3.3 Å | 2.9 Å | 3.7 Å |
| **Minor groove (mG)** | **Width** | 5.7 Å | 11.0 Å | 2.0 Å |
| | **Depth** | 7.5 Å | 2.8 Å | 13.9 Å |
| **Major groove (MG)** | **Width** | 11.7 Å | 2.7 Å | 8.8 Å |
| | **Depth** | 8.8 Å | 13.5 Å | 3.7 Å |

***Table 2.2*** *Various parameters of B-, A- and Z-DNA.*

Circular DNA, which can be found in bacterial organisms, exists in different topological shapes such as open circular and supercoiled. Supercoiling means secondary winding of the double helix around its own axes compensating torsional stress that is caused by the inner-helical twists. Moreover, it is the preferred energetic state. It is not one pre- defined state of the DNA by means of a single numerical definition and thus, not strictly or unambiguously predictable. Such geometric parameters are dependent on the formation and extend of secondary spirals. This dependency is described by the concept of the linking number $Lk$ (see Appendix A.1). Supercoiling allows for compacting DNA to fit into limited space in cells and, though appearing paradoxical, also for accessing single strand segments that are required for DNA replication and transcription.

A common way to manipulate DNA sequence, 3D structure or integrity of the entire molecule is the use of enzymes. They function as catalysts for the degradation of nucleic acids including particular subspecies that are able to cut DNA strands at predetermined and sequence-specific loci (restriction enzymes). Furthermore, enzymes enable (re)connection of DNA strands (ligases) and support the modification of structure e.g., conversion into other forms (DNA to RNA by transcriptase) or the change of topology (topoisomerase). Specifically, the restriction enzymes EcoRI and topoisomerases such as Topoisomerase I modify topology and structural properties like the transformation of circular to linear conformation by changing the winding number of the DNA strands. All

of these enzymes only cause local alterations without destroying the sequence of the nucleic acids (see Section 4.2, [137]).

### 2.6.2 Proteins

Proteins are macromolecules which have various functions within organisms including DNA replication, responding to stimuli, catalysis of metabolic reactions, providing structure to cells and transport of molecules. Structure and function of proteins is defined by the sequence of their building blocks – amino acids - which in turn are coded by the sequence of nucleotides in genes. Proteins consist of one or more chains composed of 20 different, naturally occurring types of amino acid (AA) residues which is called polypeptide with a molecular mass between $\approx 10^3$ and $10^6$ u. The distance between two AA is about $1.5$ Å. The AA are connected by peptide bonds of adjacent AA residues (Figure 2.12b). All building blocks have common features: at their opposite termini an amino group (N-terminus) and a carboxyl group (C-terminus), which generate the peptide bonds, and a side chain, specific for each AA, linked to the $\alpha$-carbon (Figure **2.12**a), which constitutes individual steric and charge properties of an AA dependent on the surrounding $pH$. The classification into acidic, basic, polar uncharged and apolar AA is derived from the charge state of the side group [138]. In addition, the N- and C-termini carry charges introduced by (de)protonation.

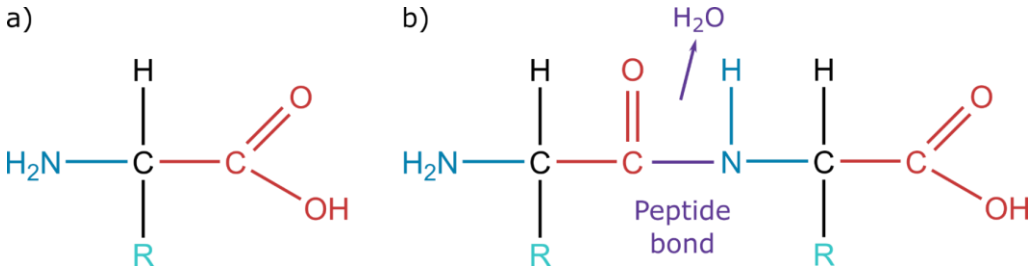


***Figure 2.12*** *a) Chemical structure of an amino acid with the amino group in blue and the carboxylic group in red. The variable side chain R is indicated in turquois. b) Chemical structure of two amino acids connected by a peptide bond (violet).*

The secondary structure is stabilized by hydrogen bonds. In 1951, two main types were suggested by Pauling et al. [139]: the $\alpha$-helix and the $\beta$-sheet. Both secondary structures provide a way to saturate hydrogen bond donors and acceptors in the peptide backbone. The $\alpha$-helixes and $\beta$- sheets are folded into globular structures which is referred to as tertiary structure. Tertiary interactions are e.g., salt bridges, hydrogen or disulfide bonds. The unique three-dimensional structure of each protein as

well as the chemical reactivity are defined by the effect of all AA side chains. The aggregation of two or more polypeptide subunits (oligomer) is called quaternary structure which is stabilized by non-covalent interactions and disulfide bonds comparable to the tertiary structure. Specifically, it is called dimer if two subunits aggregate and trimer if it contains three subunits and hexamer if there are six subunits. In aqueous solution, the hydrophobic parts of the protein chains are avoiding contact to the solvent and thus, are positioned in the centre of the protein. In contrast, the hydrophilic groups are pointing outwards and can be charged which depends on properties of the solvent as $pH$ [138].

### 2.6.3 Polyamines

Polyamines are organic compounds which have a number of secondary amino groups and can occur natural and synthetic [140, 141]. They are colourless, hygroscopic and soluble in water. At physiologically conditions (neutral $pH$), the molecules carry one or more positive charges at their amino groups introduced by protonation (polycations) due to high $pK$ values [142]. Linear polyamines with a low-molecular weight can be found in all forms of life such as triamine, tetraamine, spermidine or spermine [141]. They play a role in many cellular processes. In their cationic form, the molecules bind to DNA or RNA by hydrogen bridges [143] in order to stabilize the nucleic acids and protect them against thermal denaturation [144]. Additionally they have various other function such as modulating of ion channels, enhancing permeability of blood-brain barrier and promoting ribosomal frameshifting during translation [145].

# 3 Electrospray-controlled ion beam deposition (ES- CIBD)

Electrospray-controlled ion beam deposition (ES-CIBD) is a soft method for the deposition of large fragile and thermo-labile organic and biological molecules on single crystal substrates in UHV. The set-up, which was used for the experiments, is home- built and will be described in the following sections [49]. It uses electrospray ionization to ionize and evaporate the molecules from solution. Various RF-driven ion guides transport the ions through differentially pumped vacuum chambers from ambient pressure to the UHV regime. A digital quadrupole mass spectrometer (dQMS) analyses the ion beam and filters the ions by their mass-to-charge ($m/z$) ratio for deposition. After refocusing the ion beam, the molecules can be deposited on a sample by soft-landing or reactive landing.

## 3.1 ESI source

In Figure 3.1, a CAD image of the home-built ESI source is depicted. The syringe filled with the analyte solution is mounted in a syringe pump[8] and connected to the emitter by a hose made of fused silica using MicroTight fittings[9]. A small chamber (1), which surrounds the ion source, allows for operating in a defined environment, e.g., at reduced pressures. A vacuum flange (3) is connecting the ion source to the first vacuum chamber of the ES-CIBD set-up. A camera[10] monitors the emitter through a sealed window (2). Using micrometre drives (5), the emitter can be positioned in front of the counter electrode (9). For electric contact between high voltage supply and analyte solution, a metallic adapter (6) connects hose and emitter (8). During operation, a current of $I_{ion} \approx 10$ nA is ejected into the first vacuum chamber. A cap (7) which covers the emitter generates a defined atmosphere and a co-axial flow of dry-gas. At the atmospheric pressure interface which consists of a funnel-shaped inlet and a brass tube, two

[8] IVAC 711

[9] IDEX Health&Science

[10] Thorlabs, DCC1645C

separate heating systems (4) are installed in order to control and evenly distribute a temperature up to 200 °C.

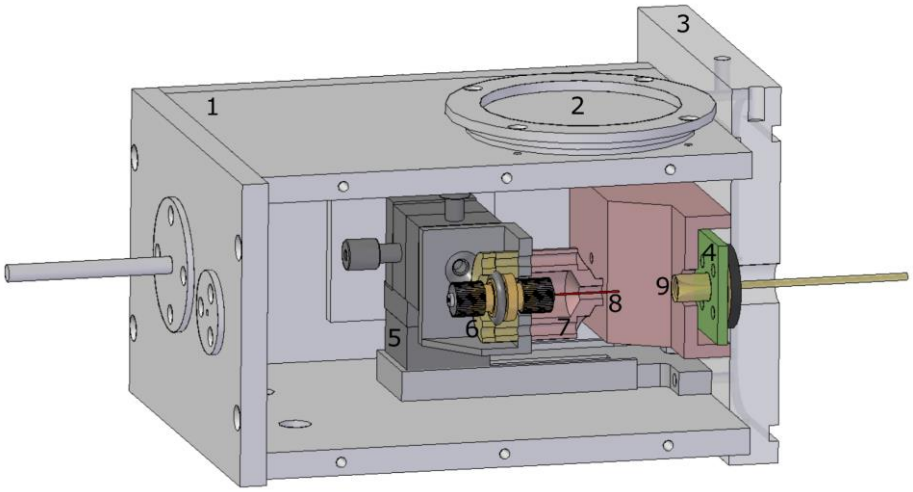


***Figure 3.1*** *Computer-aided design (CAD) of the ESI source[11]: 1) gas-tight housing, 2) window for the camera, 3) vacuum flange, 4) atmospheric heating, 5) $xyz$-motion, 6) high voltage contact and adapter, 7) dry-gas supply, 8) emitter, 9) counter electrode and atmospheric pressure interface. From [49] with modifications.*

## 3.2 ES-CIBD system

A detailed view of the electrospray-controlled ion beam deposition (ES-CIBD) set-up is shown in Figure 3.2[12].

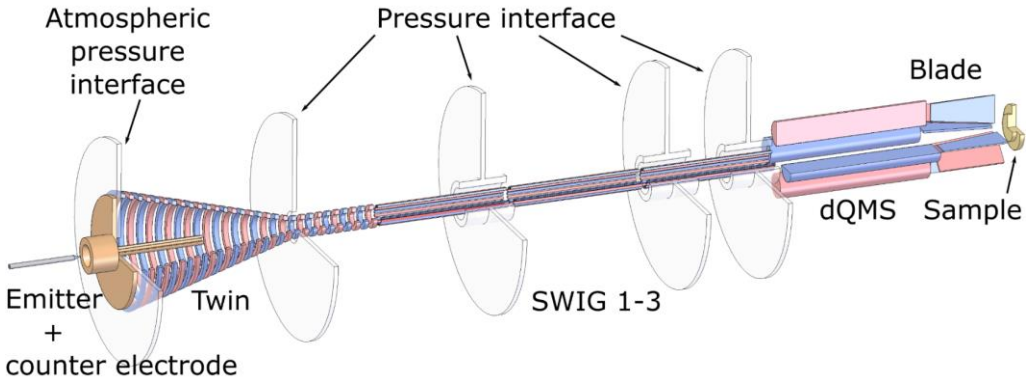


***Figure 3.2*** *CAD model of the home-built ES-CIBD system[13].*

[11] Original CAD models were mainly drawn by T. Kaposi, H. Schlichting and A. Walz during the construction phase of the machine.

[12] Patents: PCT/EP2019/058723, PCT/EP2019/058678, PCT/EP2019/058679, EP2669929

[13] Modified and adapted from CAD model drawn by H. Schlichting [146].

The ions which are generated by the ESI source are transported through the capillary of the atmospheric pressure interface into a Twin ion guide. The Twin is a combination of a funnel and a tunnel with antithetical residual gas flow in order to confine and focus the ion beam (1.5 mm). It is built as a stacked ring ion guide as it can be seen in Figure 3.2. The subsequent small wire ion guides (SWIG) transfer the ions from low pressure to the UHV regime. The SWIGs are high order multipole ion guides with 16 wire electrodes of different diameters. The SWIGs have inscribed diameters of about 2 mm.

The focused ion beam is guided to a digital quadrupole mass spectrometer (dQMS) which is used for the investigation and filtering of the ions. The quadrupole rod system[14] with pre- and post-filters has a diameter of $d_{QMS} = 19$ mm and was gold-plated by galvanization. The pre- and post-electrode systems are capacitively-coupled to the main rod system resulting in RF signals with equal frequency and phase. Large resistors are connected to each pre- and post-filter electrode pair to apply a DC offset. The offset voltage has a time-constant which is larger than typical cycle times $RC \gg f^{-1}$. Thus, the RF signal is not altered significantly. The dQMS is operated by ramping up a rectangular radio frequency (RF) signal and simultaneously, resolving DC. Because of the adjustable RF frequency, the QMS can measure over a virtually unlimited mass-to-charge range.

A Blade ion guide – a conical, high-order multipole made from 16 metal-sheet electrodes - allows for extracting ions from the dQMS and re-focusing of the ion beam towards a sample for the deposition. An ion beam with a small diameter and low kinetic energy is required for soft-landing of fragile molecules on the surface of a substrate. The Blade ion guide is a conical high order multipole with 16 radial arranged metal sheet electrodes. The inscribed radius at the exit in front of the sample is 4 mm.

All ion guides are driven by an RF signal and an additional defined DC offset to control the kinetic energy of the ions in $z$-direction. A DC gradient from the capillary of the atmospheric pressure interface to the exit of the Twin ion guide is mandatory in the first vacuum chamber as the ions are interacting with the residual gas atoms. The DC offset of the first SWIG is a reference for the kinetic energy of the ions in beam direction. The mean free path in subsequent pressure regimes is much larger than the typical length of the ion trajectories. Thus, the kinetic energy in $z$-direction $E_{kin,z}$ can be estimated by the difference between the potentials $q \cdot (U_{DC} - U_{DC,SWIG\,I})$. Therefore, soft-landing conditions may be typically around $U_{DC,SWIG\,I} \pm$ few volts. The different ion guides of the

[14] Extrel

ES-CIBD have a typical transmission efficiency of about $80\%$. A more detailed description of the ES-CIBD and its electronic supply can be found in [49].

The design of the ES-CIBD consists of four differentially pumped vacuum chambers (yellow and orange) and a separate preparation chamber (magenta) as shown in Figure 3.3 [147]. The chambers are pumped with a combination of scroll forepumps[15], root pumps[16] and turbo-molecular pumps[17]. The ESI source (yellow) operates at ambient conditions and is the entrance to the low vacuum section consisting of three differentially pumped chambers (orange) with pressures of $2$ mbar, $10^{-2}$ mbar and $10^{-7}$ mbar. The different vacuum regimes are separated by modular walls. The Twin ion guide is located in the first differentially pumped chamber. In the subsequent differentially pumped chambers and the first UHV chamber, the three SWIGs are positioned. The first and third SWIG have one or two tubular pressure interfaces to the previous and the next chambers in order to reduce leak rates. The first UHV chamber (red) at a pressure of $10^{-10}$ mbar can be isolated from the low vacuum section by an in-beam gate valve and is directly connected to the deposition chamber. The dQMS and the Blade are mounted in the deposition chamber.

## 3.3 Set-up: ES-CIBD and STM

A commercially available variable-temperature (VT) scanning tunnelling microscope (STM)[18] is attached to the ES-CIDB for investigation of the deposited layers. A CAD image of the ensemble is depicted in Figure 3.3. The UHV chambers of the STM set-up are pumped by various turbo-molecular and ion pumps. The first pumping stage consists of two separable pumping systems with two-stage-rotary vane pumps which reduce the pressure to $\approx 10^{-3}$ mbar. A small turbo molecular pump decreases the pressure to $\approx 10^{-6}$ mbar. The base pressure of the main chambers, which are pumped with a turbo molecular and an ion pump, is at about $10^{-9} - 10^{-10}$ mbar. The STM chamber (green) is connected to a preparation chamber (blue). The chambers are separated by a gate valve which avoids contaminations in the STM chamber. For sample preparation, a home-built metal evaporator, an organic molecular beam epitaxy

[15] Edwards XDS35i

[16] Pfeiffer WKP500/250

[17] Leybold Turbovac Mag W 600/400 iP

[18] „Aahrus 150“ SPECS Surface Nano Analysis GmBH (SF30,31)

(OMBE)[19] and a sputter gun[20] are flanged to the preparation chamber. Magnetically coupled transfer arms (brown) allow for sample transportation between the chambers, the preparation stage and the load lock which can be used to transfer samples into the UHV chamber without breaking the vacuum. A bayonet lock at the tip of the transfer arms allows to grab the sample. The parking in the preparation chamber consists of a preparation stage and a storage which can hold up to four samples. Samples on the preparation stage can be heated by radiative heating via a filament close to the sample for temperatures up to $500\,\mathrm{K}$ or electron bombardment heating, by applying a high voltage additional to the filament heating, for higher temperatures. The deposition chamber (magenta) of the ES-CIBD is attached to the preparation chamber, separated by a gate valve to maintain independence of both set-ups. The manipulator[21] (purple) allows for precise positioning of the sample for ES-CIBD or TPD measurements and temperature control by electron bombardment heating or liquid nitrogen/helium cooling. Additionally, for sample preparation and TPD experiments, a sputter gun[22], a residual gas analyser[23] and various leak valves are positioned in the deposition chamber.

[19] Dodecon OMBE-4C-250-001

[20] Eurovac, varian

[21] Vab Präzisions UHV-Manipulator MAX

[22] Eurovac, varian

[23] SRS, RGA 300

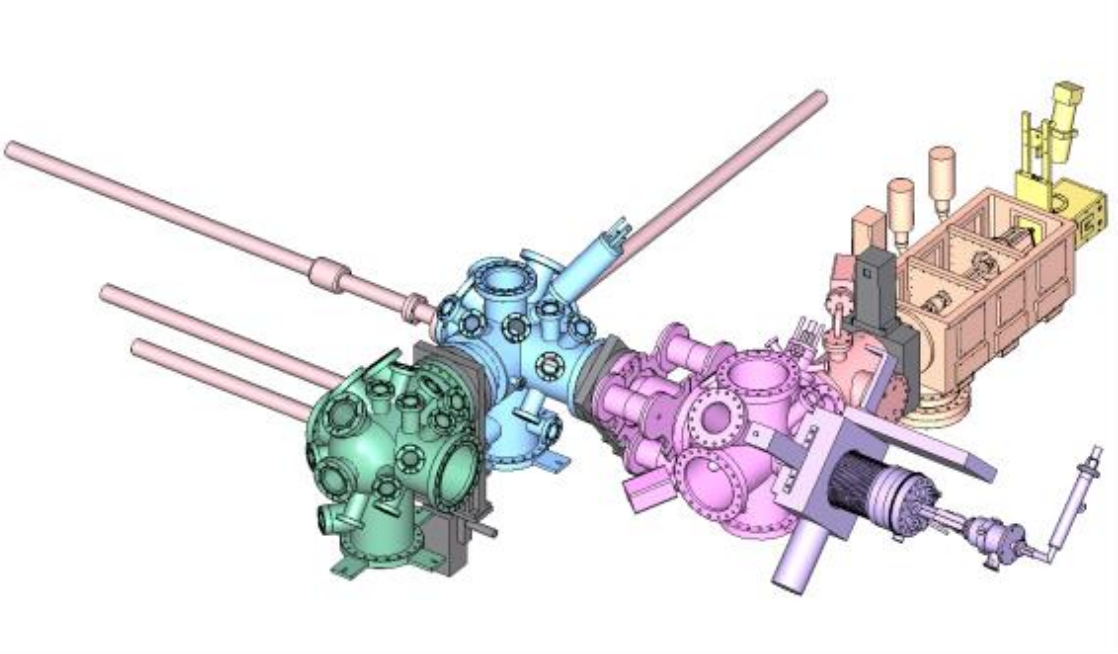

***Figure 3.3*** *CAD model of the ES-CIBD with subsequent VT-STM [24]. The set-up consists of various chambers for sample preparation and analysis: ESI source (yellow), three differentially pumped chambers (orange), first UHV chamber (red), deposition chamber (magenta), preparation chamber (blue), STM chamber (green). A manipulator (purple) allows for positioning and temperature control of the sample.*

[24] Original CAD model drawn by T. Kaposi [91].

# 4 Characterization of charge states and adsorption for biomolecules following different ionization models

In this chapter, deposition of three different biomolecules – the protein insulin, the polyamine spermine and the plasmid DNA pUC19 – by ES-CIBD and their subsequent analysis using STM are discussed. These molecules not only represent a wide range of masses from few hundred to some mega Dalton but may also be attributed to different ionization models (IEM, CRM, CEM). The investigations of these molecules were as well part of the pilot experiments of the set-up and include optimizing the composition of analyte solutions, mass spectrometry and the topographical analysis of the soft-landed deponents on Ag(111) and Cu(111) with UHV-STM. These experiments were conducted in collaboration with Dr. Annette Hüttig.

## 4.1 Mass spectrometric analysis and deposition of Insulin

Insulin is a peptide hormone, which was discovered in 1921 by Banting and Best (isolation from dog pancreas) [148]. It is built in the $\beta$-cells of the pancreas in order to regulate the metabolism, especially of carbon hydrates. It is decreasing the blood sugar level by stimulating the absorption of glucose from the blood into organs like the liver and cells (e.g., fat and muscle cells). The loss of the insulin activity results in a condition of high blood sugar level which is called diabetes mellitus.

The protein has a molecular mass of $5.8$ kDa and consists of 51 amino acids. It is a heterodimer composed of two subunits, which are connected by disulfide bonds. It belongs to the group of non-elongated biomolecules, specifically globular proteins. Thus, it is an example for the CRM which was described in Section 2.1.3.

*In vitro*, depending on the conditions in the solvent, insulin builds various physiologically non-active oligomers, additionally to the metabolic active monomers which are dominant at physiological conditions in serum [149]. Low ionic strength, low $pH$, low concentration of the analyte and low fraction of organic solvent tend to formation of monomers and dimers [150]. High ionic strength and high $pH$ could result in accumulation to tetramers, hexamers or structures of a higher order including

aggregates [151–153]. Furthermore, phenolic and chloride compounds and divalent metal ions such as zinc or cobalt ions can be promoters for high structure assemblies [154–158]. Self-aggregation of insulin in solution is considered a spontaneous process and critical for long-term storage why attempts are made to retain the monomeric form e.g., by adding special protic ionic solvents [159].

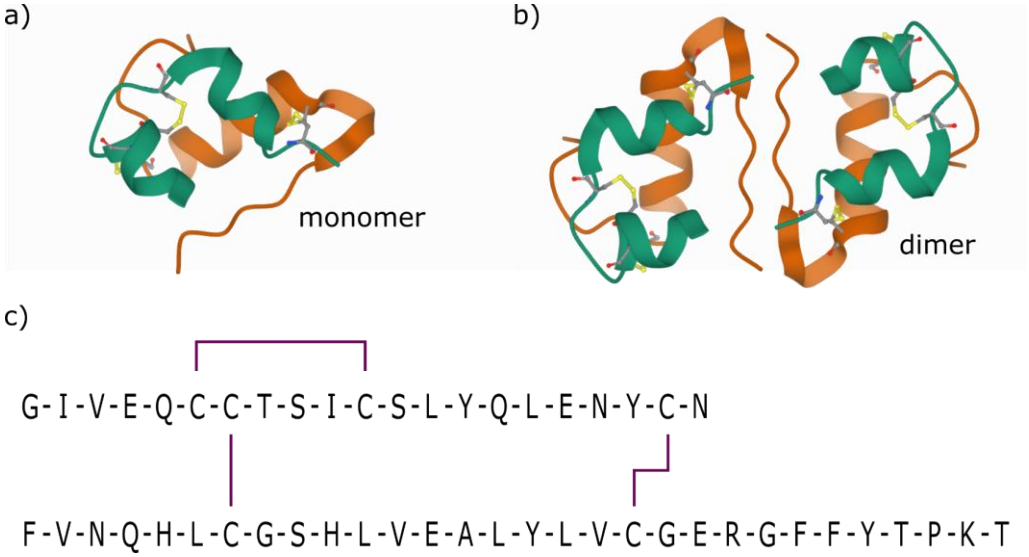


***Figure 4.1*** *Model of recombinant human insulin[25] as a) monomer and b) dimer. The alpha helices of the two subunits are depicted in orange and green [160]. c) Amino acid sequence of insulin subunits with disulfide bonds in purple.*

With $4$ basic amino acids and an isoelectric point[26] $pI$ at about $5.2$, the protein can theoretically carry up to six positive charges at the basic residues and the N-terminus of each subunit at acidic conditions. This makes the insulin accessible for ES-CIBD. When adding particular supercharging agents to the background electrolyte, up to eight charges can be observed, especially at low $pH$. Whereas low charge states are present at high $pH$ [161], experimental data shows six and eight charges on insulin monomers and dimers, respectively [151]. Calculating the Rayleigh limit [68] of a sphere suggests that a protein like insulin carries five charges as monomer and eight charges as dimer at maximum. This is a rough estimation, especially for folded proteins as not all basic amino acids are available or repulsion occurs. Additionally, based on the CRM and the Rayleigh equation [68, 162, 163], $q_{max}$ can be estimated as

[25] https://www.rcsb.org/structure/6O17

[26] $pH$ at which a molecule has no net electrical charge (electrically neutral).

$$q_{max} \approx q_{CRM} = 0.0778\sqrt{M_W} = 6e \tag{4.1}$$

for an insulin monomer which is the highest charge state which is obtained in mass spectra.

For ESI, the surface area of the protein and size of the droplet [164] and therefore, physical parameter such as flow rate of the analyte solution and the diameter of the emitter [165] play the key roles during the spray process. The experimental details about composition of the analyte solution and the spray process are described in the following section.

### 4.1.1 Sample preparation, experimental flow and analytical methods

For the stock solution, $1\,\frac{\mu g}{\mu l}$ human insulin[27] was dissolved in dd$H_2O$[28] which was titrated to $pH\ 2$ by adding acetic acid[29] and filtrated[30], subsequently. The filtration is supposed to remove remaining solid components. An analyte solution with $47.5$ vol.% of stock solution, $47.5$ vol.% acetonitrile as organic compound and $5$ vol.% acetic acid was used for ESI, mass spectrometry and deposition. The calculated concentration of the protein in the spray solution was $8 \cdot 10^{-5}$M. The concentration of insulin in the analyte solution measured using UV-Vis is shown in Figure 4.2. With an extinction coefficient of $\varepsilon = 6335\ \mathrm{M^{-1}cm^{-1}}$, the absorbance at $280$ nm and Equation 2.16, the concentration can be calculated to about $7.5 \cdot 10^{-5}$ M [166].

The emitter was cut from a fused silica tubing with an inner diameter of $50$ µm and an outer diameter of $360$ µm. The flow rate was about $10\ \mu l\ h^{-1}$. The solution was ionized in positive spray mode and a spray voltage of about $2.6$ kV. All experiments at the ES- CIBD set-up were performed at room temperature. UV-Vis measurements were carried out before each ES-CIBD experiment.

---

[27] Sigma Aldrich, Human Recombinant, dry powder, for research or further manufacturing use

[28] Carl Roth, ROTISOLV Ultra LC-MS

[29] Fluka Analytical, $\geq 99.8$ % puriss.

[30] Syringe Filter, Micropur, PES, $25$ mm, $0.2$ µm, PP housing

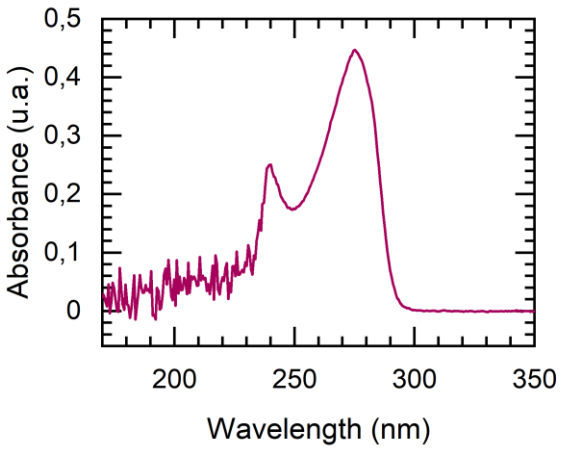


***Figure 4.2*** *UV-Vis spectrum of filtrated insulin analyte solution.*

For the depositions, the respective substrate (Cu(111) or Ag(111)) was cleaned by a sputtering and annealing routine[31]. The dQMS was operated in RF-only mode at $1100$ Th. This way, the masses below the threshold are cut and all masses which attribute to the ion current of insulin (i.e., monomers and dimers) are transmitted. The landing energy was about $1$ eV$/z$. The STM measurements were performed with an Aarhus-type variable temperature STM, which was cooled down to about $180$ K.

## 4.1.2 Results and Discussion

A mass spectrum of filtrated insulin is depicted in Figure 4.3. The signal shows predominantly two main peaks which represent the $4^+$ and $5^+$ charged monomeric molecules. In addition, less prominent peaks could be attributed to the $3^+$ and $6^+$ charged monomers by mass calculation. Some of the monomeric charges may correspond to the dimeric $m/z$ values. Thus, all except the $7^+$ charge states of the monomer can be overlaid or even replaced by the double-charged dimers, e.g., $[2\,\mathrm{Ins} + 6\,\mathrm{H}^+]^{6+}$ and $[2\,\mathrm{Ins} + 8\,\mathrm{H}^+]^{8+}$, respectively. The abundant peaks with low intensity may be assigned to dimers or adducts e.g., with attached components of the analyte solution. Thus, the peak at $1750$ Th is compatible with the oddly charged dimeric state $[2\,\mathrm{Ins} + 7\,\mathrm{H}^+]^{7+}$, in accordance with results from the Robinson group [151]. As the formation of dimers starts at levels of $2\%$ of the concentration, which is used in the analyte solution and is increasing with higher concentrations [151], their existence is

[31] 10 min $Ar$ −sputtering and 30 min annealing to $550 - 600$ K

quite likely. High states as $6^+$ species seem to emerge less probably because the composition of the electrolyte triggers rather small entities.

Adducts with water or salt molecules can emerge with $5^+$ species [167] and $4^+$ monomers, apparently. This is suggested by high-resolution experiments, which are depicted in the inset of Figure 4.3 showing a detailed view of the peak with the highest intensity. The peaks in vicinity of the $5^+$ charged monomer could be assigned to adducts with one water molecule or $Na^+$ (1) at $1166$ Th, two water molecules or $Ka^+$ (2) at $1170$ Th and acetic acid or $Na^+ + Ka^+$ (3) at $1175$ Th, which are components of the analyte solution or the electrolyte substances, respectively. Similar peaks could also be found in the vicinity of the $4^+$ charged monomeric peak.

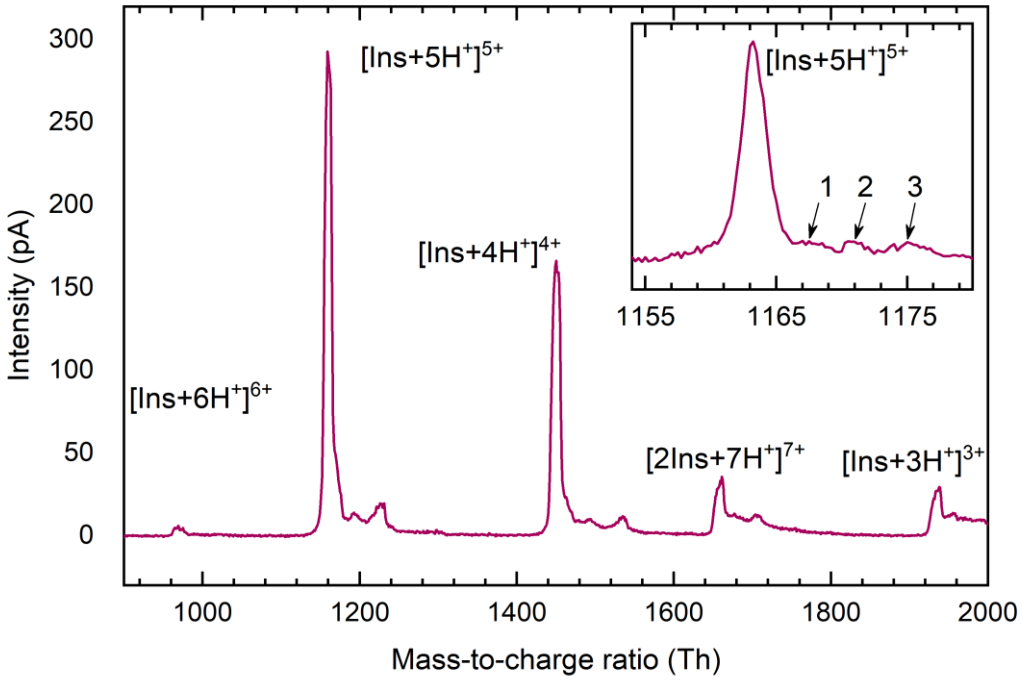


***Figure 4.3*** *Mass spectrum of insulin presenting the five most prominent charge states. The inset shows a detailed spectrum recorded with a high resolution. The peaks with low intensity in the vicinity of the* $5^+$ *peak could be assigned to the formation of adducts with one water molecule or* $Na^+$ *(1), two water molecules or* $Ka^+$ *(2) and acetic acid or* $Na^+ + Ka^+$ *(3), which are components of the analyte solution.*

The graph in Figure 4.4 compares filtrated with unfiltrated insulin. The peaks which could not be assigned to monomeric or dimeric charge states show a lower intensity in the mass spectrum of the filtrated insulin (black circles). Therefore, they may be assigned to insulin aggregates. Monomers, dimers and hexamers are considered native states of insulin. These are interpreted as ESI artefacts [168]. The lower intensity of the

$5^+$ charge states may be caused by the noise of the ES, e.g., because of a change in the spray mode or an unstable Taylor cone.

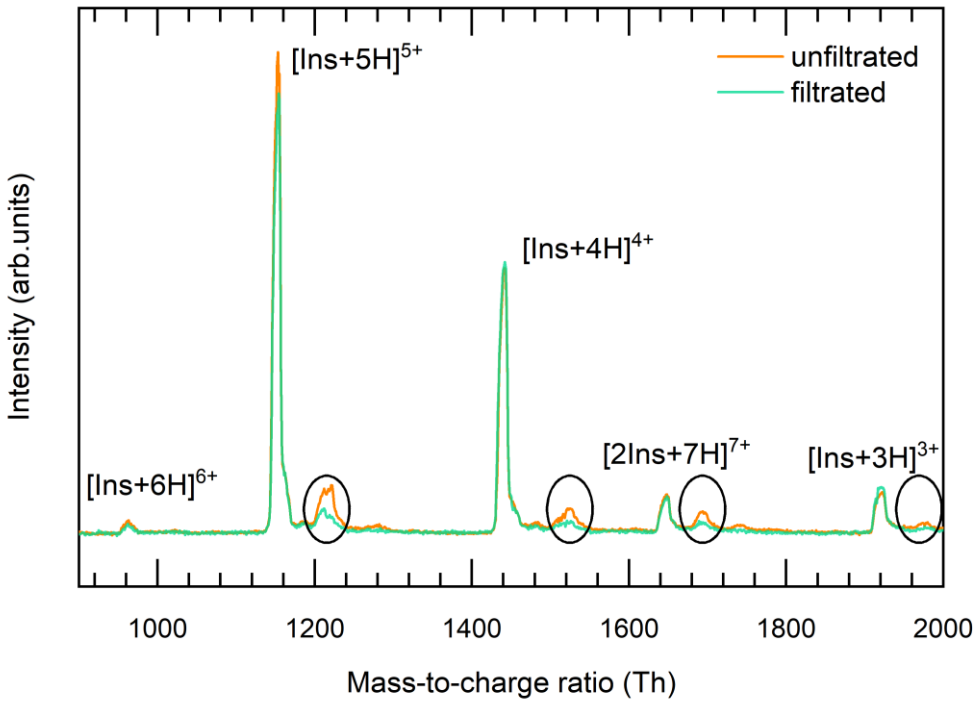


***Figure 4.4*** *Comparison of filtrated (green) and unfiltrated (orange) insulin. The peaks are assigned to monomeric and dimeric charge states as in Figure 4.3. For comparison, the* $4^+$ *peak is normalized to the same height. Black circles highlight the most prominent differences of the mass spectra.*

After analysing the ion beam and the mass spectra, the insulin molecules were deposited onto a sample substrate. The deposition parameters are summed up in section 4.1.1. With a total current of $1$ nA and a concentration of $80$ µM, the sum of all peaks of Figure 4.3, which are related to Insulin, show an overall recovery of about $0.7\%$ . After $m/z$- selection, the ES-CIBD achieves a recovery of $0.37\%$ and $0.23\%$ for the $5^+$ and $4^+$ charged molecules, respectively, with a resolution of $130$. Due to low ionization efficiency and losses during the transmission process, the deposition process normally results in a mass selected recovery of $10^{-5}\% - 1.6\ \%$ [46, 169, 170].

The deposition parameter on Cu(111) and Ag(111) estimate coverages of $70\%$ and $40\%$ of a ML, respectively. Figure 4.5 shows STM images of filtrated insulin deposited on Cu(111)(a) and Ag(111)(b). On both substrates the insulin molecules assemble preferably on step edges and do not show a coordination pattern as illustrated by Figure 4.5a for Cu(111). The bright structures are different in size and shape. As the molecule has a tetrahedral form in 3D and the STM image only shows a 2D landscape, the

different shapes might be explained by different orientations of the molecule on the substrate. The non-circular, but elliptical shaped structures may be overlaid by dimers of the insulin, which can be seen on both crystals, Cu(111) and Ag(111). As it is suggested by [171], the sulphur atoms may be interacting with the metal substrate, but also non- specific adsorption of other amino acid residues is possible. Furthermore, no contaminations can be observed on the bare surface of the substrate.

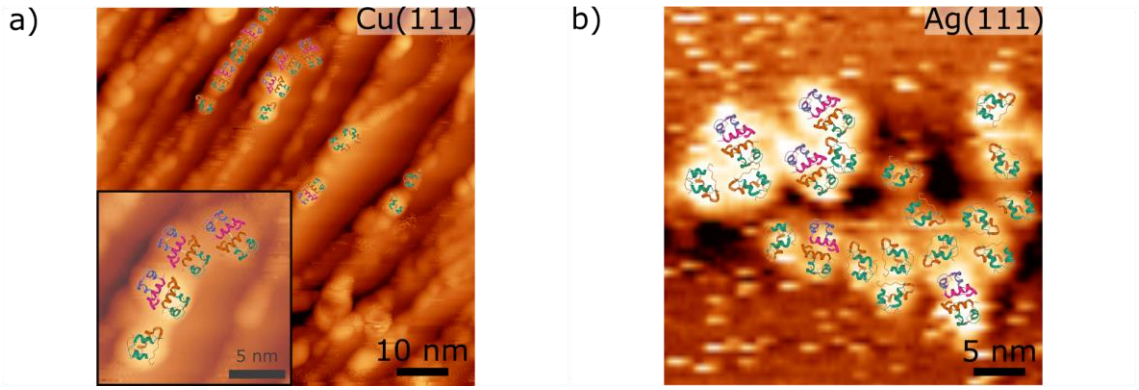


***Figure 4.5*** *STM images of Insulin. a) shows an overview image on Cu(111) with a detailed view in the inset (*$3.3\ V, 120\ pA$*). b) depicts a detailed view of insulin on Ag(111) (*$1.12\ V, 90\ pA$*).*

To conclude, distinct main peaks of the resolved mass spectrum match the expected mass-to-charge ratios of monomeric and dimeric charged states. Larger oligomers are not detected. STM images and charge states in the MS indicate that the ES-CIBD system preserves the native state of the protein. This could also be confirmed by STM images which show circular and elliptical structures. Further experiments could investigate more homogenous layers of insulin in combination with Zn-coordination in order to build insulin hexamers[32]. A more detailed insight could be achieved by operating the dQMS in $m/z$-selective mode and depositing only one charge state. Another possibility for ES- CIBD would be the deposition of insulin fibrils [151] to investigate a presumed change of the spraying behaviour from CRM to CEM. This could also be an experiment for *in-situ* preparation.

[32] Insulin hexamers are formed in the presence of $Zn$ molecules [154].

## 4.2 Mass spectrometric analysis and deposition of Spermine

Spermine, which was discovered by Antoni van Leeuwenhoek in 1677 [172], is a polyamine involved in cellular metabolism in eukaryotic cells.

As polycation, it is blocking the potassium channels during the generation of action potentials in signal transduction of neuronal cells. Furthermore, it is a component of the human sperm and other body fluids. Practical, the spermine has a stabilizing effect on DNA strands, especially on sperm.

The polycationic nature causes binding to the negatively charged phosphate backbone of the DNA, in particular to opposite phosphate groups in the two single strands stabilizing the double helix [173]. The spermine has the possibility to bind to two different sites in the DNA helix by hydrogen bridges-to the nitrogen of the purine (A/G) or the phosphorus of the pyrimidine (C/T) – as it is described in [174–176]. In this way, the DNA is also supposed to become more compact.

Moreover, La et al. [177] reported the intermolecular interaction of spermine molecules and in combination with tetrasulfonate-tetraphenylethylene (Su-TPE, by electrostatic interaction). Investigations on porphyrins modulated with four spermine arms revealed a spontaneous self-assembly of spermine molecules that is motivated by the formation of hydrogen bonds between unprotonated and protonated amino groups [178].

Proposed by Yasumoto et al. [179], the amine groups of the spermine molecule are able to catch $CO_2$ forming carbamates ($R-N-COO^-$), which – as negatively charged groups - may electrostatically interact with positively charged or polarized moieties of other monomers. This might result in the assembly into larger structures.

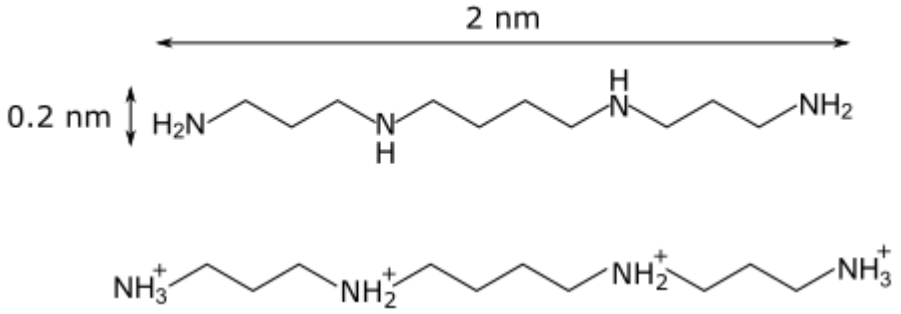


***Figure 4.6*** *Modell of spermine including dimensions. Due to its high $pK$ values [180], the compound can basically carry up to four protons at its amino groups [173]. This results in a* $[spermine]^{4+}$ *polycation in solution at neutral* $pH$*.*

Spermine has a molecular mass of $202.34$ Da. Structure and dimensions are depicted in Figure 4.6. As a chain-like molecule, spermine is supposed to ionize according to the

CEM. However, the Rayleigh limit only allows one charge per molecule for a single unit. According to MD simulations on polypropylene glycol of various lengths of $\approx 600 - 3500$ Da, a longer chain seems to be preferable for CEM [181]. This might still be the case if the spermine polymerize to longer chains upon $CO_2$ coordination. However, the low molecular mass of a single spermine, its good solubility in water and the ability to hold charges make this polyamine a candidate for representing the IEM (cf. Section 2.1.3).

### 4.2.1 Sample preparation, experimental flow and analytical methods

Spermine[33] was dissolved in dd$H_2O$ and subsequently, diluted to the desired concentration. An analyte solution with $50$ vol.% spermine solution and $50$ vol.% ACN as organic compound was used for ESI, mass spectrometry and deposition. The final concentration of the molecule in the spray solution was $10^{-3}$ M. Due to the intrinsic charged nature of spermine, addition proton donors which are common in ESI solvents, were not added. For the depositions, the emitter was cut from a fused silica tubing with an inner diameter of $50$ µm and an outer diameter of $360$ µm. For mass spectrometry, additionally a metal emitter[34] with the same dimensions was used. The flow rate was set to about $30$ µl $h^{-1}$. The solution was ionized in positive spray mode with a high voltage of about $3.6$ kV. To prevent flashovers at the emitter, the use of $CO_2$ as sheath gas was considered. But even slow flow rates of the sheath gas had a negative effect on the stability of the Taylor cone at the tip of the emitter. Thus, the experiments were performed at ambient atmosphere. Before each deposition, the substrate, Ag(111), was cleaned by a sputtering and annealing routine[35]. The dQMS was either operated in RF- only mode or $m/z$–selective mode at $200$ Th. In the RF-only mode, the $m/z$ below the threshold are cut and all masses and charges which attribute to the ion current are transmitted. This allows not only for deposition of a large mass-to-charge range, but also for analysing the composition of the ion beam. In the $m/z$–selective mode, only the selected window of mass-to-charge ratios is transmitted. In this way, the ion beam can

[33] Carl Roth, Spermine, $\geq 99\%$, for biochemistry

[34] $5$ min sputtering, $30$ min annealing

[35] 10 min $Ar$ −sputtering and 30 min annealing to $550 - 600\ K$

be $m/z$-filtered for the deposition. In some of the experiments, the RF-only mode was preferred to the $m/z$-selective mode due to low currents at the sample. The landing energy was about $4$ eV/$z$.

The STM measurements were performed with an Aarhus-type variable temperature STM, which was cooled down to about $180$ K in order to reduce diffusion processes on the surface.

### 4.2.2 Results and Discussion

Mass spectra of spermine are shown in Figure 4.7. The signal reveals one main peak at $202$ Th, which is assigned to a single charged spermine molecule. Additionally, various peaks appear at mass-to-charge ratios higher than the $m/z$ of a single charged polyamine. According to the Rayleigh limit [68], the maximum charge, a spermine can hold, is $1e$. As suggested by [179], the less prominent peaks may be attributed to single or double charged spermine/$COO^-$ - complexes by mass calculation. The charge states and the corresponding complexes are shown in Table 4.1.

| Mass-to-charge ratio | Charge | Complex |
|---|---|---|
| 449 Th | $1^+$ | 2 Spm + 1 $CO_2$ + 1 $H^+$ |
| 493 Th | $1^+$ | 2 Spm + 2 $CO_2$ + 1 $H^+$ |
| 515 Th | $2^+$ | 4 Spm + 5 $CO_2$ + 2 $H^+$ |
| 638 Th | $2^+$ | 5 Spm + 6 $CO_2$ + 2 $H^+$ |
| 695 Th | $1^+$ | 3 Spm + 2 $CO_2$ + 1 $H^+$ |
| 739 Th | $1^+$ | 3 Spm + 3 $CO_2$ + 1 $H^+$ |
| 985 Th | $1^+$ | 4 Spm + 4 $CO_2$ + 1 $H^+$ |

***Table 4.1*** *Overview of mass-to-charge ratios with high intensities and corresponding spermine/$COO^-$-complexes.*

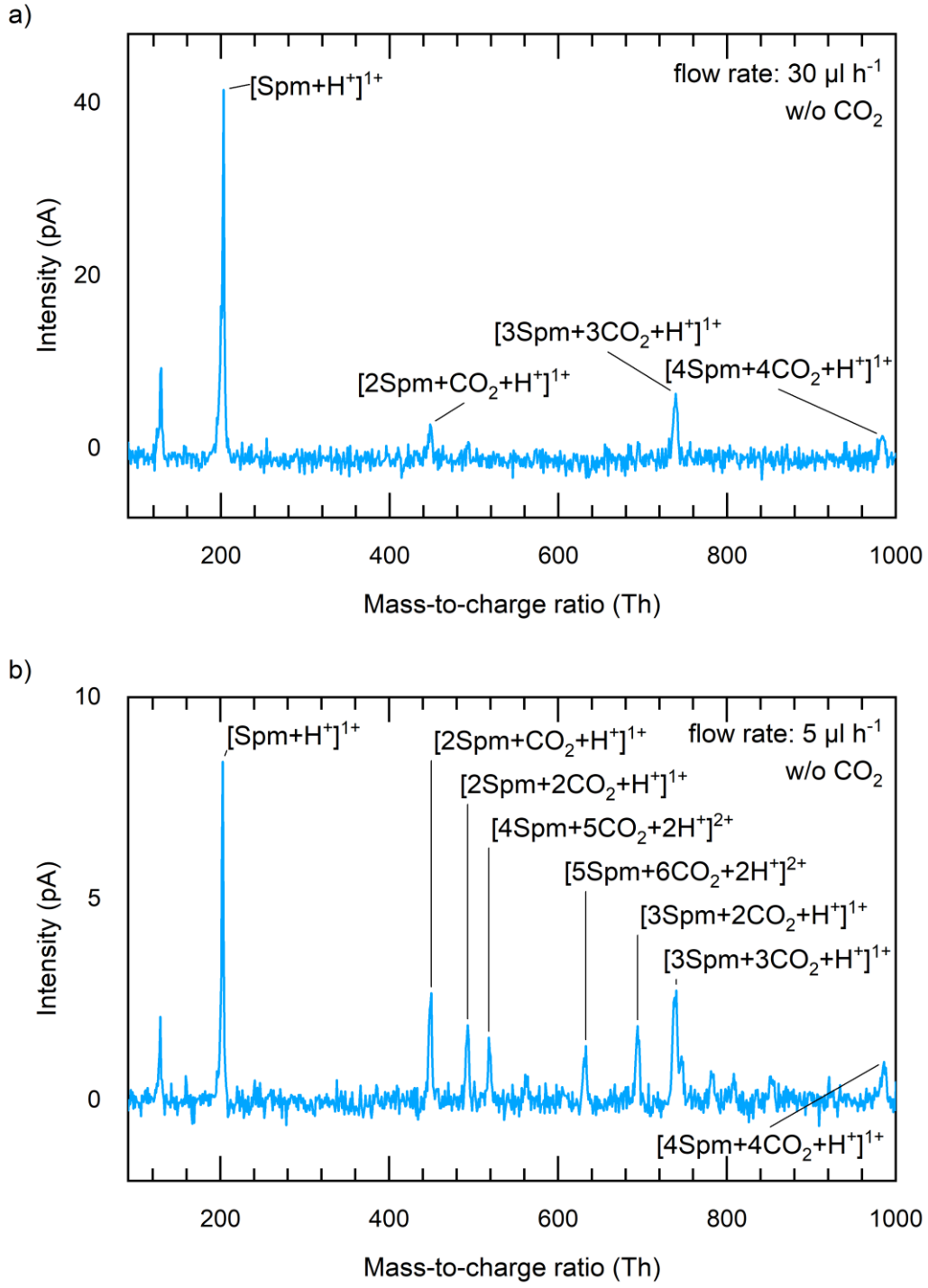


***Figure 4.7*** *Mass spectra of spermine with ambient atmosphere around the emitter and a flow rate of a)* $30\ \mu l\ h^{-1}$ *and b)* $5\ \mu l\ h^{-1}$*. Carbamate group is simplified as* $CO_2$*.*

Since molecules or complexes with double the mass and double the charge appear at the same $m/z$-ratios, the peaks could also be assigned to larger structures. Various factors seem to influence the amount and intensity of different complexes. The slower the flow rate, the higher are amount and intensity (compared to the main peak at $200$ Th) of the peaks containing carbamates (cf. Figure 4.7b). This indicates a slow reaction with atmospheric $CO_2$. Control experiments with $CO_2$ as sheath gas could not be performed due to problems with the stability of the Taylor cone even with slow flow rates of the sheath gas. The analyte solution of the spermine molecules seems to be unstable and very sensitive to $CO_2$. Furthermore, varying the composition of the analyte solution (by addition of $NH_4OAc$, DMSO or sulfolane) could not suppress the peaks at higher $m/z$- ratios. Degassing the analyte solution and using gases such as argon or nitrogen as a sheath gas might suppress the formation of complexes.

For deposition, all peaks were selected to achieve the highest possible ionic current. Respective parameters are summed up in Section 4.2.1. Furthermore, the integral of all peaks of Figure 4.7a, which are related to spermine, represents an overall recovery from solvent ($1.25 \cdot 10^{14}$ particles $s^{-1}$) to target ($1.8 \cdot 10^{9}$ particles $s^{-1}$) of about $0.14\%$. After $m/z$-selection ($4.7 \cdot 10^{8}$ particles $s^{-1}$), the ES-CIBD achieves a recovery of $0.04\%$ for the plain $1^+$ charged molecules with a resolution of $60$. These values are in the same order as compared to other ESI deposition systems, which achieve a total recovery of $0.001 - 0.3\%$ for different $m/z$-selected molecules [169, 170].

Figure 4.8a shows STM images of a spermine island on Ag(111). The coverage of the layer is $5 - 10\%$ of a monolayer[36]. The molecules assemble in different structures in islands on the surface. The unordered structures might origin from overlaying molecules probably due to a high local density with the tendency of the molecules to cluster which partly lay over other spermine molecules or rise up out of plane. The ordered pattern (Figure 4.8b) may be formed by different conformations of the spermine molecules – straight or folded. One possibility with straight molecules is proposed in Figure 4.8b. The molecules assemble in two directions (indicated by red and black) on the surface. The molecules, which are displayed in red, are coordinated along one lattice axis of the underlying Ag(111). The molecules shown in black are connected by an angle of $30°$. This kind of conformation of the polyamine could also be found in literature with

[36] Assumed by ratio of deposited molecules (integrated ion current) and surface area of the crystal substrate

molecules of similar composition [182–185]. Hydrogen bridges are suggested as coupling between nitrogen atoms of the amine groups and hydrogen of the molecules as depicted in Figure 4.8c.

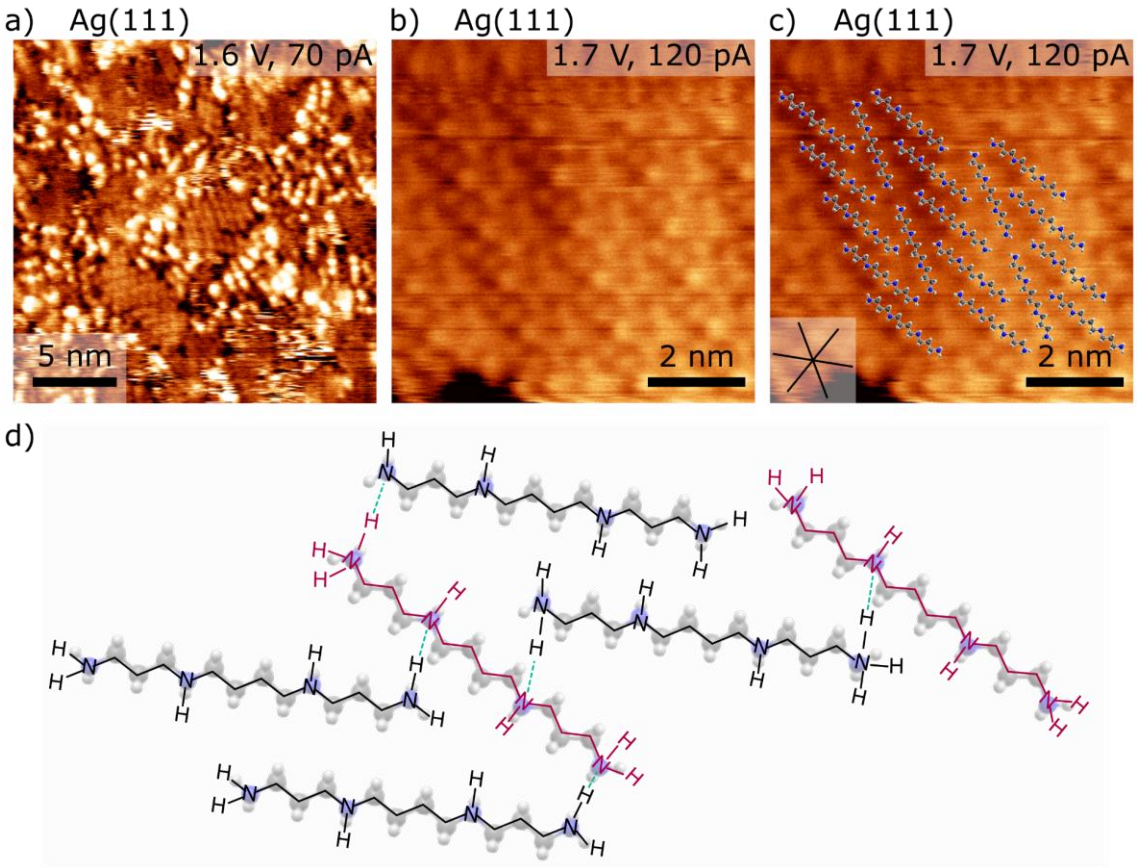


***Figure 4.8*** *STM images of spermine on Ag(111): a) Overview with a combination of ordered and unordered structures and b) self-assembly pattern c) with proposed molecule orientation. The two different directions are indicated in red and black. d) Unit- cell of spermine molecules with hydrogen bonding highlighted in green. STM measurements were performed at* $180\ K$.

In literature, spermine is mostly a part of investigations in DNA or protein complexes [186, 187] in order to analyse its function on these molecules and how it changes their properties. In this work, it could be shown that bare spermine on Ag(111) is forming self- assemblies in various patterns. It may also be that molecules like $CO_2$ or Ag (the substrate atom may help to coordinate the spermine. $M/z$-selective ES-CIBD allows for a layer of pure spermine and makes it a candidate for SAMs. In this way, a surface can be coated in order to modify its properties and to analyse the influence of spermine on other biomolecules. An application might be to further investigate the role of spermine on DNA or RNA [186]. The spermine is supposed to act as counter-ion in order to

stabilize DNA and favour the supercoiled state. This phenomenon is part of the analysis of pUC19 DNA in Section 4.3.4.

Spermine is a small, elongated molecules. According to the IEM, the molecules inside the droplet are supposed to remain in a globular (folded) conformation. Polymerized or aggregated structures as seen in the mass spectra (Figure 4.7) might form this conformation. This could also be seen unchanged on the surface as unordered structures. Duez et al. [181] propose that an elongated molecule can also be ejected in one piece following an IEM process (instead of CEM). This might lead to elongated structures on the surface which could be measured by STM.

## 4.3 Mass spectrometric analysis and deposition of pUC19 DNA

pUC19 is a double-strand (ds) circular plasmid DNA of bacterial origin in B-form (Section 2.6.1, [134, 188]). It consists of $2686$ base pairs (bp) which translates into a length of about $1$ µm (circumference) and a molecular mass of $1.74$ MDa. The full sequence can be found in the NCBI GenBank[37] [189]. As elongated molecule, it serves as representative for the CEM, which is described in Section 2.1.3. As all nucleic acids, dsDNA molecules carry negative charges on the phosphate backbone at aqueous conditions [190]. This makes them accessible for negative spray mode since each phosphodiester residue is able to carry a negative charge by eliminating the positive counter ion. The circular plasmid DNA[38] is provided predominantly in supercoiled state ($95\%$). It appears compacted, lowering the capability to carry charges compared to its relaxed, i.e. open circle form [191]. Different structural variants of the dsDNA, however, can be achieved by restriction enzymes (conversion from circular to linear strand) and topoisomerases (change of coiling level) or by electrostatic repletion using di- or multivalent counter ions (potentially inducing compaction). Figure 4.9 shows an overview of the ESI experiments that were performed with pUC19 conformations and variations in this work:

[37] Accession number M77789.2

[38] Plasmid DNA pUC19, lyophilized, C. Roth

| | | Specification | Treatment |
|---|---|---|---|
| **(i)** | **Unmodified pUC19** | Circular, dsDNA (supplier quality: 95% supercoiled) | None |
| **(ii)** | | | TE buffer as electrolyte |
| **(iii)** | **Condensed pUC19** | Circular dsDNA (supercoiling level unchanged) | Incubation with divalent cation upon shaking ($Mg^{2+}$) |
| **(iv)** | | | Incubation with polycationic polyamine at two concentrations (spermine) |
| **(v)** | **Detangled pUC19** | Circular dsDNA (supercoiling level lowered) | Incubation with Topoisomerase I |
| **(vi)** | **Linearized pUC19** | Linear dsDNA | Incubation with restriction enzyme (EcoRI) |
| **(vii)** | **Heat-denaturated, linearized pUC19** | Linear ssDNA | Incubation at $94°C$ (after EcoRI treatment) |

***Table 4.2*** *Overview of investigated pUC19 variants with their specification and corresponding treatment.*

Various pUC19 variants are investigated referring to their mass and charge distribution using mass spectrometry in the $m/z$-filtering mode and real space structures adopted on deposition targets by STM. The different molecule conformations may have different charge state distributions, that are visible in the mass spectra, and appearances on the surface in UHV. As the experiments were performed by an explorative approach, the results and observations are analysed in a descriptive way to deduce hypotheses about charge states and structural properties.

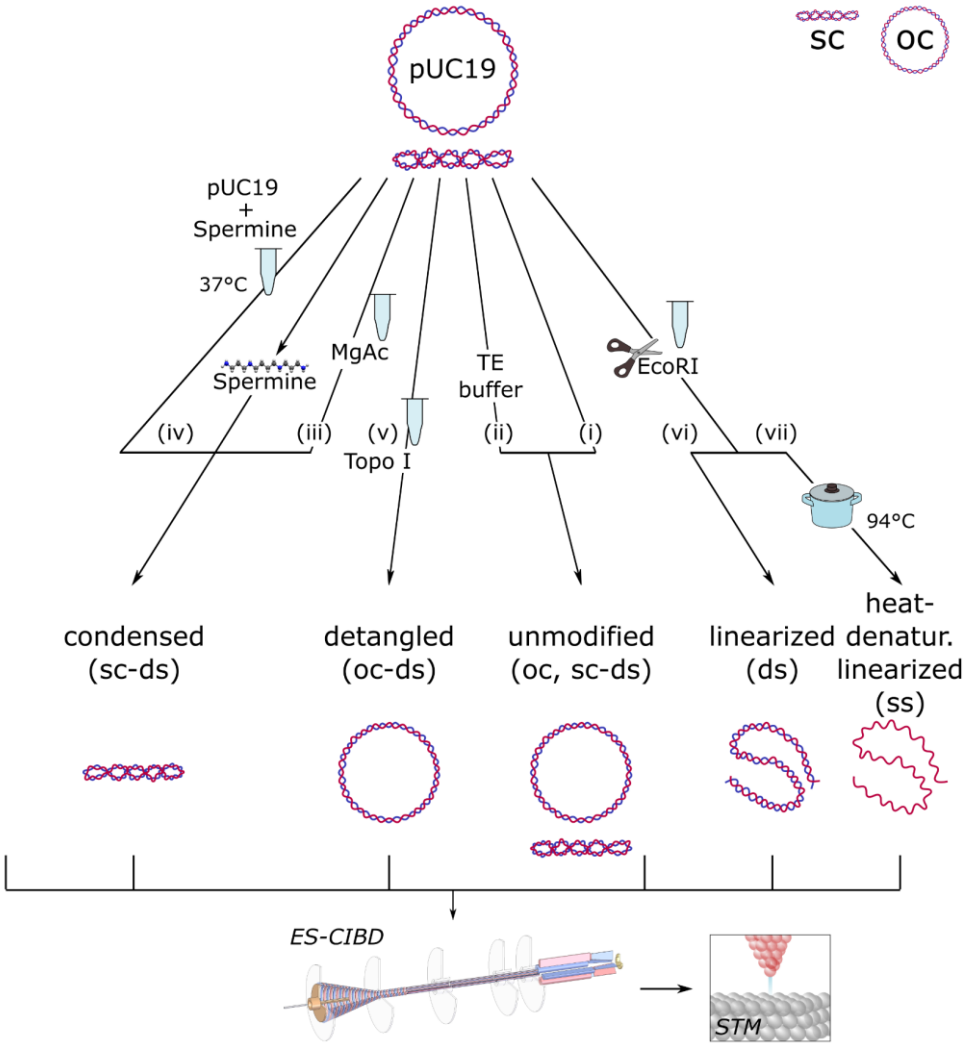


***Figure 4.9*** *Overview of the different experiments: unmodified pUC19 DNA (base configuration, 95% supercoiled-sc, 5% open circular-oc, double stranded-ds), relaxed pUC19 (oc, ds), compact pUC19 (sc, ds), linearized pUC19 (ds and single stranded-ss).*

### 4.3.1 Sample preparation, experimental flow and analytical methods

For the stock solution, pUC19[39] was dissolved in dd$H_2O$[40] to a concentration of $500\,\frac{\mu g}{ml}$ by shaking at RT overnight. For mass spectrometry and deposition, an analyte solution with $6.7$ vol.% of pUC19 stock solution or purified reaction volume, $26.3$ vol.% dd$H_2O$, $66.9$ vol.% ACN as organic compound and $0.1$ vol.% triethylamine (TEA) was used. Thus, the calculated concentration of DNA in the analyte solution is about $2 \cdot 10^{-8}$ M. The absorbance of dsDNA in the analyte solution is exemplary shown in Figure 4.10 measured using UV-Vis. An absorbance of $1$ at $260$ nm translates to $50$ µg ml$^{-1}$ pure dsDNA or $37$ µg ml$^{-1}$ pure ssDNA [192]. Thus, with an absorbance of about $0.65$, the analyte solution has a concentration of about $1.85 \cdot 10^{-8}$ M. The sample purity for the enzyme-involved preparations is determined by the absorption ratio at a wavelength of $260$ nm and $280$ nm ($\frac{A_{260}}{A_{280}}$) which should be $\geq 1.8$ for a protein-free DNA sample.

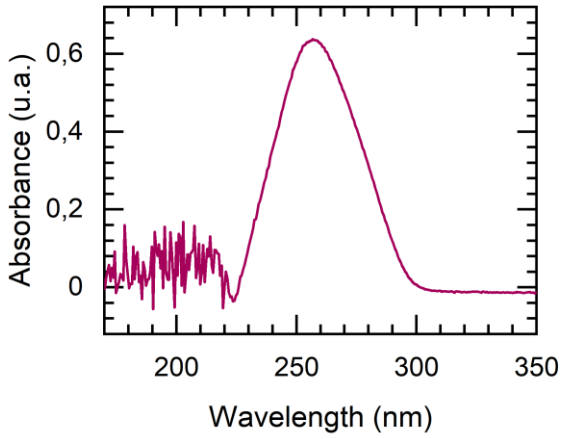


***Figure 4.10*** *UV-Vis spectrum of unmodified pUC19 dsDNA. Absorbance at* $260$ nm *for determination of DNA concentration obtained in spray solution (Reference solution: spray solution without analyte molecule).*

The TE buffer is composed of $1$ mM Tris[41] and $100$ µM EDTA[42]. The condensed variant of the pUC19 can be formed by incubating the dsDNA with ions such as $Mg^{2+}$ (iii) as

[39] Carl Roth, Plasmid DNA pUC19, lyophilized

[40] Carl Roth, ROTISOLV Ultra LC-MS

[41] Carl Roth, Tris(hydroxymethyl)aminomethane (Tris), ≥ 99.9% p.a.

[42] Carl Roth, Ethylenediaminetetraacetic acid (EDTA), ≥ 99.9% p.a.

well as the polycationic polyamine spermine (iv, see Section4.2). By introducing positive charges, the repulsion of the phosphate backbones of two opposite molecules becomes lower and the strands of two molecules can move closer together. Two different approaches were applied in order to investigate the spermine- compacted form of the bacterial DNA: subsequent or simultaneous deposition of pUC19 and spermine. For the experiment generating compacted DNA, the analyte solution without the organic compound was mixed with a concentration of $24$ mM magnesium acetate[43] (MgAc) or spermine stock solution ($250$ mM and $15$ µM) and incubated for $30$ min at RT or $1$ h at $37$°C, respectively.

The enzyme Topoisomerase I is partially unwinding the supercoiled structure by locally losing one of the strands followed by unravelling turns and final religation. This results in a higher contribution of relaxed double-strand helices which, in theory, can be charged to a higher extend than before. An enzyme reaction with EcoRI is linearizing the circular dsDNA. For the detangled (v) and linearized (vi) variant, the pUC19 DNA was enzymatically untwisted by Topoisomerase I[44] or cut with EcoRI[45], respectively, according to the instructions given by NEB [193, 194]. After incubation and subsequent inactivation of the enzyme, the reaction volume was purified using micro-spin columns[46] and diluted in dd$H_2O$. Subsequent heating a linearized plasmid DNA above the melting temperature separates the two strands into single-stranded (ss) DNA (vii). SsDNA does not only exert the phosphate backbone, but also the nucleobases to the charge-relevant environment. The surface is assumed to be lower than the surface of a dsDNA by a factor of $\sqrt{2}$. This is relevant for the Rayleigh limit and thus, an decreased charging capacity is presumed.

The emitter for the electrospray was cut from a fused silica tubing with an inner diameter of $50$ µm and an outer diameter of $360$ µm. The analyte solution was ionized in negative spray mode. Flow rates and spray voltages of the syringe are summed up in Table 4.3. All experiments were performed at room temperature. For a stable Taylor cone during the ESI-CIBD, $CO_2$ was used as a sheath gas. Before each spray test and every deposition, the pUC19 concentration in the analyte solution was checked by measuring

[43] Alfa Aesar, Magnesium acetate tetrahydrate, ACS

[44] NEB, Topoisomerase I (E. coli)

[45] NEB, EcoRI-HF

[46] GE, illustra GFX PCR DNA and Gel Band Purification Kit

the light absorption using UV-Vis. Mass spectra were recorded in $m/z$-selective mode to characterize ion properties and spray quality. For deposition, the dQMS was operated in RF-only mode. The threshold derived from the RF-only spectrum was set to a mass- to-charge ratio just below the point at which the ion current starts decreasing. In this way, the transmission of all charge states assigned to the respective pUC19 variant is ensured. The landing energy was about $1.5$ eV$/z$. The respective Ag(111) and Cu(111) substrates were cleaned with a Ar-sputtering and annealing routine. The STM measurements were performed using the Aarhus-type variable temperature STM attached to the ES-CIBD and operated at room temperature.

| | | Flow rate | Spray voltage |
|---|---|---|---|
| **(i)** | **Unmodified pUC19** | $35$ µl h$^{-1}$ | $-3.2$ kV |
| **(ii)** | **Unmodified pUC19 (TE)** | $40$ µl h$^{-1}$ | $-2.5$ kV |
| **(iii)** | **Condensed pUC19 ($Mg^{2+}$)** | $45$ µl h$^{-1}$ | $-3.2$ kV |
| **(iv)** | **Condensed pUC19 (Spm)** | $40$ µl h$^{-1}$ | $-3.1$ kV |
| **(v)** | **Detangled pUC19** | $40$ µl h$^{-1}$ | $-4.2$ kV |
| **(vi)** | **Linearized pUC19** | $40$ µl h$^{-1}$ | $-3.2$ kV |
| **(vii)** | **Heat-denaturated, linearized pUC19** | $40$ µl h$^{-1}$ | $-2.6$ kV |

***Table 4.3*** *ESI parameters: flow rate and spray voltage of the pUC19 variants*

### 4.3.2 Mass spectrum and analysis of pristine DNA (base spectrum)

A typical mass spectrum of a pUC19 DNA shows a wide distribution of mass-to-charge ratios between $900$ Th and $3150$ Th as depicted in Figure 4.11.

The broad charge distribution is typical for large, non-globular molecules and was also observed by Smith et al. on related plasmid-type species [195]. Ignoring limitations by electrostatic repulsion, which is the limiting factor when molecules are extracted from the solvent during the ionization process, the pUC19 DNA could adopt $5372$ charge

states, as each of the 5372 phosphate entities is able to carry one charge. This would result in a lower limit of the mass-to-charge ratio ion the mass spectra of about 325 Th.

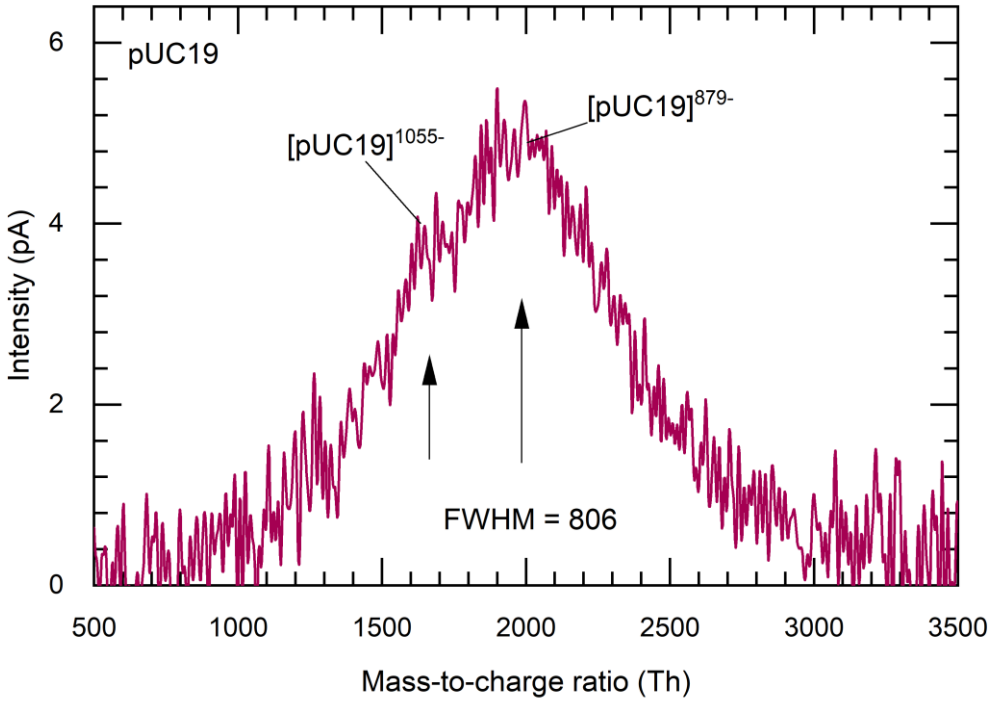


***Figure 4.11*** *Mass spectrum of the base configuration (unmodified pUC19). The wide distribution of charge states features two peaks at* 1700 Th *and* 1980 Th*, respectively. The FWHM is* 806 Th*.*

With the maximum resolution, that can be achieved by the current ES-CIBD system, single charge states cannot be resolved. Furthermore, the higher the resolution is, the lower the current of the charge state. Thus, the resulting mass spectra are always a trade-off between maximum intensity and resolution. The overall ion current of about 2 nA distributes over approximately 2250 Th.

With a lower limit of about 900 Th and an upper limit of about 3150 Th, this results in ~1380 possible charge states as calculated by following equation:

$$q_{upper\ limit} - q_{lower\ limit} = m_{pUC19} \cdot \left( \left(\frac{m}{z}\right)^{-1}_{lower\ limit} - \left(\frac{m}{z}\right)^{-1}_{upper\ limit} \right) \quad (4.2)$$

with the charge $q$, the mass $m$ and the $m/z$-ratio. The charge state with maximum intensity is in the order of 5 pA.

At the centre of the base spectrum around 1980 Th, a resolution $R$ of about 880 would be necessary in order to resolve adjacent states (here $879^-$ and $880^-$) according to

$$R_{centre} = \frac{\frac{m}{z}}{\Delta\left(\frac{m}{z}\right)} \approx 880. \tag{4.3}$$

Analogous, with a resolution of about $1930$, single charge states could be resolved in the whole spectrum (at the lower limit the charge states are $1933^-$ and $1934^-$).

The wide distribution of the mass spectrum in Figure 4.11 features two main charge states around $1650$ Th and $1980$ Th which can be translated to $1055e^-$ and $879e^-$, respectively. The Rayleigh limit for the pUC19 in water can be estimated by assuming a cylindrical shape of the dsDNA:

$$q_{ds} = \pi \cdot l\sqrt{6\gamma\varepsilon_0 r} \approx 1120e. \tag{4.4}$$

The length of dsDNA in aqueous solution $l_{ds} = 913$ nm is calculated by the number and length of bases ($l_{base} = 0.34$ nm) [196, 197]. Its radius is approximated by $r_{ds} = 1$ nm [196]. $\gamma_w = 72.75$ mN m$^{-1}$ is the surface tension of water [198] and $\varepsilon_0$ the vacuum permittivity. The resulting charge state of $1120e^-$ corresponds to $1670$ Th.

Since the real spray solutions consists of about $67\ vol.\%$ ACN and about $33\ vol.\%$ $H_2O$, the Rayleigh model with a surface tension of $\gamma_{mix} = 31.3$ mN m$^{-1}$ for the ACN-$H_2O$. [199] provides $730e$, thus, $\frac{m}{z} = 2385$ Th.

Due to different evaporation kinetics of $H_2O$ and ACN and a favoured equilibrium in the droplet during the ionization process, the composition of the single droplets may change shifting the surface tension to $\gamma_W$. Thus, for the following considerations, the surface tension of the droplet is assumed to be $\gamma_W$.

According to the Rayleigh equation, length and/or diameter have to change to model the broad distribution of charge states, assuming the weight of the pUC19. Considering an estimated mean length ($l_{sc} = 0.4 \cdot l_{ds} = 370$ nm) and radius ($r_{sc} = \sqrt{2} \cdot r_{ds}$) [200] of a supercoiled dsDNA, the Rayleigh limit is $q_{sc} = 565e$, which translates into $3080$ Th.

This value is below the observed charge state at the maximum of the peak ($1980$ Th), however, still at the upper limit of the observed mass spectrum. Supercoiled DNA is characterized by a more compact appearance compared to relaxed DNA rings. Due to various combinations of twists and writhes (see $Lk$ concept in Appendix A.1) for a given dsDNA circle, the resulting length and radius of a supercoiled DNA molecule is not fixed or constant but exists as a range of both.

According to Schultz et al. [191], altered 3D structure of the molecule (e.g., supercoiling), affects the charging capacity. Coulomb repulsion between the charges limits the maximum charge state. Thus, more extended structures allow for more charges.
The remaining deviations (unexplained $m/z$-ratios below $1670$ Th) may be explained by various hypotheses. The Rayleigh model may serve as a rough estimation of possible charges that a molecule is able to carry. Assuming the Rayleigh model is directly applicable to the pUC19 molecules, the DNA strands are either much longer, have a larger diameter than theoretical values suggest or are strongly overcharged with expected dimensions.

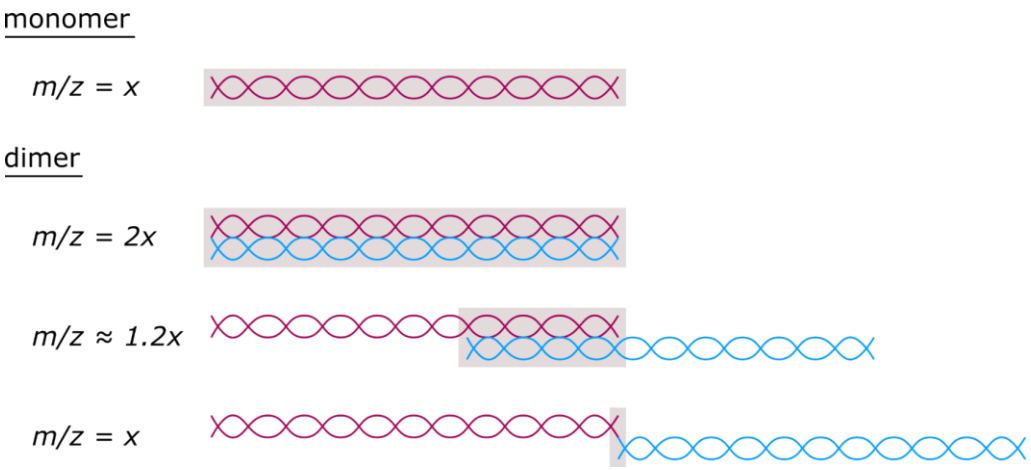


***Figure 4.12*** *Dimerization of a circular dsDNA during ESI process. Red and blue schematic helices represent the individual DNA strands in supercoiled conformation. Two monomers might form dimers by contacting each other. The monomeric molecule has a mass-to-charge ratio of* $\frac{m}{z} = x$. *For the dimer, the value of* $\frac{m}{z}$ *depends on the contact area (brown) between the individual molecules. A full contact results in* $\frac{m}{z} = 2x$ *and almost zero contact gives* $\frac{m}{z} = x$. *Thus, a decreasing contact area is proportional to an increasing charge which leads to a shift to lower values of the* $\frac{m}{z}$. *Adapted from [201] and [146] with modifications.*

Longer DNA molecules might be evoked by polymerization of multiple DNA strands which could in principle happen during chain ejection. Schultz at al. [191] discussed a dimerization process. The impact of this idea on the charge states of pUC19 (e.g., $1700$ Th : $1980$ Th $= 1 : 1.16$) is demonstrated by a simple model in Figure 4.12. In the case of a whole dimerization, the mass is double the mass of a monomer and the surface slightly increases while the charge remains almost constant. This results in a doubled mass- to- charge ratio $\left(\frac{m}{z} = 2x\right)$ in comparison to the monomeric molecule $\left(\frac{m}{z} = x\right)$. If the dimer is formed by end-to-end polymerization, the contact area of two

monomers is almost zero. The charge increases proportional to the mass as well as the surface which is accessible for charges. This leads to a value of the mass-to-charge ratio equal to the $m/z$ of the monomer $\left(\frac{m}{z} = x\right)$. Any partial overlap of two polymerizing molecules results in a mass-to-charge ratio of $x < \frac{m}{z} < 2x$ [146].

As DNA is a hydrophilic molecule, a solvation shell with a layer thickness of few water molecules around the pUC19 might be possible. MD simulations (Figure 2.4) show that few solvent molecules remain attached to the analyte molecule during chain ejection [74]. This would result in a slightly increased diameter. After evaporation of the solvation shell, the DNA molecule is overcharged in comparison to a molecule that is ejected without a solvation shell [202]. Considering the chemical limits of charging, the overcharging is possible. Other factors may additionally impact the charging efficiency. In particular, the diameter of the emitter is influencing the size of the droplet and therefore, the number of accumulated charges on the surface.

Assigning different charge states of pUC19 molecules to different conformations is not unambiguous. A gradual transition is assumed with preferably dsDNA (with solvation shell) at low $m/z$ values and supercoiled DNA at high values. In the performed experiments, a CD-MS would be necessary to separate mass from charge and to discuss the potential assembly of two DNA molecules to dimers with partially overlapping flanks (see Figure 4.12).

### 4.3.3 Impact of modified topology on mass spectrometric parameters

Various experiments with different conformations of the pUC19 DNA were performed for further analysis of different charge states that are derived from measured $m/z$ values. Typical mass spectra obtained during the experiments (Figure 4.9) show a wide distribution of mass-to-charge ratios between $750$ Th and $3150$ Th (Figure 4.13 a-e,g,h) up to $7500$ Th (Figure 4.13 f).

**Enzymatic detangling**

Figure 4.13b depicts a mass spectrum of a pUC19 DNA which was manipulated by Topoisomerase I. As the enzyme is supposed to unwind supercoiled DNA strands, the

amount of supercoiled DNA should be lower than in a solution with unmodified pUC19. In theory, this should cause higher charge states that are reflected in lower $m/z$ values. While the mass spectrum reveals a similar distribution of charge states as compared to the unmodified DNA, a small shift towards higher mass-to-charge ratios emerges. The maximum intensity at $2140$ Th translates to a charge state of $813^-$. Assuming a constant mass, the data suggests lower or unchanged charge, thus, unchanged or even more compact pUC19. This is contradictory to the expected result of the enzyme reaction. Adding the organic compound for the spray process might have an impact on the conformation of the molecules. Furthermore, it might be assumed that the process with the Topoisomerase I did not work as planned or it was "undone" after detangling and enzyme removal as well as during several months of storage at $-20$°C.

After catalysing the unwinding process (reducing a certain number of twists giving a partially open-relaxed molecule associated with a lower "artificial" linking number, see Appendix A.1), the enzyme is removed from the DNA. The pUC19 molecule may "remember" the original number of twists that is predefined by the number of base pairs and as such, it is specific for each DNA circle. However, the linking number cannot be changed back without further cutting of the strand or applying energy to the system. The only way out of this torsional tension is to introduce extra coils to the strand resulting in a supercoiled molecule. This molecule can carry less charge than the original prior to the topoisomerase treatment. This reverting effect might be hindered by an immediate processing after the unwinding reaction, maybe even at lowered temperature or by blocking the system using (intercalating) substances fixing the current topology. Additionally, a thermodynamic equilibrium between relaxed and supercoiled species might be established [203, 204].

**Enzymatic linearization**

Both versions of the linear pUC19, ds and ss, which are plotted in Figure 4.13c and d, respectively, show a shift to lower mass-to-charge ratios with respect to the unmodified DNA. Compared to supercoiled DNA, a linear relaxed dsDNA is supposed to carry a higher charge due to its longer cylindrical shape with fully exposed binding sites over the entire length of the double helix.

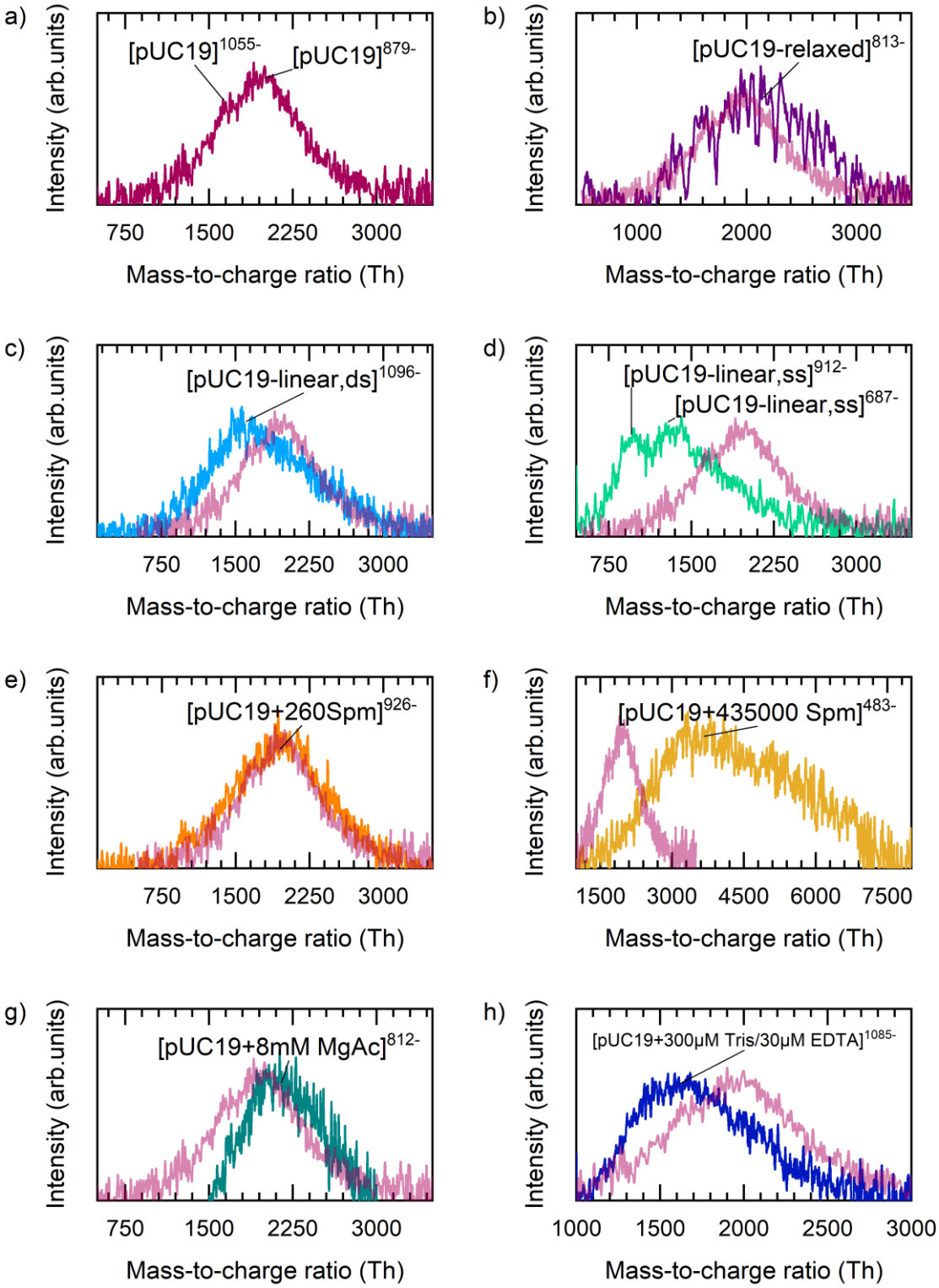


***Figure 4.13*** *Mass spectra of different conformations and variants of pUC19 DNA. a) unmodified, b) relaxed, c) linear and ds, d) linear and ss, e) and f) compacted with Spm, g) compacted with MgAc and h) with Tris/EDTA. For comparison, the maximum intensity of the peaks is normalized to* 1.

This can be explained by the Rayleigh limit (cf. Equation 4.4), as a long, cylindrical form has a larger surface than a compacted form of the same volume. The charge states of the linear dsDNA have a similar distribution as the circular/supercoiled pUC19. The charge state at the peak maximum ($\approx 1100e^-$) is close to the value which is suggested by the Rayleigh limit and may be attributed to the linearized strands.

The mass spectrum of the linear ssDNA reveals two peaks at $954$ Th and $1318$ Th which might be assigned to the single strands with charges of $912^-$ and $687^-$, respectively. The Rayleigh limit of ssDNA $q = 790e$ is estimated according to Equation 4.4 and lies between the featured charge states of the linear ssDNA. As ssDNA is supposed to be more open and less dense in contrast to dsDNA, a lower $m/z$-value can be expected [191]. Furthermore, the broad distribution of charge states at higher masses additionally suggests the presence of dsDNA.

**Compacting DNA by binding to the polycationic polyamine spermine**

Mass spectra of pUC19 which was incubated with a low and a high concentration of spermine, respectively, are depicted in Figure 4.13e and f. The spectrum of the DNA with a low concentration of spermine appears very similar to the spectrum of the unmodified DNA. It shows a broader distribution of charge states by a factor of $1.3$. The average amount of spermine molecules per DNA strand was calculated to be $260$. Adding the mass of the spermine molecules to the mass of the pUC19 results in a charge of $926e$ at the maximum intensity. The peak arises at the charge state which might be assigned to more compact DNA and preferably supercoiled DNA. The interaction of spermine and DNA might cause a rather unspecific compaction. In the same time, the mass is increased as the spermine molecules are supposed to be attached to the DNA strand which shifts the $m/z$-ratios towards higher masses.

The spectrum of the DNA with a high spermine concentration (Figure 4.13f) is shifted to a higher mass with respect to the unmodified pUC19 and shows a distribution from $1500$ Th to $7500$ Th. The Rayleigh model suggests a more compact DNA strand because of the higher mass, as the molecular weight of the spermine molecules has to be added to the pUC molecule, and thus, a lower charge. Furthermore, calculations show an average amount of spermine per DNA of $435000$ which translates to about $480$ spermine particles per nanometre of the DNA strand in axial length or about $100$ spermine per $nm^2$ of the helix surface. The broad distribution of the charge states can be explained by the high concentration of spermine. The amount of spermine which is attached to

the pUC19 is not constant across one strand as well as for all strands in the analyte solution. The spermine molecules could even form aggregates which are attached to the DNA strand (cf. Section4.2).

**Compacting DNA by $Mg^{2+}$ and treatment with TE buffer**

MgAc provides the bivalent counteraction to the DNA phosphate backbone and has a similar effect on the pUC19 DNA compared to the treatment with spermine [197, 205]. Combining potentially more than one DNA strand to a molecule with increased thickness and mass, changes the cylindrical geometry. A dimer has a radius which is increased by a factor of $\sqrt{2}$ resulting in a proportional increase of the total surface while the mass is doubled. This shifts the mass spectrum to higher $m/z$-values Figure 4.13g, suggests a lower charge and thus, a more compact DNA strand compared to the main species of the analyte solution. Here, the effect regarding the increasing mass can be neglected as the magnesium ions have a low molecular weight in comparison to the pUC19 and are only used in low concentrations. The range of mass-to charge ratios is smaller compared to all other preparations. This indicates a less variable charging behaviour of pUC19 and, thus, a more homogenous population.

Tris-EDTA is the standard buffer in which many DNA samples are supplied and handled. Usually, buffers, containing a specific salt concentration, are less suitable for ESI procedures as the ionization process is hindered. Thus, the experiment using TE buffer as component of the spray solution was performed to investigate, whether DNA samples can be processed by the ES-CIBD without prior buffer exchange.

A mass spectrum of pUC19 in combination with $300$ µM Tris and $30$ µM EDTA is shown in Figure 4.13h. The spectrum is shifted to lower mass-to-charge ratios compared to the unmodified DNA strands with a similar FWHM. This suggests a higher charge or a more relaxed DNA strand. Thus, the pUC19 molecules can be sprayed in a low concentration of the standard buffer. Using TE, a reaction takes place, which is opposite to the Mg experiment. The EDTA intercepts divalent ions from the solution (e.g., $Mg^{2+}$), thus, the DNA molecules become separated from each other. Their surface can carry more charge carriers and as a result, the $m/z$ ratio becomes lower.

While all spectra give information about different charge state distribution and thus, hint at different conformations of the pUC19 DNA, real space imaging of deposited molecules could confirm this theory.

### 4.3.4 Investigation of DNA structure on metal surfaces

The STM measurements are performed to confirm the integrity of soft-landed DNA molecules and to reveal different conformations and possibly self-assembled structures. Figure 4.14 to Figure 4.21 show STM images of different conformations and variants of pUC19 DNA in different coverages between $2\%$ and $40\%$ of a ML translating into $13$ molecules $\mu m^{-2}$ and $224$ molecules $\mu m^{-2}$. The coverages are calculated by the ionic current over time measured during the deposition and the area of crystal substrate and molecule. On both surfaces, Ag(111) and Cu(111), topological isomers of the pUC19 DNA can be observed. In contrast, deposition experiments performed by drop-casting reveal accumulated structures [200, 206, 207].

**Pilot studies of unmodified pUC19 on Ag(111)**

In Figure 4.14, STM images of an unmodified pUC19 on Ag(111) are depicted. During the measurements, the STM tip was very unstable. Furthermore, low scan voltages resulted in disassembly or even displacement of DNA strands (see Appendix A.2). This phenomenon was also reported earlier on Au(111) by Shapir et al. [208].

STM analysis of soft-landed, unmodified pUC19 on Ag(111) with coverages of about $7\%$ and $40\%$ (Figure 4.14a and b, respectively) reveals both forms which are expected from circular DNA, ring-like and rod-like structures. Individual species cannot be separated at high coverages. The close-up view shows helical twisted and supercoiled strands crossing step edges of the substrate with areas of partial clustering (highlighted in Figure 4.14c). Basically, the local clusters of DNA molecules can be functional or random, however, their nature was not subject of this thesis. Further resolving of the substructure, different widths of the DNA strands can be observed which might reflect different topologic variants of pUC19. The pUC19 is provided as a mixture of sc and relaxed, ds pUC19 with a ratio of $95\% : 5\%$ (for a more detailed analysis see Figure 4.24).

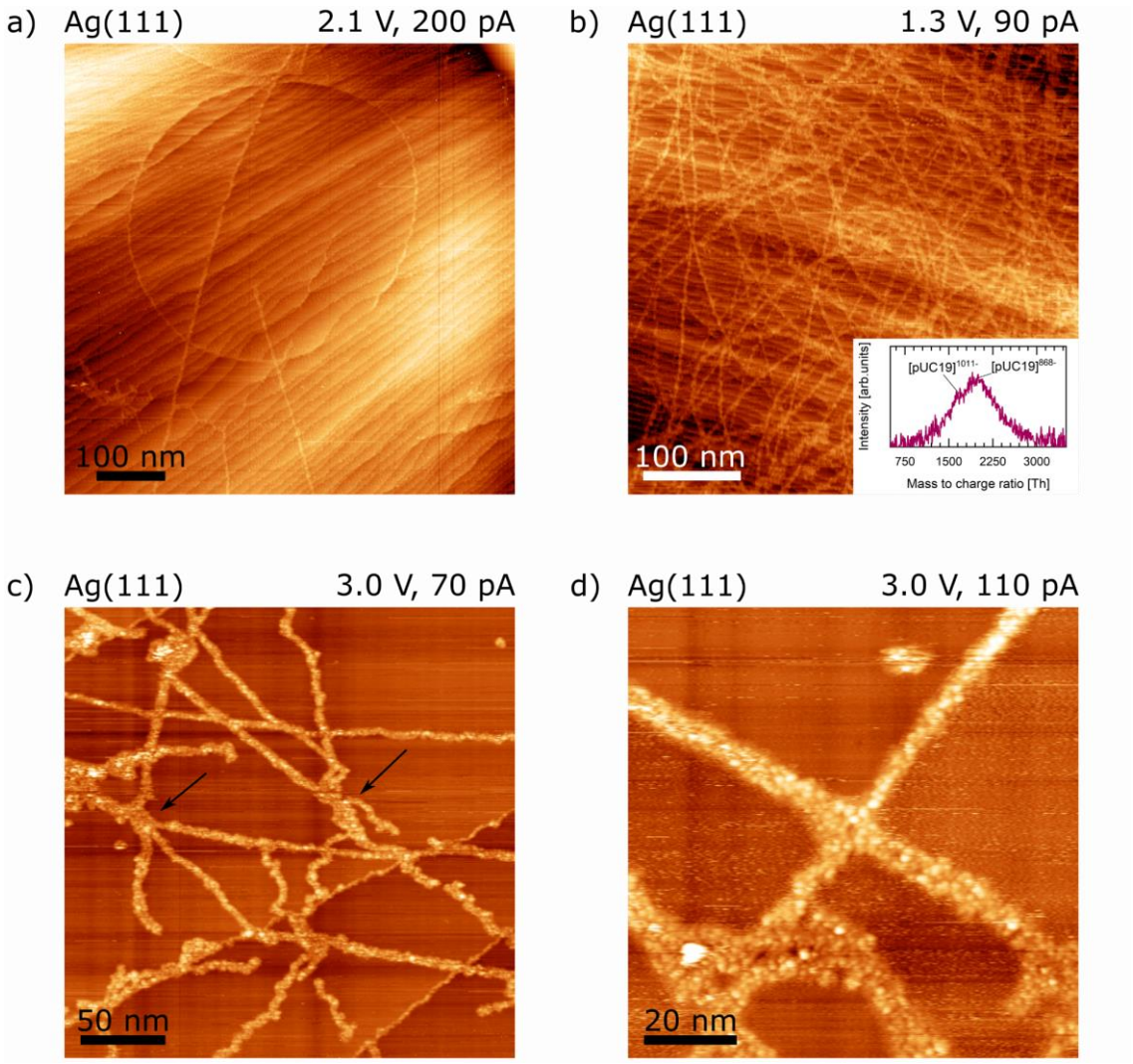


***Figure 4.14*** *Overview of pUC19 DNA on Ag(111) with a) low (7%) and b) high (40%) coverage. c),d) detailed view of the DNA strands (coverage of 10%). Circular DNA appears as ring (circumference of approximately 1 µm) or rod (length about 500 nm) probably representing a supercoiled circle. The inset (b) shows the corresponding mass spectrum. All measurements were performed at RT.*

**Studies of unmodified pUC19 on Cu(111)**

Experiments performed on a Cu(111) surface allow for investigating a potential impact of the surface on the structure in comparison to the Ag(111) surface. As copper is known to have strong interaction with DNA [209], it is supposed to fix the molecule on the surface and, thus, may help to overcome the scanning issues faced with the silver surface.

In contrast to the measurements on Ag(111), the STM tip was more stable during the measurements on Cu(111) as well as could be operated at lower voltages without breaking or moving the DNA strands as it could be observed on the silver substrate.

Respective STM data in Figure 4.15a and b show overviews of unmodified pUC19 DNA on Cu(111) with a coverage of about $3\%$.

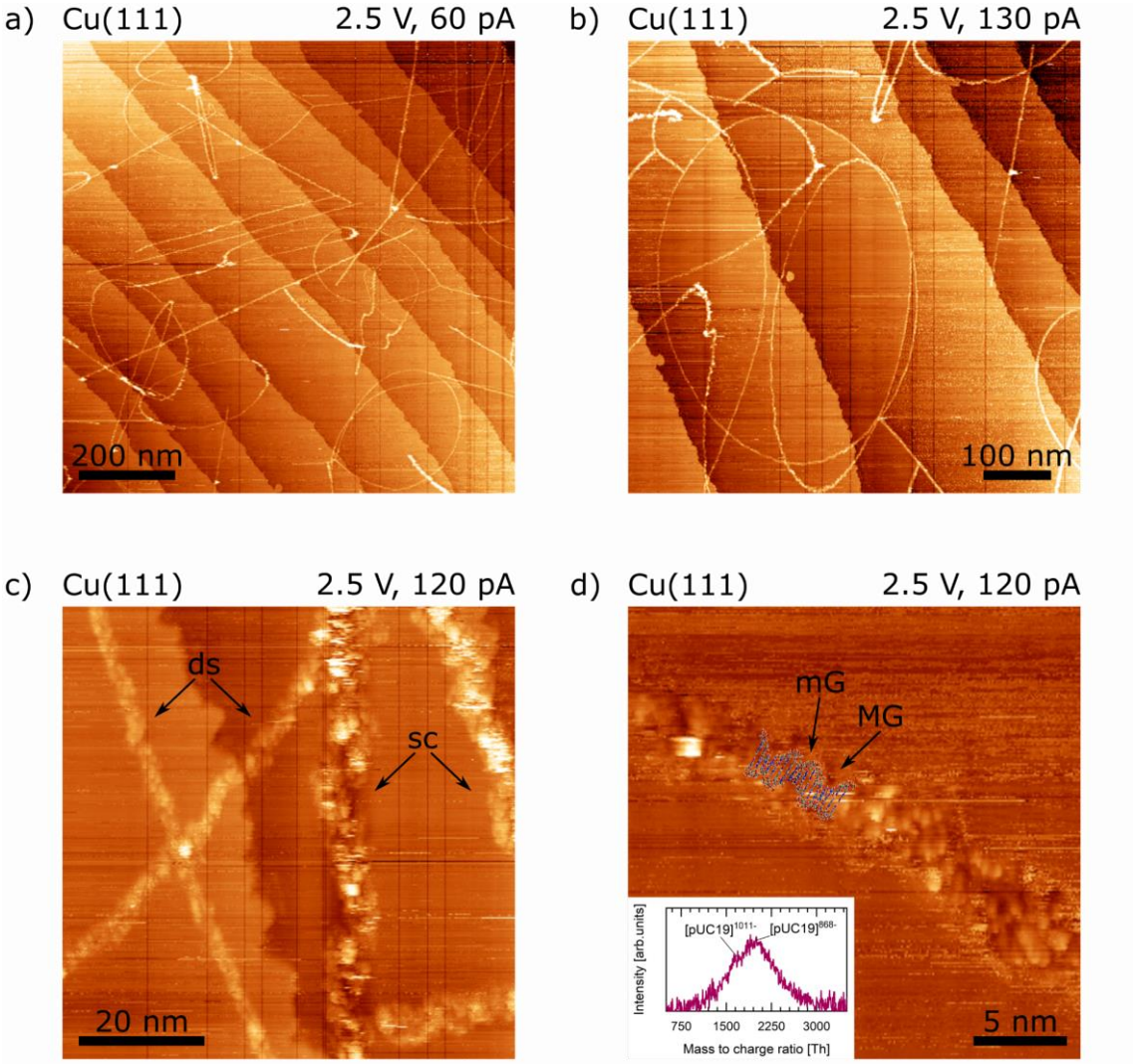


***Figure 4.15*** *a), b) Overview images of pUC19 DNA on Cu(111). Detailed images with c) dsDNA and supercoiled (sc) helices. The structural allocation to sc and ds forms is based on width assessment (Figure 4.24). Bright spots, that are visible at intersections of crossing strands, may reflect random overlays. d) major groove (MG) and minor groove (mG) marked in double helix model which is overlaid to the pUC19 image. The model is adjusted to the width of the DNA strand for simulation purposes.*

The images reveal individual, circular DNA molecules as rod-like and circular structures. On this scale, dsDNA and supercoiled DNA strands cannot be distinguished due to the resolution of the STM. With an image size of $1\mu m^2$ and a maximum resolution of $512 \times 512$, one pixel has the size of about $2 \times 2$ nm$^2$ which is in the same order as the diameter of a DNA strand. The detailed view presents two conformations – double-

stranded identified by its width of about 3 nm[47] and supercoiled DNA with a width of approximately 5 nm (Figure 4.15c). This supports some of the findings in the mass spectrum depicted in Figure 4.13a. In the close-up view, a model of double-stranded DNA is overlaid to the pUC19 image indicating structures such as major (MG) and minor (mg) groove (Section 2.6.1, Figure 4.15d).

**Studies of linearized pUC19 on Cu(111)**

The STM images in Figure 4.16 show pUC19 molecules on Cu(111)[48], which were linearized with the enzyme EcoRI prior to the ES-CIBD process. If the reaction of linearization was complete, no circles should appear on the surface.

In contrast to the unmodified DNA, the overview images (Figure 4.16a and b), reveal that all objects referring to DNA appear as rods as expected by a linearization experiment. This confirms that the reaction with the restriction enzyme was successful. On this scale, different widths of the single strands cannot be distinguished due to the resolution of the STM. The detailed images reveal different width of DNA strands. Surface, preparation and STM tip are identical. The respective widths of 3 nm correspond to the size of a double strand. In addition, strands with a width of $\approx 4.5$ nm are present on the surface (Figure 4.16c).

Theoretically, there do not exist supercoiled linear DNA strands. Linear strands have loose ends and are not able to supercoil without infringing laws of energy or entropy. However, an incomplete enzymatic reaction resulting in remaining circular species in supercoiled conformation. Furthermore, the addition of organic compounds to the spray solution might induce conformational change of the DNA strands. Moreover, the effect might be caused by the landing process. The orientation of the molecules is randomly distributed in gas phase. A DNA strand could be oriented parallel to the surface. Thus, it impinges with its entire length at once on the surface without any mechanical disturbances and with immediate discharging, resulting in a regular, stretched structure. A molecule, which is oriented perpendicular to the surface, hits the surface with its tip leading to an eventual compression due to change of the momentum. This might be visible in Figure 4.16d and possibly to a low extent in Figure 4.16c (strands on the right side). Furthermore, the deviations might be explained by scan artefacts caused by the

[47] The values, obtained in the width measurements of STM images, differ from the values determined by X-ray spectroscopy or other methods. This is an effect of the broadening induced by the STM tip.

[48] coverage about 3%

STM tip or spontaneous overlapping of two DNA strands (Figure 4.16c, upper left corner).

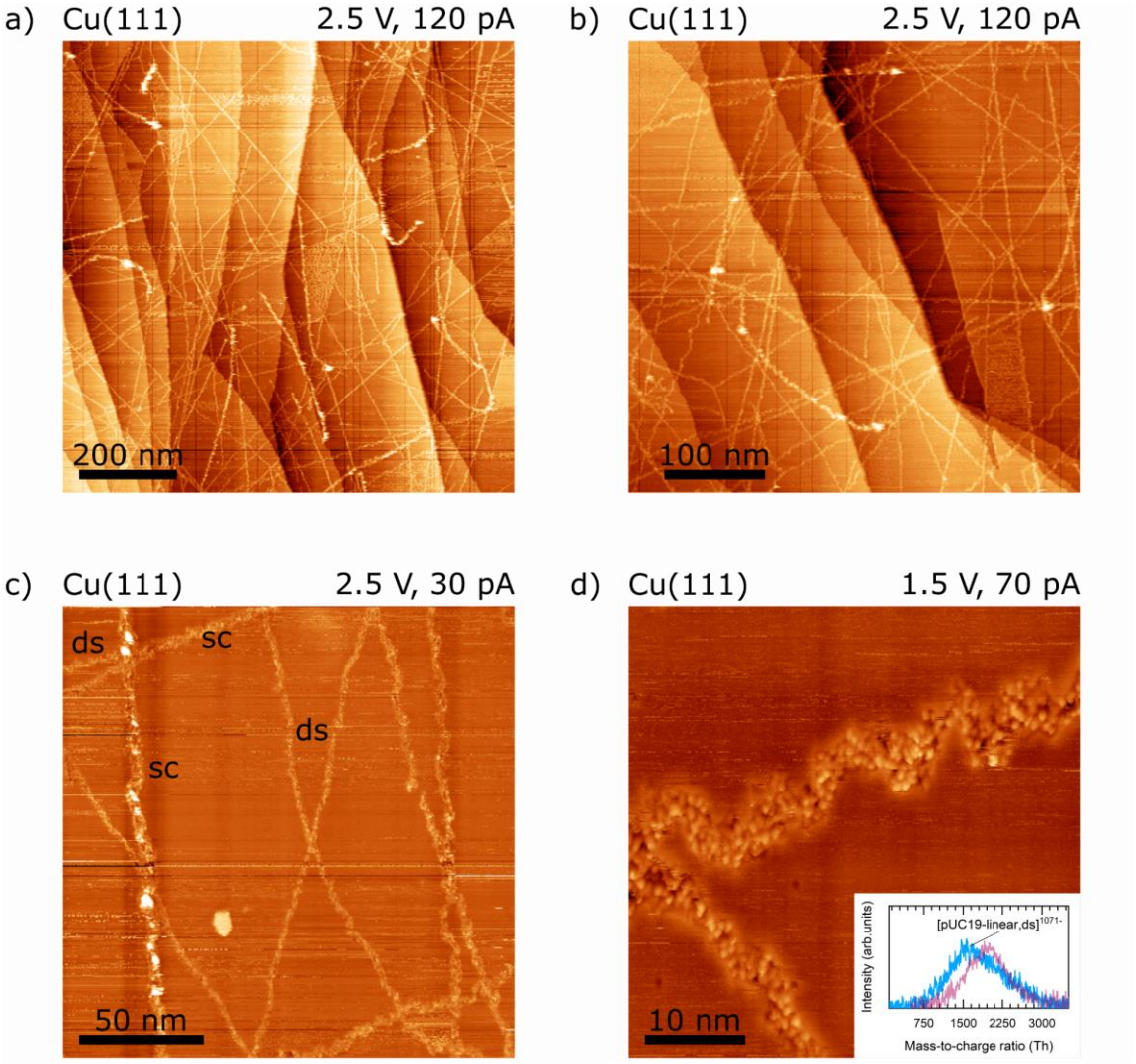


***Figure 4.16*** *a), b) Overview images of linearized, double stranded pUC19. While circular conformations are absent, the linear DNA strands appear with widths of* $\approx 3$ *nm which reveals dsDNA. Molecules with a width of* $\approx 4.5$ *nm may be attributed to supercoiled species, scan artefacts or an effect of the orientation during the landing process (for more details, see text). The detailed image in c) and high magnification image in d) show that the DNA strands seem less rigid than the circular pUC19 The coverage is about* $3\%$.

Single-stranded DNA is produced by heating linear dsDNA to $94$°C for some minutes and freezing the current conformation. This procedure is supposed to separate the double-strands into single strands (ssDNA) In Figure 4.17, linear, single-stranded pUC19 was deposited on a Cu(111) substrate for STM analysis.

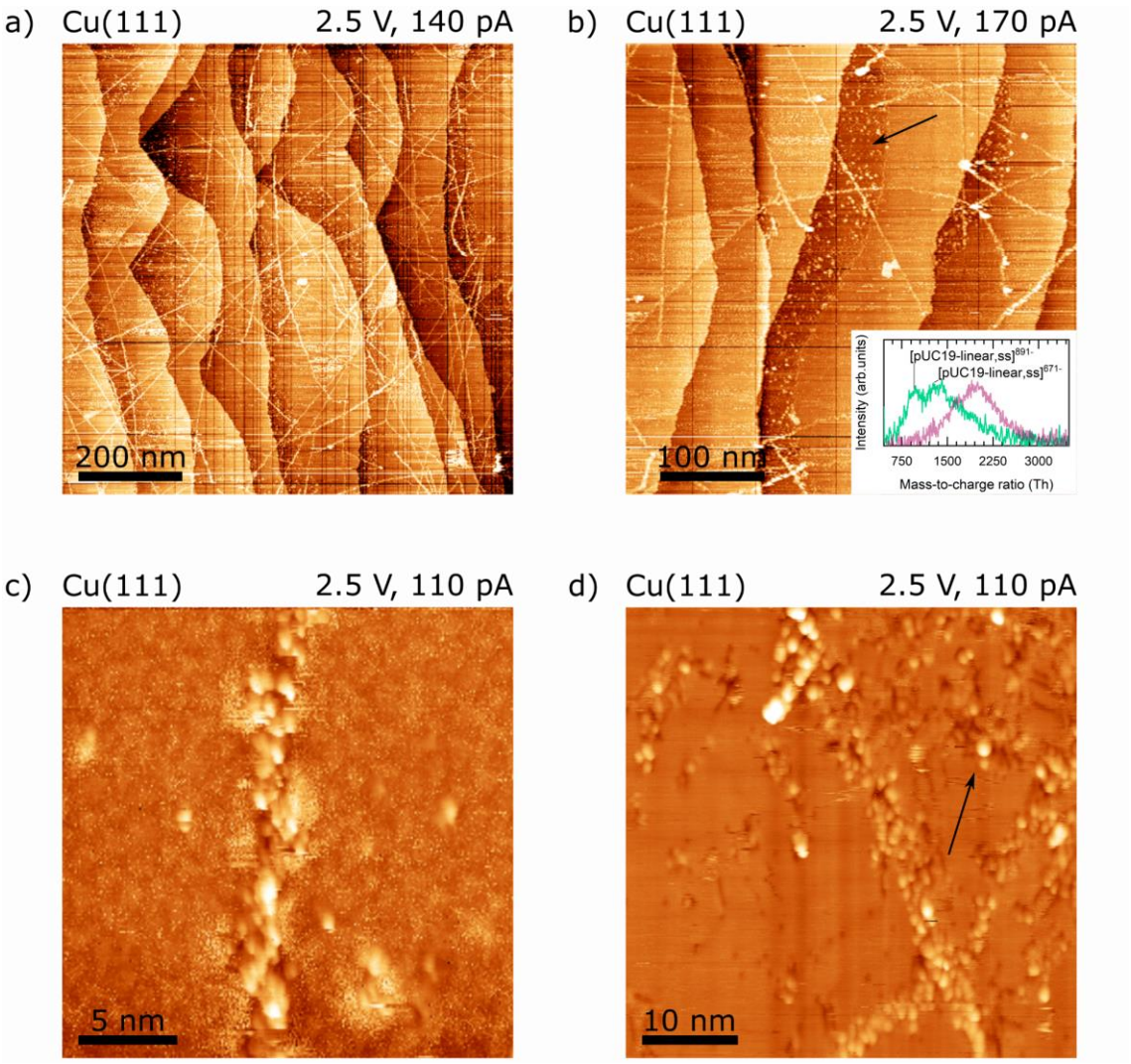


***Figure 4.17*** *a), b) Overview images of linear, single-stranded pUC19 on Cu(111). Fibers which reflect linear DNA with substructures in close proximity to DNA strands (arrow). c), d) Detailed views of the DNA showing regular patterns (substructure built by unknown objects) surrounding the DNA molecule (c) and partial clustering of single-stranded molecules (d). The coverage of the surface is about* $4\%$.

Quenching on ice and immediate processing are required as ssDNA tends to reassemble with the complementary strand forming the basic double-strand conformation according to sequence-dependent kinetics. On the overview images (Figure 4.17a,b), individual molecules can be observed in rod-like conformation, similar to the double-stranded, linearized pUC19. The expected width according of the ssDNA cannot be resolved by the STM. Figure 4.17c reveals a substructure around the elongated molecule, while in Figure 4.17d, the DNA or at least parts of the molecules seem to form clusters.

**Studies of pUC19 topoisomers on Cu(111)**

The STM images (Figure 4.18a and b) show the artificially relaxed pUC19 on Cu(111) with a coverage of about 4%. The pUC19 DNA was exposed *in vitro* to Topoisomerase I aiming to detangle some of the supercoils. As discussed in the MS section, this procedure is supposed to unwind the DNA molecule to a certain extent resulting in a less compact molecule (Figure 4.18d). This is expected to appear as wide, possibly flexible rings instead of stiff rods on STM images.

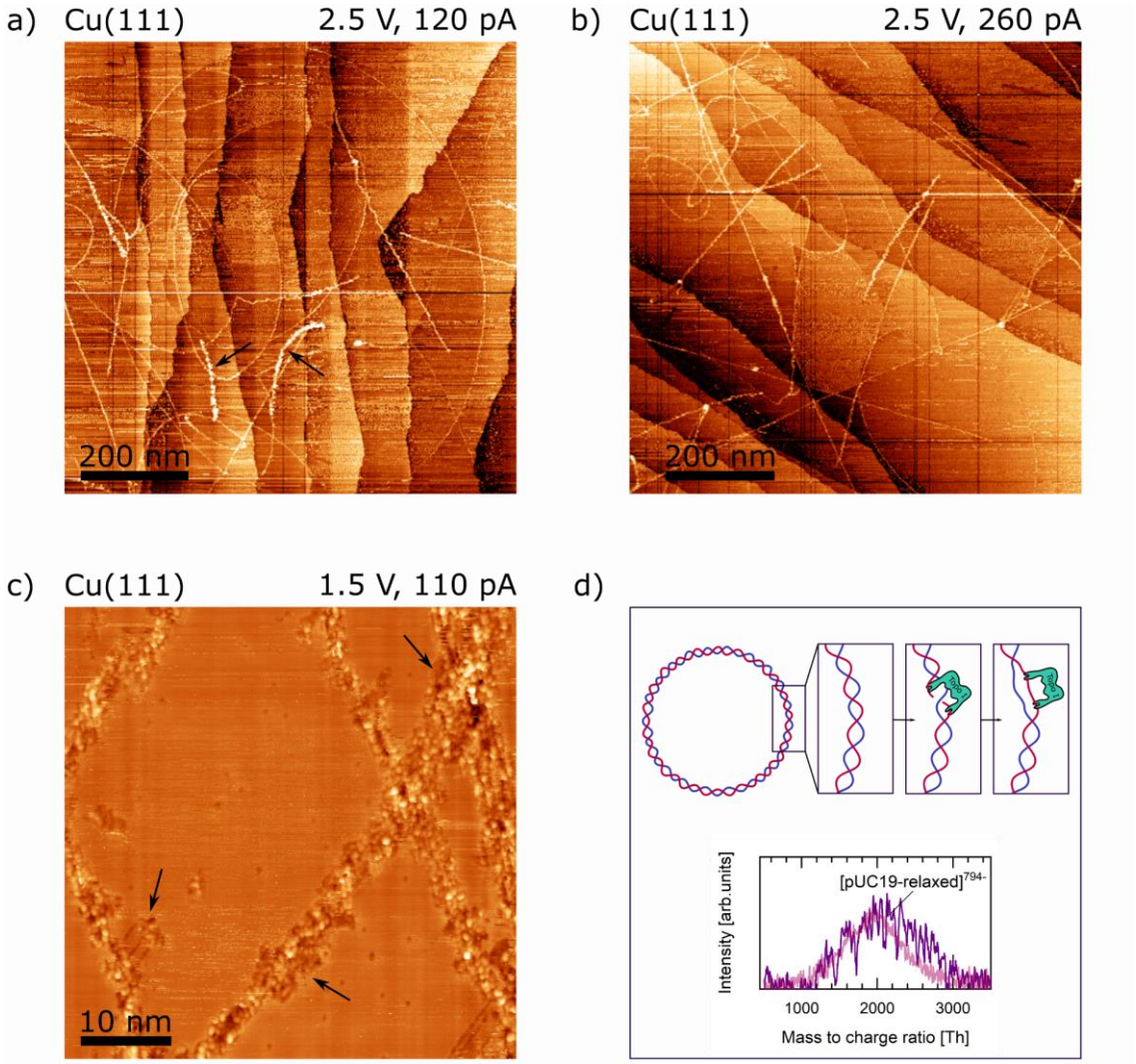


***Figure 4.18*** *Overview (a, b) of intentionally relaxed pUC19 on Cu(111). The images show circular and rod-like dsDNA. Bright structures may represent sc domains. c) detailed view: In addition to standard structures, adducts of unknown origination (in both, ordered and unordered patterns) seem to be attached to the DNA strands (arrows). (d) detangling principle of Topoisomerase I (Topo I) and mass spectrum of detangled pUC19 DNA (extracted from Figure 4.13).*

Both overview pictures reveal individual pUC19 molecules as circles with unexpected variable diameters and as rods. The reason of different radii might be explained by polymerization or clustering of two or more DNA strands. This might be induced by irregular ligation that was catalysed by the Topoisomerase I enzyme or during the spray process[49]. The small circular structures of the pUC19, observed in Figure 4.18b, might not be individual molecules but part of further (overlapping or intersecting) structures. In addition, short, thick and bright spots or traces appear. These might be attributed to extremely supercoiled DNA which is the opposite of the effect, that was expected by the treatment, or even dimerized monomers of pUC19 (cf. Figure 4.12). The close-up view (Figure 4.18c) depicts pUC19 molecules with substructure and there are signs of unidentified adducts which bind to the DNA strands. The latter might explain the shift towards high $m/z$-ratios in the mass spectrum depicted in Figure 4.13b suggesting that the adducts travel with the DNA from ambient pressure to UHV target without losing contact to the carrier molecule.

**Studies of compacted DNA on Ag(111) and Cu(111)**

Compaction of DNA can be forced by the polycationic spermine which serves as counter ion to the negatively charged phosphate backbone of DNA. To investigate the interaction of pUC19, regarding narrower structures on the surface, is performed by two approaches, the deposition of a pUC19-spermine complex which was formed in solution prior to deposition and the subsequent deposition of DNA and spermine. The images of the simultaneous preparation were captured on Ag(111) while the subsequent deposition was measured on Cu(111), which might have an impact on the assembly behaviour. Figure 4.20 shows results of the concomitant approach on Ag(111) with two different concentrations of spermine: $250$ spermine particles per DNA molecule, which translates into a mean coverage of one spermine every $3.5$ nm of the DNA in axial length or every $10$ to $11$ bp (about a helical turn), and about $10^8$ spermine molecules per DNA which translates into $10^6$ spermine per nanometre of the DNA in axial length. The spermine molecules have various possibilities to bind to the DNA strands: along or perpendicular to the helical axis as well as with one end bound to the pUC19 and the other end freely rotating. The different configurations might impact the geometry and thus, the conformation of the pUC19.

[49] See theory about electrospinning in the text below

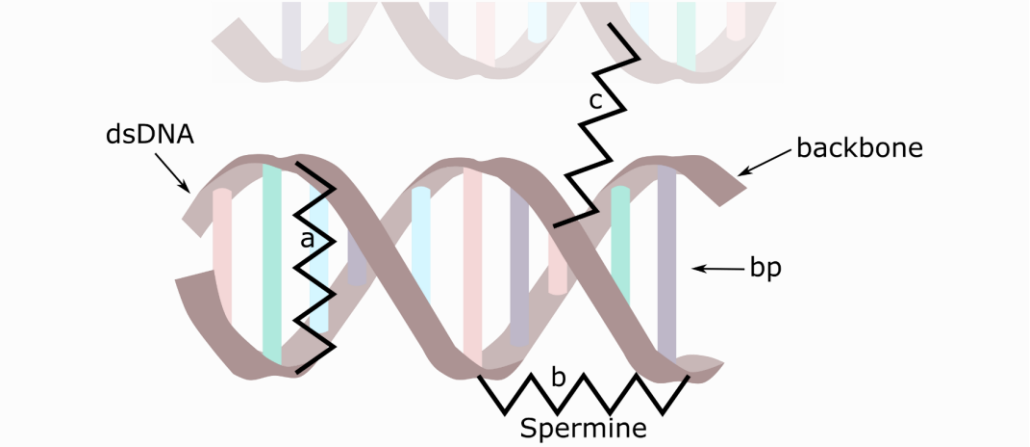


***Figure 4.19*** *Schematic of DNA-spermine interaction. The spermine molecules can bind to the DNA triggering compaction (b) or dimerization (intermolecular interaction - c). Binding type a does not have an impact on conformation or polymerization, but might change the intramolecular appearance [201]. Adapted from [176] and [210] with modifications.*

Spermine molecules, which bind to the DNA in configurations “a” or “b”, suggest compaction of the double-strand DNA (Figure 4.19, minimization of energy). Binding of spermine in configuration “c” can causes increased intermolecular compaction and by intramolecular connections of the loose end, dimerization by intermolecular binding or a higher interaction to the underlying surface [176, 210].

In Figure 4.20a and b, the amount of spermine is about $450000$ times higher than the DNA leading to a surface which seems completely covered with small structures and while the DNA molecules seem to be hidden. It seems that the spermine is ordered regularly in small patches of varying orientations. The distance between single molecules is similar to the distance of bar spermine molecules on Ag(111) (cf. Section 4.2.2). The concentration of spermine in Figure 4.20c and d is approximately $250$ per DNA molecule. The surface could be measured with a much lower voltage than with the bare pUC19 which might be assigned to a lower height of the DNA strands or a higher interaction with the surface due to the spermine molecules. On the STM images in Figure 4.20b and d, the substructures with a length of about $2$ nm might be attributed to spermine which are bound to the DNA strands in configuration “a” or “b” (Figure 4.19) as depicted in the inset of Figure 4.20d. Molecular strands which exceed the assumed width of a supercoiled DNA might originate from an intermolecular spermine connecting two DNA strands (configuration “c” in Figure 4.19).

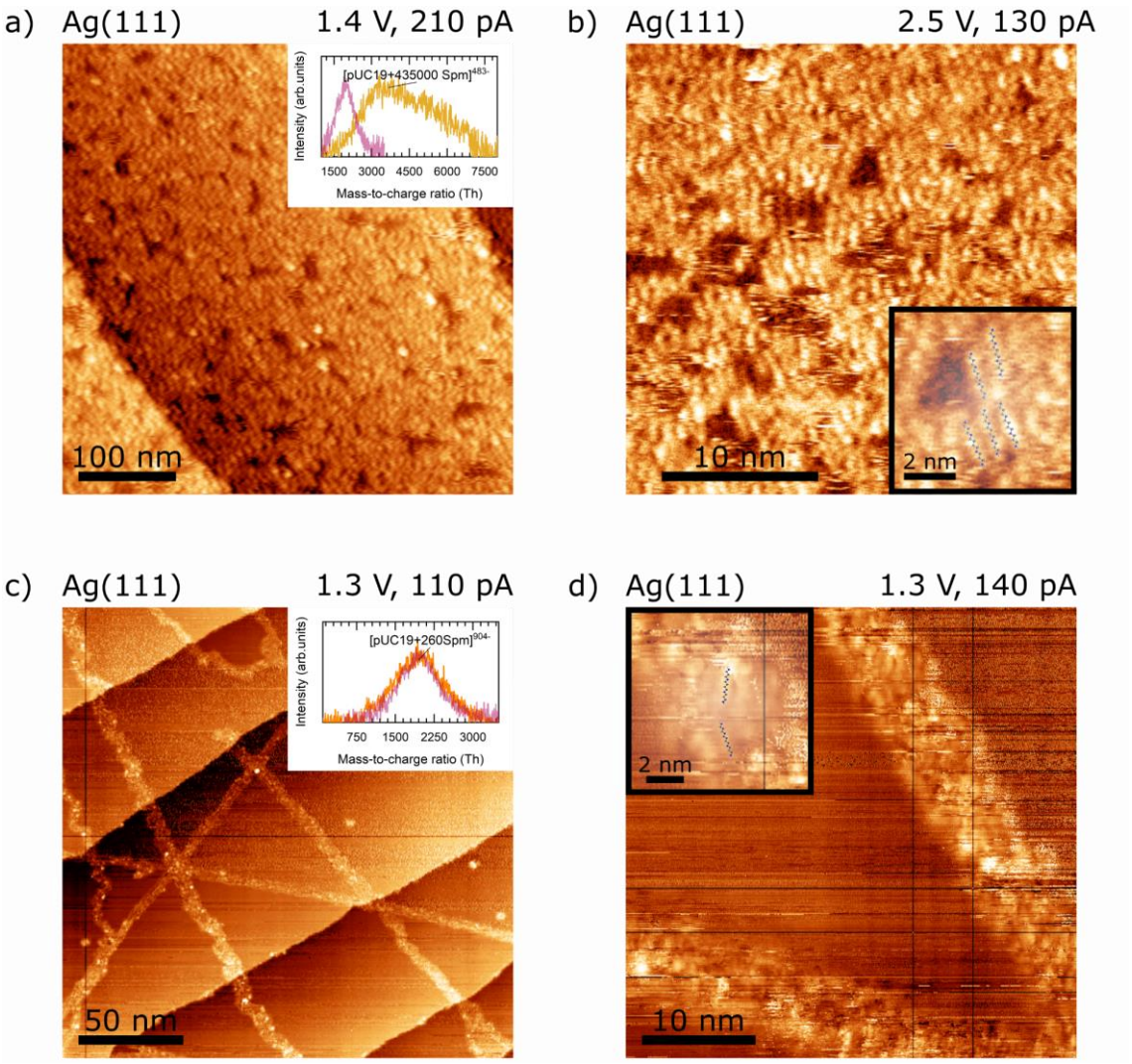


***Figure 4.20*** *a), b) Images of pUC19 incubated $10^8$ spermine molecules per DNA. Patches of regular structure in various directions can be observed. c), d) Images of pUC19 in combination with about $250$ spermine per DNA molecule. The spermine molecules seem to be evenly distributed along the DNA without clustering. DNA strands of different widths are revealed which might be attributed to different interactions of spermine with DNA (Figure 4.19).*

Figure 4.21 shows STM images of pUC19 on Cu(111) in combination with consecutively deposited spermine. The images reveal DNA strands in different conformations. Bright features can be observed on all images which might be accumulated spermine molecules or locally compacted DNA. In addition, islands of spermine are visible in the vicinity of the DNA strands (Figure 4.21b) as well as on the step edges (cf. Figure 4.21d). The interaction with spermine does not mediate a directed assembly event. In contrast to the simultaneous preparation with low concentration, the spermine molecules seem to bind to the DNA in a low or unstructured manner (see bright spots in Figure 4.21).

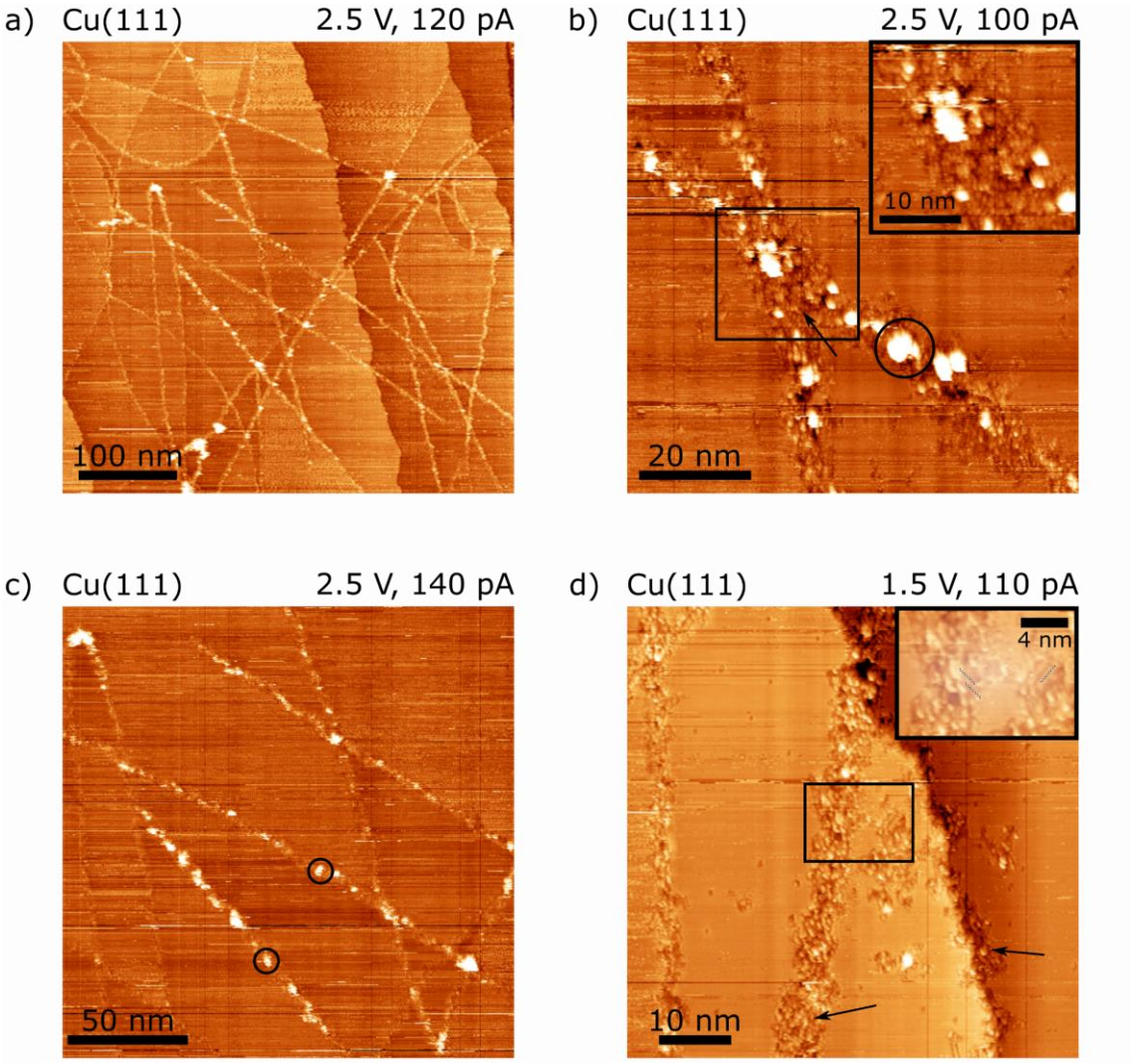


***Figure 4.21*** *STM images of the subsequent deposition of pUC19 and spermine on Cu(111). a) Overview image: The coverage of DNA molecules is about* $3\%$ *and the ratio between DNA and polyamine is about* $1:2000$*. b) The structure on the DNA strands (magnification in inset) is similar to the patterns that could be observed in Figure 4.20a and b. The bright spots (highlighted by black circles in b and c), which are distributed across the DNA strands, might be attributed to clustered spermine molecules or local compaction of DNA. d) Spermine islands are visible in vicinity of DNA strands and step edges (arrows). The inset shows elongated structures which might be assigned to spermine molecules which bind to the DNA strands in configuration a, b or c (Figure 4.19).*

Additionally, structured patterns can be observed on the DNA strands (Figure 4.21b). The edges of the DNA strands are not smooth (as seen in Figure 4.20c,d) but reveal protrusion which might be assigned to spermine bound to the DNA in configuration “c” (Figure 4.19). This leads to the assumption that the DNA strands function as a kind of spermine attractor or even catcher. Moreover, as depicted in the inset of Figure 4.21d,

the elongated substructure in the pUC19 might be assigned to spermine molecules attached to the DNA in configuration “a”, “b” or “c” (Figure 4.19).

The different widths of the DNA strands are not comparable to the width that can be measured on the surface of the simultaneous preparation. Firstly, the protrusions on the DNA strands have an impact on the diameter of a double strand. In addition, the experiments were performed on different substrates with different reactivity and thus, leading to different geometries of the molecules.

**Evaluation of length and width measurements**

As the length of a pUC19 molecule depends on the width and vice versa, a simultaneous measurement of the same DNA strands would be the most significant study. However, due to the large ratio of length to width, the statistical analysis of these two dimensions had to be performed separately.

The elongated pUC19 molecules do not show any self-assembly patterns. This may be due to the extended length, the lack of specific groups favouring such assembly and due to their immobility because of the interaction with the surface.

A statistical analysis of the investigated pUC19 variants was performed to carve out specific parameters to distinguish the DNA phenotypes. Even if the pUC19 is preserved in its native state upon deposition, the DNA strands cross on the surface which might make it difficult to resolve individual molecules. However, in all overview images, similar structures can be found (cf. Figure 4.22a):

- Circular structures - big and small (highlighted in green)
- Rod-like structures - long and short (highlighted in red)
- Racket-like structures (highlighted in blue).

As shown in Figure 4.22b, the length distributions of these structures reveal that most measurements fit to the calculated values of pUC19. The length for circular and linearized dsDNA appearing as circular and rod-like structures, respectively, is $913$ nm - latter especially for pUC19 which was manipulated with EcoRI. Furthermore, the sample size is very low for the linear species as the length of a linear pUC19 molecule is in the same range as the maximum distance the scanner of the STM can move. If the circular DNA looked like a rod-like strand, but is not supercoiled, the length would be $457$ nm ($50\%$ of full length). The mean length of the supercoiled DNA strands is assumed to be approximately $365$ nm which is $40\%$ of the circular dsDNA (i.e. $80\%$ of half the

circumference). According to the $Lk$ concept (Appendix A.1), the length (and width) of a supercoiled DNA strand is variable.

For the unmodified pUC19, the percentage of rod-like, circular and racket-like structures are relatively evenly distributed with a sample size of about $80$. This is an unexpected result, as the pUC19 is supposed to be mainly in supercoiled conformation (ratio $95\%: 5\%$). The differences might be attributed to the addition of organic solvent to the DNA stock solution or an unknown process might occur during the ionization.

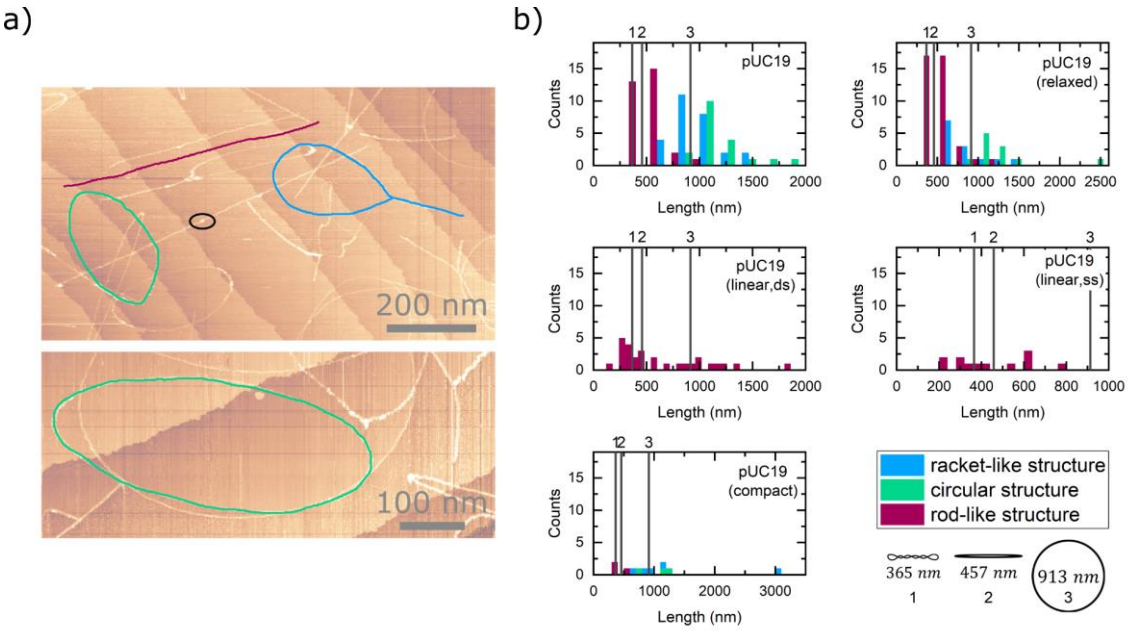


***Figure 4.22*** *a) Overview of different structures of pUC19 found on metal substrates. Racket-like structures are highlighted in blue, circular structures in green and rod-like structures in red. The black circle indicates exemplary indicates a bright spot on a DNA strand which might be due to overlapping or intermolecular connection. b) Distribution of length measurements of various conformations and variants of pUC19. Symbolic length values: circumference of open circular DNA according to number of base pairs (right); circular DNA collapsed in one direction (middle); assumed length of a sc strand (left) representing an exemplary value as intermediate coiling states depend on writhes.*

The detangled molecules are supposed to reveal a higher contribution of circular structures compared to the unmodified DNA. The results of the length measurements are contradictory. The amount of circular structures decreases at a sample size of about $65$ which is comparable to the unmodified pUC19. In addition, racket-like structures decrease and shrink in size while the supercoiled structures increase. A higher sample size would be necessary to support these finding. The sample sizes of the linearized and compacted species are very low and thus, do not allow for a meaningful

interpretation. Additionally, it is hard to find a whole molecule on the $1$ µm$^2$ sized image as this is the same order as the length of linear pUC19 molecule.

Larger deviations from the calculated length might be explained by various hypotheses. The DNA strands might polymerize and form dimers ([191], Figure 4.12), which may explain the length measurements with higher values than the theoretical lengths in Figure 4.22.

Furthermore, it needs to be pointed out that electrical and mechanical forces may have an effect on the molecules. By applying high voltages and temperatures to the emitter and thus, to the analyte solution, the DNA strands might undergo not only a conformational change but also a process called electrospinning [211]. This DNA fusion, that forms long chains by e.g., van der Waals interaction, is triggered by applying high voltages to a DNA solution which leads to overcoming the surface tension force of a polymer solution. The ES-CIBD is operated with lower voltages and lower concentrations, but also with less volume. In this way, the electrospinning might be an unwanted side effect. It is proposed that the beads (cf. Figure 4.22a, highlighted in black) represent two interconnected DNA strands. Moreover, the distance between two knots is about $400$ nm which fits to the theoretical value of pUC19.

Intersections of DNA strands and partly overlaying molecules make it difficult to tell the number of individual molecules only by visual inspection. This might explain measurement results below or above expected lengths (e.g., a length of $3000$ nm for a racket-like structure of a compact pUC19). Furthermore, depending on the position on the STM images, different lengths of the same molecule can be measured as the scanner of the STM causes distortions (Appendix A.3). Moreover, in the case of the linearized pUC19, the wrinkles might cause deviations from the expected lengths as they cannot be observed well in the overview images.

A reason for the short structures might be, that one molecule which is intersecting or overlapping (itself) might be accidentally counted as two separate molecules.

In Figure 4.23, the procedure, how the width of the DNA strands is measured, is illustrated by an example. Line profiles perpendicular to individual molecules are plotted and averaged subsequently. The width of the DNA strand results from the $FWHM$ of the averaged profile.

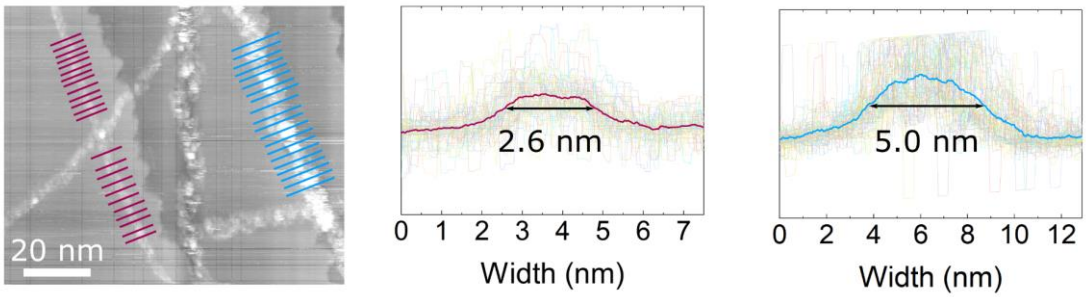


***Figure 4.23*** *Exemplary line profiles of two different DNA strands representing dsDNA (red) and supercoiled conformation (blue). The line plots (red and blue) are the averaged results all line profiles on individual strands.*

Figure 4.24 shows the statistical result of width measurements carried out on various variants and conformations of pUC19 DNA. Analysing all experiments reveals at least two different widths, which may be assigned to double strands and supercoiled helices. On the substrates with linear ssDNA and compacted pUC19 (which was incubated with spermine) a third species is found which might be associated with single strands and more compact supercoiled DNA, respectively.

The measured width of the double-stranded circular or linear pUC19 on Cu(111) and pUC19 in combination with spermine on Ag(111) is about 3 nm for all variants. This is 1.5 times the theoretical value in aqueous solution and is in good agreement with the value Tanaka et al. obtained with a different plasmid variant [196, 212]. The supercoiled DNA strands are between 4 nm and 4.5 nm wide which is 1.3 to 1.5 times the width of the dsDNA. This is in good agreement with values found in literature [200].

The heights of a DNA strand can be approximated by comparing the height of a step on the crystal since the intensities of the pixels are not dependent on topography but on tunnelling currents. Exemplary measurements (not shown here) reveal heights between 1.1 nm and 1.3 nm which is corresponding to the value resulting from the calculated values (about 1.3 nm height with a width of 3 nm)[50]. This leads to the assumption that the substrate is reactive and results in a 3D-flattening of the DNA strands which explains the deviations compared to the data obtained by neutron scattering in solution. Additional broadening effects of the STM tip have to be accounted especially for different substrates.

[50] derived from crystallography measurements in aqueous solution [196].

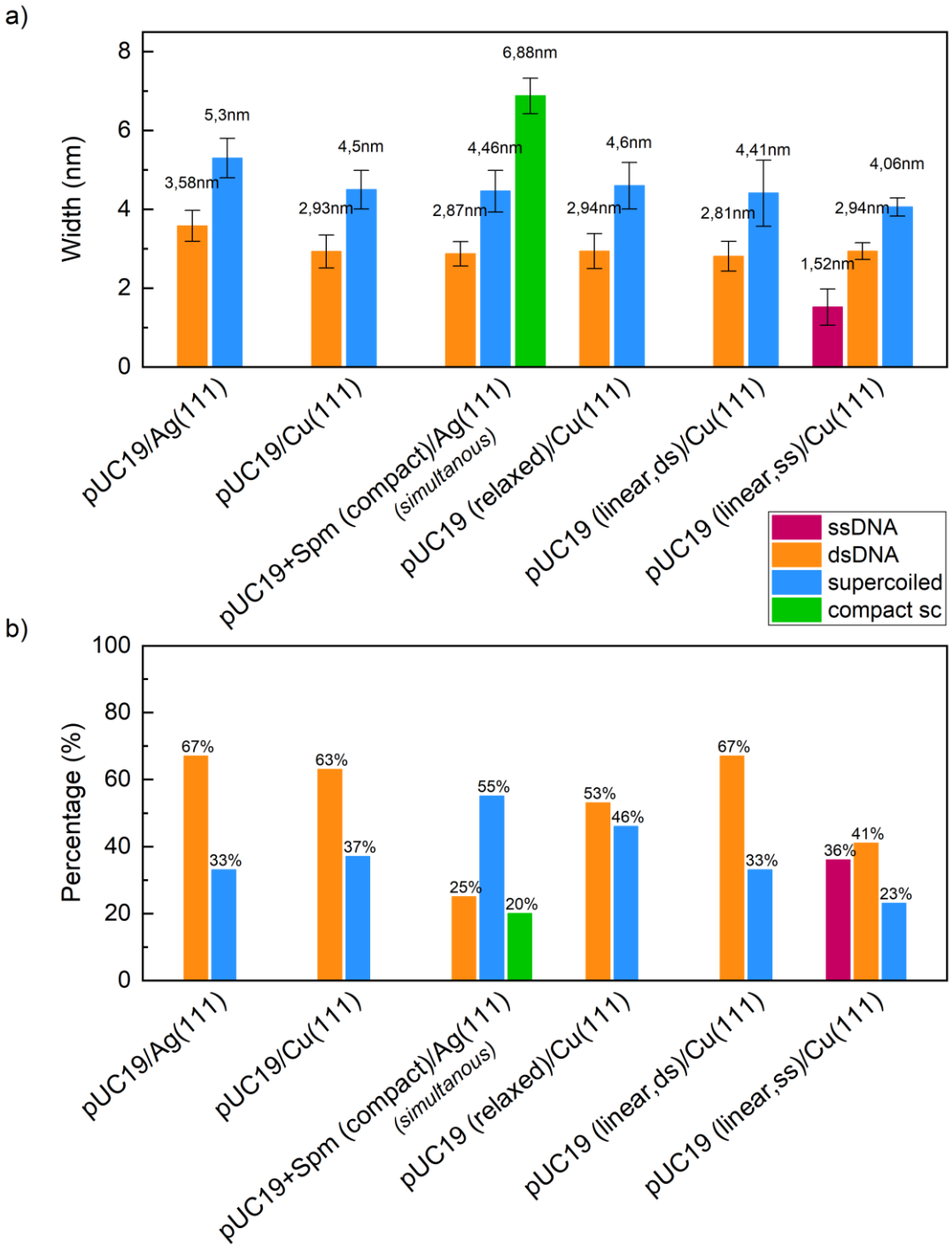


***Figure 4.24*** *a) Average widths and b) percentages of different conformations of pUC19 variants. The transitions between the groups which are attributed to different conformations of the DNA are not strict, but gradual.*

Moreover, the unmodified DNA strands appear to be broader on Ag(111) than on Cu(111). As there were a lot of difficulties during the scanning on the silver substrate, this might be due to an unstable STM tip. Furthermore, the copper substrate tends to

be more reactive than the silver and thus, the DNA strands are expected to be flatter and broader on the copper.

The percentage of different conformations for all investigated pUC19 variants is illustrated in Figure 4.24b. The amount of dsDNA is double the amount of supercoiled DNA for the unmodified pUC19 on both substrates, Cu(111) and Ag(111), and the linearized dsDNA. The simultaneous deposition of spermine and pUC19 has a higher amount of supercoiled DNA than dsDNA. For the relaxed pUC19, the statistics reveal similar amounts of relaxed and supercoiled DNA. For the preposition with linear ssDNA, $36\%$ are assigned to ssDNA, $41\%$ to dsDNA and $23\%$ to supercoiled species.

The pUC19 is delivered as $95\%$ of supercoiled DNA. Thus, it is assumed that the ESI process and the addition of organic solvents has an impact on this distribution. The pUC19 DNA might be delivered with a higher amount of open circular DNA strands than expected. Furthermore, the stock solution was frozen at $-20$°C for a while before the depositions. Potentially, this might lead to rearrangement driven by thermodynamic equilibrium. Moreover, the organic solvent or electrical and mechanical forces which are generated during the ESI process might lead to conformational changes of the analyte molecule. In addition, the single strands might be more fragile or may be reassembled to double strands after the heating process, in the droplet, in the gas phase or on the surface which might explain the lack of single-stranded species for the respective preparation. The presence of supercoiled species may suggest that the enzyme reaction was incomplete.

Further experiments would be necessary for a better insight: deposition with different landing energies and a reference measurement before the ES- CIBD such as gel electrophoresis are proposed.

**Observation of potential self-assembly on surfaces with linear, single-stranded and relaxed DNA**

Occasionally and in addition to the DNA strands, potential self-assembly of small building blocks is found on Cu(111) prepared with relaxed and linear, single-stranded DNA.

On the surface with the detangled pUC19, islands grow in the vicinity of the DNA strands and appear as long chains (up to a length of $100$ nm) arranged in crystal directions (cf. Figure 4.25). The molecules occupy every 3$^{rd}$ to 8$^{th}$ row of the Cu(111), translating into a distance of about $0.87$nm to $2.3$ nm between the lines. Putative building blocks are

proposed to be components of the DNA strands such as nucleobases, nucleotides and sugar phosphates. As the analyte solution is purified after the enzymatic reaction, the Topoisomerase I is not likely to be in the analyte solution and is thus, not supposed to be on the surface. Compared to the relaxed DNA, the pattern on the surface with linear ssDNA appears different. In the overview STM images, islands with a substructure can be found close to step edges and around DNA strands. The building blocks assemble to a closed layer without chain formation (Figure 4.26).

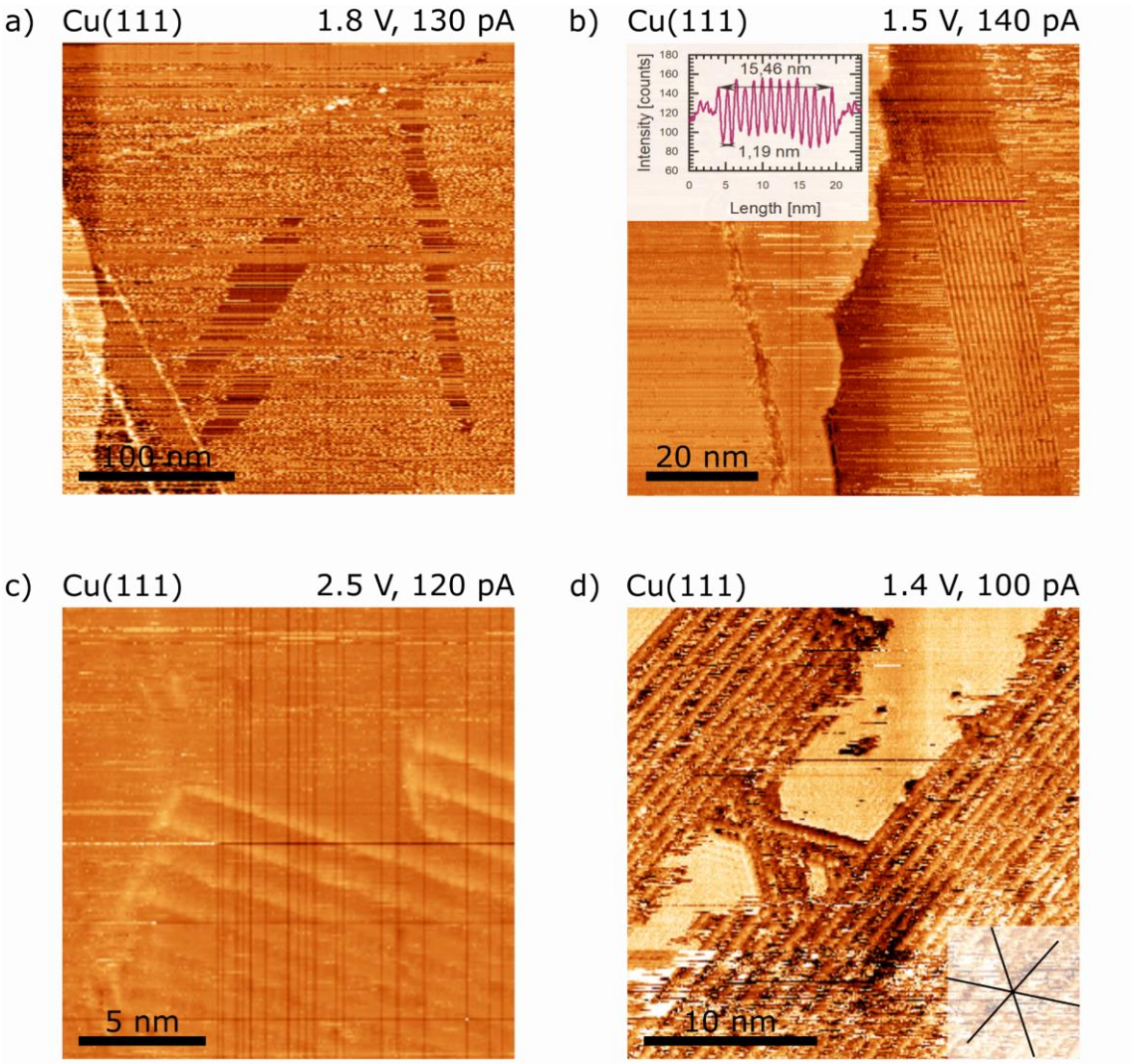


***Figure 4.25*** *Self-assembly patterns on the substrate with relaxed pUC19. a) overview image showing that the islands are protruding from the DNA strands. b) parallel polymerized chains with high regularity (inset) The mean distance between the lines is* 1.19 *nm. c), d) detailed view of substructure. The parallel molecular chains are assembled in crystal directions.*

Furthermore, the extended pattern formation suggests that the amount of available building blocks is high. The behaviour of the self-assembly seems to follow a different

mechanism compared to the chain-like pattern. In addition, due to their size (about 0.5 nm), they are supposed to move fast on the surface. The origin of the building blocks might be explained by various hypotheses. If they are already present in solution, the objects stick to the DNA during the ES-CIBD process accompanied by a potential alteration of the corresponding mass spectrum. A shift to higher masses is assumed as it can be observed in Figure 4.13b. The impact on the charging behaviour remains unclear. Any small objects, that are not attached to the DNA carrier, are filtered by the dQMS and do not reach the target.

Furthermore, the landing energy might have an effect on the integrity of the molecules. If the energy is high enough, the DNA strand might be partially and locally decomposed leaving small fragments on the surface (close to a DNA strand). These may just stick to the surface, at step edges or reconnect to the main DNA strand by diffusion. Building blocks such as nucleotides or nucleobases tend to reassemble on surfaces, due to their small size (about 1 nm and 0.6 nm, respectively), tentatively to regular patterns. This has been demonstrated multiple times by various groups [213–221].

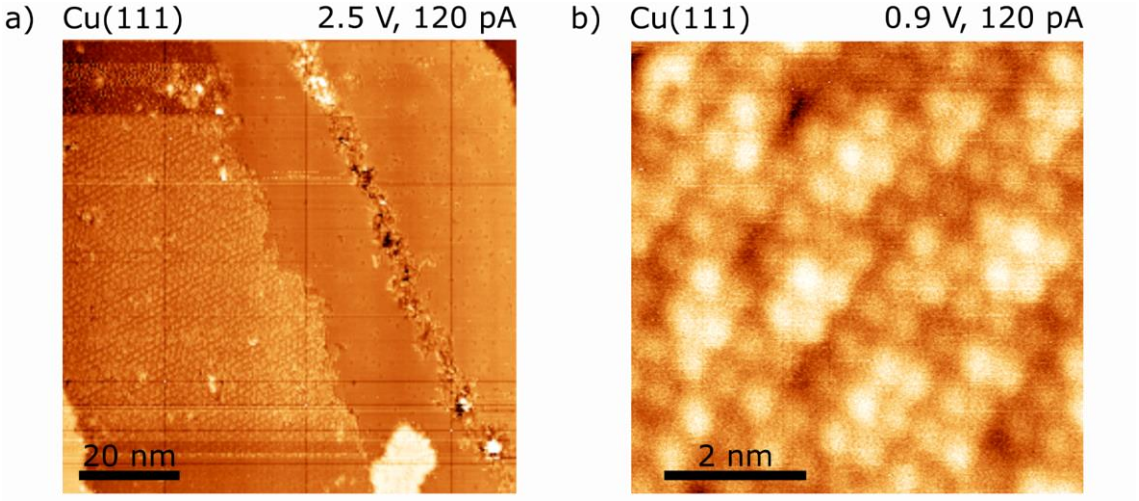


***Figure 4.26*** *Self-assembly patterns on the substrate with linear single-stranded pUC19. a) overview image: large island with visible substructure close to a DNA strand and at a step edge. b) The islands reveal a regular pattern of tentatively self-assembled building blocks.*

The extent of decomposition depends on the size of the molecule and its super-structure. While large molecules can easily relax by their atoms, single strands are more fragile than supercoiled and open circular DNA structures. Schultz et al. already mentioned the fragmentation of ssDNA in [191].

For further analysis and interpretation of the observed substructures, various reference experiments with the proposed building blocks would be necessary.

**Summary**

DNA in the order of MDa was the subject of investigation in ESI-settings a few times until now. The experiments were mostly analytical in order to determine the molecular masses by CD-MS [191, 222] and ESI-FTICR [195]. The deposition of these large dsDNA was achieved by rather simple ESI sources without $m/z$-selection and incomplete desolvation [223]. *In-situ* deposition by pulse injection is shown by other groups, but reveals solvents and other impurities on the substrate [224–226]. UHV deposition with $m/z$-filtering was only shown for salmon sperm DNA with low molecular weight so far [48].

In this thesis, a high molecular weight plasmid DNA was deposited in various variants by $m/z$-filtered ES-CIBD as pure fraction of the target molecules without contaminations from solvents, residual neutral gas atoms and unwanted interaction with molecular fragments (especially for the unmodified and linearized dsDNA as well as the pUC19/spermine complex). Moreover, the integrity of the molecule remains preserved. Mass spectra of various pUC19 variants reveal different charge states for different conformations of DNA. According to the Rayleigh model, following $m/z$-relations might be extracted for different pUC19 conformations based on the cylindrical geometry [204]:

$$\frac{m}{z}_{linear,ss} < \frac{m}{z}_{linear,ds} \approx \frac{m}{z}_{relaxed\ circ.} < \frac{m}{z}_{relaxed\ circ.(collapsed)} < \frac{m}{z}_{supercoiled\ (ccc)}. \quad (4.5)$$

Additionally, the charge state is influenced by the ejection process of the droplet and collision with neutral or charged molecules in the gas phase (leading to a discharge). These findings are supported by STM images. Different structures, properties and conformations of the DNA could be characterized and measured in length and width. On the substrates with relaxed dsDNA and linear ssDNA, islands of self-assembled substructures are formed by different building blocks. Hence, further experiments are necessary for a more detailed analysis.

## 4.4 Conclusion

The investigated molecules spermine (202 Da), insulin (5.8 kDa) and pUC19 (1.7 MDa), which are candidates of the most common ionization models (IEM, CRM, CEM), could successfully be deposited in UHV using the home-built ES-CIBD system.

The analyte solutions were adapted to the properties of each molecule separately. The main components as dd$H_2O$ and ACN are combined with basic or acidic compounds such as TEA or acetic acid in order to dissolve the molecules and/or increase the conductivity of the solution, provide charges as H donor (acid) or to support deprotonation (base). The intensity of the ion beam reaches currents up to 2.2 nA during the deposition.

The recorded mass spectra give access to the chemical integrity, the charge states and the composition of the analyte solution. The mass-to-charge ratios of the spermine molecules hint to the formation of adducts with $CO_2$ in addition to the pure analyte. The number of complexes may depend on factors like the flow rate of the spray solution. The spectra of insulin make monomeric and one dimeric species visible. Further dimers are likely masked by corresponding monomers. Additionally, formation of adducts with $H_2O$ molecules, $Na^+$ or $Ka^+$ could be observed in high- resolution spectra. While the spermine and insulin molecules reveal resolved peaks, pUC19 has a huge distribution of possible charge states coming from the elongated conformation and the sheer size of the molecule. Experiments with various pUC19 variants shift the distribution of the charge states to higher or lower values in comparison to the unmodified molecules. This might indicate different conformations of the DNA, such as supercoiled, double-stranded and single-stranded molecules, but also the formation of dimers or adducts with spermine or fragmented DNA molecules as in the case of the relaxed pUC19 which was treated with the enzyme Topoisomerase I.

Subsequent investigation with the STM reveal mostly intact molecules. With previous treatment, the DNA molecules tend to shear or are susceptible to electromechanical stress (e.g., ssDNA) and odd structures were observed that may originate from a partial fragmentation and subsequent self-assembly. The molecular layers on the surfaces appeared without impurities of residual gas, solvent or (in most cases) ion fragments. On the surface with spermine, both self-assembled and un-coordinated structures could be observed. The small, ordered islands may be coordinated by hydrogen bridges or carbamate moieties between the single molecules. The unordered islands might be

due to overlapping molecules, multilayer formation or molecules which point out of the plane. The STM images of insulin reveal both, monomeric and dimeric structures, which was already indicated by the mass spectra. The molecules accumulate on the step edges of the silver and copper crystal without showing a self-assembling behaviour. Plasmid DNA pUC19 appears in its predicted topoisomers on silver and copper surfaces including rod-like and circular conformations as well as racket-like structures as an intermediate state. In the presence of spermine, the DNA strands may act as molecular catcher as spermine is attached to pUC19 molecules while these complexes are preserved during the electrospray process. Moreover, the intramolecular structure of the DNA looks different compared to a surface of DNA without spermine. Linear, single-stranded pUC19[51] and relaxed pUC19[52] reveal additional islands of small building blocks on the surface. This might be due to a loss of stability according to the treatment with conformation-modifying enzymes. Length and width measurements reveal the existence of different conformations such as supercoiled, double-stranded and single-stranded DNA and the probable existence of dimeric/oligomeric molecules. Due to the reactivity of the surface, the molecules are flatter and broader compared to the values obtained in solution [200].

The analysis of mass spectrometry and STM demonstrates, that the relationship of a molecular size/geometry and behaviour of the molecule regarding ionization can be approached by the Rayleigh model, but not completely understood.

The underlying physical principles of the spray process including ionization mechanisms, resulting charging efficiency and subsequent behaviour in gas phase is not a simple function. The complexity of the ionization models which are still developed by several groups, is determined by properties of electrolyte mixtures such as surface tension and vapour pressure, geometries of molecules including varying molecular structures and topologies, electrostatic events during the spray process, etc. The Rayleigh model, which is based on a simple sphere model and a single-component electrolyte (water), has its limitations for complex structures as analysed in this thesis. Postulated water shells around the molecules may contribute to the geometry of the analyte species and therefore, have an impact on the charging behaviour. Thus,

[51] Treated with EcoRI and subsequently, cooked

[52] Treated with Topoisomerase I

complementing simulations such as molecular dynamics calculations and further systematic studies (e.g., spermine-DNA titration) would be necessary.

# Part B

## Analysis of thermal programmed desorption measurements on organic molecules

# 5 TPD-Fundamentals and theory

In this chapter, the theory of adsorption and desorption is discussed as well as basic terms and parameters are introduced. Adsorption processes and layer growth are discussed and the desorption process is described in detail. An overview of the conventional analysis of kinetic parameters, the principles of the simulations using the Runge-Kutta method and a short outline of Monte-Carlo simulations are given.

## 5.1 Adsorption processes and scattering

Molecules hitting a surface out of the gas phase may be adsorbed or scattered in their original state. Alternatively, they may disintegrate or undergo a reaction with the reaction products staying adsorbed or leaving the surface. If the molecules stay intact, the sticking coefficient $s$ can be measured and provides important information as it depends on various parameters e.g., coverage and temperature:

$$s = \frac{amount\ of\ irreversible\ adsorbed\ molecules}{amount\ of\ molecules\ hitting\ the\ surface} \tag{5.1}$$

In literature, there are a lot of summaries, which describe the experimental and theoretical processes of scattering and sticking [227–231].

### 5.1.1 Possible processes on the surface

Regarding atomic gases and molecules, accordingly, five different processes can be classified: Direct adsorption describes how particles lose their kinetic energy, when hitting a surface and directly stick to it (Figure 5.1a). If the particle does not lose enough energy to immediately stick on first impact, the process is called hopping adsorption. In that case, the particle can move across the surface until it hits a collision partner and adsorbs. The statistical character of this process is important (Figure 5.1b). Selective adsorption describes a process that is based on the possibility that momentum (according to a reciprocal lattice vector) is transferred between the particle and the crystal provided that the energy and the angle of the incident particle are suitable. This results in a movement parallel to the surface. The particle is moving with transversal velocity and the total energy is still positive, though it is bound to the surface. It can

dissipate its energy at surface defects to stick or it can desorb e.g., by interacting with a defect (Figure 5.1c) [232–235]. If the conditions for selective adsorption are not fulfilled, momentum or energy can still be transferred between the particle and the surface which is called elastic or inelastic scattering (Figure 5.1d). A special case of elastic scattering is the so-called rainbow scattering, i.e. scattering on a periodically structured surface. Because of the periodic deflection, different accumulated intensities result from different scattering angles.

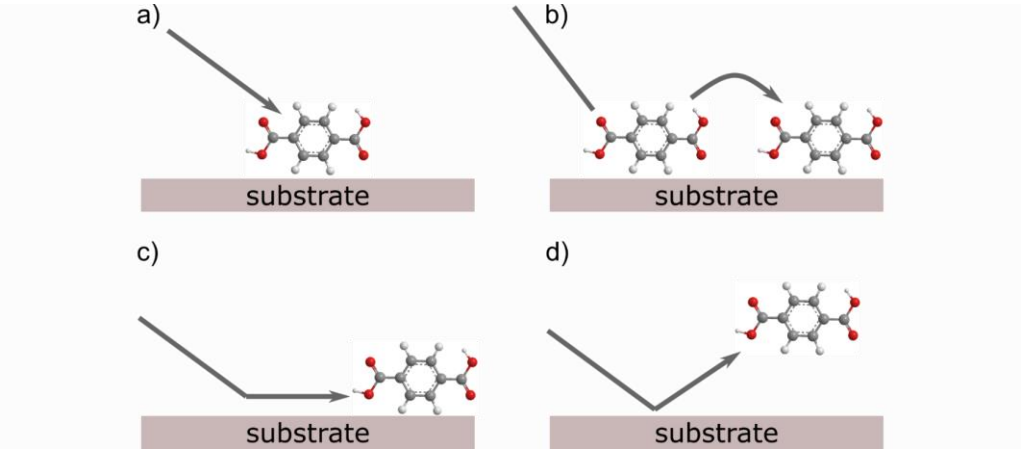


***Figure 5.1:*** *Schematic illustration of different molecule-surface interactions: a) direct adsorption, b) hopping adsorption, c) selective adsorption and d) elastic/inelastic scattering*

### 5.1.2 Layer growth

Depending on type and strength of the interaction between substrate and adsorbate, three growth modes are distinguished [236]:

1. Layer growth (Frank-van der Merwe growth): the interaction between particles in a layer is weaker than between particles of adjacent layers or the substrate. The attractive interaction of the substrate decreases with increasing distance from the surface but is significant across several layers. In result, a single layer will be completely closed before the next one starts (“complete wetting”) (Figure 5.2a).
2. Island growth (Vollmer-Weber growth): the interaction between substrate and adsorbate is low in comparison with the interaction between the adsorbate particles. 3D- growth starts before a first confluent layer is built (Figure 5.2c).

3. Stranski-Krastanov growth is a mixed form where the first layer will be closed, the following layers, however, are growing as described in the island growth (Figure 5.2b).

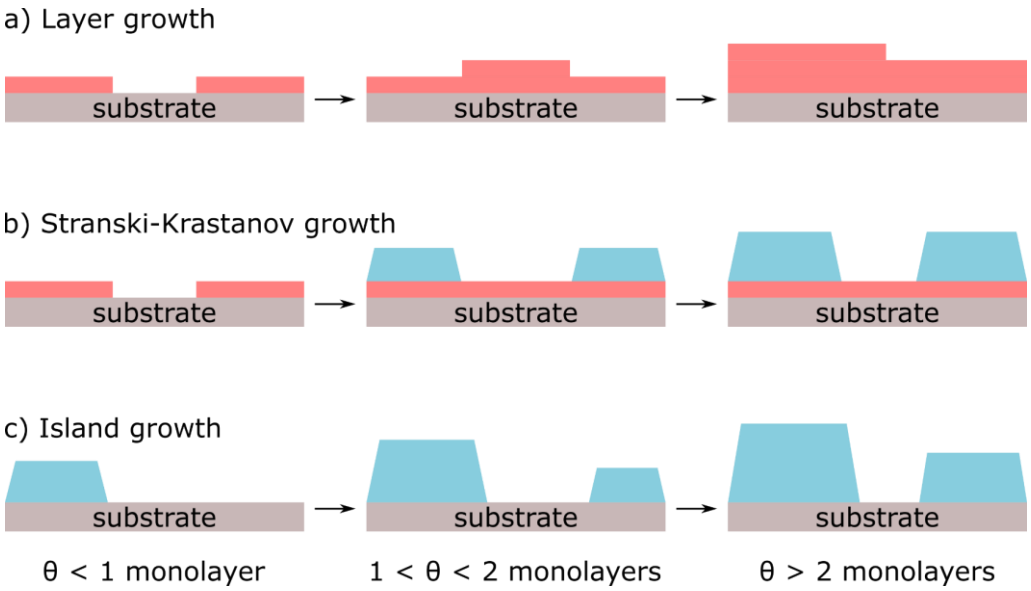


**Figure 5.2** *Possible growth modes of monolayers and multilayers: a) layer growth, b) Stranski-Krastanov growth and c) island growth. Colours for better layer differentiation.*

These modes are based on mere energetic arguments, i.e. it is considered an equilibrium classification. All particles reside in their energetic lowest state. Thought kinetic restraints may keep an adsorbate system in its local energetic minimum. The hopping barrier may be higher than the actual temperature. By tempering the system, the hopping barrier can be overcome to verify this kind of "wrong" classification.

## 5.2 Influence of coverage and precursor

The adsorption process is influenced by the extent of the coverage on the surface. The reaction of impinging adsorbate particles is remarkably sensitive to free or occupied sites. This sensitivity is due to the energy loss $\Delta E$ of the impinging particle which strongly depends on the mass ratio of the colliding particles $\mu$ [237]. An impinging particle has to transfer a sufficient amount of energy $\Delta E$ to the surface to reduce its kinetic energy to zero. Assuming the particle is hitting a single adsorbate particle or surface atom, respectively, and the coverage is sufficiently low that the interaction with neighbouring atoms can be neglected, the mass of the collision partners is the predominant factor for the energy loss. The simplest model for this energy loss is the classical, central hard-core collision:

$$\Delta E = \frac{4\mu}{(1+\mu)^2}(E_0 + E_{Kin}) \tag{5.2}$$

with the binding energy $E_0$ and the kinetic energy $E_{Kin}$ [237]. From Equation 5.2, it can be deduced that $\mu = 1$ is leading to an energy and momentum transfer of 100% from the adsorbate particle to the fixed collision particle. Thus, a particle, which is already sticking to the surface, serves as ideal partner to deposit energy. Both particles will (re)distribute the energy from such a precursor state, as discussed below. The common case is the distribution of energy between adsorbate and surface as the impact will not be centred. Collisions with surface atoms are in most cases less effective than with a fixed adsorbate particle, as these atoms have comparably high masses to the surface atom. This model is very simple and may be applied only to particles with small internal degrees of freedom, as these may absorb relevant parts of the kinetic energy.

The definition of the precursor state - a special state of adsorbate particles that is passed during the adsorption process - is a binding state that is different from the final state mostly due to a weaker binding and higher mobility. Figure 2.3a shows the potential ratio of the precursor state $E_P$, the binding energy $E_0$ and the activation energy $E_A$. Depending on the adsorption site, two different cases are possible: intrinsic (above a free binding site) or extrinsic precursor, respectively as depicted in Figure 5.3b [238–240].

The amount of adsorbed species or coverage $\theta$ can be described as the highest possible amount of atoms or molecules in one layer independent from the ordering on the surface with values between $0$ and $1$ monolayers (ML). This definition has both, advantages and disadvantages. On the one hand, calculations are simplified because of low exponents in the rate equation (see Section 5.3.1). On the other hand, every layer has its own “coverage”.

In literature, the definition of the coverage is handled differently, e.g., relating the coverage to the number of substrate atoms or using the area density [241, 242].

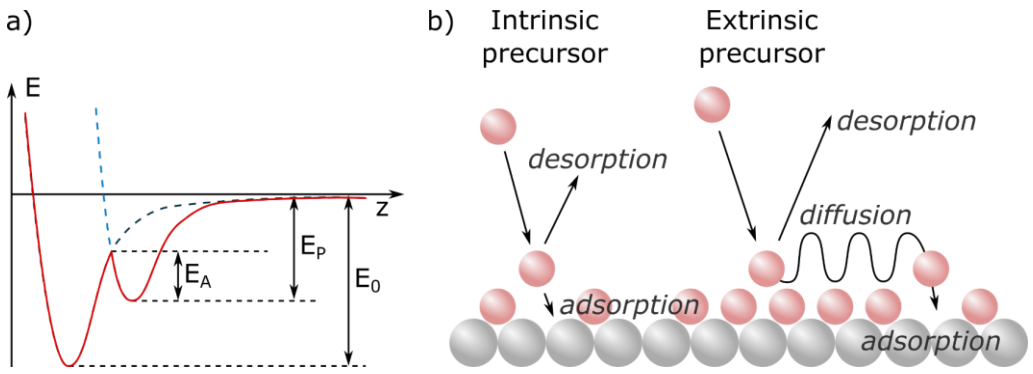


**Figure 5.3** *a) Schematic of a potential of the precursor state with the depth $E_P$ and the activation energy of the adsorption $E_A$. The binding energy of the adsorption state is $E_0$. b) Depiction of the intrinsic and extrinsic precursor state. The intrinsic state (over empty sites) can adsorb or desorb. The extrinsic state (over filled sites) can diffuse to an empty side to eventually adsorb or desorb.*

## 5.3 Desorption from monolayer

The desorption models described in this chapter assume at least equilibrium between adsorbate and surface in the initial state of desorption. That is, the number of adsorbate particles and the temperature are sufficient to characterize the initial state. Besides, mostly 2D-ordered coverages up to 1 ML are considered.

### 5.3.1 Polanyi – Wigner equation

The simplest phenomenological model of the thermal desorption process is an Arrhenius-like desorption rate. It is assumed that the desorption-rate $r$ is proportional to the number of particles $n$, which are ready to desorb from the surface. The following Polanyi-Wigner equation describes the process [243–246]:

$$r = -\frac{dn}{dt} = n^m \cdot \nu \exp\left(-\frac{E_0}{k_B T}\right) \tag{5.3}$$

with the pre-exponential term $\nu$, the binding energy $E_0$, the Boltzmann constant $k_B$ and the temperature $T$. Polanyi and Wigner [246] define $\nu$ as the vibrational frequency of the "possibly" desorbing particle.

The number of particles $n$ can be normalized to 1 ML introducing the coverage $\theta$**.** Thus, the dimension of rate $r$ transforms to ML/s. Davis [247] extracted the factor $\theta^m$ from $n^m$ to describe a generalized recombination process before desorption. In case this

process is time-limiting, the desorption rate depends on the probability of atoms of the adsorbed species joining each other, $r \propto \theta^2$.

$$r = -\frac{d\theta}{dt} = \theta^m k_0 \exp\left(-\frac{E_0}{k_B T}\right) \tag{5.4}$$

The factor of proportionality $k_0$ is often called pre-exponential and describes the frequency of movement of the desorbing particle (e.g., the vibrational frequency perpendicular to the surface). In Equation 5.4, the pre-exponential $k_0$ is independent from the coverage. The binding energy $E_0$ is the energy difference between the state bound on the surface and the energetically highest state during the desorption process. If there is a maximum in the movement of the particle between the bound state and the desorbed state, $E_0$ is called activation energy, otherwise binding energy. In most evaluations, $E_0$ and $k_0$ are assumed to be independent from coverage and temperature, which is a reasonable approximation because of the strong exponential temperature dependence. Most published desorption spectra are not calibrated (arb. units) which is not necessary in order to observe maximum temperature and shape of the peaks or appearance of shoulders. For comparison of the desorption rate to Equation 5.4 or for simulations, a calibration of the $y$-axis is required. The factor $\theta^m$ eliminates the linear relation in any case with $m \neq 1$. This in not directly visible in a spectrum of rate $r$ that is plotted with respect to temperature $T$, but further processing of data will shed light on that. Using Equation 5.3, a step from $m = 1$ to $m = 2$ changes $\nu$ by a factor of typically $10^{13}$. Knowing the coverage of a layer from the preparation or from other experimental techniques, allows for an easy calibration by integrating rate $r$ (equivalent to partial pressure $p$) over time $t$[53]

$$\theta(t,T) = \frac{p(t,T)}{\int_{T=0}^{T=\infty} p\,dt} \tag{5.5}$$

This simple model makes some assumptions which obviously contrasts to reality in some cases: The binding energy $E_0(\theta)$ may depend on coverage representing the interaction between the available adsorbate molecules. This is often assumed if desorption takes place from different locations with different number of nearest neighbours. Despite the wide application of this extension to the Polanyi–Wigner model,

[53] Not temperature $T$

a close look at such a "continuous change" of binding energy is needed. A more sophisticated model based on different, discrete species at different locations with different desorption parameters as well as the introduction of a conversion rate between these species looks more compatible to the underlying physical problem (see Chapter 9). In another case, the whole layer might expand, changing the distance between the adsorbate particles during desorption and thus, the interaction energy of the adsorbate particles may change to lower values. This leads to a continuous change in binding energy which is based on the physical process.

Another parameter that can vary is the order of desorption $m$ which is just a simple assumption for the availability of the desorbing molecules [243, 248, 249]. An order of $m = 1$ insinuates that the number of possibly desorbing particles is proportional to the number of remaining particles. Apparently, this is wrong in case of the decoration of steps and a desorption from the ends of a chain. Melting of 2D islands and desorption from the free area beneath is another example for a strong deviation from order $m = 1$. An order of $m = 2$ insinuates a recombination of two particles before desorption. This leads to a probability depending on $\theta^2$ in the case of a time-limiting recombination. If the subsequent desorption is the relevant process, $\theta^1$ should be assumed. In another example, the desorption of particles may be the time-limiting process. In this case, the process itself needs to be considered in order to determine and assume an order. In reality, the coverage dependence $\theta^m$ is simply a factor that indicates the availability of particles for the desorption. Depending on the model, the dependence $\theta^1$, which is widely assigned to a simple "first order" non-recombining desorption, can be replaced e.g., by $\frac{\theta}{1-\theta}$ derived from an Ising model and the quasi chemical approximation [250, 251]. As a consequence, the order $m$ in the Polanyi- Wigner equation (Equation 5.4) may result in non-integer values [252–255]. Thus, the fractional order $m$ becomes more or less a fitting parameter. From that point on, it is clear that the dimensionless coverage $\theta$ should be preferred to $n$ in order to clearly separate coverage dependence from pre-exponential $k_0$. Interferences with dimension and size are avoided as well. The pre-exponential factor $k_0$ varies with the position of the desorbing molecules on the surface and, thus, with the coverage. Moreover, the pre-exponential and the binding energy may depend on the temperature [256]. To conclude, the Polanyi-Wigner equation (Equation 5.4) is a very basic model which has to be adapted to each physical problem specifically. Finally - in the focus of current research - the desorption event can be a product of surface-assisted chemical reactions. The cyclodehydrogenation of

tetraphenylporphyrin (TPP) derivatives and the subsequent desorption of hydrogen is an example for such a covalent coupling reaction [257].

### 5.3.2 Transition state theory and microscopic reversibility

The transition state theory is derived from the chemical consideration of the reaction kinetics by Glasstone, Laidler and Eyring [258, 259]. It may be used as an alternative thermal desorption model as well as an interpretation of the Polanyi-Wigner equation. It is based on the assumption of equilibrium between 3D gas phase and adsorbed molecules, i.e. desorption rate equals adsorption rate.

Starting from the chemical reaction partners $X$ and $Y$, an intermediate state of the reaction called the transition state $XY^{\#}$ has to be passed forming the chemical product $XY$. In case of thermal desorption, these reaction partners are the adsorbed molecules, ready to leave the surface. The potential barrier $E_0$ – roughly the binding energy – separates initial and final state – the adsorbed and desorbed state. The highest point of the barrier is the transition state as depicted in Figure 5.4. In both potentials (initial and final state) as well as in the transition state, there are energy levels of different densities according to the degrees of freedom. The accompanying partition functions $Z$ result from the location and degeneration of these energy levels. In general, the reaction rate with $n_X = n_Y = n$ can be defined as:

$$r = n^m \frac{k_B T}{h} \frac{Z^{\#}}{Z_{Ads}} \kappa \exp\left(-\frac{E_0}{k_B T}\right) \tag{5.6}$$

with the Planck constant $h$ and the probability of passing the 'point of no return' $\kappa$. In comparison with Equation 5.3, the pre-exponential can be written as

$$k_0 = \frac{k_B T}{h} \frac{Z^{\#}}{Z_{Ads}} \kappa = \frac{k_B T}{h} \cdot k_0^{*}. \tag{5.7}$$

The factor $\frac{k_B T}{h}$ describes the frequency of the transition state crossing the potential barrier. At room temperature, it is determined by $\frac{k_B \cdot 300K}{h} = 6.25 \cdot 10^{12}\ \mathrm{s}^{-1}$. Thus, $k_0 = 10^{13}\ \mathrm{s}^{-1}$ is used as a rough simplification. The leverage of the partition functions (in most cases strongly coverage-dependent), the influence of $\kappa$ (it will be identified as the sticking coefficient) and the temperature dependence are ignored. On the other side, the artificially introduced and strongly simplifying factor $n^m$ (or $\theta^m$) is overanalysed. All

variations in $E_0(\theta)$, which are attributed to changes in coverage, are tried to be represented by the two orders $m = 1$ and $m = 2$ while it should be assigned to the coverage dependence of $k_0^*(\theta)$ caused by the partition functions $Z(\theta)$:

$$r(T,\theta) = \theta^m \cdot k_0^*(\theta) \cdot \frac{k_B T}{h} \cdot \exp\left(-\frac{E_0(\theta)}{k_B T}\right). \tag{5.8}$$

This model is very flexible and covers most thermal desorption processes as it is based on the widely discussed assumption that desorption and adsorption rates are independent. While being in equilibrium, the desorption rate will not be disturbed if adsorption is “removed”. That means, Equation 5.8 can be used to describe the desorption process without being in equilibrium with adsorption and thus, describes desorption into UHV. This assumption is called microscopic reversibility [260–264]. On the other hand, the (neglected) adsorption rate helps a lot in interpreting the desorption. The probability of passing the ‘point of no return’ $\kappa$ may be interpreted as a reflection at the transition state, i.e. desorption does not take place even though the actual energy was sufficient. This corresponds to the sticking coefficient $s$ in adsorption. Thus, measuring this sticking coefficient $s$ gives information about $\kappa$. Unfortunately, in most cases 3D gas phase and surface are not in real equilibrium, as the surface temperature is different from the 3D gas temperature, which results in a limitation of the usability of this identification.

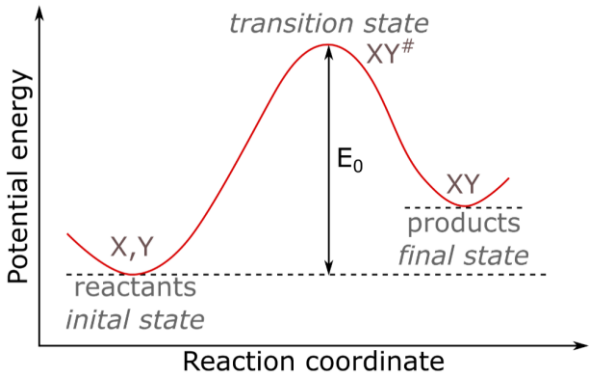


***Figure 5.4*** *Potential diagram of the transition state with the activation energy $E_0$. $X$ and $Y$ are the reactants, while $XY^{\#}$ marks the transition state and $XY$ the products.*

### 5.3.3 Desorption from multilayer-equilibrium on the surface

A realistic situation on the surface is shown in Figure 5.5. At a temperature, which is low enough to keep the molecules on the surface, a mixture of different phases exists, while

all of them are involved in the desorption process [265]. The condensed phase $(C_1)$ – the phase implicitly addressed in the preceding chapters – is in direct contact with the substrate. It provides the maximum density which is possible with respect to the available adsorption sites and the minimum distance of the adsorbed species, i.e. the particles in this phase cannot change their position. Nevertheless, particles can break away from this phase and form the 2D-gas phase $(G_1)$ on the substrate while they are still in contact to the surface. The typical density of the 2D-gas phase is $5 - 20\%$ of the density of the condensed phase, the mobility of the adsorbed species is typically high, though they can freeze to the surface. High particle exchange between condensed and 2D- gas phase allows to equilibrate the chemical potentials. The same "arrangement" of 2D condensed $(C_2)$ and gas phase $(G_2)$ may be found in the second layer, as well as in further layers (not shown in Figure 5.5). Furthermore, exchange with the 3D-gas $(G_{3D})$ phase is indicated in Figure 5.5.

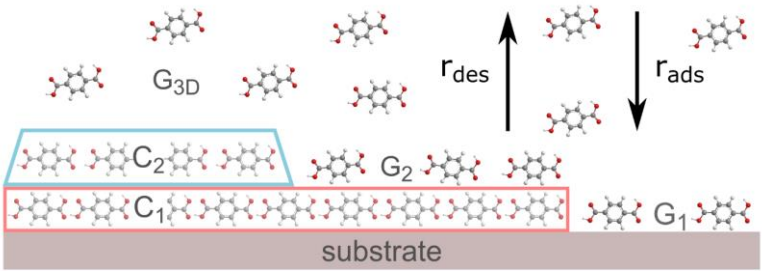


***Figure 5.5*** *Different phases on the surface and the equilibrium between adsorption and desorption.*

In 1976, Venables and Bienfait found that in such a model, the desorption rate of a distinct layer is independent from the ratio of condensed phase to 2D-gas phase on the surface, as long as not all of the condensed phase is "molten". This proceeds from the assumption that the chemical potentials in all phases are equal [266]. Further different approaches can be found in literature to interpret experimental data [251, 252, 254, 255, 265, 267–276].

### 5.3.4 Order in the first monolayer

The order of atoms in the first monolayer is an extensively observed experimental and theoretical topic. Historically, Low-Energy Electron Diffraction (LEED) and Molecular Beam Scattering (MBS) are used to investigate layers as a mean over millimetres to

reveal the geometric structure of adsorbates. Actually, Scanning Probe Microscopy (SPM) is the leading technique to explore the arrangements on an atomic level.

The order of the adsorbate atoms on the surface is assumed to be a fixed grid, a lattice gas model [277]. Depending on the coverage, the size of the mesh can vary. As already mentioned in Section 5.2, the molecules or atoms are hitting the surface in a statistical process with a constant probability for every adsorption site. Assuming a sticking coefficient that is independent from the coverage, the particles would adsorb with a constant probability where they land. If all sites were energetically and statistically equivalent, a statistical distribution would be revealed across the surface. If an interaction between the adsorbates exists, the equivalence of the adsorption sites is no longer valid because of the changing number of nearest neighbours. This effect is compensated by coverage independent binding energies. Furthermore, the sticking coefficient cannot be constant with respect to the coverage as the number of free sites increases with decreasing coverage. Thus, the sticking coefficient is dependent on the coverage. Additionally, diffusion could take place when the substrate temperature is higher than the adsorption temperature but still lower than the desorption temperature. As the binding energy is increasing on existing clusters, the statistical distribution is also disturbed. Moreover, a uniform distribution of the atoms on the surface with diffusion is hampered by defects, such as steps. The size of the terraces has an influence on the distribution of the molecules. The diffusion is a requirement for changes to the arrangement of the molecules on the substrate. The hopping of single atoms can be described by following diffusion equation [278]:

$$< x^2 > = 2Dt \tag{5.9}$$

$$D = D_0 \exp - \frac{E_d}{k_B T} \tag{5.10}$$

$$D_0 = \frac{1}{2} k_d l_0^2. \tag{5.11}$$

$x(t)$ is the distance from the starting point with respect to time, $D$ is the temperature dependent diffusion constant, $E_d$ is the activation energy of the diffusion, $l_0$ is the distance per jump and $k_d$ is the frequency [279]. If the coverage is high, the adsorbate atoms influence each other [279, 280]. Gomer shows different theoretical approaches

to define $D$. Additionally, Monte-Carlo simulations show a connection between hopping and diffusion [281, 282]. Steps act as diffusion barriers and germinal centres [236, 279, 283].

# 6 Experimental methods and analysis

This chapter introduces the basic principles of the experimental techniques used in this part of the work. All applied methods are based on the detection of electrons or small quantity of molecules, which requires an ultra-high vacuum (UHV) environment. Thus, UHV and its application in surface science are discussed first. Next, temperature- programmed desorption (TPD) and X-ray photoelectron spectroscopy (XPS) are described. TPD reveals the desorption of adsorbates, fragments of molecules or reaction products and allows to model desorption processes and chemical reactions, which are taking place while heating the surface. A detailed description of the desorption theory is given in Section 5.3. XPS is a technique to investigate the chemical state of organic and metal-organic adsorbate molecules and surfaces. In combination with a mostly linear heating of the substrate, this method is called temperature-programmed XPS (TP-XPS) and reveals thermally triggered chemical transformations which could come from surface-assisted chemical reactions, desorption of molecular species or changes in the morphology of the adsorbate. Combining TPD and TP-XPS allows to unravel chemical reactions on surfaces as desorption of adsorbed species, fragments and reaction products can be monitored.

## 6.1 Ultra-high vacuum and surface science

The aim of surface science is to understand physical and chemical phenomena on surfaces. Investigations on atomic-scale reveal properties of molecules on surfaces in the adsorbed state and chemical transitions. These are highly relevant for on-surface synthesis and self-assembly in order to create functional systems [284]. Such studies require an entirely clean environment – free of contaminants. At a pressure of $3 \cdot 10^{-6}$ mbar, a typical adsorption site on a metal surface is hit by a residual gas atom once per second. Thus, a UHV system with a base pressure below $10^{-9}$ mbar ensures an hour of operation before a full monolayer is adsorbed (sticking factor $s = 1$ at cryogenic sample temperatures). The UHV also allows for the detection of electrons used in the XPS device.

## 6.2 Temperature-programmed desorption

Temperature-programmed desorption is a very sensitive tool for the investigation of bonding interactions between adsorbed species and the supporting surface. Heating the surface leads to the desorption of molecules or atoms which are detected by a quadrupole mass spectrometer (QMS). The high mass and time resolution of the QMS allows for recording the desorbing species and reaction products. Thus, in combination with TP-XPS, which gives information about the species remaining on the surface, TPD is a powerful tool to investigate surface supported chemical modifications.

### 6.2.1 Measurement of desorption rate

Models of thermal desorption connect actual coverage $\theta$, adsorbate temperature $T$ and desorption rate $r$ as described in Section 5.3. In this chapter, the methods to compare theory and experiment are discussed. In the following, the temperature of the adsorbate is assumed to be identical to the temperature of the substrate. The measuring inaccuracy which originates from this assumption is insignificant at heating rates up to $10\,\mathrm{K\ s^{-1}}$ and up to some hundreds of monolayers of coverage on the substrate. The temperature difference in the adsorbate layer caused by the heat flow from or to external heat sources and into the adsorbate, which has a low specific heat, is negligible as long as the substrate itself is heated. Nevertheless, this does not mean that the adsorbate layer is necessarily in thermal equilibrium, though there may be a kinetic hindrance as stated in the models below.

The remaining coverage $\theta$ rigorously depends on the measured desorption rate $r$ provided that there is no “conversion” between different species:

$$\theta(t) = \int_0^t r(t')dt'. \tag{6.1}$$

Assuming $\lim_{t\to\infty} \theta(t) = 0$ and $\lim_{t\to\infty} r(t) = 0$ at high temperatures, it is sufficient to measure one of the quantities, the coverage by TP-XPS or the desorption rate by controlled heating which is called temperature-programmed desorption (TPD). This method introduced 1933 by Taylor and Langmuir [50] records rate $r$ and temperature $T$ as a function of time $t$ while the substrate temperature is increased with a roughly linear heating rate $\beta$. In first experiments, the pressure in the UHV was monitored by a

pressure gauge. Nowadays, it is more common to measure the partial pressure using a mass spectrometer [285]. As a result of the heating, coverage decreases over time with increasing temperature, i.e., coverage and rate depend on the heating rate $\beta$ at a certain temperature. This effect is caused by the Jacobian determinant $\frac{dT}{dt}$ which is necessary for integrating the function $r(T)$ over time. For that reason, most of the conventional analysis techniques require knowing the heating rate $\beta$ in addition to the temperature $T$ and the desorption rate $r$.

### 6.2.2 Conventional analysis of kinetic parameters

Typical desorption traces according to Equation 5.4 are simulated in Figure 6.1 to illustrate the analysis methods.

The Redhead analysis, introduced by Redhead in 1963 [286], is a first and quick method for the extraction of the activation energy $E_0$ from the peak temperature $T_P$ of a TPD spectrum at a constant (time-linear) heating rate $\beta$. The binding energy $E_0$ in units of kJ mol$^{-1}$ is delivered by a single point of one desorption trace and defined by

$$E_0 = RT_P \left( \ln \frac{k_0 T_P}{\beta} - 3.461 \right). \tag{6.2}$$

A single species, a constant binding energy $E_0$[54] and a pre-exponential of $k_0 = 10^{13}$ s$^{-1}$, as well as strict first order kinetics ($m = 1$) and equilibrium in the layer are assumed. Furthermore, Redhead derived from differentiation of Equation 5.3:

$$\frac{E_0}{k_B T_P^2} = \frac{1}{\beta} m\, n^{m-1}\, k_0 \exp\left( -\frac{E_0}{k_B T_P} \right) \tag{6.3}$$

With guessing an order of $m = 1$ or $m = 2$ and assuming $k_0 = \frac{k_B T}{h}$ [287], the energy $E_0$ can be extracted from a plot of $\ln \frac{T_P^2}{\beta}$ with respect to $\frac{1}{T_P}$ as supported by Lord and Kittelberger in 1974 [288]. Corrections to $k_0$ regarding the equilibrium in the layer such as the influence of the sticking factor $s$, different partition functions $Z$ or coverage dependencies of $E_0$ and/or $k_0$ are neglected. The order $m$, which models the desorption behaviour,

[54] independent from coverage and temperature

is deduced by the width of the peak or concluded from the peak position, when varying the coverage as shown in Figure 6.1.

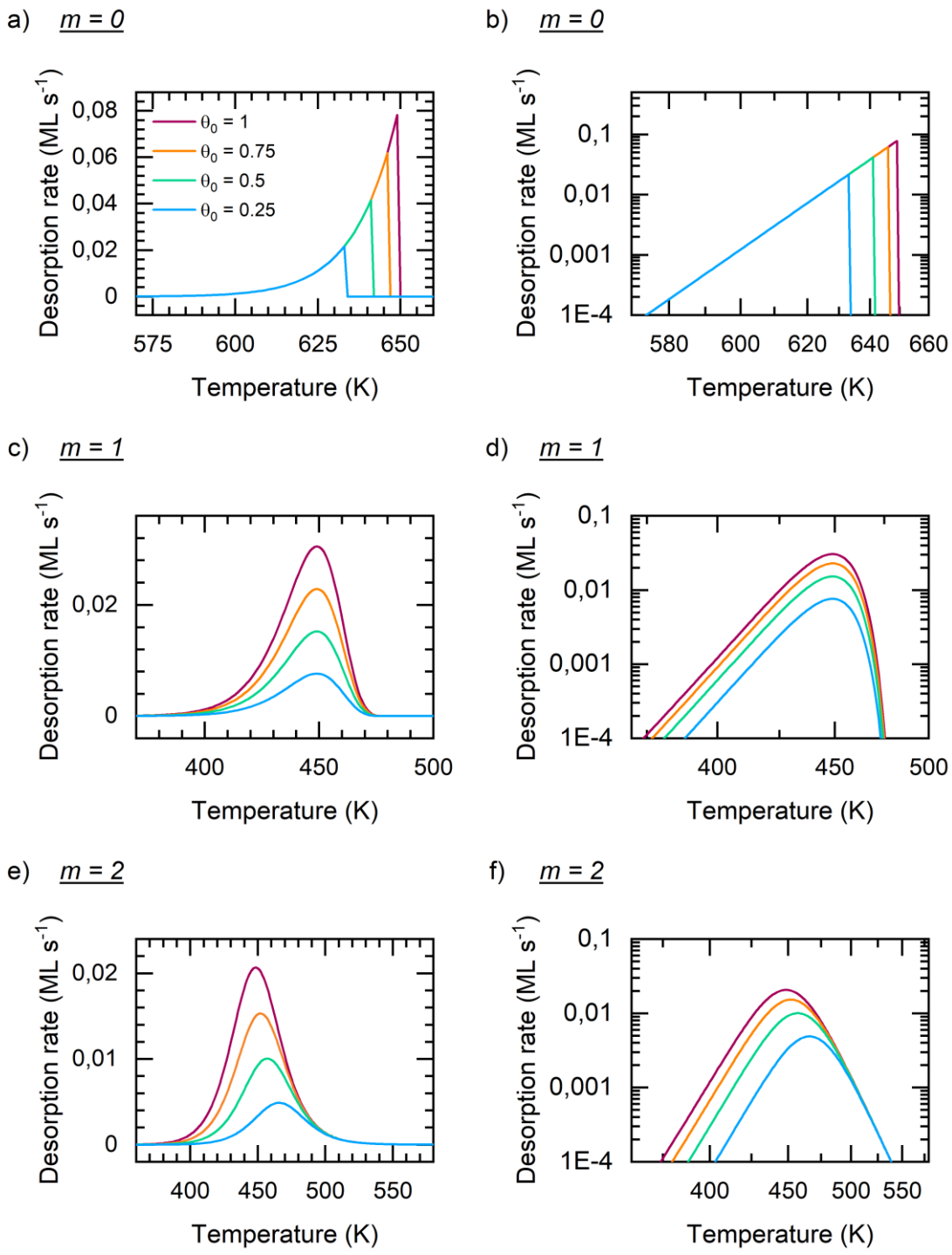


***Figure 6.1*** *Simulation based on Equation 5.4 calculated for variable coverages of* 1 *ML,* 0.75 *ML,* 0.5 *ML and* 0.25 *ML. a) and b) show the 0th order desorption process as linear and MS plot. 1st and 2nd order processes are shown in c), d) and e), f), respectively.*

If $m = 0$, all spectra have the same, coverage independent slope and a higher peak temperature with increasing coverage (Figure 6.1 a, b). If $m = 1$, the peak temperature is independent from the initial coverage. In contrast, the position of the onset is shifted to lower temperatures with increasing initial coverage. The temperature dependence, i.e. the slope of the onset which corresponds to $E_0$, remains constant. For $m = 2$, the peak temperature shifts to lower values with increasing initial coverage. Similar to $m = 1$, the slope of the onset corresponding to $E_0$ is independent from the initial coverage. The position of the onset shifts even stronger to lower temperatures with increasing initial coverage. The CAW analysis proposed by Chan, Aris and Weinberg [289] in 1978, extends the Redhead analysis by using peak position and peak width to extract pre-exponential and binding energy. Another very simple method to extract the binding energy $E_0$ from a single spectrum by using the peak width is proposed in 1976 by Edwards [290]. More sophisticated analysis methods either rely on experiments with varying initial coverages or heating rates. The advantage of a heating rate variation is the availability of a large range of temperatures. The disadvantage is a high temperature error due to strong variations of the energy which is applied to the sample at different heating rates. A well-known and strictly constant linear heating rate is crucial for these methods.

A very different method, called complete analysis, was introduced in 1969 by Tracy and Palmberg [291] performing work function $\phi$ measurements. In 1971, King, Madey and Yates applied this technique to TPD measurements [292]. Experiments with different initial coverages are used to extract temperature ($T_\theta$) - rate ($r_\theta$) pairs at a fixed $n_\theta$. Plotting these pairs as Arrhenius plot, the slope provides the binding energy $E_0(\theta)$ and the pre-exponential $k_0(\theta)$ can be extracted from the intercept at a given coverage $\theta$. Assuming the layer is in internal equilibrium, a set of $E_0(\theta)$ and $k_0(\theta)$ can be collected by points of equal coverage in each desorption spectrum.

The heating rate variation (HRV) analysis, introduced by Gerlach and Rhodin [293] in 1970 and taken up in 1975 by Falconer and Madix [294], uses an alternative set of desorption spectra generated by different heating rates, leading to similar results as the coverage variation, whereas both methods are sensitive to different type of errors (see above).

Any diffusion or conversion process on the investigated temperature scale or systematic errors in temperature makes complete analysis and HRV analysis not applicable anymore.

The leading-edge or HK analysis, which was first applied by Habenschaden and Küppers in 1984 [295], is based on the same principle as the HRV method. The leading edge of a single desorption spectrum is used if the approximation of a constant coverage holds. For this purpose, the original spectrum is plotted as Arrhenius to directly determine the temperature range for the linear fit. Checking the accordance of the fitted line and experimental data, it is easily visible how long the approximation of constant coverage holds, starting at the highest coverage. Thus, each $E_0(\theta)$ and $k_0(\theta)$, which is extracted from a single spectrum of the coverage variation, is calculated independently. Thereby, errors of temperature and preparation are reduced to a minimum. Furthermore, any deviation that is generated by missing internal equilibrium or different superposed species becomes visible as a deviation of the straight line.

A fit to a single desorption trace (line shape analysis) or even to a set of traces with different initial coverages or heating rates allows for the maximum exploitation of available data. Winterbottom [296, 297] uses a quite sophisticated desorption model consisting of an array of different desorbing particles to achieve good agreement with experimental data. Nevertheless, the simple models, as discussed as analysis methods according to Equation 5.4 are easily applicable.

The compensation effect is a problem for such fitting procedures. It describes that a constant rate $r$ at a given temperature $T$ can be explained by opposed varying $k_0$ and $E_0$. Pisani et al. [298] applied two different models to fit a desorption spectra of nitrogen on W with two peaks according Equation 5.4: on the one hand the superposition of a first- and a second order peak, on the other hand two second order peaks. Both simulations, with different sets for $k_0$ and $E_0$, were in good agreement to experimental data but nearly impossible to differentiate. This reveals the problem of deriving kinetic parameter from a single spectrum without alignment to further desorption traces as coverage or heating rate variations.

In 1975, D.A. King [245] reviewed popular analysis methods. De Jong and Niemantsverdriet [299] investigated the accordance of various analysis methods with computer simulations using an Arrhenius equation with pre-exponential and binding energy as a function of coverage. The best results were achieved by the complete analysis and the leading edge method.

If the coverage of a monolayer is known, a calibration to monolayer per second can be carried out by dividing the rate by the integral of the monolayer (Figure 6.1 a, c, e).

Such spectra can be plotted by combining the traditional direction of the temperature axis and the linear behaviour of desorption at a constant energy according to the Polanyi Wigner equation, thus, by the logarithmic rate $\ln(r)$ with respect to the reciprocal temperature $T^{-1}$ (Arrhenius plot, Figure 6.1 b, d, f). The slope describes the binding energy $E_0$ and the intercept the pre-exponential $k_0$ [291]. The counterintuitive inverse temperature scale of the Arrhenius plot is flipped keeping the equidistant reciprocal temperature $T^{-1}$, while re-annotating with the more intuitive temperature $T$. This flipped Arrhenius plot is called Menzel-Schlichting (MS) plot [300–302]. The temperature scale rises from left to right and the peaks look similar to the linear plot, while the slope still indicates binding energy and pre-exponential. This allows for a precise determination of the point at which the approximation of constant coverage breaks down.

### 6.2.3 Analytical simulation of desorption spectra

In contrast to conventional analysis techniques, a linear temperature profile is not necessary for the simulation of the TPD spectra. Knowing temperature and desorption rate at any time is sufficient. The differential equations are solved by a stepwise numerical solver according to the Runge-Kutta method in MATLAB[55]. If there exist more than one rate to describe the desorption process, the rates are simulated separately and summed up afterwards.

The widely used rate equation, to simulate desorption processes, is the Polanyi-Wigner equation (see Equation 5.4). Figure 6.2a shows simulations of TPD spectra with $E_0 = -14500\,\mathrm{K}$, $k_0 = 10^{13}\,\mathrm{s^{-1}}$, $\beta = 0.1\,\mathrm{K\,s^{-1}}$ and a varying order from $m = 0$ to $m = 2$. The peak temperature depends only weakly on the order. In contrast, the coverage at the maximum is dependent on order $m$. In the logarithmic plot, binding energy and pre-exponential can be extracted from the graph directly[56]. Figure 6.2b shows a desorption process of order $m = 1$ and a variation of the heating rate $\beta$ from $0.1\,\mathrm{K\,s^{-1}}$ to $2\,\mathrm{K\,s^{-1}}$. It can be recognized that slope and intercept are the same for all heating rates at a coverage close to the starting value, i.e., at low temperatures. Starting at about $85\%$ of the initial coverage (cf. area under the curve), the order influences the

[55] MATLAB R2017b

[56] Visually as well

rate. From all spectra, the binding energy and the pre-exponential can be extracted directly.

Additionally, the linear contribution of the temperature to the rate (see Equation 5.8) is discussed.

a) $E_0$ = -14500 K, $k_0 = 10^{13}\ s^{-1}$, $\theta_0$ = 1, $\beta$ = 1 K/s

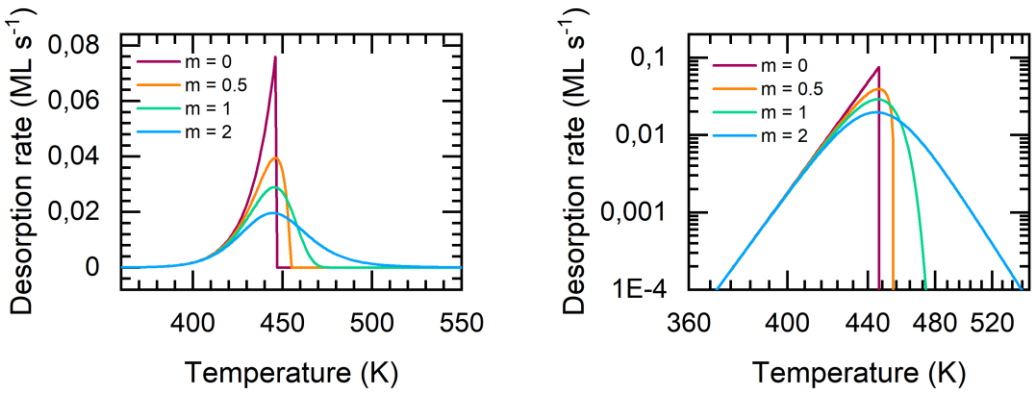


b) $E_0$ = -14500 K, $k_0 = 10^{13}\ s^{-1}$, $\theta_0$ = 1, $m$ = 1

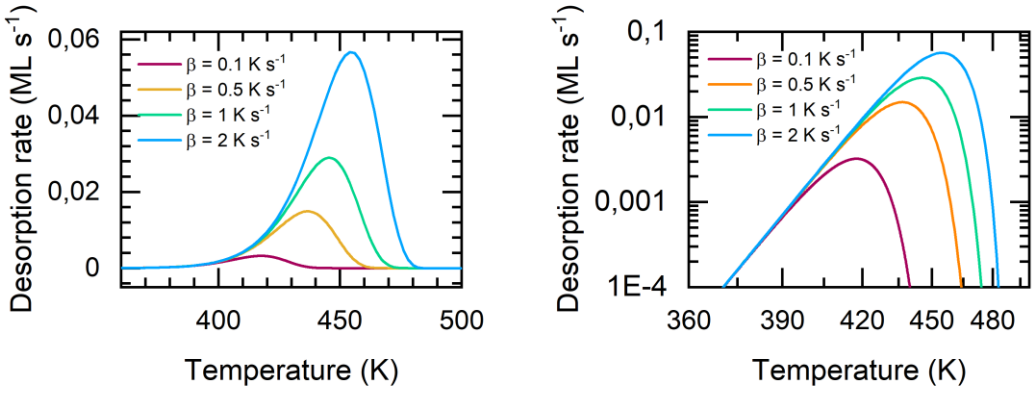


***Figure 6.2*** *Simulation based on the model of Equation 5.4 plotted as linear and MS plot. a) Variation of the order $m$. b) Variation of the heating rate $\beta$.*

Based on the slightly different model (according to Equation 5.8), the pre-exponential is estimated to be $k_0 = \frac{k_B T}{h} k_0^*$ with $k_0^* \approx 1$. Figure 6.3a shows the resulting desorption spectra with different initial coverages and order $m = 1$. A slightly bended onset is visible in the MS plot due to small variations of the temperature (about 2%) in the relevant range. The extraction of the kinetic parameters by the slope is not affected. The variation of the heating rate is depicted in Figure 6.3b and shows no significant deviation from the first model.

Another detailed overview and discussion including experimental tests of the suggested approaches and analysis methods for the extraction of kinetic parameters is provided by L. K. Ono and B. Roldan Cuenya in Ref. [303]. However, the fitting results seem to have a quite low reliability. A correct and unambiguous extraction and analysis of kinetic parameters from TPD experiments is not trivial, even if the surface reactions are supposed to be simple. Thus, more sophisticated models are necessary.

a) $E_0$ = -14500 K, $k_0^*$ = 1 $s^{-1}$, $m$ = 1, $\beta$ = 1 K/s

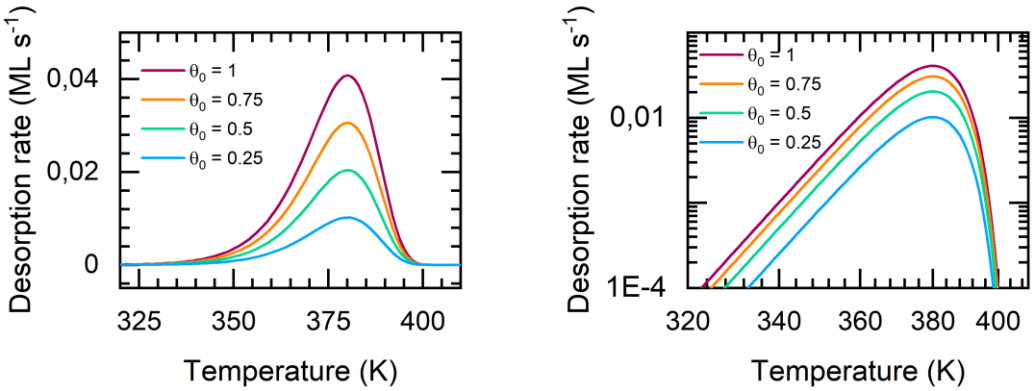


b) $E_0$ = -14500 K, $k_0^*$ = 1 $s^{-1}$, $m$ = 1, $\theta_0$ = 1

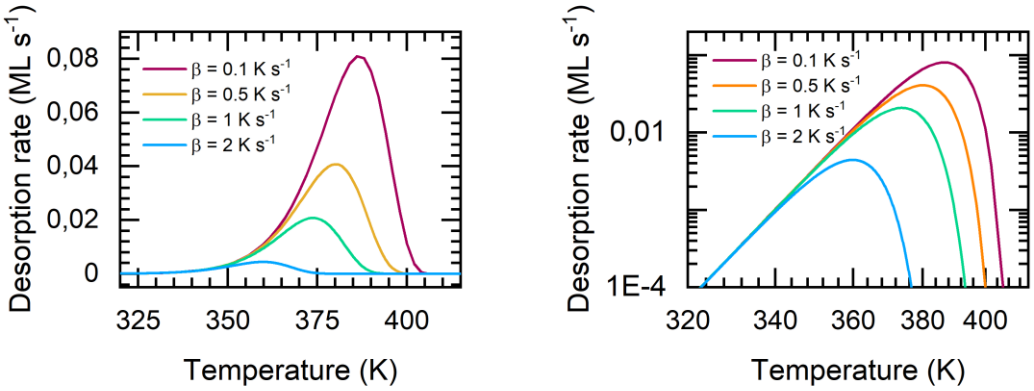


***Figure 6.3*** *Simulations with $\frac{k_B T}{h}$ as approach for $k_0$ (see Equation 5.8), illustrated as linear and MS plot. a) Variation of the initial coverage $\theta_0$. b) Variation of the heating rate $\beta$. A slightly bended onset reflects the $\propto T$ behaviour, distinguishing the slope of the model in Figure 6.1c and Figure 6.2b.*

For example, if there are two coexisting phases on the surface or two reactions take place, the model consists of more than one differential equation, which needs to be solved dependently or independently from each other (see Chapter 0). If diffusion

processes need to be considered or the surface quality is important, a microscopic simulation is proposed [304].

### 6.2.4 Monte-Carlo Simulation of a first order desorption process

In Section 6.2.3, the simulations are based on desorption from the macroscopic and thermodynamic point of view. Microscopic properties are transformed into thermodynamic quantities, which describe the desorption rate by complex equations. The molecules on the surface are assumed to be in an equilibrium with the 3D gas phase. The number of particles is infinite. On the surface of a crystal, there are terraces with few ($10^4$) particles, forming a "desorption system" with $10^{15}$ particles typically. Calculating the total desorption rate means integrating over independent terraces followed by summing up their rates. The analytical models ignore this aspect. Thus, an alternative way of describing and simulating a desorption process is the microscopic Monte-Carlo simulation. It is not possible to monitor the temporal evolution of $10^{15}$ particles, thus, a few simplifications have to be made. The surface is divided into equal parts similar to the size of a terrace which are treated independently from each other. The total desorption rate results from adding up the desorption rates of several terraces of different sizes. The atoms or molecules that have equidistant positions on the surface (lattice gas or solid) have a potential energy depending on the amount and type of neighbours (and substrate atoms). The desorption probability results from the potential energy using the Arrhenius equation. The hopping probability is calculated from the potential barrier between two binding sites. Equilibrium in the layer is or is not ensured by hopping processes. The energy of an adsorbate with $i$ nearest neighbours and $j$ substrate atoms is described by

$$E_{ij} = E_0 + i \cdot E_{neighbour} + j \cdot E_{substrate} \tag{6.4}$$

The desorption probability of a molecules with an energy $E_{ij}$ is:

$$p_E = k_E \exp\left(-\frac{E_{ij}}{k_B T}\right) \tag{6.5}$$

The hopping barrier between two binding sites with an energy difference $d$ can be calculated by the intersection of two harmonic potentials which are shifted by the energy difference [240]:

$$D_0 = d_0 + \frac{d}{2} + \frac{d^2}{16 \cdot d_0} \tag{6.6}$$

With $d_0$ being the barrier on the uncovered surface. The hopping probability is

$$P_D = k_D \exp\left(-\frac{D}{k_B T}\right) \tag{6.7}$$

For the simulation, a full (or less than one) monolayer is considered with one molecule per adsorption site. The fully covered surface is heated with a given heating rate while both, desorption and hopping is allowed at the same time. The time steps are chosen in a way that one hopping or desorption event is happening per step on average. That is, with increasing temperature the intervals are getting smaller. Both processes take place until all molecules have desorbed from the surface. Figure 6.4 shows a flow diagram of the Monte Carlo algorithm. In order to show the principle, Monte Carlos simulations of a simple 1st order desorption process of a full ML were performed. The binding energy to the substrate and the pre-exponential are constant. In Figure 6.5, array sizes of $50^2$, $100^2$ and $500^2$ molecules are simulated. Diffusion processes are not accounted. The averaged result of $50$ simulations is very close to the analytical simulation described in Section 6.2.3. The higher the number of molecules the better the accordance to the macroscopic simulation. More advanced simulations could describe more complicated desorption processes with neighbour interactions and diffusion but are out of scope for this work.

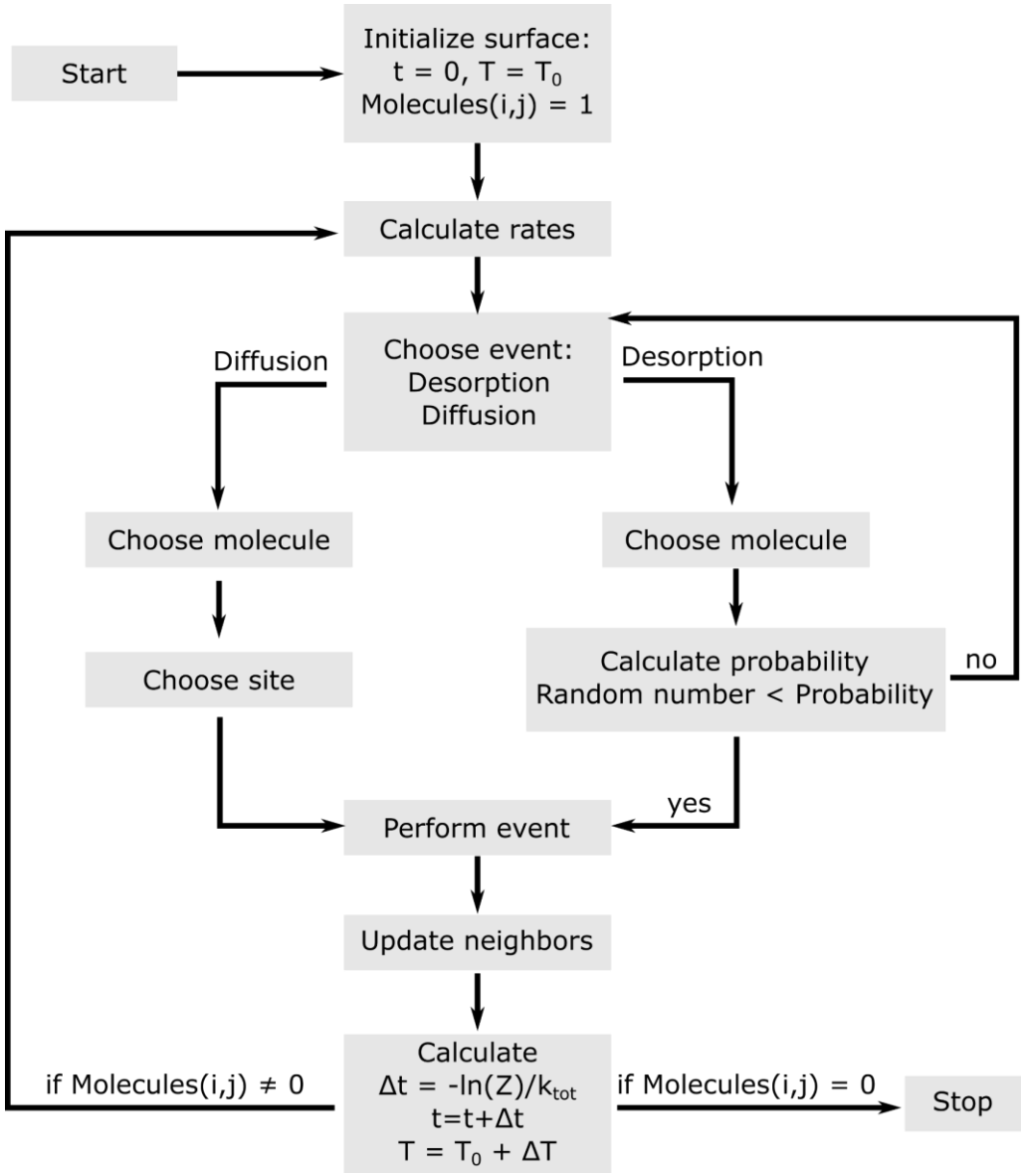


***Figure 6.4*** *Flow diagram of the Monte Carlo algorithm.*

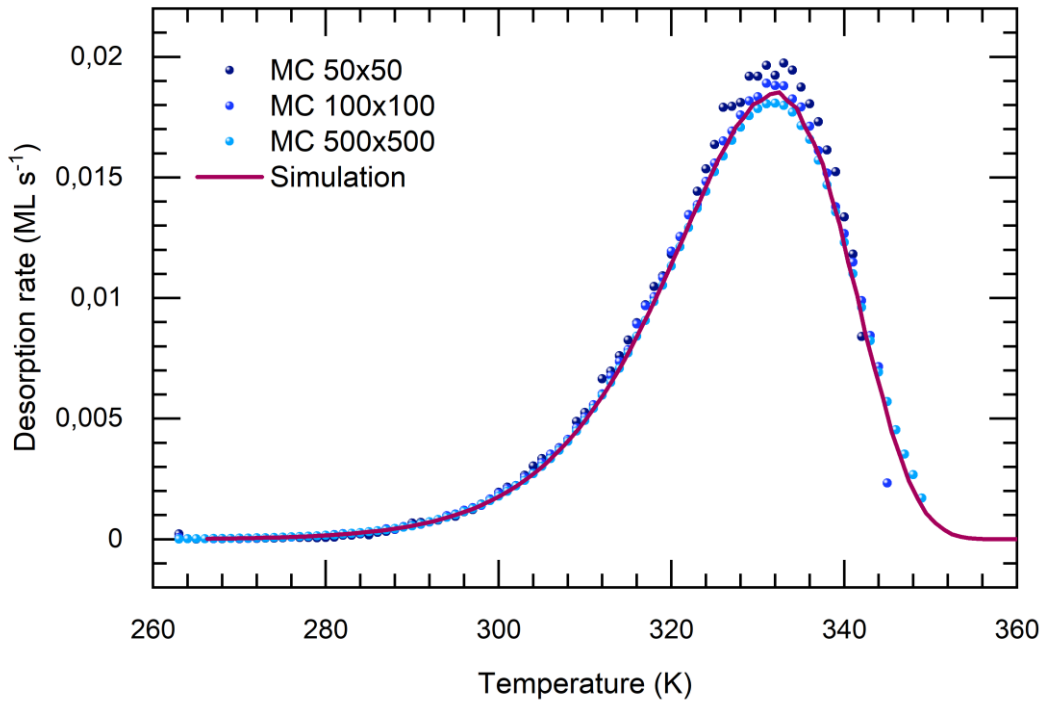


***Figure 6.5*** *Depiction of 1st order Monte-Carlo simulations of different array sizes and constant binding energies and pre-exponentials. The blue bullets show an average of 50 simulations. For comparison, an analytical simulation (line) was performed with the same parameters according to Section 6.2.3.*

## 6.3 X-ray photoelectron spectroscopy

XPS is an experimental method to gain information about electronic, stoichiometric and chemical properties of surfaces and adsorbed molecules based on the photoelectric effect. A. Einstein first explained this effect in 1905 [305] and was awarded with the noble prize in 1921. The photoelectric effect describes that an electron can leave matter when it gets enough energy by absorbing a photon. The working principle of XPS is measuring core electrons as shown in Figure 6.6. Electrons are emitted due to adsorption of X-rays. The following equation describes the kinetic energy $E_{kin}$ of the photoemitted electron:

$$E_{kin} = h\nu - E_b - \Phi_{det} \tag{6.8}$$

with the energy of the incident photon $h\nu$, the binding energy of the electron with respect to the Fermi level $E_b$ and the work function of the electron detector $\Phi_{det}$ [306]. The photon energy of the emitted X-rays and the work function of the detector are fixed. Thus, the detection of the kinetic energy directly gives access to the binding energy by

using Equation 6.8. Each element has a specific binding energy with peak positions providing details about the chemical environment. The photons have an energy range from $10\ \text{eV} - 1000\ \text{eV}$ which means that the photoelectrons have an inelastic mean free path of $\lambda_{mfp} = 0.3 - 2\ \text{nm}$ [307]. Therefore, XPS can be used to analyse elemental compositions and allows for chemical analysis of the first few atomic layers of a material. An XP spectrum is depicted with the binding energy on the $x$-axis in reversed order as calculated from the kinetic energy (cf. Equation 6.8). The strong interaction of electrons with matter leads to a large number of inelastically scattered and secondary electrons. These contribute to the XP spectra as featureless background which the element- specific core level lines are superimposed onto. As chemical reactions and transformations are often triggered by increasing temperatures, temperature programmed XPS is a good way to monitor the thermal evolution of a system. Using a proportional-integral-derivative (PID) controller the temperature of the sample can be increased with a constant heating rate. Subsequently recorded XP spectra show changing binding energies with respect to the temperature.

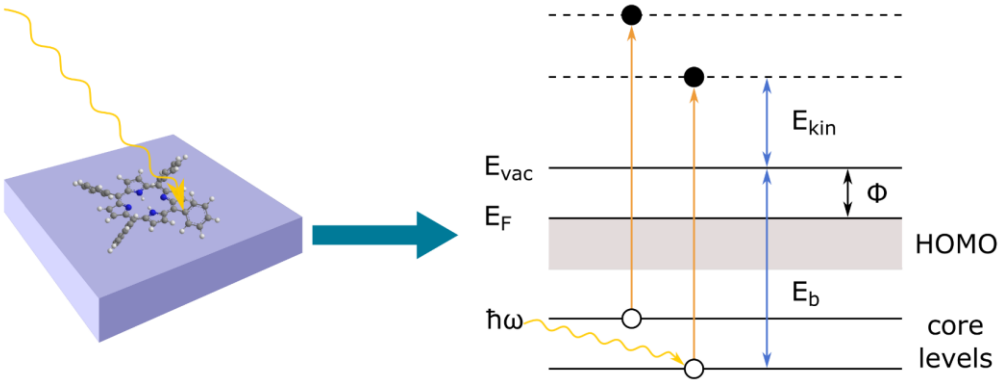


***Figure 6.6*** *Depiction of the working principle of XPS showing the emission of core electrons due to the absorption of X-ray radiation.*

# 7 Instrumentation

All experiments are carried out in UHV in order to provide well-controlled and ultra-clean conditions (see Section 6.1) and because it is a prerequisite for the applied experimental techniques. The vacuum chambers are continuously pumped by a combination of turbo-molecular and ion pumps. Measuring devices and additional facilities for recording pressures, cleaning procedures, sublimating molecules or evaporating metals etc. are vacuum-tightly mounted onto the chamber. A manipulator allows for precise positioning of the sample which is required for the various methods. In Figure 7.1, the custom-made UHV setup used for the experiments is depicted. Its base pressure is close to $10^{-11}$ mbar. During liquid nitrogen cooling, it can drop down close to $10^{-12}$ mbar. A sputter gun[57] (1) is used for sample preparation and for thin film deposition, molecular and ribbon evaporators (2) can be positioned on three flanges to the chamber. Quartz-glass crucibles[58], which are heated inside boron nitride crucibles, are used for evaporating the molecules. In order to control the deposition of the molecules from gas phase, the sample is positioned in front of a micro capillary-/needle doser (3). A gas dosing system (GDS, 4) provides gases for both, the needle doser and the sputter gun and is separately pumped. Using precision leak valves, more than one gas can be dosed simultaneously. Two valves (5) separate the needle doser and the sputter gun from the main chamber. In combination with the pneumatically driven valve towards the needle doser, a manometer[59] allows measuring the absolute pressure in the GDS and thus, exposing the sample to pre-defined gas pressures. Moreover, the chamber consists of a hemispherical analyser[60] (6) which is combined with a camera[61] and a twin anode X-ray source (7) for the generation of X-rays providing non- monochromatized radiation with photon energies of $1486.6$ eV (Al – K$\alpha$) and $1253.6$ eV (Mg – K$\alpha$). The analyser allows to perform XPS in normal electron emission (NE) geometry and the angle $\varepsilon$ between the entrance axis of the analyser and the X-ray source is smaller than $90°$. The software package SpecsLab2[62] is used to record the XP

[57] Varian (model 981-2043)

[58] Gaßner Glastechnik GmbH, Munich (outside diameter $4.9$ mm, wall thickness $0.5$ mm, height $9$ mm)

[59] Baratron by MKS

[60] SPECS Phoibos 100 CCD

[61] pixelfly by PCO

[62] version 2.74-r24090 by SPECS

spectra. The four degrees-of-freedom manipulator (8) is able to rotate around the $z$-axis and translate in $x$-, $y$- and $z$-directions. Additionally, the mounted sample (9) can be cooled down to temperatures around $85\,\mathrm{K}$ by liquid nitrogen flowing through the manipulator. For heating, a filament is placed directly behind the sample, which has direct contact to a K-type thermocouple. The temperature as well as the heating rate are controlled by a proportional-integral-derivative (PID) controller. [63] Most experiments require cooling down to reduce the residual gas pressure, which often needs a continuous counter-heating. The TPD measurements are recorded with a quadrupole mass spectrometer (QMS, 10) [308] which is placed inside a copper Feulner cap (11). The Feulner cap has a diameter of $8\,\mathrm{mm}$ and, thus, is slightly smaller than the sample with a diameter of $10\,\mathrm{mm}$. In order to suppress background pressure, the sample can be positioned very close ($\approx 1\,\mathrm{mm}$) to the copper cap. Additionally, the surfaces within the cap and a cold trap which are nitrogen cooled are covered by a freshly deposited titanium film for cryo-trapping and efficiently trapping of background pressures and especially hydrogen $H_2$ and H [308]. It gets very important to reduce background pressure when measuring desorbing hydrogen. The mass spectrometer and the electron analyser are aligned in the way that they face the sample along its surface normal. Furthermore, a LEED (low energy electron diffraction) spectrometer (12) [64] is mounted to analyse the surface structure.

[63] Schlichting Physikalische Instrumente HS 130

[64] BDL800IR-LMX-ISH by OCI Vacuum Microengineering Inc.

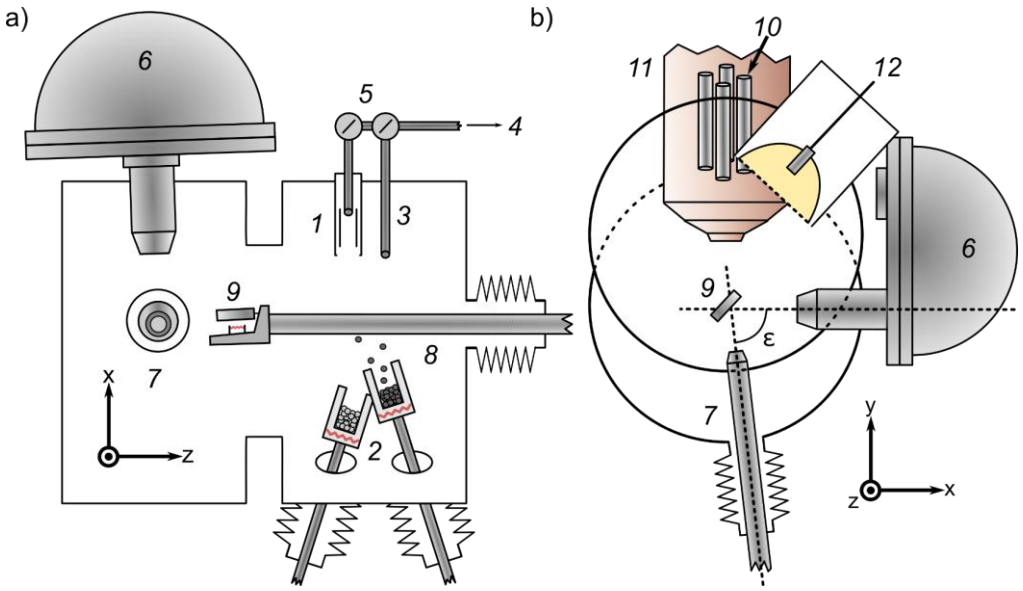


***Figure 7.1*** *Schematic of the UHV chamber in a) top and b) front view along the $z$-axis (axis of the manipulator). A more detailed description of the labelled components can be found in the text. Adopted from [309] with modifications.*

# 8 Desorption kinetics of the dehydrogenation of Bisphenol A and Diethylstilbestrol

*This chapter includes content that has been published in*

P. S. Deimel, K. Stoiber, L. Jiang, J. A. Lloyd, S. C. Oh, S. Fischer, Ö. Sağlam, H. Schlichting, A. C. Papageorgiou, J. V. Barth, F. Allegretti, and J. Reichert,

**"Bisphenol A and Diethylstilbestrol on Cu(111): On-Surface Polymerization Initiated by Hydroxy-Directed *Ortho* C-H Bond Activation"**

The Journal of Physical Chemistry C, vol. **123**, no. 2, pp. 1354–1361, 2018. Reproduced with permission. Copyright (2019) American Chemical Society.

*TPD measurements, LEED and XPS measurements and analysis have been performed by*

P. S. Deimel, F. Allegretti

*Scanning tunnelling microscopy measurements and images have been made by*

L. Jiang, J. A. Lloyd, S. C. Oh, S. Fischer, Ö. Sağlam, A. C. Papageorgiou and J. Reichert

Using covalent coupling and polymerization on surfaces for bottom-up fabrication of low dimensional networks [310–317] has potential application in nano-electronics, catalysis and gas sensing [318–320]. In order to control on-surface polymerization processes, reactive sites are created by the surface-assisted thermal dissociation of halogen-carbon bond [321–324]. In the case of these surface assisted Ullmann coupling reactions [325], the chemisorbed halogen species can influence or even hinder the formation of covalently bound networks [326–328]. Thus, amongst others [329–333], C−C covalent coupling as a by-product-free alternative to Ullmann coupling reactions is an explored route for polymerization [316, 334]. In order to show the hydroxy-directed C−C coupling mechanism, the products of the competitive dehydrogenation and deoxygenation are directly monitored. Furthermore, the role of the directing groups, the molecular modules and the selected substrate are investigated using various methods like TPD, XPS, LEED and STM.

Thus, the chemical and structural evolution of two model compounds, Bisphenol A (BPA) and Diethylstilbestrol (DES), on an atomically well-defined Cu(111) surface is explored. A depiction of the molecular structure is shown in Figure 8.1. Each molecule

features two terminal hydroxyl groups, both linked to phenol rings. The aromatic rings are connected by a dimethylmethane and diethylstilbene bridges in BPA and DES, respectively. Both molecules are assumed to have adverse health effects like interfering with the hormone system, causing transgenerational damage and alteration of the epigenetic code [335, 336]. BPA is still used for the production of plastic products and coatings [337]. Whereas, the use of DES as oestrogen blockers during pregnancies has been restricted since 1971 because it was shown to be teratogenic [338, 339].

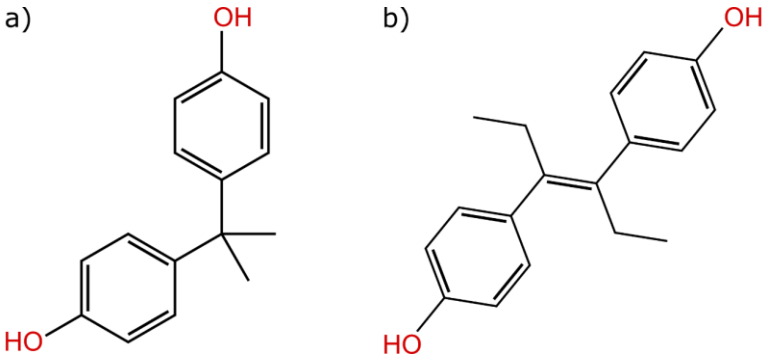


***Figure 8.1*** *Chemical structure of a) BPA and b) DES with the terminal hydroxyl groups highlighted.*

## 8.1 Experimental procedures

The XPS, TP-XPS, TPD and LEED experiments were performed at the UHV chamber described in Chapter 7. A different custom-designed UHV chamber was used for the STM measurements to investigate the structural evolution and the topography of BPA and DES. The set-up consists of a preparation chamber and subsequent analysis chamber with a variable temperature STM[65] (for details see [340]).

For the preparation of clean surfaces, the Cu(111) single crystals[66] were sputtered for $30$ min with $Ne^+$ or $Ar^+$ ions at room temperature (RT). A subsequent annealing to $770\ \text{K} - 800\ \text{K}$ for $5 - 10$ min restores the surface order. BPA[67] was deposited at $340$ K using a home-built molecular beam evaporator, whereas the substrate was kept at $200$ K. DES[68] was evaporated at $\approx 335$ K with the Cu(111) crystal at $200$ K. Before the

[65] SPECS Aarhus type

[66] Surface Preparation Laboratory, the Netherlands

[67] Sigma Aldrich, purity $> 99$ %

[68] Sigma Aldrich, purity $99$ %

first deposition, both, the BPA and DES powders, were outgassed to a maximum temperature of $350$ K for $10$ min and $360$ K for $5$ min, respectively.

The XPS measurement were performed with non-monochromatized Al – K emission, thus, a photon energy of $1486.6$ eV. The standard XPS experiments were carried out in the medium area (MA) lens mode. All TP-XP spectra were acquired out with the large area (LA) lens mode of the analyser and in NE geometry with a heating rate of $0.1$ K $s^{-1}$. The calibration of the binding energy of all spectra was performed against the Cu $2p_{3/2}$ core level of the Cu(111) substrate at a binding energy of $932.67$ eV [341]. The O $1s$ TP-XPS contour plots (shown in Figure 8.5) were obtained by subtracting the same linear background from all spectra with subsequent normalization to both ends of the spectra. To generate the plots of the corresponding O $1s$ and C $1s$ intensities with respect to the temperature (see Figure 8.6), two subsequent individual core-level spectra were averaged and fitted by Gaussians on a linear background (for more details see [340]). Finally, calculating the area under the fits by integrating results in the intensities.

The LEED measurements were performed without counter-heating, that is with the sample at $\approx 85$ K.

The TPD spectra were recorded with the distance between the Cu(111) crystal and the Feulner-cap [308] aperture adjusted as close as possible. In addition, because of the cooled manipulator, the sample needs counter-heating in order to reach temperatures above $85$ K. The data was acquired in terms of time-dependent partial pressure $p(t,T)$ while heating the sample with a constant heating rate. For the analysis, a background correction was performed by subtracting a 3rd order polynomial starting before the 1st desorption peak and ending after the 3rd one. Testing different linear backgrounds did not lead to significant changes of the result. In order to simulate the individual peaks, the desorption rate is normalized such that all hydrogen atoms desorbing within a given peak of the BPA/DES layer are defined as one ML. The normalization of the partial pressure $\theta(t,T) = \frac{p(t,T)}{\int_{T=0}^{T=\infty} p dt}$ separates the pre-exponential factor from the coverage, which allows for a meaningful variation of the desorption order, see Section 5.3.1. The coverage $\theta$, which is the amount of the desorbing species of the actual reaction, is expressed in units of ML.

## 8.2 Modelling of the TPD spectra

The desorption spectra of both, BPA and DES, are modelled as three separate peaks, each described by a Polanyi-Wigner equation. The rate is calculated numerically in discrete time steps followed by a recalculation of the actual coverage (cf. Runge-Kutta method, Section 6.2.3). Pre-exponential factor $k_0$ and binding energy $E_B$ are kept constant over the coverage, but are free fitting parameters. The order of desorption $m$ is a third fitting parameter. To improve consistency of data, the fitting parameters are varied while taking into account the implicit mutual dependence of $k_0$ and $E_B$ for reproduction of the overall peak position (compensation effect) [256, 342, 343].

The simulated rate (see Figure 8.2) is compared to the experimental data by visual inspection in linear and MS-plot and by a reliability factor $R$. The $R-$factor is the normalized square derivative summed up over all data points of the TPD spectrum:

$$R = \frac{\sum_T \left( \frac{d\theta}{dt_{exp}} - \frac{d\theta}{dt_{th}} \right)^2}{\sum_T \left( \frac{d\theta^2}{dt_{exp}} + \frac{d\theta^2}{dt_{th}} \right)}. \qquad (8.1)$$

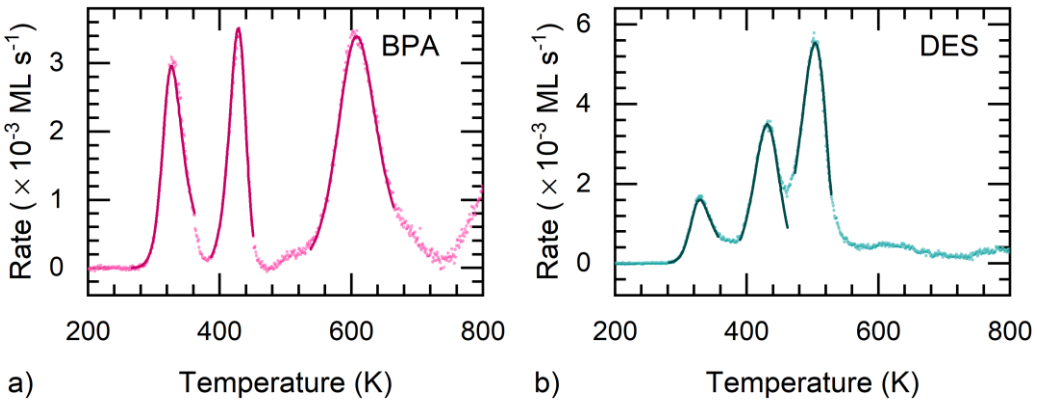


***Figure 8.2*** *TPD spectra of $H_2$ from a) BPA/Cu(111) (magenta curves) and b) DES/Cu(111) (green curves) at a heating rate of $0.5\ K\ s^{-1}$. The dots mark the experimental rate and the solid lines indicate the simulation results. The rate is normalized in a way that all desorbing hydrogen atoms in a full BPA/DES layer are counted as one ML.*

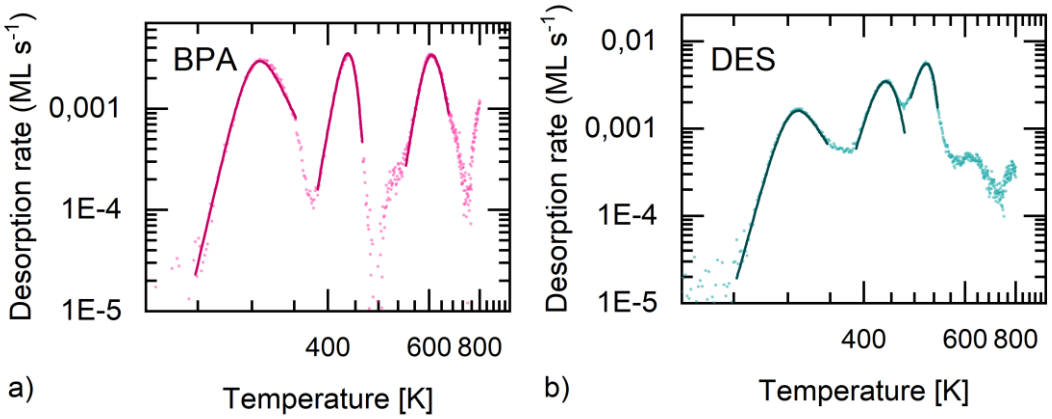


***Figure 8.3*** *TPD spectra of $H_2$ from (a) BPA/Cu(111) (magenta curves) and (b) DES/Cu(111) (green curves) in logarithmic scale (MS plot) as indicated in Figure 8.2.*

## 8.3 Results and Discussion

After the deposition and a subsequent annealing to $\approx 380$ K, both molecules, BPA and DES, self-assemble into well-ordered molecular overlayers [344, 345]. The STM images show densely packed hexagonal superstructures (Figure 8.4, [344, 346]) which corresponds to the respective LEED patterns (cf. Figure Appendix B). Heating to higher temperatures ($470$ K for BPA, $460$ K for DES), reveals branched, polymer-like chains with molecular features imaged as distinct protrusions. This suggests a covalent linking of individual molecules which is irreversible. After annealing to even higher temperatures (BPA: $730$ K; DES: $540$ K), the sharp features convert into smeared out motifs indicating a further modification of the polymer chains. As the temperature induced evolution and chain formation for both molecules is very similar, they seem to have a common reaction mechanism despite having different chemical structures. To further investigate the three-step chemical evolution, XPS and TP-XPS experiments were performed.

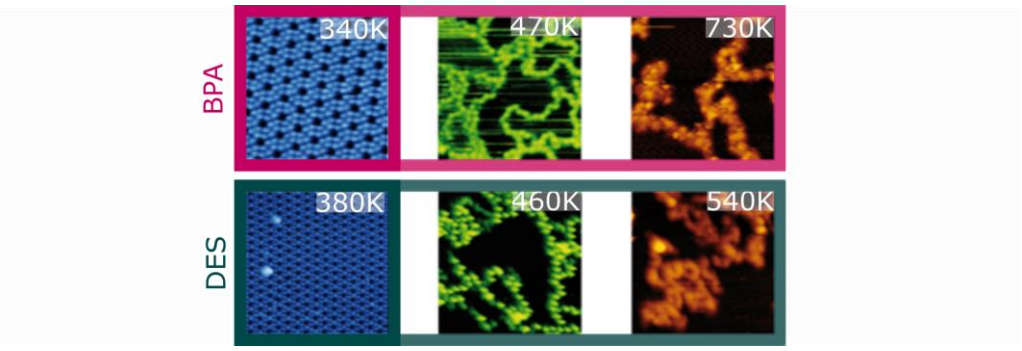


***Figure 8.4*** *STM images of BPA (red) and DES (black) at distinct temperatures showing the thermal evolution from well-ordered overlayers to polymer chains.*

DES shows a dominant O $1s$ feature at a binding energy of $533.1$ eV (Figure 8.5b, Peak 1), which is attributed to the terminal hydroxyl groups [51, 347–349]. This clearly reveals intact hydroxyl groups at these temperatures. A new component at $530.9$ eV, referred to as Peak 2, replaces Peak 1 after annealing above $300$ K. This new feature is attributed to deprotonated hydroxyl groups with a binding energy that is characteristic for a carbonyl species close to the copper surface [344, 350–352]. At temperatures above $500$ K, the O $1s$ component changes again, back to a higher binding energy of $\approx 533.6$ eV (Peak 3) replacing the carbonyl related peak 2. Figure 8.5 reveals that the conversion from peak 2 to peak 3 ends in a complete disappearance of oxygen, when the temperature reaches $650$ K. The C $1s$ TP-XP spectra show that the molecular backbone stays adsorbed and mostly intact up to $750$ K. This suggests a deoxygenation as a consequence of the progressive loss of the oxygen signal. The chemical evolution of BPA on Cu(111) comes out very similar having the same subsequent components 1,2 and 3 as DES (Figure 8.5a). Only the temperature of the uptake of peak 3 as well as the overall loss of oxygen is significantly higher for BPA, above $550$ K.

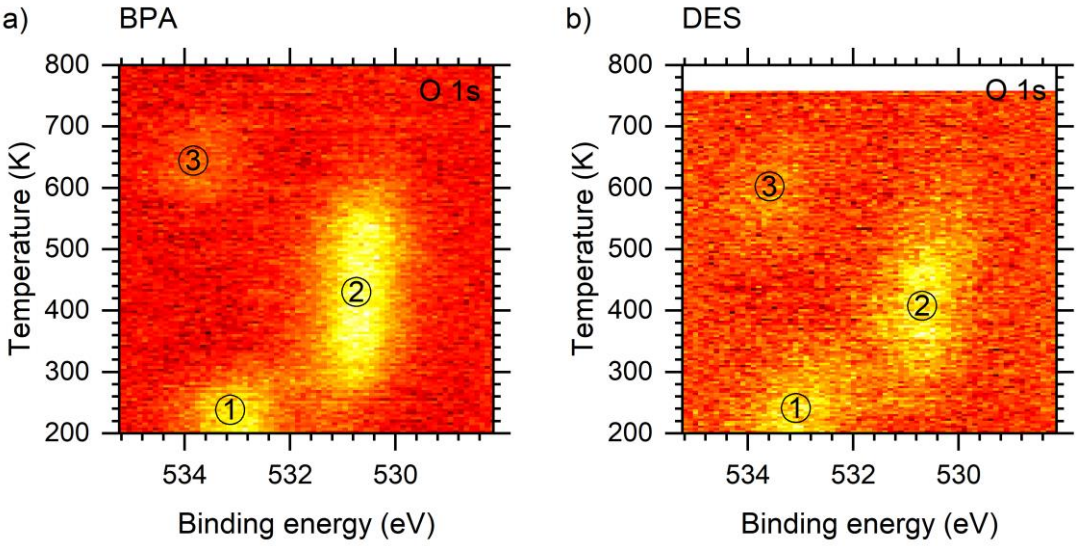


***Figure 8.5*** *O $1s$ TP-XPS heatmaps for a) BPA and b) DES on Cu(111). The experiment was performed with a heating rate of $\beta = 0.1\ K\ s^{-1}$. The observed features are labelled 1,2 and 3.*

Figure 8.6 shows the integrated intensities of the individual O $1s$ components 1 and 2 as a function of the temperature. These could be simulated according to the integrated form of the Polanyi-Wigner equation assuming that the population and depopulation rate obeys an Arrhenius behaviour equivalent to a standard TPD reaction:

$$n = \int_0^t k_0 n^{m_C} \exp\left(-\frac{E_C}{k_B T}\right) dt' \tag{8.2}$$

The fitted conversion energies are listed in Table 8.1. The reliability of the fits is quite low due to the limited dynamic range and the higher noise of the TP-XPS intensities as the data acquisition is much more time-consuming. In contrast, the conversion temperature which is the peak temperature of the conversion rate and the first derivative of Equation 8.2, is very reliable. The results of the simulations are summed up in Table 8.1. The different conversion temperatures $T_{1\rightarrow2}$ of both molecules, BPA and DES, which have equal conversion energies $E_{1\rightarrow2}$, come from different pre-exponential factors $k_{0,1\rightarrow2}$ of the conversion rate (not discussed here in detail).

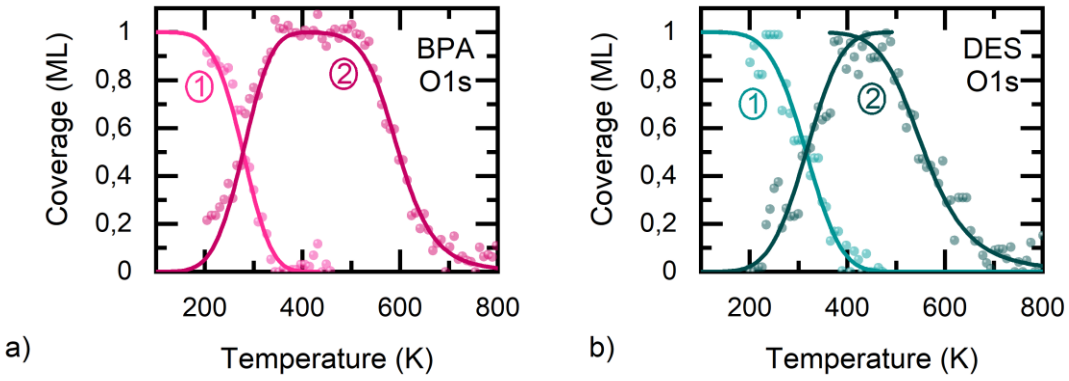


***Figure 8.6*** *Integrated intensity of the individual O 1s components (1 and 2 Figure 8.5) as a function of temperature: (a) BPA/Cu(111) and (b) DES/Cu(111). The measured intensities are dotted, the solid lines show the simulation of the O 1s "coverage".*

| | O 1s component | $E_{Conversion}$ | $m_{Conversion}$ | $T_{Conversion}$ |
|---|---|---|---|---|
| BPA | $1 \rightarrow 2$ | 0.12 eV | 1 | 275 K |
| | $2 \rightarrow 3$ | 0.73 eV | 2 | 578 K |
| DES | $1 \rightarrow 2$ | 0.12 eV | 1 | 304 K |
| | $2 \rightarrow 3$ | 0.48 eV | 2 | 541 K |

***Table 8.1*** *Fitted conversion energies between the individual O 1s components 1,2 and 3. The reliability of the conversion energies is low due to the higher noise. The conversion temperatures at a heating rate of $0.1\ K\ s^{-1}$ are very reliable.*

TPD experiments were performed for a clear understanding of the correlation between the chemical changes, which were shown by XPS, and the structural evolution of the

molecules, which was observed with STM. In Figure B.2 the spectra for $H_2$, $H_2O$, CO, $O_2$ and $CO_2$ desorption are depicted. The corresponding STM images indicate the structural transformation at distinct temperatures as described above. The mass spectra of $H_2$ show three major desorption events for BPA and DES as it can be seen in Figure 8.2. The first peak arises at about $320$ K for both molecules. It is attributed to the deprotonation of the hydroxyl groups, which is supported by the transition of the O $1s$ component from peak 1 to peak 2 (cf. Figure 8.5). Apparently, the chemisorbed hydrogen of the deprotonation desorbs from the surface as molecular hydrogen, which is in accordance with previous studies [353]. The second desorption feature of the $H_2$ spectra at $\approx 430$ K does not correlate with any visible change in the O $1s$ core level but the transition from well-ordered overlayers to branched molecular chains was shown by STM. There is no signal in the $H_2O$, CO, $O_2$ and $CO_2$ TPD spectra. Thus, it can be concluded that there is no chemical change of the carbonyl species involved in the second reaction step, but likely a hydroxy-directed ortho-ortho coupling [51]. The third $H_2$ desorption peak arises at $\approx 600K$ for BPA and $\approx 500K$ for DES simultaneously with the desorption of $H_2O$ and the change in O $1s$ component. Apparently, there is no desorption of the molecules (cf. constant C $1s$ intensity, high mass fragments) as well as no degradation of the adsorbed species below $600\,K$ (cf. CO desorption). The parameters resulting from the analytical simulation are quite stable versus the compensation effect, i.e. the shapes of the experimental desorption peaks are sufficiently meaningful. The coverage dependence of the desorption event which is parametrized in the Polanyi-Wigner equation by $\theta^m$ is still quite artificial. Thus, the order can only be seen as a fitting parameter. A high value indicates a hampered, complex desorption process. At best, a recombination of two hydrogen atoms to $H_2$ could result in a 2nd order desorption process if the surface is fully vacant. All fitting results of the simulation are summed up in Table 8.2. More sophisticated methods like a Monte Carlo simulation (including diffusion in a highly complex topology) are needed for a more precise statement regarding the details of the H recombination.

| | Desorbate | $E_{Bind}$ | $m$ | Reliability |
|---|---|---|---|---|
| **BPA** | $H_2$ – Peak 1 | 1.00 eV | 3 | 0.002 |
| | $H_2$ – Peak 2 | 1.41 eV | 1.3 | 0.001 |
| | $H_2$ – Peak 3 | 1.48 eV | 2 | 0.001 |
| | $H_2O$ | 1.06 eV | 1.7 | 0.008 |
| **DES** | $H_2$ – Peak 1 | 0.96 eV | 3 | 0.001 |
| | $H_2$ – Peak 2 | 0.99 eV | 1.5 | 0.005 |
| | $H_2$ – Peak 3 | 1.09 eV | 1 | 0.001 |
| | $H_2O$ | 2.45 eV | 1.9 | 0.008 |

***Table 8.2*** *Results of the simulation of desorption of $H_2$ and $H_2O$ from BPA/Cu(111) and DES/Cu(111) at a heating rate of $0.5\ K\ s^{-1}$. The very low reliability factors indicate a very good agreement between data and simulation.*

In the MS plot (Figure 8.3), an Arrhenius-like rate still appears as a straight line, so the onset, where the coverage dependence influences the reaction, can easily be detected. Furthermore, it can be shown whether the decay is overlapped by another process and the limits of the background subtraction can be recognized. Anger et al. [353] performed TPD measurements of molecularly adsorbed hydrogen on Cu(111) with a heating rate of $3\ K\ s^{-1}$. Thus, the simulation ($H_2$ – peak 1) was recalculated with $3\ K\ s^{-1}$ which results in a peak temperature of $344\ K$ for BPA and $343\ K$ for DES. Taking in to account the density of molecules (e.g., BPA: $10^{14}$ molecules $cm^{-2}$), the estimated coverage and the number of hydroxyl species in a molecule, the effective number of hydroxyl species in a molecule is $\leq 10^{14}$ molecules $cm^{-2}$, approximately. This is in accordance with the corresponding traces “d” and “e” in Figure 7 in [353] which show peak temperatures of $340 - 345\ K$ and a comparable hydrogen coverage.

In combination, TPD, XPS and STM measurements can reveal the chemical transformations from adsorbed molecules to conjugated polymers of both molecules, BPA and DES on Cu(111) in detail. The TPS and XPS data indicate two reaction steps, a deprotonation followed by the desorption of $H_2$ as depicted in Figure 8.7. The conversion rate can be calculated as first derivative of the coverage (shown in Figure 8.6) and simulated with $0.1\ K\ s^{-1}$. Additionally, to correlate the $H_2$-rate with the conversion rate, it is recalibrated to a heating rate of $0.1\ K\ s^{-1}$. Both, the original and

the recalculated rates are depicted in Figure 8.7. The conversion temperatures of the O $1s$ components from $1$ to $2$ is reached at $275$ K for BPA, and at $304$ K for DES. The detached hydrogens remain chemisorbed on the surface before they desorb at about $312$ K upon recombination into $H_2$ with an energy of about $1$ eV (cf. Table 8.2, [340]). This is in good agreement with a previous study of chemisorbed hydrogen on Cu(111) which revealed values between $0.7$ eV and $0.9$ eV [353]. In addition, the STM and LEED data shows ordered overlayers after annealing to $340$ K and $380$ K which is attributed to the deprotonated BPA and DES, respectively (Figure B.3, step I). A resulting $C-H$ activation is followed by the desorption of $H_2$ at about $430$ K for both molecules and ortho-ortho coupling between neighbouring molecules (Figure B.3, step II). Regarding the 3rd peak, the difference in the bridging between the phenol groups seems important. For both molecules, the $H_2$ desorption at $600$ K (BPA) and $510$ K (DES) correlates with the release of water. Simultaneously, the XP spectra show that O $1s$ component $2$ is slowly transformed to component $3$ at a higher binding energy (cf. Figure 8.5) whereas it loses intensity. A possible reason for the desorption of $H_2$ and the high binding energy could be the formation of a $C-O-C$ linkage between a carbonyl oxygen and an ethyl from the bridge group of a neighbouring species (Figure B.3, red ellipse). Further speculations lead to deoxygenation triggered by abstracted hydrogen or $C-C$ bond formation within the disordered polymers. The higher temperature for BPA could be explained by its different structure. It could hamper a formation of $C-O-C$ linkage and thus, leads to a weaker and retarded O $1s$ component 3.

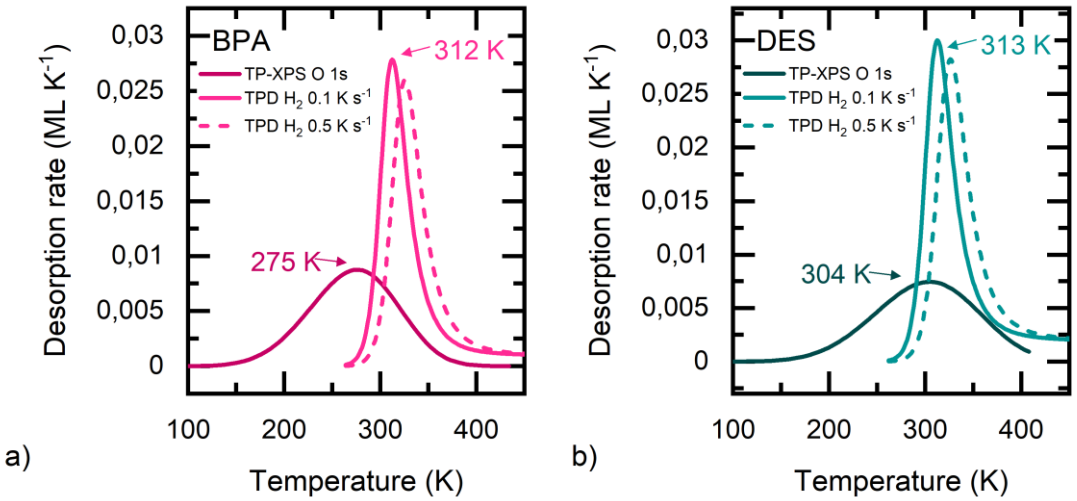


***Figure 8.7*** *Correlation between conversion rate $r_{1\to2}$ of O $1s$ component $1 \to 2$ and desorption rate of $H_2$ from (a) BPA/Cu(111) and (b) DES/Cu(111). The conversion rate $r_{1\to2}$ is the first derivative of the coverage in Figure 8.6. The heating rate of $0.1\,K\,s^{-1}$ (solid) is the recalibration of the original $H_2$-rate (dashed). Accordingly, compatible peak temperatures are reported. To consider the different heating rates, the scaling of the $y$-axis is in units of ML $K^{-1}$.*

## 8.4 Conclusion

The combination of spectroscopic methods and real-space imaging allows for disentangling the sequence of surface-assisted reactions of BPA and DES molecules on a Cu(111) surface as both, volatile desorbing products and the chemical identity of products remaining adsorbed on the surface are monitored. Despite their differences in the chemical structure, both molecules seem to follow a similar reaction pattern. Subsequent to the initial deprotonation which reveals binding energies of $1.00$ eV for BPA and $0.96$ eV for DES and a 3rd order process, an enol-keto tautomerization mediated monoselective ortho C – H activation takes place. The conversion energy is $0.12$ eV for both, BPA and DES). A first polymerisation step (C – C coupling) is determined by the desorption of molecular hydrogen with binding energies of $1.41$ eV for BPA and $0.99$ eV for DES. This is followed by formation of C – O – C bridges and deoxygenation which reveals a conversion energy of $0.73$ eV for BPA and $0.48$ eV for DES. Simultaneously, desorbing hydrogen ($1.48$ eV – BPA, $1.09$ eV – DES) and water species ($1.06$ eV – BPA, $2.45$ eV – DES) can be observed. While the Cu(111) substrate is further heated, a final transition of the molecules to a network of branched, polymerized chains takes place.

# 9 Desorption kinetics associated to cyclodehydrogenation reaction of metallo-tetraphenyl porphyrins

The adsorption of porphyrins on noble metal surfaces came into vogue in the field of surface science in the last decade thanks to the wide variety of properties such as their catalytic activity [354–356], photosensitivity [7] and electronic and magnetic properties [357, 358]. Especially, metallo-tetraphenyl porphyrins (M-TPP), which have the 5,10,15,20-tetraphenyl-21H,23H-porphyrin (2H-TPP, Figure 9.1) as base, are the focus of interest due to the possibility of thermal evaporation and high stability [359]. The ability of the tetrapyrrole macrocycle to coordinate metal atoms and other moieties into its centre, reveals unique properties of this class of molecules [358, 360]. The 2H-TPP base can be even metalated *in situ* with co-adsorbed metal adatoms [358, 360–363] or native surface adatoms. [358, 363–365]. Recent research shows that these molecules are able to undergo a process where the outer phenyl rings react with the inner porphyrin macrocycle when adsorbed onto Ag(111). This reaction is called intramolecular cyclodehydrogenation (CDH) and is depicted schematically for 2H-TPP in Figure 9.1 [257, 366–368]. Near edge X-ray absorption fine structure (NEXAFS) experiments show that the outer phenyl rings and the inner macrocycle are aligned along the same plane after the reaction took place ending up parallel to the substrate ("flattening") [366]. Specifically, the original studies by Di Santo et al. [366] revealed that 2H-TPP molecules adsorbed on Ag(111) are flattened after annealing to temperatures in the range $525\ \mathrm{K} - 550\ \mathrm{K}$. However, the same flattening effect could not be observed in measurements with a Co-TPP species on Ag(111) [367]. Furthermore, investigations on Zn-TPP monolayers were performed on Ag(110) and Si(111) surfaces.
While the molecules showed a flattening on the silver substrate after annealing to $500\ \mathrm{K}$, the phenyl rings of the molecules remain tilted on the silicon crystal [369] instead of being flat. In 2014, Röckert et al. [370, 371] performed comprehensive TPD studies of 2H-TPPs on the Cu(111) surface which provide important information about metalation and the actual flattening mechanisms. The process was found to be stepwise – the metalation with the Cu substrate adatoms is followed by the CDH reaction [370].

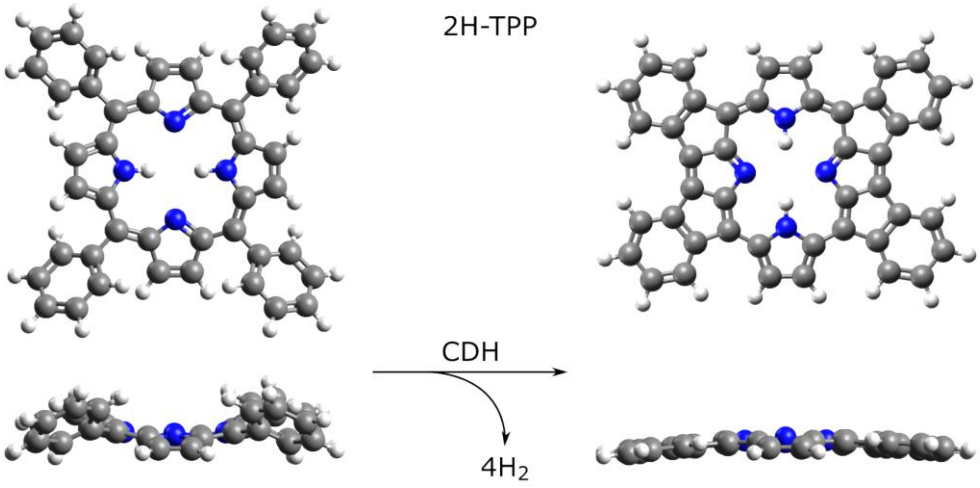


***Figure 9.1*** *Schematic of one possible cyclodehydrogenation reaction [257] pathway of 2H-TPP. Upon high temperature annealing, the unreacted porphyrin couples the outer phenyl rings one-by-one to the inner macrocycle by the dissociation of* $4 \cdot H_2$ *[136].*

Experiments on hydrogen and deuterium desorption for the TPP metalation showed that the central atoms ($H$ or $D$) recombine on the surface rather than directly upon Cu insertion. Moreover, the Cu(111) surface acts as reservoir for $H/D$ atoms which are in equilibrium with the tilted phenyl rings of the TPP species. Released hydrogen atoms transiently re-hydrogenate the periphery of the molecules [371]. For the flattening, the CDH reaction rate depends on the actual TPP density: at surface coverages above $0.43\ \mathrm{nm}^{-2}$, the initially disordered Cu-TPPs arrange as checkerboard structure and the CDH reaction changes into a two-step process [370]. The second effect was ascribed to stabilizing T-type interactions of neighbouring phenyl rings [372]. In general, each of the four phenyl rings is able to link to two sites of the macrocycle, thus, leading to different possible reaction products. A study on the selectivity of the CDH reaction of TPP on Ag(111) was performed by Wiengarten et al. [257]. One of four final products dominates the flattening (cf. Figure 1, Structure A in Ref. [257]). This was ascribed to the position of the two central $H$ atoms of the pyrrolic rings that define the two-fold symmetry of the molecule. Instead, the CDH of the four-fold symmetric Ru-TPP on Ag(111) produces all four possible derivatives in comparable quantities. These geometrically different reaction products might explain the loss of long-range order of the Ru-TPP overlayer that could be observed in STM measurements [257]. Zn-TPP on Ag(111) shows a similar behaviour [373]. The loss of long-range order may be ascribed to the flatting process and an associated loss of T-type interaction.

According to the behaviour on Ag(111), the central moiety of the M-TPP molecules seems to have a significant effect on the reactivity of the phenyl rings attached to the macrocycle. Not only the temperature, which is required for the flattening, differs, but also the reaction pathway. Responsible for these differences might be the character of the central moiety, the reduction of symmetry, the interaction of the adsorbed species with the surface and the intermolecular interactions [370, 372].
In this work, a systematic temperature programmed desorption (TPD) study on 2H-TPP, Ti-TPP, TiO-TPP and Ru-TPP species on Ag(111) is presented in order to further reveal the intricate thermal behaviour of TPP derivatives on metal supports. Moreover, it is assessed how the chemical nature of the central moiety determines the ability of the CDH reaction to proceed. TPD provides insight into kinetics of surface reactions by recording the desorption rate of the reactions products as a function of substrate temperature.

## 9.1 Experimental procedures

The TPD and TP-XPS experiments were performed on a custom-built set-up with a base pressure between $10^{-10}$ and $10^{-11}$ mbar and a quadrupole mass spectrometer (QMS). A Feulner cap covers the QMS [308, 374, 375] and the opening of the cap is brought close to the sample (distance $\approx 1$ mm) in order to minimize perturbation originating from background pressure. The Feulner cap (cf. setup in Ref. [308]) was cooled down by liquid nitrogen and built-in titanium sublimators were used before each measurement to minimize the background pressure of $m/z = 2$ inside the enclosed volume of the QMS. Additionally, a separate cold trap which is covered by titanium films before each measurement, was used to reduce the background pressure in the entire UHV chamber. The sample was heated by a proportional-integral-derivative (PID) controller[69]. The temperature of the sample was recorded by a K-type thermocouple in direct contact with the crystal. The Ag(111) was cleaned by sputtering with $Ar$ or $Ne$, followed by annealing to $725$ K for $5 - 10$ min.
The 2H-TPP[70] and Ru(CO)-TPP[71] were evaporated from quartz glass crucibles in a custom-built organic molecular beam evaporator. Ti-TPP was formed by *in-situ*

[69] Schlichting Physikalische Instrumente HS 130

[70] Sigma Aldrich, $\geq 99\%$

[71] Aldrich Chemistry, $\approx 80\%$

metalation. Ti metal was deposited onto a surface, which was prepared with a 2H-TPP layer, using a custom-built metal evaporator [376, 377]. The evaporators were cooled with water during operation. For forming TiO-TPP, the sample was exposed to oxygen gas ($\approx 100 - 3000$ L) using a directed doser.

LEED[72] and X-ray photoelectron spectroscopy[73] were used to determine the superstructures of the adsorbed TPP overlayers and to characterize the purity of the substrate and the chemical state of the respective overlayers.

For TPD and LEED experiments, saturated monolayers/saturation layer[74] and sub- monolayers were prepared by evaporating 2H-TPP and Ru(CO)TPP on Ag(111) (at $300$ K) and subsequent heating to $475$ K for $2$ min (2H-TPP) and $570$ K/$550$ K for $10$ min (Ru-TPP), respectively, in order to remove multilayers. Ti and $O_2$ were dosed at $300$ K to obtain Ti-TPP and TiO-TPP, respectively [376, 377]. After $Ti$ evaporation, the system was annealed to $540$ K to $2$ min to trigger the complete metalation to Ti-TPP.

The raw data of the TPD measurements is smoothed using a built-in function of MATLAB called *sgolayfilt* to reduce the noise of data, recorded points at low heating rates. For the analysis of the spectra, a background correction was performed by subtracting a Boltzmann function fitted to the data points before and after the desorption peak to align the derivative of rate and background. Subsequently, the desorption rate $r$ is normalized to units of ML $s^{-1}$. The integral of all hydrogen atoms desorbing from a saturated layer is defined as $1$ ML ($\theta_{CDH}$), which corresponds to the number of all hydrogen atoms involved in the CDH and detected as $m = 2$ in the QMS of a saturated monolayer until CDH is finished. (for Ti-TPP, the metalation peak is excluded). For the initial coverage of the saturated monolayer $\theta_{intial}$, the desorption of intact molecules ($\theta_{excess\ molecules}$) has to be considered:

$$\theta_{initial} = \theta_{CDH} + \theta_{excess\ molecules} > 1\text{ML}. \tag{9.1}$$

Once the sensitivity of the mass spectrometer is calibrated, other coverages can be normalized with the same factor (see Sections 5.3.1 and 6.2.1 for more details).

---

[72] BDL800IR-LMX-ISH, OCI Vacuum Microengineering Inc.

[73] Phoibos 100 CCD hemispherical electron analyser, Al and Mg K$\alpha$ radiation from a standard dual anode X-ray source

[74] Corresponds to highest achievable monolayer coverage/density of molecules after multilayer desorption

TPD simulations are performed using the Polanyi-Wigner equation (Equation 5.4) which is solved numerically in discrete time steps followed by a recalculation of the actual coverage (cf. Runge-Kutta method, Section 6.2.3). The pre-exponential correction $k_0^*$, binding energy $E_B$, and the order of the desorption $m$ are fitting parameters. For the simulation with the advanced model, further fitting parameters will introduced (Section 9.4.4). To improve consistency of data, the least squares optimization is used.

## 9.2 Low-energy electron diffraction (LEED)

The initial overlayer structures prior to TPD experiments are investigated by LEED measurements, shown in Figure 9.2.

The reciprocal lattice, as reported by Zaglmayr et al. [378], is overlaid to the images of 2H-TPP, TiO-TPP, Ti-TPP and the sub-monolayer Ru-TPP. The saturation layer of Ru- TPP shows a different LEED pattern and thus, has a different overlayer structure which cannot be explained by the superstructure matrix $\begin{pmatrix} 5.5 & 1.5 \\ 1.5 & 5.5 \end{pmatrix}$ which is proposed by Zaglmayr et al.

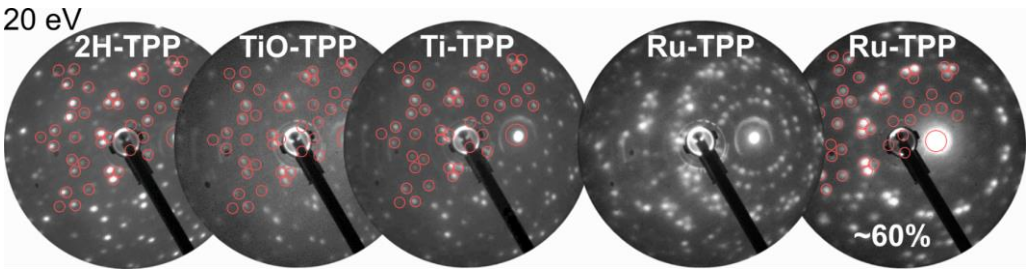


***Figure 9.2*** *LEED images of the initial overlayer structures of 2H-TPP, TiO-TPP, Ti-TPP and Ru-TPP (saturation layer and sub-monolayer) before the TPD experiments. The images were taken with $E_P = 20$ eV at $T \approx 90$ K. The superimposed reciprocal lattice patterns resemble the structure reported by Zaglmayr et al [378]. The proposed superstructure matrix $\begin{pmatrix} 5.5 & 1.5 \\ 1.5 & 5.5 \end{pmatrix}$ is generated by LEEDpat [379].*

Further detail concerning the LEED patterns are investigated in [380].

## 9.3 X-ray photoelectron spectroscopy (XPS) and multilayer desorption

Extensive multi-method investigations [380] prove the CDH reaction of Ru-TPP on Ag(111) taking place in the temperature range between $620$ K and $770$ K. Figure 9.3

shows the XP spectra (C $1s$ and Ru $3d$) of a multilayer and a saturated monolayer. Normalizing the coverage of the saturated layer by the C $1s$ intensity after the CDH reaction to $1$ ML (blue line) reveals a coverage of $1.4$ ML (red line) for the multilayer.

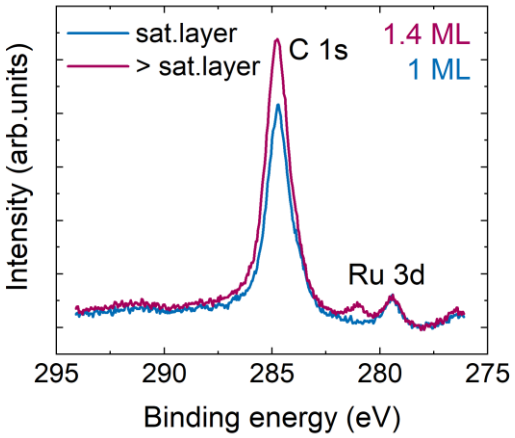


***Figure 9.3*** *XP spectra of a multilayer (red) and a saturated monolayer (blue) of Ru-TPP on Ag(111) at* $300$ *K. The saturation layer was prepared by annealing to* $570$ *K for* $10$ *min after Ru(CO)-TPP evaporation. The red spectrum corresponds to a system which was annealed to* $505$ *K for* $10$ *min after the deposition of Ru(CO)-TPP. Integrating the C* $1s$ *peak of both preparations reveals a coverage of* $1.4$ *ML for the multilayer.*

Figure 9.4 shows heat maps of the averaged XP signal of C $1s$ and Ru $3d_{5/2}$ the temperature axis which is increased with a linear heating rate of $0.1$ K s$^{-1}$ (TP-XPS). Starting at $560$ K (2H-TPP) and $655$ K (Ru-TPP), the binding energy of C $1s$ shifts to lower values as expected from Figure 9.3. Both molecules undergo a CDH reaction. In Figure 9.4b and d, the area of the C $1s$ features are integrated and plotted with respect to temperature $T$. This corresponds to the coverage of C and Ru on the surface as a function of the temperature and thus, the temperature profile of the CDH reaction. A loss of about $33\%$ (2H-TPP) and about $22\%$ of the initial saturation coverage is revealed by XPS.

Looking ahead to the TPD results of Section 9.4, the XPS coverage is compared to the integral of the mass-to charge ratio $m/z = 12$ (TPP fragment) which is recorded by the QMS while heating up the sample (see Figure 9.4b and d, top). The TPP fragment is

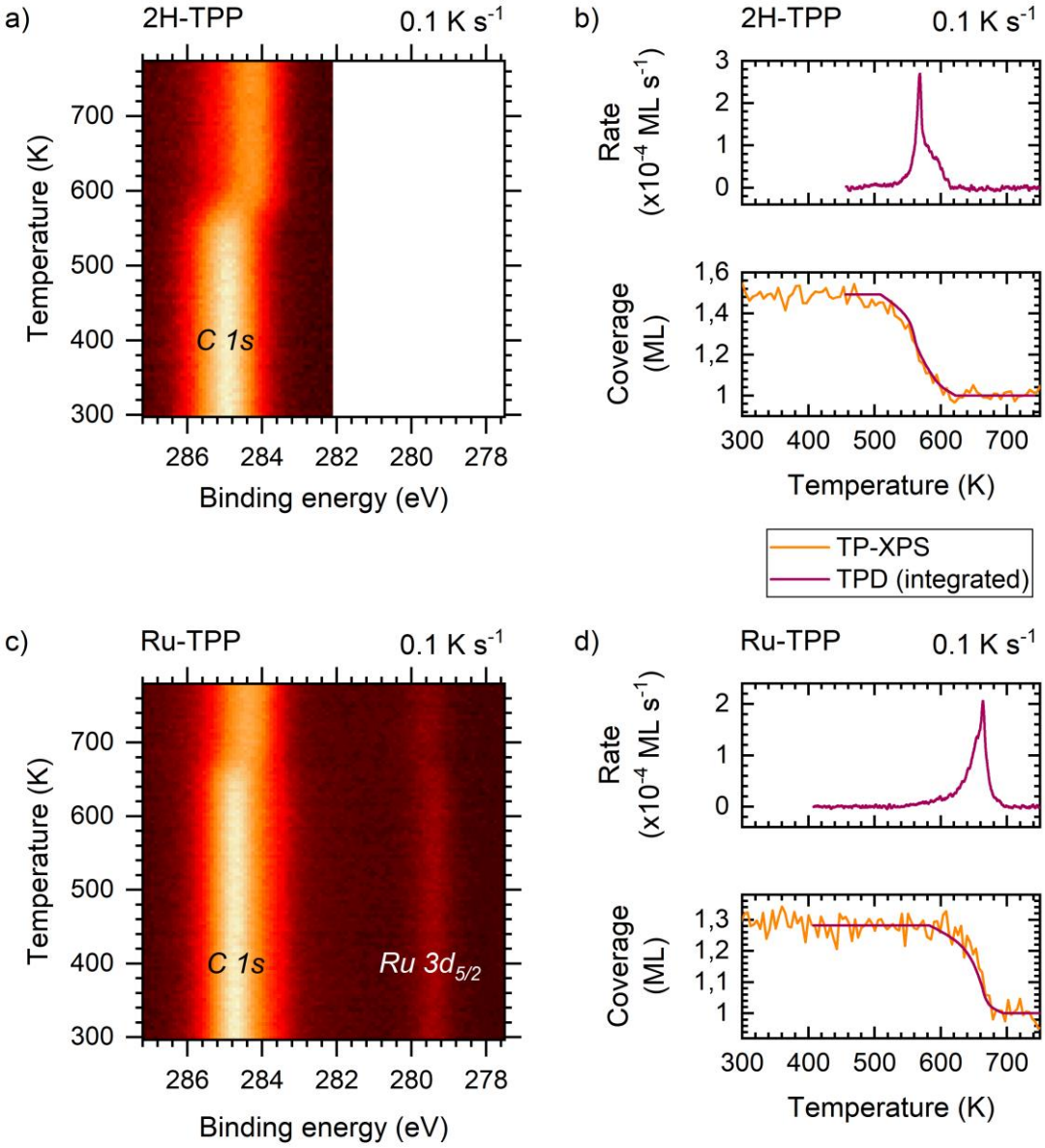


***Figure 9.4*** *TP-XP spectra of a saturated monolayer of a) 2H-TPP and c) Ru-TPP. TP- XPS is normalized and Shirley background subtracted. Binding energies are calibrated against the Ag $3d_{5/2}$ core-level line of Ag(111). Additional TPD experiments were recorded with the same heating rate of $0.1\ K\ s^{-1}$. The top panels of b) and d) show the TPD spectra of $m/z = 12$ for 2H-TPP and Ru-TPP, respectively. In the bottom panels of b) and d), the coverage is depicted as function of the temperature for 2H-TPP and Ru-TPP, respectively. The averaged C $1s$ signal along the temperature axis (orange) is compared to the integrated desorption rate (red). The loss of molecules of $33\%$ (2H- TPP) and $22\%$ (Ru-TPP) is associated with the CDH reaction.*

assigned to the desorption of intact molecules which cannot be recorded due to limitations of the QMS. The carbon signal is probably caused by the decay of intact molecules in the ion source of the QMS.

Both coverage plots are in very good agreement as illustrated in the lower part of Figure 9.4b and d. For this purpose, the $H_2$ spectra were normalized to $1$ ML of desorbing molecular hydrogen after the CDH reaction (for more details see Section 9.1). The number of desorbing molecules $\theta_{excess} > 1$ ML is determined by the XPS signal. This is the base for the calibration of the carbon desorption peak as all preparations have the same amount of molecules.

Thus, the carbon desorption during the CDH reaction is coincident with the decrease of XPS intensity during CDH reaction ($\theta_{CDH}$) normalized to $1$ ML of XPS intensity after the molecules are fully flattened.

Corresponding to the XPS measurements, TPD spectra of multilayer desorption were recorded for Ru-TPP. Molecular hydrogen ($H_2$, $\frac{m}{z} = 2$) and a TPP fragment ($\frac{m}{z} = 12$) which is representative for the intact molecule, are measured simultaneously, as depicted in Figure 9.5.

The first carbon desorption peak represents the desorption of $0.4$ ML which is the number of excess molecules of the multilayer compared to the saturation layer. Directly comparing the two peaks of the desorption spectrum reveals that $0.24$ ML of the molecule desorb during the CDH reaction of the Ru-TPP, which is in very good agreement with the TP-XP spectra shown in Figure 9.4.

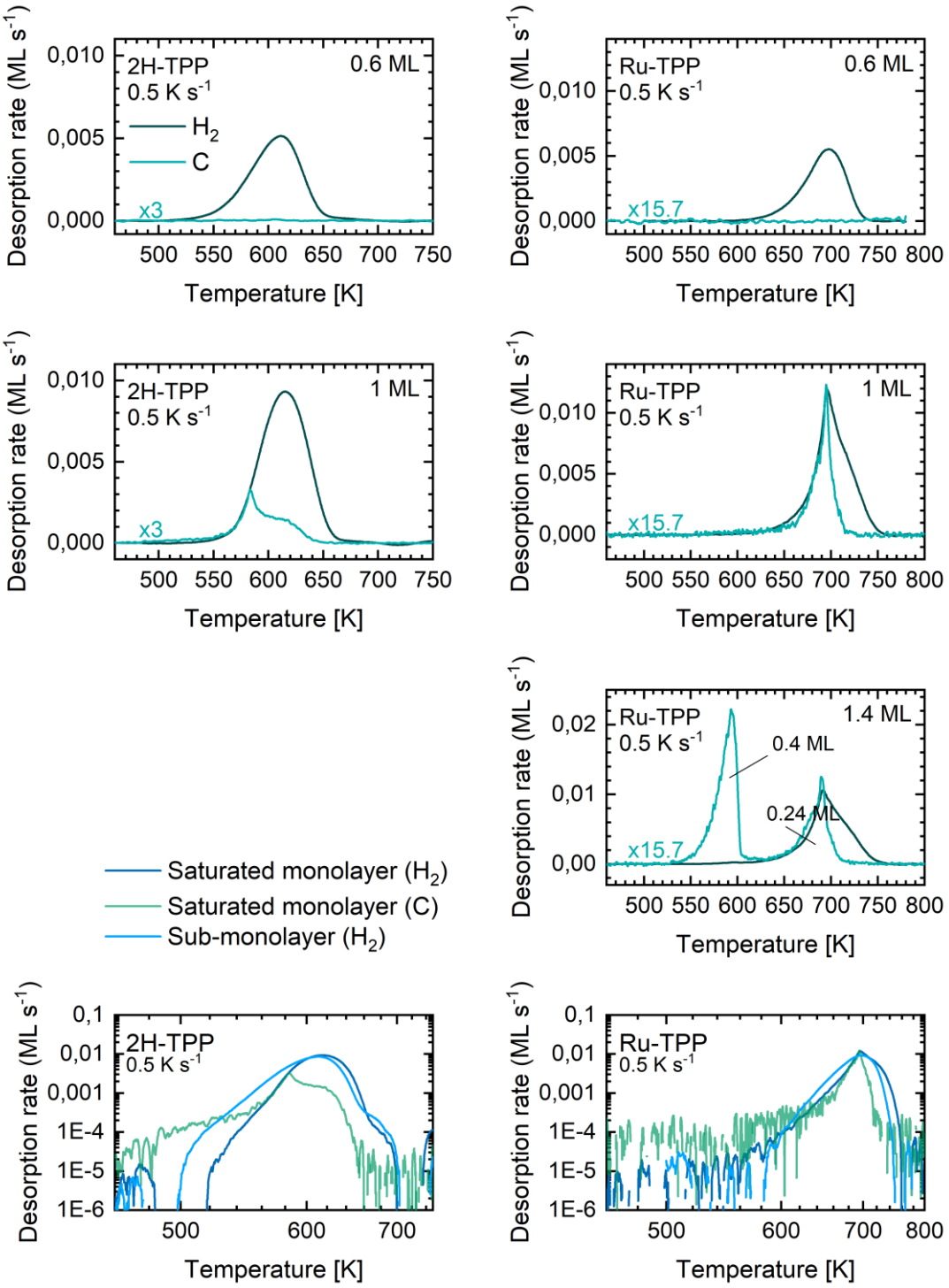


***Figure 9.5*** *Experimental spectra of $H_2$ and C desorption for 2H-TPP and Ru-TPP on Ag(111) recorded with different coverages (see inset: $0.6\,ML$, $1\,ML$ and $1.4\,ML$) and a heating rate of $0.5\,K\,s^{-1}$. All spectra are normalized according to their coverage of flattened molecule species, while carbon spectra are additionally multiplied by an arbitrary factor ($x3$ for 2H-TPP and $x15.7$ for Ru-TPP). Bottom: MS-plot of sub-monolayers and saturated monolayers showing a delayed start of the CDH reaction for a full layer of 2H-TPP and Ru-TPP.*

## 9.4 Temperature programmed desorption (TPD)

### 9.4.1 Monolayers of 2H-TPP, Ru-TPP, Ti-TPP and TiO-TPP

For each TPD spectrum, $H_2$ ($\frac{m}{z} = 2$) and a TPP fragment ($\frac{m}{z} = 12$), which is supposed to be representative for the intact molecule, are measured simultaneously as depicted in Figure 9.6 and Figure 9.7. For 2H-TPP, Ru-TPP, Ti-TPP and TiO-TPP at various heating rates ($2\ \mathrm{K\ s^{-1}}$, $1\ \mathrm{K\ s^{-1}}$, $0.5\ \mathrm{K\ s^{-1}}$, $0.1\ \mathrm{K\ s^{-1}}$) were recorded. Apparently, the peak temperatures for all species are shifting towards higher temperatures for higher heating rates. The as-prepared saturated monolayers of 2H-TPP and Ru-TPP display a single $H_2$ desorption peak which can be attributed to the CDH reaction. While the shape of the 2H-TPP seems to be similar to a classical first or second order desorption, the spectra of the Ru-TPP show a much sharper, asymmetric peak similar to zeroth order desorption, but without the straight falling edge. The spectra of Ti-TPP show two distinct features for molecular hydrogen. The first desorption peak is assigned to the metalation of the 2H-TPP with the deposited titanium atoms (cf. metalation of Cu-TPP [370, 371]). The second peak is ascribed to the flattening of the Ti-TPP, while the shoulder towards lower temperatures can be attributed to the CDH of residual, non-metalated free-base 2H-TPP species as the Ti- TPP overlayer was prepared upon *in-situ* metalation of the 2H-TPP overlayer with a sub-saturation coverage of Ti. Indeed, the peak position of the 2H-TPP is in the same temperature range as the shoulder in the corresponding Ti-TPP spectra. Moreover, the spectra of TiO-TPP feature one main peak as well as a weak shoulder around $615\ \mathrm{K}$. Accordingly, peak and shoulder can be assigned to the CDH of TiO-TPP and a residual, non-metalated free-base 2H-TPP species, respectively. The additional peak in the hydrogen spectra of TiO-TPP at a heating rate of $0.1\ \mathrm{K\ s^{-1}}$ towards high temperatures, may be ascribed to subsequent oligomerization/polymerization reactions. This phenomenon may occur after the CDH reaction as reported by a scanning probe microscopy study of 2H-TPP on Ag(111) (cf. Figure S3 of Ref. [257]).

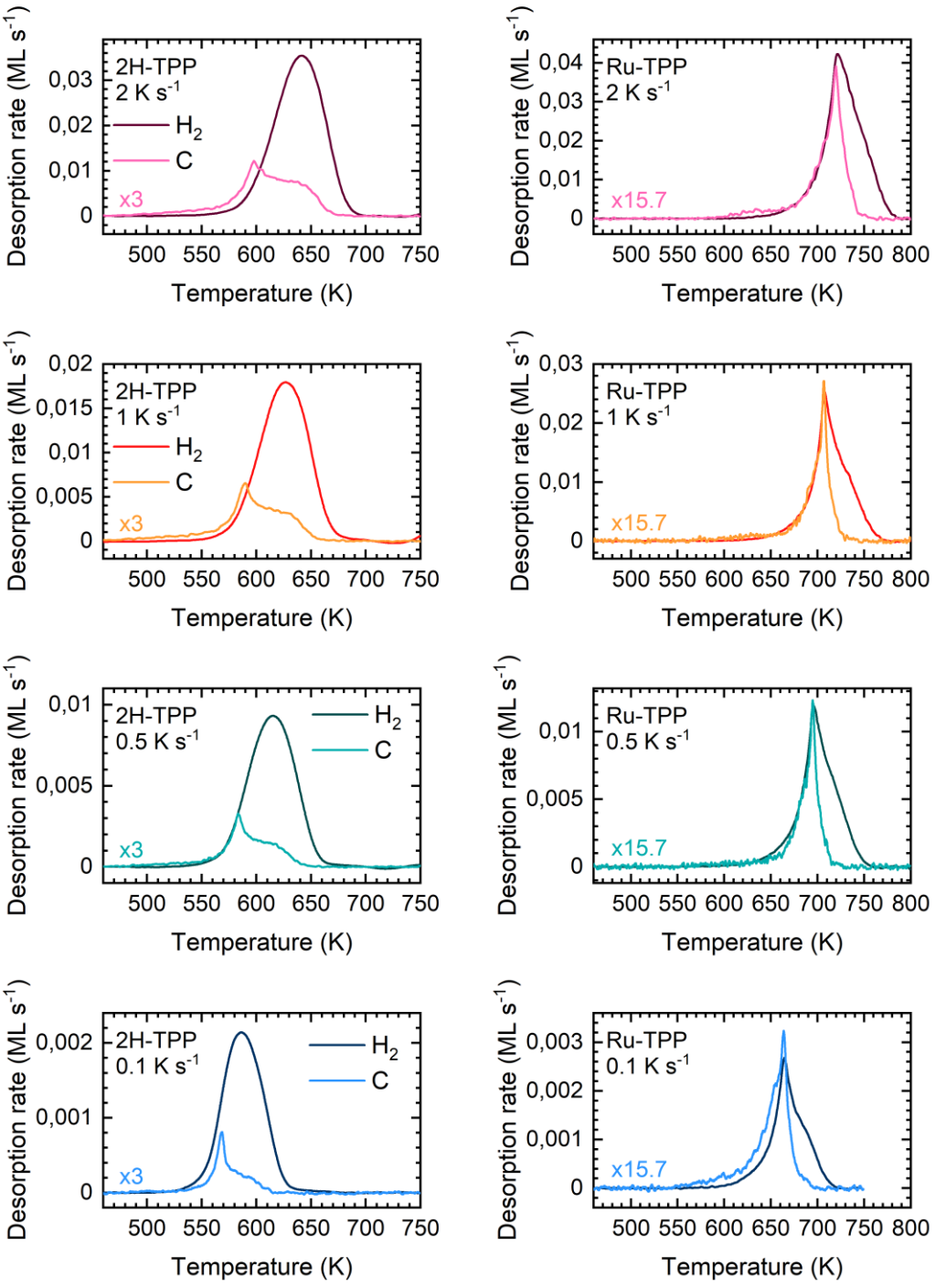


***Figure 9.6*** *Experimental spectra of molecular hydrogen ($m/z = 2$) and TPP fragment ($m/z = 12$) desorption for 2H-TPP and Ru-TPP prepared as a saturated monolayer on Ag(111). All $H_2$ plots are normalized such that all hydrogen atoms desorbing within the given peak of the porphyrin layer are defined as 1 ML for the simulation. The plots of $m/z = 12$ are multiplied by a distinct factor for each molecule to show the correlation with the desorption of molecular hydrogen. The similar onset of $H_2$ and TPP fragment desorption is apparent for all heating rates. A small relative shift in temperature is visible. As both masses were recorded in the same experiment, this is not attributed to experimental errors.*

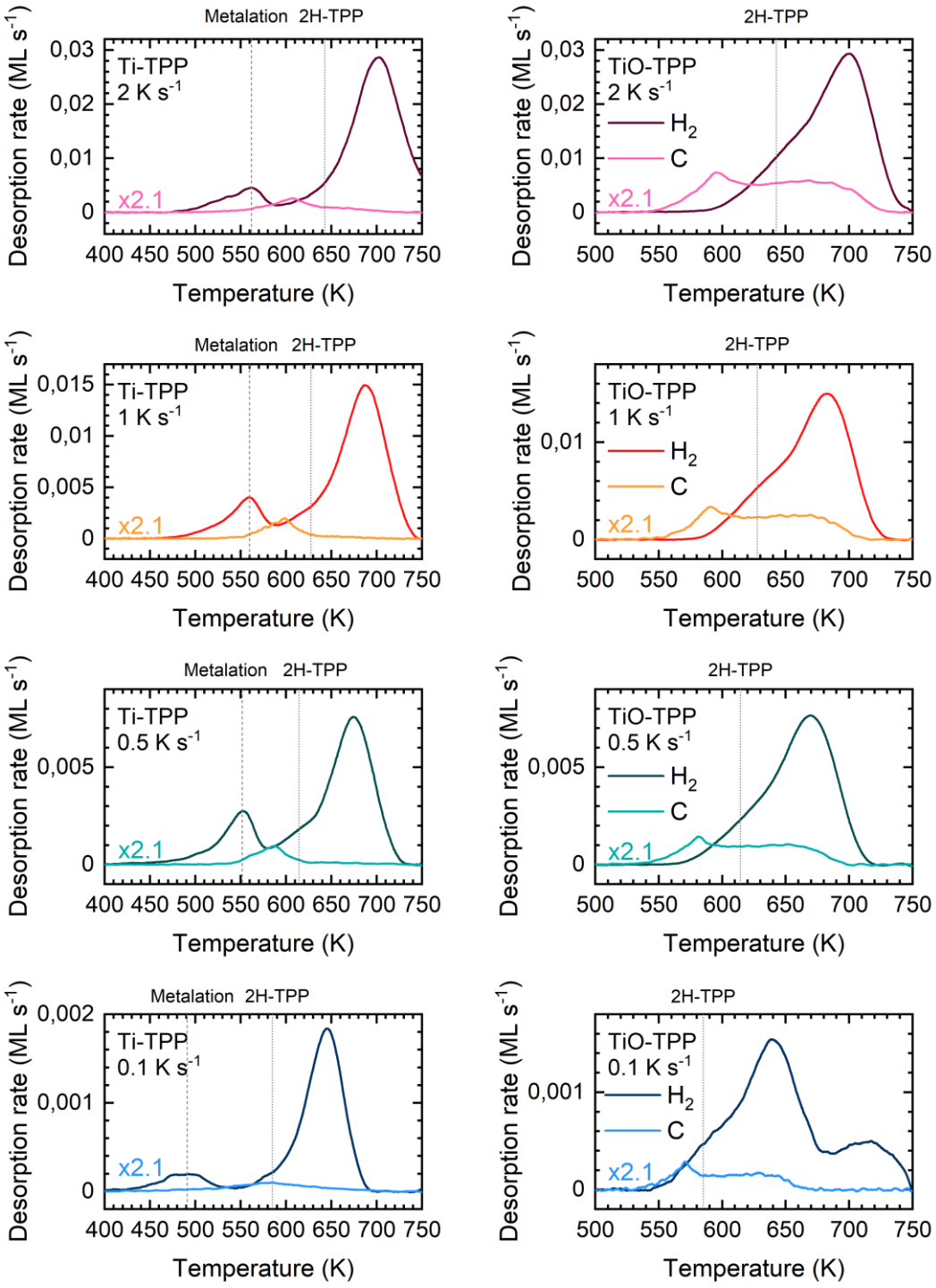


***Figure 9.7*** *Experimental spectra of $H_2$ $(m/z = 2)$ and TPP fragment $(m/z = 12)$ desorption for Ti-TPP and TiO-TPP prepared on Ag(111) as saturated monolayer. For all graphs, normalization was performed as in Figure 9.6. For Ti-TPP, the metalation peak was not accounted for the normalization. The plots of the TPP fragment are multiplied by a distinct factor for each molecule to show the correlation with the desorption of molecular hydrogen. The dashed lines indicate the maximum of the metalation, while the dotted lines represent the $H_2$ desorption maximum of the 2H-TPP species.*

The shapes of the carbon desorption peaks (Figure 9.8) differ depending on the porphyrin species. The desorption of 2H-TPP molecules shows a sharp peak at the onset of the flattening process with similar slopes prior to the maximum of the hydrogen desorption feature. Additionally, the distinct shoulder of the carbon signal at the hydrogen desorption maximum indicates that a fraction of 2H-TPP desorbs simultaneous to the CDH reaction of the porphyrin overlayer. The signal is shifting in temperature and changes its shape depending on the heating rate which might be due to a conversion process on a large time scale. This might be induced by the free space upon desorption of intact molecules. This also may imply a non-equilibrium situation during the CDH. The carbon signal of the Ru-TPP spectra has a rather different shape. The onset of the desorption spectra is similar to the hydrogen desorption and even overlaps up to their common desorption maximum. For better comparison, the spectrum of the carbon is multiplied by a factor of $15.7$ (Figure 9.6). The flattening reaction seems to proceed further after the TPP fragment desorption has almost stopped. This might be due to a stronger interaction of Ru-TPP with the surface than 2H-TPP.

The C peak in the Ti-TPP spectrum, plotted in Figure 9.7 with a multiplication factor of $2.1$, is not as sharp as for the 2H-TPP and Ru-TPP. Furthermore, it does not show a strong correlation to the corresponding hydrogen peak. The carbon desorption in the Ti-TPP spectrum starts already during the metalation process and proceeds during the CDH of the residual 2H-TPP. During the actual flattening of the Ti-TPP, the desorption of porphyrin molecules has almost stopped. It might be that only a fraction of the residual 2H-TPP species desorb due to the stronger interaction of Ti-TPP mediated by the Ti ions [377].

The broad carbon signal in the TiO-TPP spectra consists of two peaks as depicted in Figure 9.7. The first peak is at the same position as the sharp fragment feature of the 2H-TPP (see Figure 9.8). The maximum of the second peak is at a similar temperature as the maximum of the corresponding hydrogen peak. It might be that predominantly the minority of residual 2H-TPP species desorb instead of the metalized species due to higher interaction to the surface.

In particular for Ru-TPP, the removal of excess molecules appears to be the determining factor in the CDH reaction of the saturated monolayer as the shapes of the onset of the fragment pattern closely resemble the $H_2$ desorption feature up to its maximum. Analogously, the partly overlapping onset of hydrogen and carbon desorption of the

2H-TPP suggest a decisive role of partial desorption of molecular overlayers for the CDH reaction. To further reveal this role, coverages of about $60\%$ of a monolayer are investigated in addition to the saturation layers. Corresponding TPD spectra of both, hydrogen and TPP fragments, are depicted in Figure 9.5 for 2H-TPP and Ru-TPP. In contrast to the saturated monolayer, no significant desorption of carbon can be detected along with the desorption of molecular hydrogen and thus, the CDH reaction. Furthermore, both $H_2$ spectra resemble a similar shape as classical desorption peaks of first or second order processes with a distinct tail towards low temperatures. Consequently, the flattening reaction and the associated desorption of excess TPP species seem to be directly linked in the case of saturated overlayers, strongly influencing the shape of the corresponding $H_2$ desorption spectra, as emphasized by the comparison of Figure 9.5 for 2H-TPP and Ru-TPP at a heating rate of $0.5$ K $s^{-1}$. This correlation makes a direct quantitative analysis of the underlying kinetics difficult.

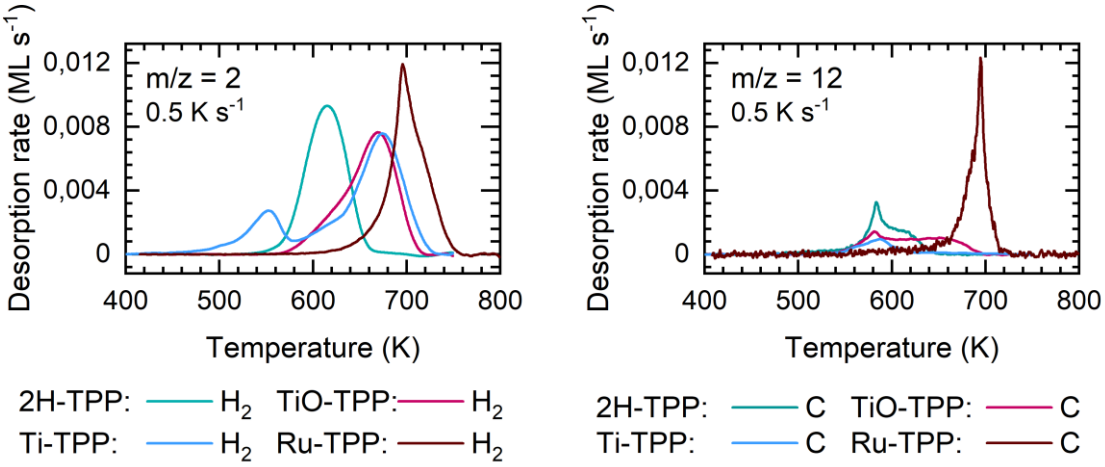


***Figure 9.8*** *Comparison of experimental spectra of molecular hydrogen and TPP fragment desorption for 2H-TPP (green), Ti-TPP (blue), TiO-TPP (red) and Ru-TPP (brown) adsorbed on Ag(111), recorded with a heating rate of* $0.5$ *K* $s^{-1}$*. Normalization is performed as in Figure 9.6. The initial coverage is in the range of* $1.3$ *ML.The desorption maxima shift in temperature depending on the centre of the molecules.*

A similar increase of the signal towards high temperatures could be observed in the raw data of all discussed porphyrin molecules. On Ag(111) thermally induced oligomerization has also been reported for the bare porphine species [381].

Comparing the $H_2$ TPD spectra of all four porphyrin species at $0.5$ K $s^{-1}$ (see Figure 9.8 left) shows a clear and consistent shift of the main desorption peak. This indicates that the metalation of 2H-TPP results in a significant increase of the CDH temperature $T_{CDH}$,

while oxidizing the metal centre results in a very subtle decrease of $T_{CDH}$. Ru-TPP shows the highest reaction temperature among all four species:

$$T_{CDH}(2H-TPP) \ll T_{CDH}(TiO-TPP) < T_{CDH}(Ti-TPP) \ll T_{CDH}(Ru-TPP) \tag{9.2}$$

The TPD spectra of $m/z = 12$, (Figure 9.8 right) which are depicted in addition to the corresponding $H_2$ TPD spectra ($m/z = 2$) of all four species, as well as the data at different heating rates (Figure 9.6 and Figure 9.7), show the desorption of the TPP fragment which takes almost place simultaneously to the desorption of molecular hydrogen. The detection of these mass fragment is assigned to the desorption of the M-TPP molecules, which could not be recorded with the installed experimental set-up. The fragmentation of the desorbing molecules is caused by ionization in the mass spectrometer. Thus, the $H_2$ and C spectra of the saturated monolayers of all four porphyrin species (Figure 9.6 and Figure 9.7) indicate that a fraction of the molecules desorbs from the surface during the CDH process. In contrast, TPD measurements of sub-monolayer coverages do not show a signal for $\frac{m}{z} = 12$, as depicted in Figure 9.5. The hypothesis is supported by corresponding temperature programmed XP spectra which are depicted in Figure 9.4a and c for 2H-TPP and Ru-TPP, respectively.

### 9.4.2 Sub-monolayers of 2H-TPP and Ru-TPP

The TPD spectra of the sub-monolayer coverages of the 2H-TPP and Ru-TPP species do not reveal desorption of TPP fragment, thus, the CDH reaction appears to be comparatively simple in contrast to the saturated layers. In this case, the flattening process is modelled by the Arrhenius-like Polanyi-Wigner equation. The standard pre- exponential $k_0^* = \frac{k_B T}{h}$, which consists of the elementary constants and the temperature dependence, is extracted (see Equation 5.6). The correction for the sticking coefficient and the ratio of the partition functions are comprised in $k_0^*$

$$r_{CDH} = \theta^m \frac{k_B T}{h} k_0^* \exp\left(-\frac{E_B}{k_B T}\right). \tag{9.3}$$

The rate $r_{CDH}$ is calculated numerically as described in Section 6.2.3. Binding energy $E_B$ and pre-exponential correction $k_0^*$ are free fitting parameters and kept constant over the coverage. The order of desorption $m$ is a third fitting parameter. The parameters are

varied by a MATLAB optimization routine called *fminsearch*. The simulated rate $r_{CDH}$ is compared to the experimental data by the minimum of least squares.

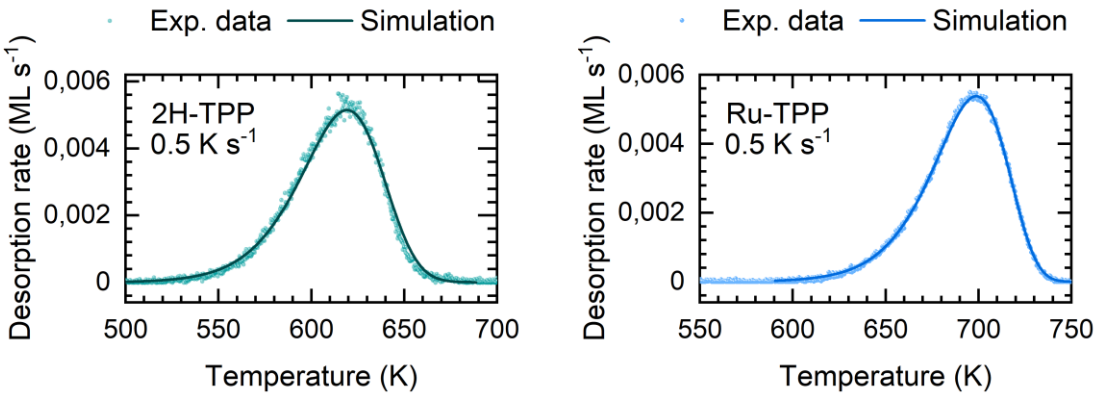


***Figure 9.9*** *Experimental $H_2$ TPD plots of the sub-saturation layers of 2H-TPP (green scatter) and Ru-TPP (blue scatter). Additionally, the simulation using the Arrhenius-like Polanyi-Wigner Equation 5.3 is shown for 2H-TPP (green line) and Ru-TPP (blue line). The fitting parameters are summed up in Table 9.1.*

In Figure 9.9, experimental (scatter plot) and simulated data (line plot) are plotted. The fitting procedure reveals a 1st order desorption process with binding energies $E_{Bind}$ of $1.47$ eV (2H-TPP) and $2.00$ eV (Ru-TPP), see Table 9.1. As already indicated by the peak temperatures $T_{CDH}$ in Equation 9.2, the CDH of Ru-TPP has a higher reaction energy and thus, requires more energy than the flattening of the 2H-TPP.

| | $m$ | $E_{Bind}$ | $k_0$ | Reliability |
|---|---|---|---|---|
| **2H-TPP** | 1.0 | 1.4 eV | $2.0 \cdot 10^{10}$ s$^{-1}$ | $2.0 \cdot 10^{-5}$ |
| **Ru-TPP** | 1.0 | 2.0 eV | $6.3 \cdot 10^{12}$ s$^{-1}$ | $3.7 \cdot 10^{-6}$ |

***Table 9.1*** *Fitting parameters (order of desorption $m$, binding energy $E_{Bind}$ and pre- exponential factor $k_0$) and reliability factor of the TPD analysis for simulated $H_2$ desorption in the CDH reaction from a sub-monolayer porphyrin coverage.*

### 9.4.3 Saturated monolayers of 2H-TPP and Ru-TPP – The section model

In contrast to the sub-monolayer coverage, the $H_2$ spectra of the saturation layers cannot be satisfactorily modelled by a single peak. This is depicted exemplarily in Figure 9.10 for 2H-TPP at a heating rate of $0.5$ K s$^{-1}$. The fitting is performed as described in Section 9.4.2.

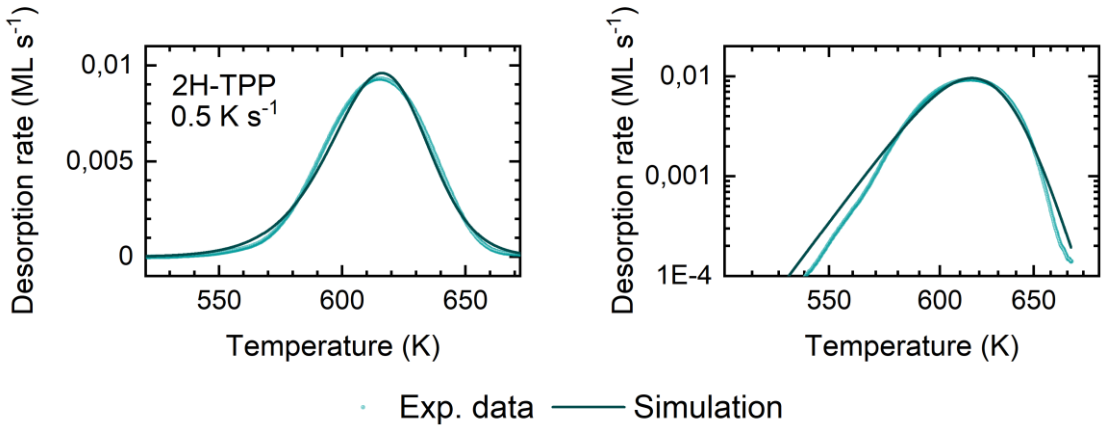


***Figure 9.10*** *Single peak simulation of $H_2$ TPD data of the saturation layers of 2H-TPP at a heating rate of $0.5\ K\ s^{-1}$ (green scatter) in linear and MS plot. A single Polanyi-Wigner equation (Equation 5.4) is used (black line).*

The best fit with a single species of desorbing particles using a classical Polanyi-Wigner equation (Equation 5.4) does not match the $H_2$ desorption. Due to the concomitant desorption of porphyrin species, the simulation and the interpretation of the CDH reaction is far from trivial. A coverage dependent binding energy $E_B(\theta)$ in combination with a coverage dependent pre-exponential $k_0(\theta)$ would be necessary to fulfil the constraints of the compensation effect as $E_B$ and $k_0$ are not orthogonal parameters. In principle, each desorption rate can be perfectly fitted in this way. The number of parameters amounts to twice the number of data points in the recorded desorption rate, which is not a reasonable approach. Thus, the resulting coverage evolution would not be meaningful, as such a "coverage dependence" is just a "transformation of base vectors". Thus, an alternative analysis is necessary to gain deeper insight.

As a first approach to model the flattening of a saturated monolayer, the hydrogen spectrum is subdivided into three sections ($I$, $II$ and $III$) with three different Polanyi- Wigner equations and thus, three different sets of parameters. Compared to any of the common analysis performed by the Redhead method, CAW, HRV, complete analysis or the leading-edge analysis (see Section 6.2.2, [286, 382, 383]), such a modelling (even though segmented in three sections) will provide significantly more information. Pre-exponential factors $k_0^*$, binding energies $E_B$ and orders $m$ are free fitting parameters and are kept constant in the respective section. The simulated rate is compared to the experimental data by visual inspection in linear and MS plots.

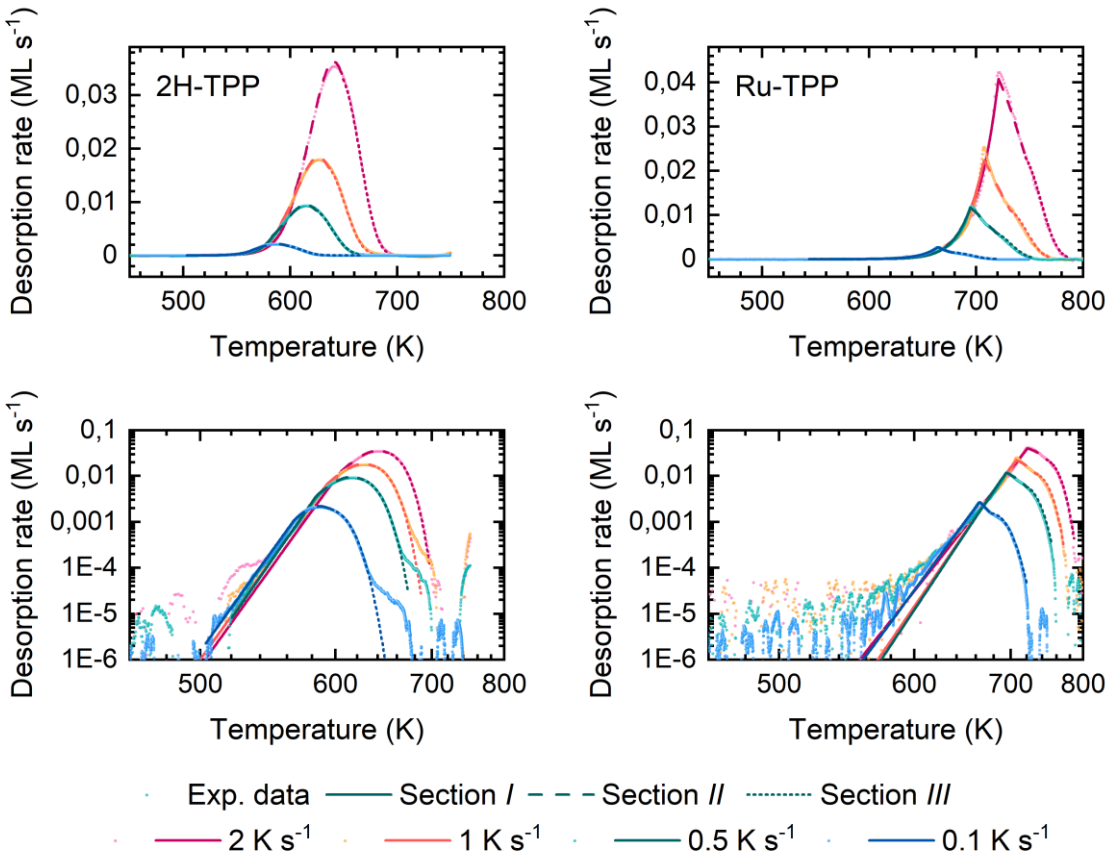


***Figure 9.11*** *Section-simulation with the Polanyi-Wigner equation for the saturated monolayers of 2H-TPP and Ru-TPP. The desorption is subdivided into three sections with different sets of fitting parameters (see Table 9.2). The graphs show the hydrogen desorption peaks of 2H-TPP and Ru-TPP at heating rates of* $2\,K\,s^{-1}$ *(red),* $1\,K\,s^{-1}$ *(orange),* $0.5\,K\,s^{-1}$ *(green) and* $0.1\,K\,s^{-1}$ *(blue) in linear and logarithmic scale. The simulation is plotted accordingly with section* $I$ *(dotted), section* $II$ *(dash-dot) and section* $III$ *(dashed). Section* $I$ *resembles the desorption of TPP fragment (see Figure 9.12), while section* $II$ *has similar parameters to the sub-monolayer desorption.*

Figure 9.11 shows the simulated rate in comparison to experimental data for 2H-TPP and Ru-TPP saturated monolayers. The fitting results for binding energy $E_{Bind}$ and order $m$ are summed up in Table 9.2.

Section $I$, which reaches approximately up to the peak temperature of the $\frac{m}{z} = 12$ signal, reveals binding energies around $2.4$ eV and $2.3$ eV $-$ $2.6$ eV for 2H-TPP and Ru- TPP, respectively. As the shape of the $H_2$ desorption resembles the start of the $C$ desorption, the fitting parameters of section $I$ and the onset of the carbon signal are expected to be similar.

| | | *I* | | *II* | | | *III* | |
|---|---|---|---|---|---|---|---|---|
| 2H-TPP | $m$ | $E_{Bind}$ | $k_0$ | $E_{Bind}$ | $m$ | $m$ | $E_{Bind}$ | $k_0$ |
| $2\ \mathrm{K\ s^{-1}}$ | 0.01 | 2.4 eV | $1.1 \cdot 10^{17}\ \mathrm{s^{-1}}$ | 1.8 eV | 1.4 | 1.0 | 1.5 eV | $2.4 \cdot 10^{10}\ \mathrm{s^{-1}}$ |
| $1\ \mathrm{K\ s^{-1}}$ | 0.01 | 2.4 eV | $1.6 \cdot 10^{17}\ \mathrm{s^{-1}}$ | 1.8 eV | 1.4 | 1.0 | 1.5 eV | $2.4 \cdot 10^{10}\ \mathrm{s^{-1}}$ |
| $0.5\ \mathrm{K\ s^{-1}}$ | 0.09 | 2.5 eV | $9.5 \cdot 10^{17}\ \mathrm{s^{-1}}$ | 1.8 eV | 1.5 | 1.1 | 1.5 eV | $2.4 \cdot 10^{10}\ \mathrm{s^{-1}}$ |
| $0.1\ \mathrm{K\ s^{-1}}$ | 0.17 | 2.4 eV | $3.0 \cdot 10^{17}\ \mathrm{s^{-1}}$ | 2.2 eV | 1.7 | 1.1 | 1.5 eV | $1.2 \cdot 10^{10}\ \mathrm{s^{-1}}$ |
| Ru-TPP | | | | | | | | |
| $2\ \mathrm{K\ s^{-1}}$ | 0.00 | 2.4 eV | $3.6 \cdot 10^{13}\ \mathrm{s^{-1}}$ | 0.7 eV | 0.9 | 1.0 | 2.0 eV | $3.6 \cdot 10^{12}\ \mathrm{s^{-1}}$ |
| $1\ \mathrm{K\ s^{-1}}$ | 0.01 | 2.6 eV | $1.9 \cdot 10^{14}\ \mathrm{s^{-1}}$ | 0.7 eV | 1.0 | 1.1 | 2.0 eV | $3.6 \cdot 10^{12}\ \mathrm{s^{-1}}$ |
| $0.5\ \mathrm{K\ s^{-1}}$ | 0.19 | 2.6 eV | $6.0 \cdot 10^{16}\ \mathrm{s^{-1}}$ | 0.7 eV | 0.9 | 1.1 | 2.0 eV | $3.6 \cdot 10^{12}\ \mathrm{s^{-1}}$ |
| $0.1\ \mathrm{K\ s^{-1}}$ | 0.04 | 2.3 eV | $1.1 \cdot 10^{15}\ \mathrm{s^{-1}}$ | 0.7 eV | 1.3 | 1.2 | 2.0 eV | $4.8 \cdot 10^{12}\ \mathrm{s^{-1}}$ |

***Table 9.2*** *Fitting parameters (binding energy $E_{Bind}$ and order $m$) for section $I$ to $III$ and pre-exponential factors $k_0$ for sections $I$ and $III$ of the simulated saturated monolayer $H_2$ desorption peaks of 2H-TPP and Ru-TPP. The simulation is extended to three different sections with different sets of parameters.*

In the MS plot, the onset of the carbon peak can be fitted with a straight line reflecting the binding energy of the simulated Arrhenius-like equation. In Figure 9.12, the carbon desorption spectra of 2H-TPP and Ru-TPP are plotted in comparison to the corresponding simulation of the hydrogen desorption (section $I$). Especially for heating rates of $0.5\ \mathrm{K\ s^{-1}}$, $1\ \mathrm{K\ s^{-1}}$ and $2\ \mathrm{K\ s^{-1}}$, the simulated data of section $I$ is in very good accordance to the onset of the carbon peak. This suggests, that the $H_2$ desorption in section $I$ is not reflecting the actual flattening process, but the desorption of non-flattened TPP molecules from the saturated monolayer. This could imply that the release of free space on the surface (cf. Figure 9.4) is directly linked to the CDH reaction.

In section $III$, the hydrogen desorption can be fitted by first order kinetics $m \approx 1$ and binding energies of $1.5$ eV (2H-TPP) and $2.0$ eV (Ru-TPP), respectively. The values of the TPD spectrum at $0.5\ \mathrm{K\ s^{-1}}$ are very similar to the fitting parameters of the sub- monolayer desorption (see Table 9.2). It may be assumed that the CDH proceeds unrestrictedly in this temperature section, hence is no longer limited by the desorption of adsorbate molecules. This suggests that in this case, enough space for the flattening of the molecule has been provided.

The fitting parameters of section $II$ reflect a transition between the process in section $I$ and section $III$. A clear interpretation of this intermediate state is, however, not possible with the rather simple model which is used for these simulations.

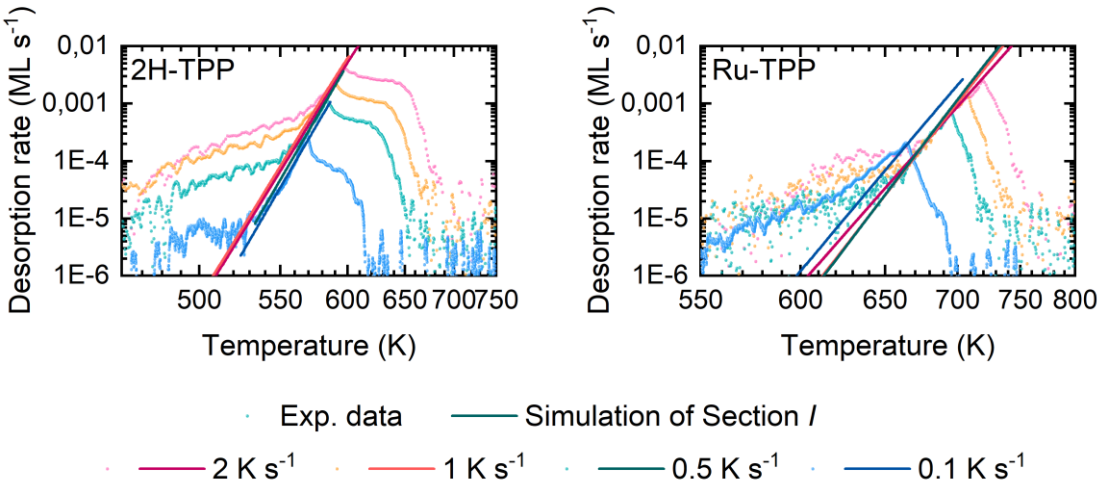


***Figure 9.12*** *Comparison of the carbon signal and the simulated hydrogen desorption (section $I$), which is depicted in Figure 9.11, for 2H-TPP and Ru-TPP. The simulated binding energy $E_B$, represented by the slope of section $I$ in the MS plot, is in very good agreement with the experimental desorption signal of $\frac{m}{z} = 12$. Deviations at low coverages might be due to imperfect preparation of the saturated monolayer or background correction. Deviations around the peak maximum will be discussed in the full model.*

### 9.4.4 Saturated monolayer of 2H-TPP and Ru-TPP – The coherent model

In a more sophisticated approach, which aims to verify the detailed reaction kinetics, a model correlating both desorption processes ($H_2$ and TPP fragment) and covering all three sections (Section 9.4.3), i.e. the full temperature range of desorbing molecules and all conversion processes, is developed. The direct desorption of the adsorbed species as well as the desorption of the hydrogen molecules for the flattening reaction is simulated. All involved rates are modelled according to the Polanyi-Wigner equation with a linear contribution of the temperature (Equation 9.3). The modelling is based on various processes occurring on the surface during heating (Figure 9.14).

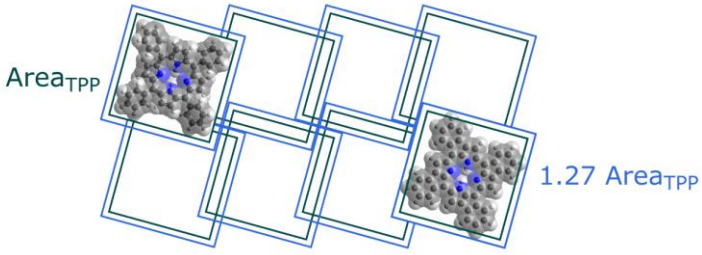


***Figure 9.13*** *Schematic of the different footprints of a 2H-TPP molecule before (green) and after (blue) the CDH. The geometric arrangement fits to the proposed unit cell based on LEED for the initial overlayer (cf. Figure 9.2).*

The adsorbed porphyrin species can be part of four groups depending on their conformation before and after the CDH and the space they have on the surface:

- Molecules with “no space” for the CDH
- Molecules with “little space”, thus, not enough for the CDH
- Molecules with “enough space” for the CDH
- Molecules which are flattened following the CDH reaction.

A compressed layer of intact molecules (termed as “no space” in the model) was prepared on the surface.

A delayed start of the CDH reaction can be observed on the saturated monolayers of 2H-TPP and Ru-TPP compared to the sub-monolayer (Figure 9.5). Something prevents the start of the CDH on the saturated monolayer which does not take place on the sub-monolayer. One reason might be the desorption of intact molecules which is reflected in the carbon desorption. The footprint of a flattened porphyrin is slightly larger than the area of a TPP before the CDH reaction took place (see Figure 9.13). Thus, to make the flattening possible, a desorption of the intact molecule (with rate $r_1$ in the model) is modelled. The desorbing molecules release free space on the surface. Surrounding molecules then can pass to two possible populations: “enough space” in which the CDH reaction can take place without gain of further free area and “little space”. The area, which is attributed to the molecules in this latter population, is larger than before but not large enough for the molecule to be flattened. The rate, i.e. the temperature dependence, of both conversion processes is assumed to be strictly coupled to the desorption of intact molecules and, thus, to the availability of free space on the surface. The mean number of molecules distributing over the remaining area is determined by steric arguments. In the model, the free factors $A$ and $B$ are independent from the coverage and describe the weight of the two reaction channels. The molecules, which have “enough space” (population rate $Br_1$) for the flattening will undergo the CDH

reaction with a conversion rate $r_3$. The excess hydrogen will desorb with the rate $r_{CDH}$, which is equal to the conversion rate $r_3$. The population of "little space" (conversion rate $Ar_1$) gains more area with each desorbing intact molecule. Possibly, an equilibration of space between the molecules within the layer takes place as well. Any process in this context is encompassed in a conversion rate $r_2$, when the actual population of "little space" converts to "enough space". Thus, "little space" is introduced as a temporary buffer to model the assumed evolution in the compressed layer when the temperature raises. Due to the different size of intact and flattened molecules, the process starts with an additional $20\%$ to $30\%$ of molecules on the surface with respect to the coverage of flattened molecules after the CDH reaction. The experimental desorption rates of molecular hydrogen are calibrated to $1$ ML according to the remaining species by integration of the desorbing hydrogen molecules. The model has to reproduce this change which is experimentally known from TP-XPS data and STM measurements [257].

Based on these considerations, the proposed model is schematically illustrated in Figure 9.14.

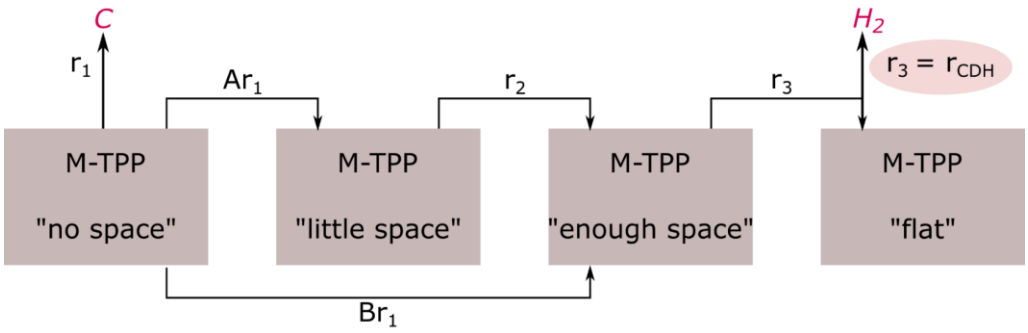


***Figure 9.14*** *Schematic of the proposed model for the CDH reaction. The TPP molecules are subdivided into four groups ("no space", "little space", "enough space" and "flat"). The exchange processes are modelled by the rates $r_1$, $Ar_1$, $Br_1$, $r_2$ and $r_3$. Each $r_x$ is defined according to Equation 5.8. The factors $A$ and $B$ are constant values, representing the proportion of participating molecules. The size of the last group is defined as $1$ ML leading to a higher coverage of not flattened molecules in the "no space" initial situation. The experimentally known number of intact molecules, which desorb directly (measured as desorbing TPP fragment), has to be added. The measured desorption rate of molecular hydrogen is represented and fitted by rate $r_3$ [384].*

As it can be observed in the experimental data, the onset of the peaks (c.f. Figure 9.10) comprises different slopes and thus, different binding energies are involved in the process. The increase of the binding energy close to the maximum of the peak and the sharp drop of the rate at the maximum, which can be observed in the MS plot of the

raw data for all heating rates (Ru-TPP, Figure 9.11 and Figure 9.12), is extremely unusual. This feature cannot be explained by conventional analysis methods or simulations.

At the start of the simulation ($t = 0$), only compressed species, located in the population "no space", exist. The populations "little space", "enough space" and "flat" are empty. Thus, the initial coverage at $t = 0$ is about $1.3$ ML (2H-TPP) and $1.5$ ML (Ru-TPP), referenced to the number of flattened molecules in the population "flat".

The model consists of 11 fitting parameters: orders $m_1$,$m_2$ and $m_3$, pre-exponentials $k^*_{0,1}$, $k^*_{0,2}$ and $k^*_{0,3}$ and binding energies $E_{B,1}$, $E_{B,2}$ and $E_{B,3}$ for the rate equations $r_1$, $r_2$ and $r_3$, respectively, as well as the proportionality factors $A$ and $B$. The factors $A$ and $B$ describe the conversion of molecules to have "little" or "enough" space for the CDH after initial desorption of a molecule. The parameters are varied by the MATLAB optimization routine *fminsearch*. For each simulation, the rate is compared to the experimental data of a single spectrum at a distinct heating rate and is optimized by the minimum of least squares.

**Significance and selectivity of the parameters in the model**

In this full model, some of the fitting parameters are very sensitive to slight changes.

In Figure 9.15, exemplary simulations for 2H-TPP at a heating rate of $0.5\,\mathrm{K\,s^{-1}}$ are depicted varying the fitting parameters by $\pm 10\%$.

Importantly, the simulation results are rather insensitive to the variation of the parameters $m_1$, $m_2$, $k^*_{0,2}$, $E_{B,2}$, $m_3$, $A$ and $B$[75]. In contrast, the parameters $k^*_{0,1}$, $E_{B,1}$, $k^*_{0,3}$ and $E_{B,3}$ induce strong variations of the desorption rate if the values are increased or decreased by $10\%$. Specifically, the maximum of the desorption peak is shifted and the maximum intensity changes.

[75] As population „little space" is hardly filled, the insensitivity is expected. For more details, see below.

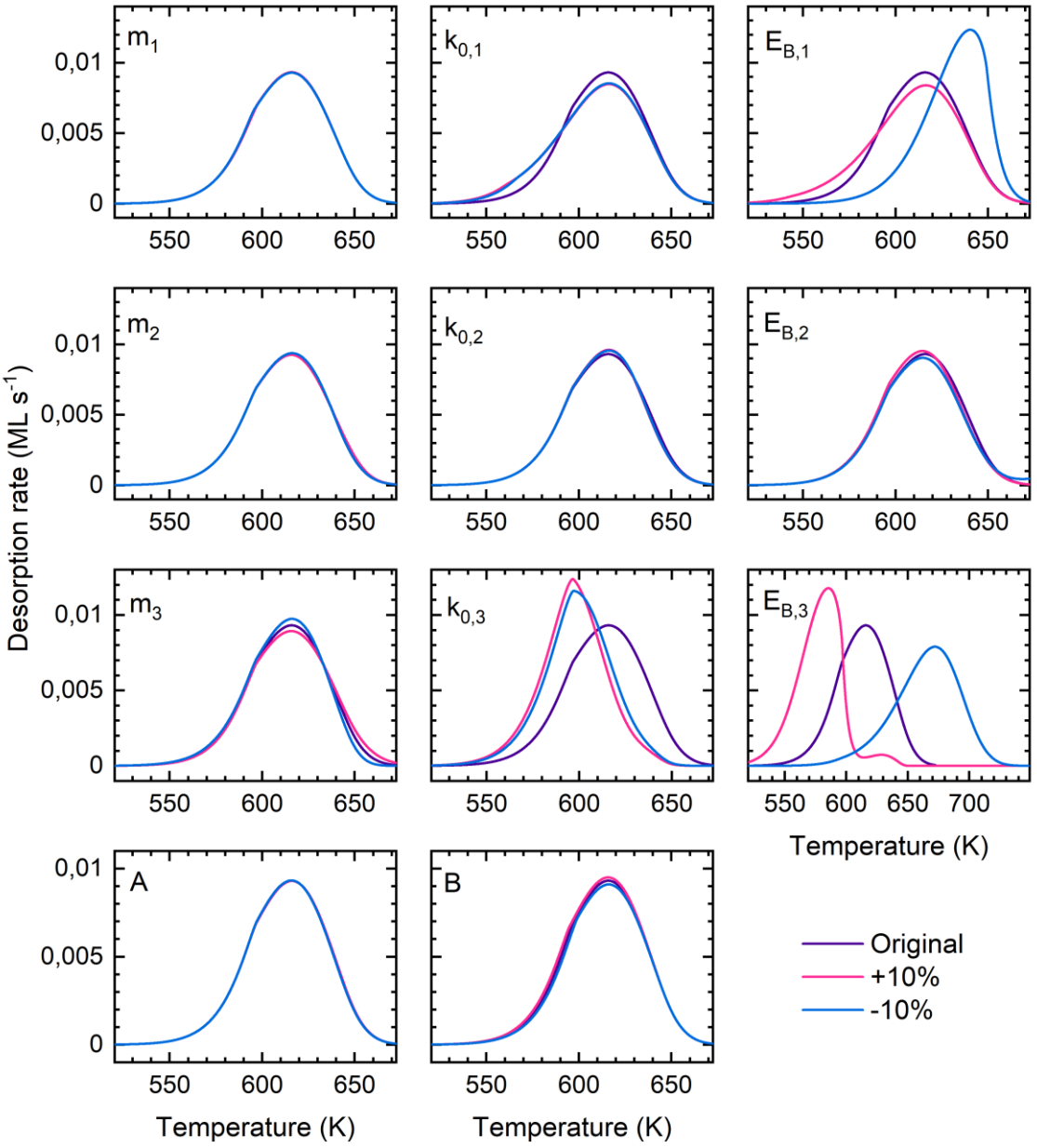


***Figure 9.15*** *Optimized simulations for the full model of Figure 9.14 and effect of* $\pm 10\%$ *variation of fitting parameters based on 2H-TPP TPD spectra at* $0.5\ K\ s^{-1}$*. The observed changes illustrate the sensitivity of the targeted parameters.*

**Simulation results of the full model**

The model is simulated at heating rates of $2\,\mathrm{K\,s^{-1}}$, $1\,\mathrm{K\,s^{-1}}$, $0.5\,\mathrm{K\,s^{-1}}$ and $0.1\,\mathrm{K\,s^{-1}}$ for 2H-TPP and Ru-TPP, corresponding to the experimental data. Figure 9.16 shows the simulations with the best fit for each measurement. Despite the different shapes, the hydrogen desorption peaks of both molecules, 2H-TPP and Ru-TPP, can be simulated by the proposed model with reliabilities (calculated by the deviation per total area of the peak) in the order of $10^{-5}$.

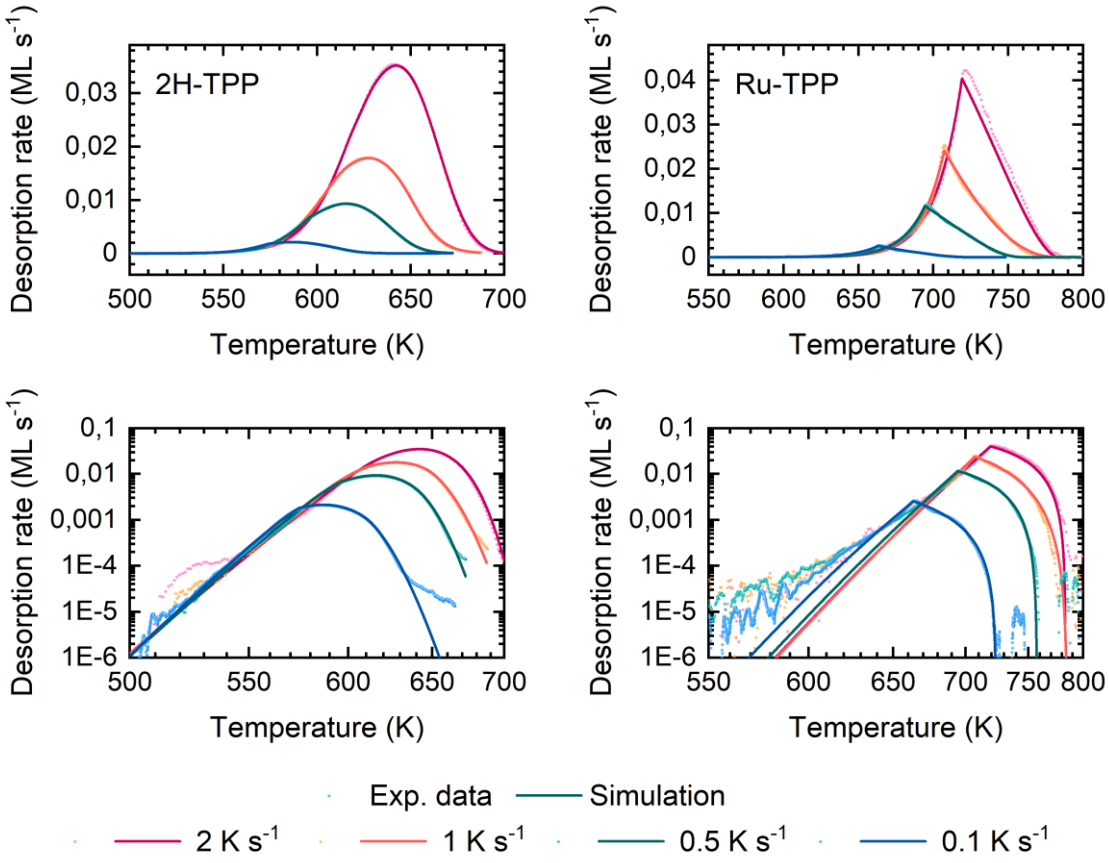


***Figure 9.16*** *Simulations with the best fits and thus, different sets of parameters for each heating rate (see Table 9.3) as linear and MS plot. Experimental data are illustrated as scatter plots, while the simulated data are depicted as line plots. The simulated curves reflect the characteristic onsets and shapes of each data set for both molecules, 2H- TPP and Ru-TPP.*

The resulting fitting parameters $E_{B,1}$, $m_1$, $E_{B,2}$, $m_2$, $E_{B,3}$, $m_3$, $A$ and $B$ are summed up in Table 9.3 and the pre-exponentials $k_{0,1}$, $k_{0,2}$ and $k_{0,3}$ are listed in Table 9.4 for 2H-TPP and Ru-TPP. The simulations for both molecule species are performed with the MATLAB fitting routine (see details in Appendix B.5).

| | $r_1$ | | $r_2$ | | $r_3$ | | | |
|---|---|---|---|---|---|---|---|---|
| **2H-TPP** | $E_{B,1}$ | $m_1$ | $E_{B,2}$ | $m_2$ | $E_{B,3}$ | $m_3$ | $A$ | $B$ |
| 2 K s$^{-1}$ | 0.7eV | 0.4 | 2.0 eV | 0.6 | 1.4 eV | 1.0 | 0.2 | 2 |
| 1 K s$^{-1}$ | 0.7 eV | 0.5 | 2.0 eV | 0.7 | 1.4 eV | 1.1 | 0.2 | 2 |
| 0.5 K s$^{-1}$ | 0.8 eV | 0.3 | 2.1 eV | 0.8 | 1.4 eV | 1.1 | 0.1 | 2 |
| 0.1 K s$^{-1}$ | 0.8 eV | 0.1 | 2.0 eV | 0.6 | 1.5 eV | 1.2 | 0.1 | 2 |
| **Ru-TPP** | | | | | | | | |
| 2 K s$^{-1}$ | 3.0 eV | 0.0 | – – | – – | 0.2 eV | 0.6 | 0 | 2 |
| 1 K s$^{-1}$ | 3.1 eV | 0.0 | – – | – – | 0.1 eV | 0.7 | 0 | 3 |
| 0.5 K s$^{-1}$ | 3.0 eV | 0.0 | – – | – – | 0.1 eV | 0.6 | 0 | 3 |
| 0.1 K s$^{-1}$ | 3.0 eV | 0.0 | – – | – – | 0.1 eV | 0.6 | 0 | 3 |

***Table 9.3*** *Different sets of parameters for each heating rate of the best fit for both porphyrin species, 2H-TPP and Ru-TPP.*

| **2H-TPP** | $k_{0,1}$ | $k_{0,2}$ | $k_{0,3}$ |
|---|---|---|---|
| 2 K s$^{-1}$ | $1.9 \cdot 10^4$ s$^{-1}$ | $1.1 \cdot 10^{14}$ s$^{-1}$ | $1.4 \cdot 10^9$ s$^{-1}$ |
| 1 K s$^{-1}$ | $2.2 \cdot 10^4$ s$^{-1}$ | $4.0 \cdot 10^{13}$ s$^{-1}$ | $1.4 \cdot 10^9$ s$^{-1}$ |
| 0.5 K s$^{-1}$ | $2.2 \cdot 10^4$s$^{-1}$ | $1.8 \cdot 10^{14}$ s$^{-1}$ | $2.3 \cdot 10^9$ s$^{-1}$ |
| 0.1 K s$^{-1}$ | $1.5 \cdot 10^4$ s$^{-1}$ | $6.2 \cdot 10^{14}$ s$^{-1}$ | $2.7 \cdot 10^9$ s$^{-1}$ |
| **Ru-TPP** | | | |
| 2 K s$^{-1}$ | $1.8 \cdot 10^{17}$ s$^{-1}$ | – – | 0.2 |
| 1 K s$^{-1}$ | $5.4 \cdot 10^{17}$ s$^{-1}$ | – – | 0.1 |
| 0.5 K s$^{-1}$ | $2.0 \cdot 10^{17}$ s$^{-1}$ | – – | 0.1 |
| 0.1 K s$^{-1}$ | $5.0 \cdot 10^{17}$s$^{-1}$ | – – | 0.1 |

***Table 9.4*** *Pre-exponential factors of rates $r_1$, $r_2$ and $r_3$, for 2H-TPP and Ru-TPP.*

The quality of the fitting results is different for 2H-TPP and Ru-TPP. This might indicate that the proposed model is not applicable for both porphyrin species in an equal manner. In the simulation and by comparing the hydrogen rates of sub-monolayer and saturated monolayer, it can be observed that the conversion may be related to the onset of the carbon desorption. The desorption rates of sub monolayer and saturated monolayer are not equal and thus, reveal different binding energies, at the same temperature, especially at the beginning of the CDH reaction (Figure 9.5). This leads to the assumption, that there is no equilibrium in the layer on the surface. The simulation of the hydrogen desorption is modelled by two possible pathways ("buffers"). As the value for factor $A$ is (nearly) zero and thus, population "little space" is (almost) always empty, rate $r_2$ has no impact on the desorption. Consequently, rate $r_1$ mainly determines the total desorption rate $r_{CDH}$. The values of $E_{B,1}$ and $k_{0,1}$ (2H-TPP and Ru-TPP) are (slightly) lower than the results of the section model (see Table 9.2), which matches the experimental data. Therefore, rate $r_1$ may not be directly comparable to section $I$ of the section model, which reflects the "local" experimental values for $k_0$ and $E_B$ summed over all processes.

For 2H-TPP, the values of $m_3$ and $E_{B,3}$ are similar to section $III$ of the section model, while the pre-exponentials are lower by a factor of $10$ (cf. Table 9.1). However, the binding energy $E_{B,3}$ of Ru-TPP is very low, also compared to the results of the section model (Table 9.1). Furthermore, the pre-exponential factor $k_{0,3}$ is by a factor of $10^{13}$ lower than expected which might be attributed to the compensation effect (see Section 6.2.2).

According to Knecht et al. [380], the Ru-TPP molecules change the overlayer structure from compressed phase to square phase at about $85\%$ of the initial overlayer which is not directly visible in the experimental data of the TPD measurements. The fit and thus, the coherent model averages the parameters for the falling edge of the desorption in contrast to the parameters for sections $II$ and $III$ of the section model in Section 9.4.3. Upon closer observation (Figure 9.6, especially of the desorption rate at $0.1$ K s$^{-1}$), the shape of the desorption rate changes at about $675$ K[76] which might be due to different desorption kinetics at high temperatures and low coverages tentatively induced by the phase change at $85$ % of the initial coverage or a second process which is limiting the CDH reaction.

[76] This cannot be observed for 2H-TPP.

Experimental data and simulation are in good agreement, but the corresponding fitting parameters show ambiguities in the physical sense. Thus, the model is a good start for the interpretation of the underlying reaction mechanics. However, further investigations are necessary to fully understand the reaction kinetics.

Figure 9.17 depicts the simulation for all heating rates using the parameters that were optimized for $0.5\ \mathrm{K\,s^{-1}}$, instead of simulating each data set with different parameters to achieve the best fit. For both molecules, it can be observed, that there are deviations from the experimental data. For 2H-TPP, the peak maxima of the simulation are shifted towards higher temperatures with respect to the experimental data and with increasing heating rate. In addition, the shape of the peak changes while the area remains similar. For Ru-TPP, the peak temperature is not affected, but the CDH reaction takes place slower and thus, takes longer, the higher the heating rate is. The deviations from the experimental data might be caused by the desorption of intact molecules which shifts the hydrogen desorption peak depending on the heating rates (cf. Figure 9.6). It may be assumed that the temperature dependence varies for different heating rates and that a rearrangement takes place in the layer, i.e., that there is no equilibrium. A rearrangement is suggested at a coverage of about $80\ \%$, related to the amount of TPP fragment at $2\ \mathrm{K\ s^{-1}}$, leading to a slightly different peak shape for 2H-TPP. The total amount of desorbing molecules in the monolayer decreases by a factor of $4$ at low heating rates for 2H-TPP, i.e. a slow process, which takes place in parallel to the CDH, is not visible in the TPD data. This process may be too slow to catch up at high heating rates and, thus, the hydrogen desorption starts with a time delay. For Ru-TPP, this process might be so slow or delayed that it causes a sudden start of the hydrogen desorption leading to the sharp peak. A modified or different model might cover the desorption of both molecules simultaneously with plausible parameters.

As the desorption rates of 2H-TPP and Ru-TPP differ in shape, the coverages of the modelled sub-groups throughout the flattening process are different as well. The simulated coverages and corresponding rates are shown exemplary for $0.5\ \mathrm{K\ s^{-1}}$ in Figure 9.18.

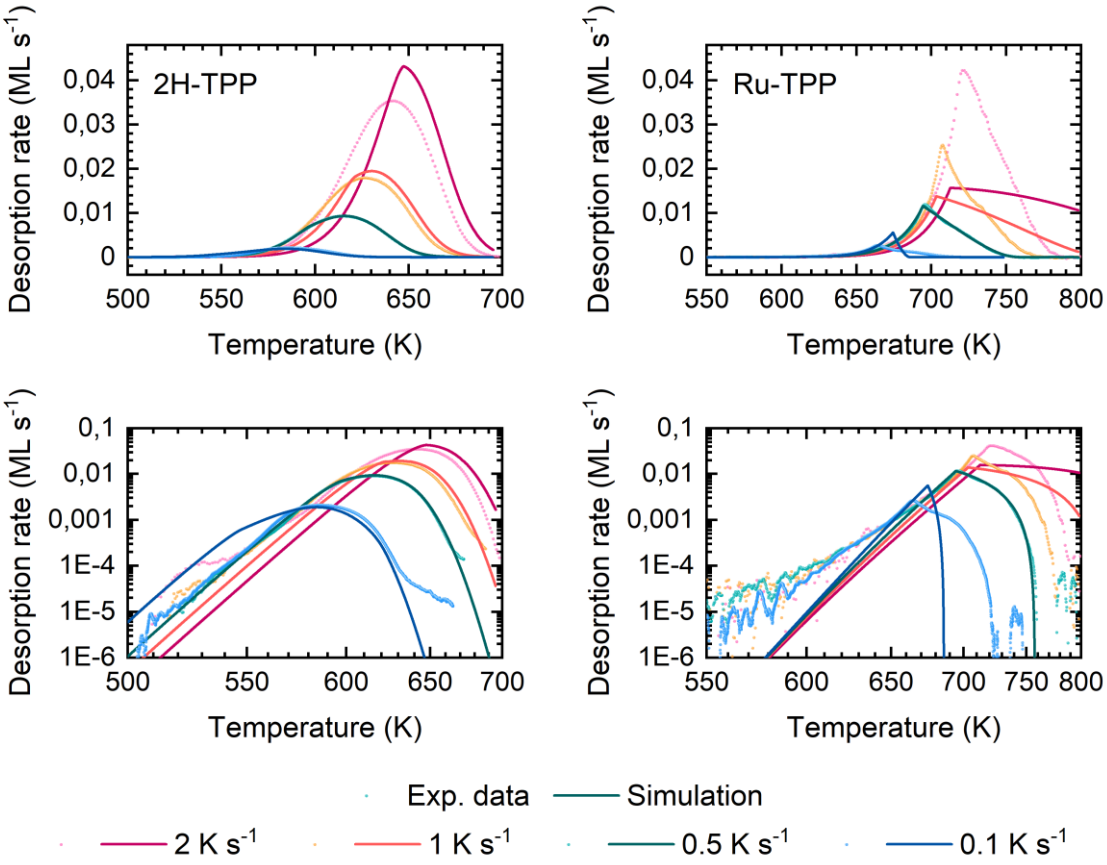


***Figure 9.17*** *Simulation with equal parameters at all heating rates and best fit for* $0.5\ K\ s^{-1}$ *shown as linear and MS plot. Experimental data are depicted as scatter plot and the simulated data as line plots. The deviations from the experimental data indicate processes which are depending on the heating rate (cf. Figure 9.6).*

For 2H-TPP, the initial coverage is $1.49$ ML. $0.49$ ML of the porphyrin species desorb with rate $r_1$ from the surface. As the population "little space" is hardly used leading to $Ar_1 \approx 0$ and $r_2 \approx 0$, mostly all molecules which remain on the surface are transferred in "enough space" with rate $Br_1$. The subgroup "little space" was introduced to model diffusion processes. Hence, a simulation with the suggested model and thus, with the described diffusion does not fit to the experimental data. As a result, either the distribution of the molecules across the surface is not limiting for the CDH reaction or a different model is necessary to be able to describe the diffusion process. At a temperature of $T \approx 600$ K, the population of "no space" has vanished and the group "enough space" has reached its maximum population. Flattened molecules start to evolve at $600$ K ($r_{CDH}$). The CDH reaction is finished at about $660$ K when the coverage of flattened molecules has reached $1$ ML.

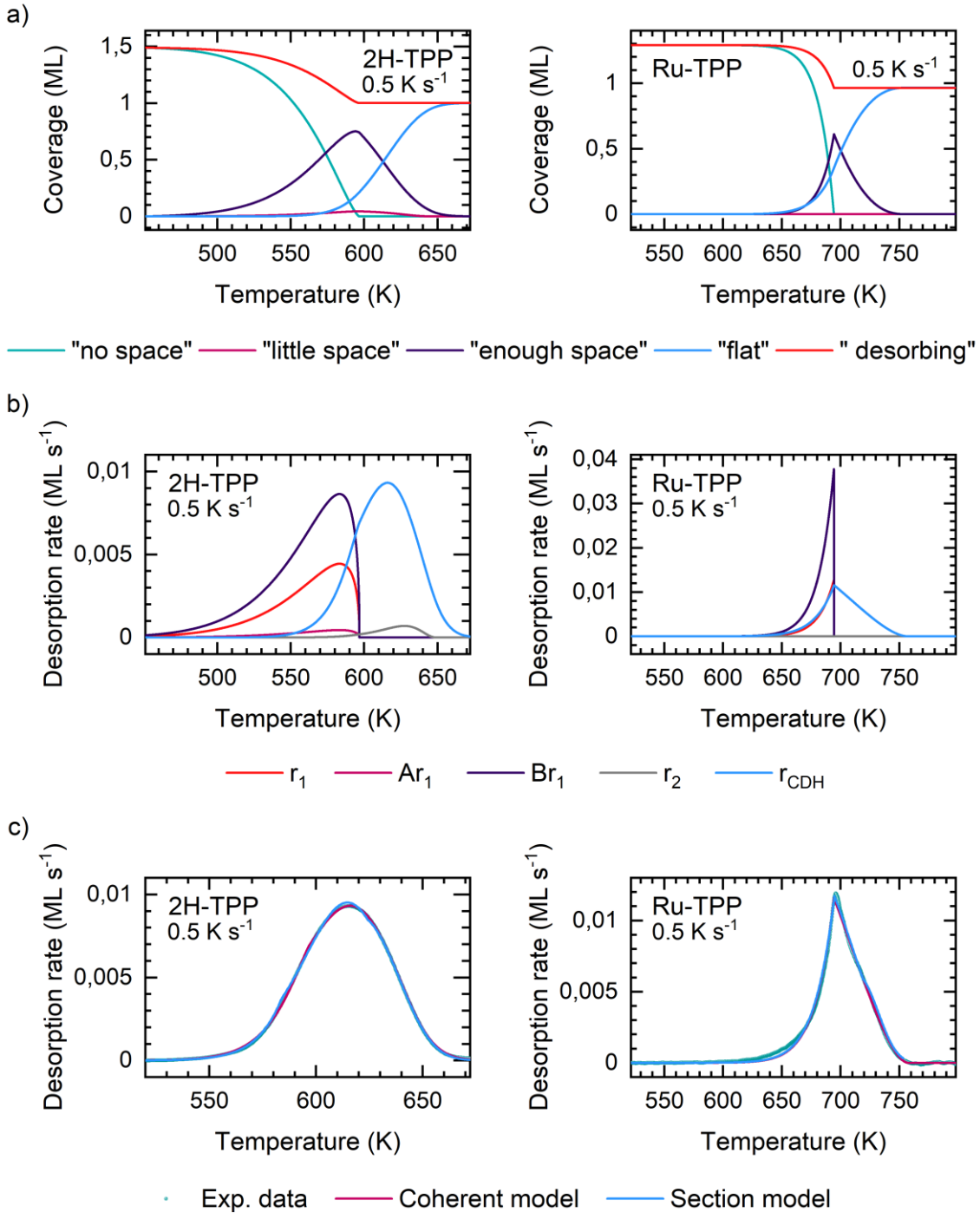


***Figure 9.18*** *a) Simulated coverages of the subgroups „no space" (green), "little space"(red), "enough space" (purple), "flat" (blue) and "desorbing" (orange) of intact molecules throughout the flattening process. b) Simulated rates of* $r_1$ *(orange),* $Ar_1$ *(red),* $Br_1$ *(purple),* $r_2$ *(grey) and* $r_{CDH}$ *(blue) throughout the flattening process. c) Comparison of the section model (blue) and the coherent model (red). Coverages and rates are exemplary shown for a heating rate of* $0.5\ K\ s^{-1}$.

For Ru-TPP, the simulations start with an initial coverage of $1.29$ ML. During the CDH reaction $0.29$ ML of intact molecules are desorbing from the surface with rate $r_1$. The molecules, which do not desorb from the surface, are directly transferred to population "enough space" with rate $Br_2$, as factor $A = 0$ and thus, population "little space" remains empty ($Ar_1 = 0$ and consequently, $r_2 = 0$) throughout the CDH reaction. While the population of "no space" has vanished, the maximum population of "enough space" is reached at a temperature of $T \approx 700$ K. The evolution of flattened molecules ($r_{CDH}$) starts at about $700$ K and finishes at about $740$ K, reaching $1$ ML.

The simulated desorption of the TPP fragment takes place around $560$ K (2H-TPP) and $690$ K (Ru-TPP) which is in the same range (difference about $20$ K for 2H-TPP) as seen in the experimental data (Figure B.6). Furthermore, a similar shift of the TPP fragment desorption to high temperatures with increasing heating rate can be observed as stated by the experimental data.

The most prominent difference between 2H-TPP and Ru-TPP is the shape of the "enough space" coverage. According to the populations of the subgroups "enough space" and "desorbing" and the simulation of the hydrogen desorption with the same parameters for all heating rates, the desorption of intact molecules directly affects the actual CDH reaction. This desorption of intact porphyrin species seems to be demanding for the actual flattening to take place. Furthermore, the CDH reaction processes of Ru-TPP on Ag(111) are faster than 2H-TPP according to the coverage plots. This might be a further indication for the proposed slow process which hampers the CDH reaction for saturated monolayers.

Rate $r_1$ describes the desorption of intact TPP molecules as well as the transitions to populations "little space" and "enough space" which are assumed to be proportional to the TPP desorption. Thus, in the coherent model, desorption and diffusion processes are coupled. DFT calculations by Rojas et al. [385] suggest a binding energy of $0.44$ eV and a diffusion barrier of $32$ meV for 2H-TPP on Ag(111). These values are lower than the binding energy $E_{B,1}$ resulting from the coherent model. The deviations might be explained by the low pre-exponential factor (compensation effect), even if a lower pre-exponential factor might be expected as many molecules have to move simultaneously. STM measurements show that diffusion takes place during the CDH reaction as the porphyrin overlayer is ordered prior to the CDH reaction which changes to an unordered overlayer after the CDH reaction. A different model, which considers diffusion and desorption processes separately without assuming a proportionality, might help to

simulate the flattening of the porphyrin species. The intramolecular interaction and the interaction of the molecules with the surface may depend on the central moiety of the metallo-porphyrin. Thus, the desorption energy of intact molecules and the diffusion energy on the surface might be dependent on the temperature. This processes may then hamper the flattening of the porphyrin species while the activation energy of the CDH reaction might be independent from the temperature.

## 9.5 Conclusion

Experimental data and simulations show that the central moiety influences the kinetics associated with molecular hydrogen desorption and CDH of TPP species. Deduced from the sub-monolayers and saturated monolayers of 2H-TPP and Ru-TPP, the interaction with the surface seems to be higher for Ru-TPP than for 2H-TPP molecules and the CDH reaction progresses faster. According to Buchner et al. [372], the intermolecular interactions and not the central moiety determines the supramolecular ordering of TPP species on Ag(111). However, this seems not to be true for Ru-TPP as the saturation layer has two phases [380] and thus, is different from that of the other TPPs. The interaction of the central moiety of the porphyrin with the underlying support may still influence the effects which are mediated by the substrate [385]. In this regard, the Ru(0) and Ti(II) moieties are expected to interact more strongly with the silver substrate than the 2H moiety and the oxidizing the Ti metal centre (Ti(IV), cf. [377]) would weaken the interaction reflecting the trend of $T_{CDH}$ (cf. Equation 9.2)). The intermolecular interactions between the TPP molecules are supposed to be T-type interactions [370, 372]. These are reported to influence the self-assembly on Ag(111) at RT [372] and thus, may be responsible for the different desorption rates.

The underlying mechanisms of the CDH reaction may be hampered by the desorption of porphyrin species and diffusion processes on the surface. The energies of these processes might be temperature dependent, which shifts the hydrogen desorption to higher temperatures for increasing heating rates. In addition, the simulation with the section model shows that the CDH reaction seems to be correlated to the desorption of intact molecules. Thus, it is assumed that there is no equilibrium in the layer during the CDH reaction of a saturated monolayer.

The coherent model tries to correlate the $\frac{m}{z} = 2$ and $\frac{m}{z} = 12$ desorption including diffusion processes on the surface due to available free space after the desorption of intact molecules. However, the results show that the model does not sufficiently describe the diffusion processes, tentatively, as they are assumed to be strongly coupled to the desorption of intact molecules with a distinct factor. In the experimental data of the saturated monolayers, a shift of the hydrogen spectra with respect to the carbon spectra can be observed depending on different heating rates, resulting in a delayed start of the CDH reaction with increasing heating rates. Furthermore, in contrast to Ru-TPP, the heating rate variation of 2H-TPP reveals, that the amount of TPP fragment is increasing with increasing heating rate. This might indicate that Ru-TPP is in a non-equilibrium situation at even higher temperatures than 2H-TPP. The effect may also be observed by the different peak temperatures of the porphyrin species. In the simulations an equilibrium is assumed in all populations. However, as the data sets of heat rate and coverage variation indicate a non-equilibrium situation on the surface, this leads to an inconsistency between simulation and experiment. Thus, the fitting parameters of the saturated monolayers are not very reliable and the presented models are not sufficient to completely describe the flattening process yet.

It might be assumed that the CDH reaction proceeds in a similar way, but shifted in temperature, for both TPP species. Thus, with a correct model, it might be, that the CDH reaction of both, 2H-TPP and Ru-TPP, can be modelled.

# 10 Conclusion and Outlook

Different biomolecules – spermine, insulin and pUC19 - were investigated regarding ionization, charge states, deposition and adsorption properties Furthermore, desorption and reaction kinetics of organic molecules – BPA and DES, different M- TPPs – were analysed by qualitative simulations based on the Polanyi-Wigner equation.

With the current ES-CIBD system as a valuable tool to deposit molecules, which are non-sublimable, various biomolecules ranging from $200$ Da to $1.7$ MDa could be deposited successfully. The investigated molecules spermine, insulin and pUC19 serve as representatives for the most common ionization models IEM, CRM and CEM, respectively. A high intensity of the ion beam (up to $2.2$ nA) during the deposition allows for fast sample production, typically below $1-2$ h. For a clean deposition, the ion beam is purified with the dQMS. The time integral of the deposited current combined with the size and charge state of the molecules gives information on the coverage of the sample surface.

The selection of the solvent for the electrospray turned out to be a challenge. The composition of the solution always needs to be tailored for the specific analyte molecule. It has to be capable of dissolving the molecule and to meet requirements on vaporization and charging carrier. Acidic and basic components are added to deliver necessary electrical conductivity. Factors such as surface tension, density, viscosity, vapour pressure and electrical permittivity and conductivity have to be accounted for in order to provide a solution with high ionization efficiency and a stable ion current of the desired analytes.

The analysis of the mass-to-charge ratios allows to verify the chemical stability of the analyte as well as the composition of the spray regarding charge states, formation of oligomers or complexes with adducts.

The subsequent investigations using STM reveal clean depositions without detectable impurities of residual gas, solvent molecules or in most cases fragmented ions. Furthermore, the molecules remain in their native states showing both coordinated and uncoordinated behaviours. Structural analysis indicates intermolecular coordination with hydrogen bridges in the case of spermine, the presence of monomers and dimers for insulin, and the existence of different conformations such as supercoiled, double stranded and single-stranded DNA as well as dimeric or even oligomeric molecules.

In further investigations, the range of biomolecules such as other proteins or DNA variants (e.g., oligomers of ds or ssDNA, DNA origami, nucleotides) might be tested. The home-built ES-CIBD system, which was used for the experiments, is in a stage of development. The performed experiments are mainly pilot experiments. Systematic approaches might be performed e.g., using different deposition energies in the regime of reactive landing. Experiments for Zn-coordination of insulin [154] in order to build hexamers could be realized by subsequent and simultaneous deposition. Furthermore, the fibrillation of insulin [386] might be investigated *in-situ* or *in vitro* with subsequent deposition.

The combination of various experimental techniques, such as temperature programmed desorption (TPD), X-ray photoelectron spectroscopy (XPS) and STM, was used for the comprehensive characterization of physical and chemical phenomena on the surface.
The sequential thermal evolution of Diethylstilbestrol (DES) and Bisphenol A (BPA) on Cu(111) from self-assembled overlayer to branched molecular chains could be revealed. TPD measurements show a complete deprotonation of the terminal hydroxyl groups. The first deprotonation step is assumed to be followed by enol-keto tautomerization mediated C-H activation at the carbon atoms in ortho-position [51]. This leads to a subsequent ortho-ortho coupling of neighbouring molecules in a second step. Both, BPA and DES, have almost identical reaction behaviours as observed by TPD, TP-XPS and STM measurements. A third reaction process occurs at different temperatures for BPA and DES and shows a hydrogen desorption accompanied by the desorption of water. This indicates a chemical modification of the polymeric chains, which is associated with the formation of C-O-C bridges and C-C bonds within the disordered polymers. Simulating the TPD spectra by a classical Polanyi-Wigner equation reveals the orders and binding energies for the reaction steps. Furthermore, conversion temperatures could be extracted from the O $1s$ XP spectra.
The cyclodehydrogenation of various metallo-tetraphenylporphyrins (M-TPP) was investigated by TPD and TP-XPS experiments which reveal desorption features of hydrogen and carbon. Different approaches are used to simulate the underlying reaction mechanics. While the sub-monolayer coverages of 2H-TPP and Ru-TPP could be described by a classical Polanyi-Wigner equation, the flattening processes seems to be more complicated in the case of a saturated monolayer. In contrast to the sub-monolayers, a desorption peak of $\frac{m}{z} = 12$ and a change of the C $1s$ signal could be

observed for saturated monolayers, which was attributed to the desorption of intact molecules due to lack of space on the surface for the CDH reaction. The simulation with the section model shows correlations of the hydrogen desorption (saturated monolayer) to both, the desorption of carbon and thus, the desorption of intact molecules (section I) and the kinetics of the hydrogen desorption (sub-monolayer, section III). With a more sophisticated coherent model including the desorption of intact molecules and diffusion processes, the desorption kinetics of molecular hydrogen are simulated. According to the results of the simulation, the diffusion of TPP molecules on the surface, which was assumed to occur due to free available space, seems to be negligible for the flattening process. Furthermore, while the simulation results for 2H-TPP fit to the experimental data, the results for Ru-TPP are less reliable, as it does not completely follow the descending flank of the experimental data. To conclude, the presented model is a new approach of simulating desorption processes and provides basic insights into the reaction mechanism of the CDH. However, it is not yet predicting the real kinetics. For further investigations, the model needs to be adjusted or a new model has to be designed to fully describe the flattening process of both TPP species in the simulation algorithm.

# Appendix A

## A.1 $Lk$ concept

Supercoiling is not one pre-defined state of the DNA, i.e. a single numerical definition, and thus, not strictly or unambiguously predictable. The geometric parameters depend on formation and extend of secondary spirals. This dependency is described by the concept of linking number $Lk$. The linking number is the sum of twists $Tw$ (windings of two single-strands around each other to form a double helix) and writhes $Wr$ (windings of the double helix around itself forming supercoiled structures):

$$Lk = Tw + Wr. \tag{10.1}$$

The linking number is usually defined by the number of total base pairs and base pairs per turn (see DNA Forms Section 2.6.1) $Lk = \frac{bp_{total}}{bp_{turn}}$. For pUC19 is about $256$ and its supercoiling structure was simulated by MD [387].

If the double-strand is relaxed, i.e. there are no secondary spirals of the helix which is expressed as $Wr = 0$, $Lk$ is equal to the number of twists $Tw$ of the helix. In natural circular DNA strands, the number of twists is almost always lower than in the relaxed DNA. This results in negative supercoiling. The decrease of twists is balanced by writhes $Wr$. The relationship of $Lk$, $Tw$ and $Wr$ is demonstrated by an example in Figure 10.1. The writhes define the number of intersection in the DNA helix. While the values for $Tw$ and $Wr$ change, the value for $Lk$ remains constant. For this reason, the circular DNA molecules with a given linking number can have various combinations of twists and writhes and therefore different structures [134, 388].

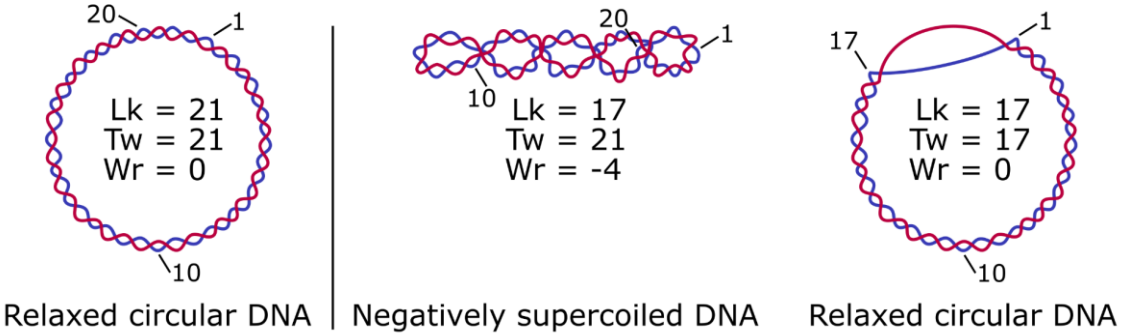


***Figure 10.1*** *Illustration of linking number $Lk$, twist $Tw$ and writhe $Wr$. On the left side, a relaxed circular DNA with 21 helical turns ($Tw$) and thus, a linking number of $Lk = 21$ is shown. The twist of this unconstrained planar circle is $Tw = 21$ while the writhe is $Wr = 0$. Unwinding of $4$ helical turns (e.g., by topoisomerase treatment) results in a lower $Lk$ and can produce two topological forms: a relaxed helical ring with a partially "melted" region (right panel), which reflects the former $4$ twists, or a negatively supercoiled conformation (middle) with an identical number of twists, compensated by additional $4$ negatively oriented writhes. The latter is preferred by energetic states.*

# A.2 Displacement of DNA strands on Ag(111)

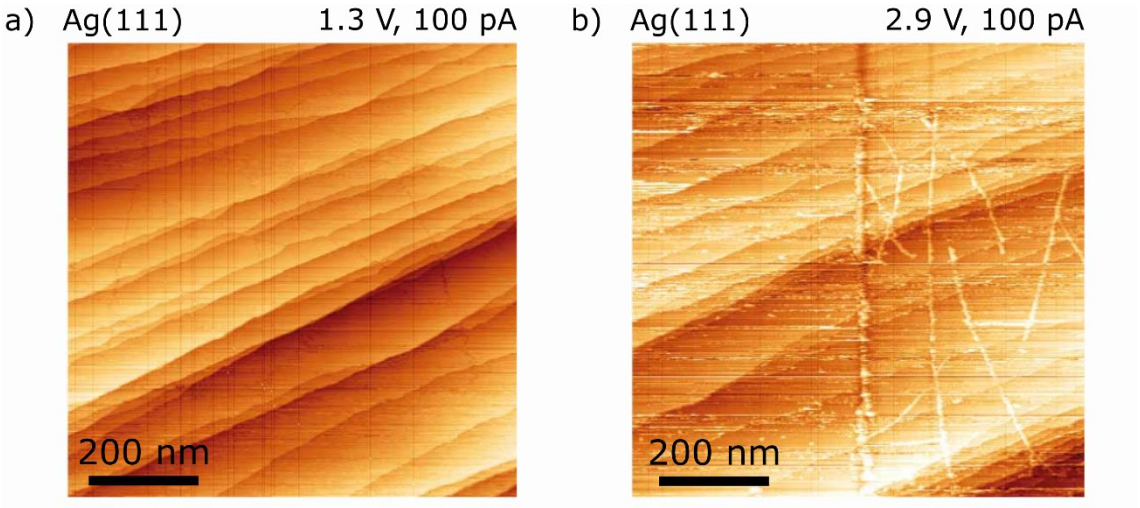


***Figure 10.2*** *Displacement of DNA stands caused by STM tip.*

# A.3 STM: distortion of scanner

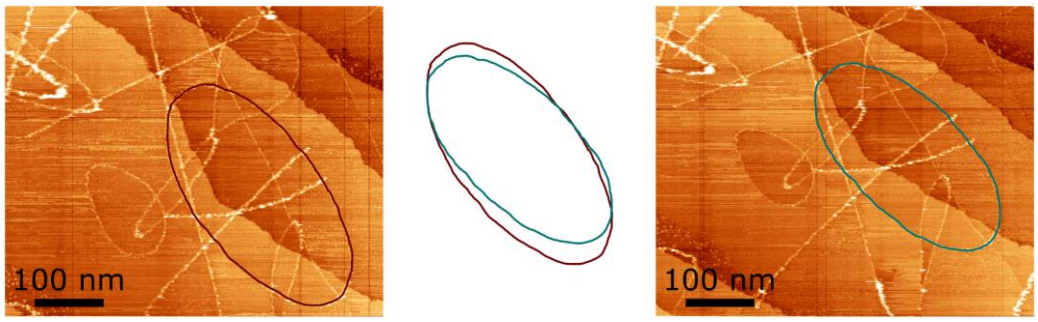


***Figure 10.3*** *Visualization of the distortion of the STM scanner.*

# Appendix B

## B.1 LEED pattern of BPA/Cu(111) and DES/Cu(111)

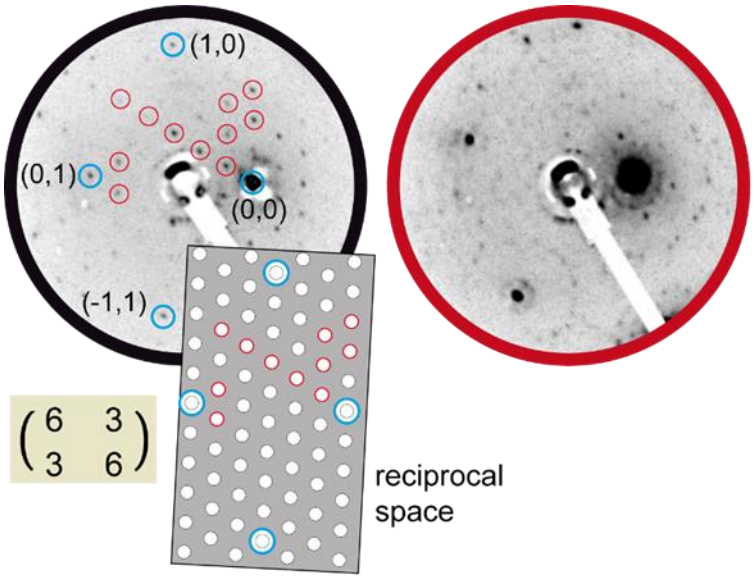


***Figure B.1*** *LEED pattern of DES/Cu(111) (left, black edging) and BPA/Cu(111) (right, red edging) after annealing to* $380$ *K and* $340$ *K for* $5$ *min, respectively. Both images are taken at* $E_p = 70$ *eV and* $T_{sample} \approx 85$ *K. For DES the reciprocal lattice pattern is shown: it corresponds to a commensurate superstructure with matrix* $\begin{pmatrix} 6 & 3 \\ 3 & 6 \end{pmatrix}$*. Encircled diffraction spots (red: superstructure; blue: integer spots) underline the correspondence between the experimental and simulated pattern (adopted from [340]).*

## B.2 TPD ($H_2$, $H_2O$, CO, $O_2$ and $CO_2$) of BPA/Cu(111) and DES/Cu(111)

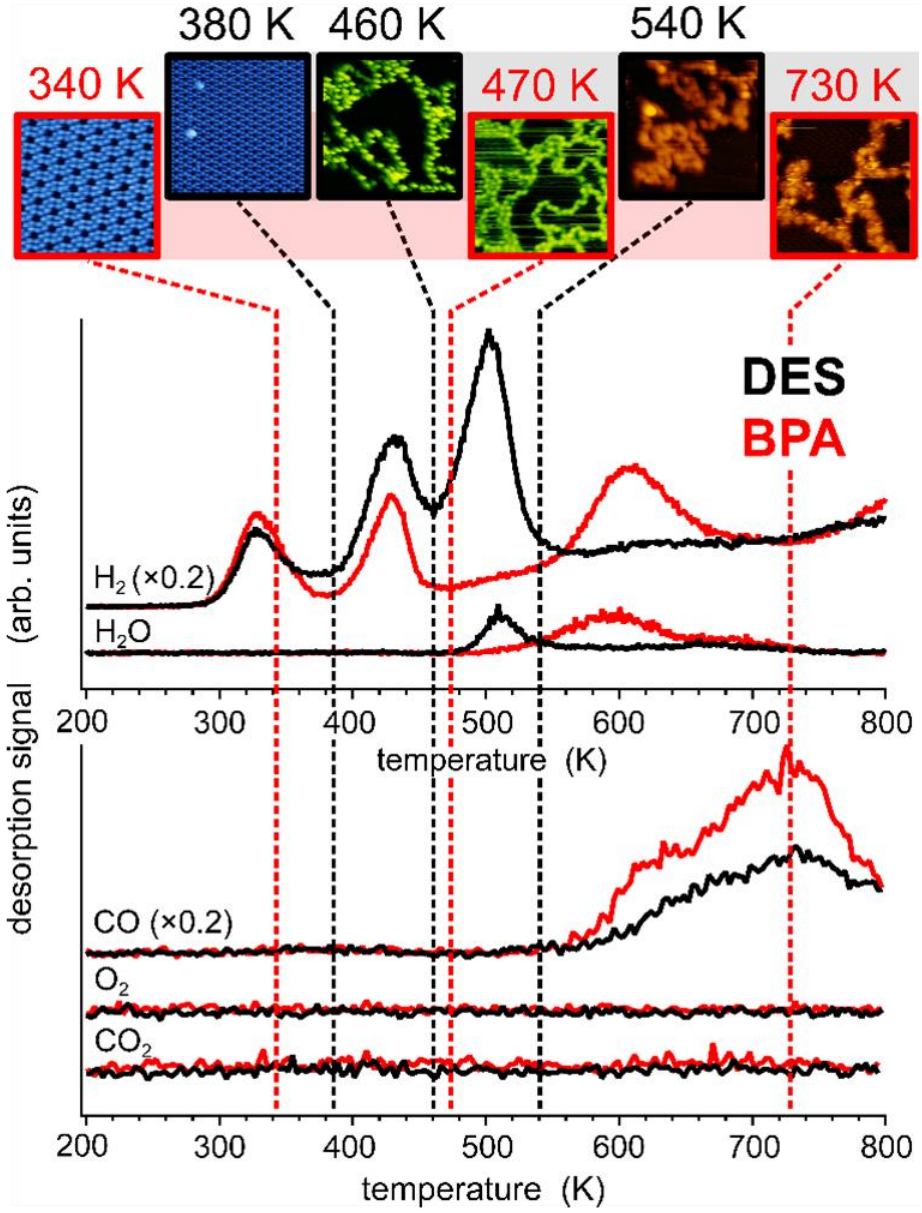


***Figure B.2*** *TPD measurements of DES/Cu(111) (black) and BPA/Cu(111) (red) after molecular deposition onto the sample held at* $200\ K$ *and with a heating rate of* $0.5\ K\ s^{-1}$*. The* $H_2$ *(*$\frac{m}{z} = 2$*) and CO (*$\frac{m}{z} = 28$*) signals were scaled down by a factor* $0.2$ *and the curves are vertically stacked for clarity. Note that quantitative comparison of the intensities of top and bottom TPD curves is not possible, as different control electronics of the mass spectrometer were used in order to cover two different mass ranges. The STM images of Figure 8.4 are shown in the insets to facilitate data interpretation (adopted from [340]).*

# B.3 Proposed reaction sequence of DES/Cu(111)

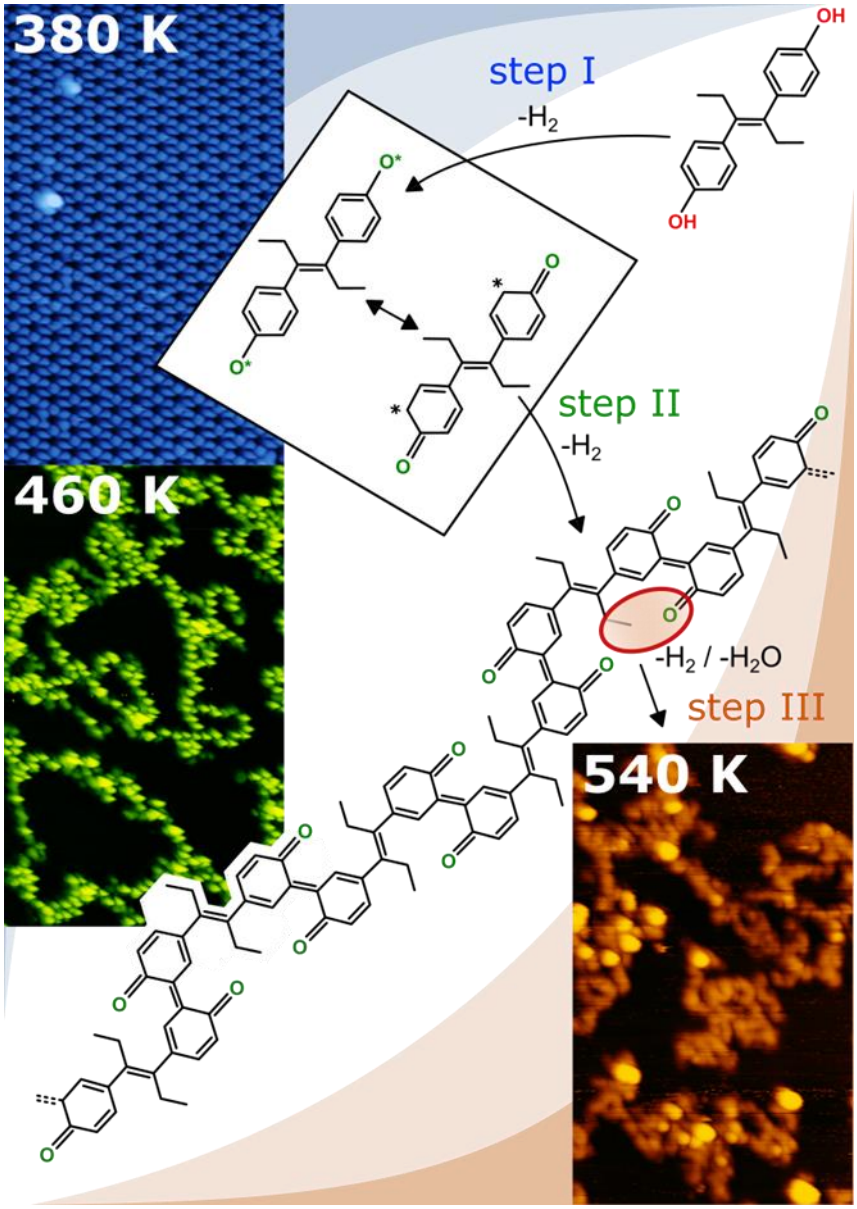


***Figure B.3*** *Proposed sequence of thermally activated chemical reactions of DES on Cu(111): tentative (simplified) structural models along with the corresponding STM images from Figure 8.4 (due to the complexity of the system, no structural model is presented for the outcome of step III) (adopted from [340]).*

## B.4 Matlab code - Example: Simulation of the sub-monolayer (Ru-TPP)

```
clear all;
close all;

global Start End HeatRate TempData IntDataNormPeak n0 TempStep

%details (for generating file name)
molecule = 'RuTPP';
mass = '2';
HeatRate = 0.5;

%-------locations--------
%location of Matlab file
filePath = 'D:\Documents\MATLAB\TPD\Porphyrins\';
%location of data
dataPath = 'D:\Documents\Data\TPD\Daten_norm\';
%adds path of file location to enable functions;
addpath(genpath(filePath));
folder = molecule;

%-------parameters-----------
%normalization factor for H2 desorption; coverage of flat molecules
n0 = 0.57;
%temperature at which peak starts
StartTemp = 590.3;
%temperature at which peak ends
EndTemp = 750;
%initial value for order
OrderPeak = 1;
%initial value for pre-exponential
Preexponential = exp(20.15);
%initial value for binding energy
BindingE = 21000;
%turn fit on and off
Fit = 1; %0: simulation with initial values; 1: simulation using fminsearch

%--------generating array for inital values---------
initial = [OrderPeak Preexponential BindingE];

for a = 1:length(mass) %loop in the case of more than one spectrum
    %--------load data--------
    fileID = fopen(char(strcat(dataPath,folder,'\',molecule,'_',mass(a), ...
        '_', num2str(HeatRate),'Ks_',num2str(n0),'ML.txt')),'r');
    formatSpec = '%f %f %f';
    sizeData = [2 Inf];
    data = fscanf(fileID,formatSpec,sizeData);
    fclose(fileID);

    %--------separate data--------
    % exp. temperature array
    TempData = data(1,:);
    % exp. intensity array
    IntDataNormPeak = data(2,:);
    Intensity(a,:) = IntDataNormPeak(1,:);
    % reciprocal exp. temperature array
    RezTempData = TempData.^(-1);

    %----calculation of temp.&time step, start and end of the peak----
    % initial temperature in K
    InitTemp = TempData(1);
    TempDiff = zeros(1,length(TempData)-1);
```

```
    for i = 2:length(TempData)
        TempDiff(i-1) = TempData(i)-TempData(i-1);
    end

    TempStep = mean(TempDiff);
    TimeStep = TempStep/HeatRate;

    Start = round(1+length(TempData)/(TempData(end)-InitTemp) ...
        *(StartTemp(a)-InitTemp));
    End = round(1+length(TempData)/(TempData(end)-InitTemp) ...
        *(EndTemp(a)-InitTemp));
    StartPeak = Start;
    EndPeak = End;
end

%--------plotting experimental data--------
f = figure;
plot(TempData,IntDataNormPeak(1,:),'Color','[0 0.4470 0.7410]')
set(gca,'XMinorTick','on','YMinorTick','on', 'FontSize', 11)
axis([TempData(1) TempData(length(TempData)) -Inf Inf])
title(char(strcat(molecule,'- ',num2str(HeatRate),' K/s')))
xlabel('Temperature [K]')
ylabel('Desorption rate [ML/s]')
dim = [.15 .57 .3 .3];
set(gcf,'units','centimeters','position',[10,10,13,7])
set(f,'Visible','Off')

%-------start fitting--------
%Options for fitting routine
options = optimset('Display','iter','MaxIter',5000,'MaxFunEvals',5000, ...
    'TolFun',1e-12, 'TolX',1e-12);

%-----lower and upper bounds for the constrained fitting routine------
%lb = [0.95*initial(1) 0 0.5*initial(3)];
%ub = [1.05*initial(1) Inf 1.5*initial(3)];

if Fit == 1
    disp('start fitting...')
    %give init.values and options to optimization routine fminsearch
    paropt = fminsearch(@objective,initial,options);
    %constrained optimization routine fmincon fitting routine
    %paropt = fmincon(@objective,initial,[],[],[],[],lb,ub);
else
    paropt = initial;
end

%------new temperature array for simulation-------------
%temperature array for simulation
TempSim = (TempData(1):TempStep/10:TempData(end));
%reciprocal temperature
RezTempSim = TempSim.^(-1);
%time array for simulation
TimeSim = (TempSim-TempSim(1))/HeatRate;
%calculation of time and temperature step
TimeDiffSim = zeros(1,length(TimeSim)-1);
TempDiffSim = zeros(1,length(TempSim)-1);

for i = 2:length(TimeSim)
    TimeDiffSim(i-1) = TimeSim(i)-TimeSim(i-1);
    TempDiffSim(i-1) = TempSim(i)-TempSim(i-1);
end

TimeStepSim = mean(TimeDiffSim);
TempStepSim = mean(TempDiffSim);

%--------starting point and ending point of simulation--------
StartSim = round(1+length(TempSim)/(TempSim(end)-TempSim(1)) ...
```

```
    *(StartTemp-TempSim(1)));
EndSim = round(1+length(TempSim)/(TempSim(end)-TempSim(1)) ...
    *(EndTemp-TempSim(1)));
TempSimPeak = TempSim(StartSim:EndSim);

%--------simulation model with optimized parameters-------
%-----pre-definitions-----
Coverage = zeros(1,length(StartSim(1):EndSim(1)));
Rate     = zeros(1,length(StartSim(1):EndSim(1)));

Order = paropt(1);
Preexp = paropt(2);
Ebind = paropt(3);

%-----actual simulation-----
for k = 1 : length(StartSim(1):EndSim(1))
    if k == 1
        %initial coverage
        Coverage(1,k) = n0;

        %rate of the simulation;
        Rate(1,k) = Coverage(1,k)^Order*TempSim(StartSim(1)+k-1)*Preexp...
            *exp(-Ebind/(TempSim(StartSim(1)+k-1)));
    else

        %coverages of the peak after initial step
        Coverage(1,k) = Coverage(1,k-1)-Rate(1,k-1)*TempStepSim/HeatRate;

        %constraints for coverages
        if Coverage(1,k) < 0
            Coverage(1,k) = 0;
        end

        %rates of the peak after initial step
        Rate(1,k) = Coverage(1,k)^Order*TempSim(StartSim(1)+k-1)*Preexp...
            *exp(-Ebind/(TempSim(StartSim(1)+k-1)));
    end
end

%area under the curves (experimental & simulated) for testing reasons
AreaData = sum(IntDataNormPeak)*TempStep/HeatRate;
AreaSim = sum(Rate)*TempStepSim/HeatRate;

%--------plotting of simulated coverages--------
figure;
plot(TempSim(StartSim(1):EndSim(1)),Coverage)
xlabel('Temperature [K]');
ylabel('Coverage [ML]');

%--------log plot of simulated rates--------
figure;
plot(RezTempData(Start(1):End(1)),IntDataNormPeak(Start(1):End(1)), ...
    RezTempSim(StartSim(1):EndSim(1)),Rate)
set(gca,'yscale','log');
set(gca,'XDir','Reverse');
xt=int16(xticks.^(-1));
set(gca,'xticklabel',xt)
axis([-inf inf 10e-6 inf]);
h=legend('Data','Rate','Rate1','Rate2','Rate3','Rate4');
set(h,'Location','best')
xlabel('Temperature [K]');
ylabel('Intensity [ML/s]');

%--------linear plot of simulated rates--------
f=figure;
plot(TempData(Start(1):End(1)),IntDataNormPeak(Start(1):End(1)), ...
```

```
    TempSim(StartSim(1):EndSim(1)),Rate)
axis([-inf inf 10e-6 inf]);
h=legend('Data','Rate','Rate1','Rate2','Rate3','Rate4');
set(h,'Location','best')
xlabel('Temperature [K]');
ylabel('Intensity [ML/s]');
%set(f,'Visible','Off');

%--------optimized parameters vs. initial parameters--------
%round optimized parameters
paropt_save = round(paropt,2);
initial_log = [initial(1) log(initial(2)) initial(3)];
paropt_log = [paropt(1) log(paropt(2)) paropt(3)];
compare = [initial_log;paropt_log;initial_log./paropt_log];

%--------result array for export to origin--------
origin_rate_exp = [TempData(Start:End)' IntDataNormPeak(Start:End)'];
origin_rate_sim = [TempSim(StartSim:EndSim)' Rate'];
origin_coverage = [TempSim(StartSim:EndSim)' Coverage'];

%--------objective function for optimization routine--------
function [J,coverage,rate] = objective(par)
    global Start End HeatRate TempData IntDataNormPeak n0 TempStep

    %--------pre-definitions--------
    lenPeak   = length(Start(1):End(1));
    beta      = HeatRate;
    temp      = TempData;
    intensity = IntDataNormPeak(1,Start(1):End(1));

    coverage = zeros(1,lenPeak);
    rate     = zeros(1,lenPeak);

    order = par(1);
    preexp = par(2);
    ebind = par(3);

    for k = 1 : lenPeak
        if k == 1
            %initial coverages
            coverage(1,k) = n0;

            %calculations of corresponding rates
            rate(1,k) = coverage(1,k)^order*temp(Start(1)+k-1)*preexp...
                *exp(-ebind/(temp(Start(1)+k-1)));

        else
            %coverages of the simulation after initial step
            coverage(1,k) = coverage(1,k-1)-rate(1,k-1)*TempStep/beta;

            %constraints for coverages
            if coverage(1,k) < 0
                coverage(1,k) = 0;
            end

            %rates of the simulation
            rate(1,k) = coverage(1,k)^order*temp(Start(1)+k-1)*preexp...
                *exp(-ebind/(temp(Start(1)+k-1)));
        end
    end

    %optimization criterion: least square optimization
    res(1) = sum((rate(1,:)-intensity(1,:)).^2);
    res = res./beta;
    J = sum(res);
end
```

## B.5 Matlab code - Example: Simulation of saturated monolayer (Ru-TPP)

```
clear all;
close all;

global Start End HeatRate TempData IntDataNormPeak n0 TempStep Excess

%details (for generating file name)
molecule = 'RuTPP';
mass = '2';
HeatRate = 0.5;

%-------locations--------
%location of Matlab file
filePath = 'D:\Documents\MATLAB\TPD\Porphyrins\';
%location of data
dataPath = 'D:\Documents\Data\TPD\Daten_norm\';
%adds path of file location to enable functions;
addpath(genpath(filePath));
folder = molecule;

%-------parameters-----------
%normalization factor for H2 desorption; coverage of flat molecules
n0 = 1;
%coverage of desorbing TPP species
Excess = 0.19;

%temperature at which peak starts
StartTemp = 521.7;
%temperature at which peak ends
EndTemp = 798;
%initial values for orders
OrderPeak = [0.01 0.1  1.4];
%initial values for pre-exponentials
Preexponential = [exp(40.45) exp(23.27) exp(22.466)];
%initial values for binding energies
BindingE = [29472 23557 22810];
%initial values for proportionality factors A and B
Factor = [3 2];
%turn fit on and off
Fit = 0; %0: simulation with initial values; 1: simulation using fminsearch

%--------generating array for inital values---------
initial = [OrderPeak(1) Preexponential(1) BindingE(1) OrderPeak(2)...
       Preexponential(2) BindingE(2) OrderPeak(3) Preexponential(3) ...
       BindingE(3) Factor(1) Factor(2)];

for a = 1:length(mass) %loop in the case of more than one spectrum
    %--------load data--------
    fileID = fopen(char(strcat(dataPath,folder,'\', molecule,'_',mass(a), ...
        '_', num2str(HeatRate),'Ks_',num2str(n0),'ML.txt')),'r');
    formatSpec = '%f %f %f';
    sizeData = [2 Inf];
    data = fscanf(fileID,formatSpec,sizeData);
    fclose(fileID);

    %--------separate data--------
    % exp. temperature array
    TempData = data(1,:);
    % exp. intensity array
    IntDataNormPeak = data(2,:);
    Intensity(a,:) = IntDataNormPeak(1,:);
```

```
    % reciprocal exp. temperature array
    RezTempData = TempData.^(-1);

    %----calculation of temp.&time step, start and end of the peak----
    % initial temperature in K
    InitTemp = TempData(1);
    TempDiff = zeros(1,length(TempData)-1);
    for i = 2:length(TempData)
        TempDiff(i-1) = TempData(i)-TempData(i-1);
    end

    TempStep = mean(TempDiff);
    TimeStep = TempStep/HeatRate;

    Start = round(1+length(TempData)/(TempData(end)-InitTemp) ...
        *(StartTemp(a)-InitTemp));
    End = round(1+length(TempData)/(TempData(end)-InitTemp) ...
        *(EndTemp(a)-InitTemp));
    StartPeak = Start;
    EndPeak = End;
end

%--------plotting experimental data--------
f = figure;
plot(TempData,IntDataNormPeak(1,:),'Color','[0 0.4470 0.7410]')
set(gca,'XMinorTick','on','YMinorTick','on', 'FontSize', 11)
axis([TempData(1) TempData(length(TempData)) -Inf Inf])
title(char(strcat(molecule,'- ',num2str(HeatRate),' K/s')))
xlabel('Temperature [K]')
ylabel('Desorption rate [ML/s]')
dim = [.15 .57 .3 .3];
set(gcf,'units','centimeters','position',[10,10,13,7])
set(f,'Visible','Off')

%-------start fitting--------
%Options for fitting routine
options = optimset('Display','iter','MaxIter',5000,'MaxFunEvals',5000, ...
 'TolFun',1e-12, 'TolX',1e-12);

%-----lower and upper bounds for the constrained fitting routine------
%lb = [0.95*initial(1) 0 0.5*initial(3) 0.8*initial(4) 0 0.8*initial(6) ...
%    -Inf -Inf];
%ub = [1.05*initial(1) Inf 1.5*initial(3) 1.2*initial(4) Inf ...
%    1.2*initial(6) Inf Inf];

if Fit == 1
    disp('start fitting...')
    %give init.values and options to optimization routine fminsearch
    paropt = fminsearch(@objective,initial,options);
    %constrained optimization routine fmincon fitting routine
    %paropt = fmincon(@objective,initial,[],[],[],[],lb,ub);
else
    paropt = initial;
end

%------new temperature array for simulation-------------
%temperature array for simulation
TempSim = (TempData(1):TempStep/10:TempData(end));
%reciprocal temperature
RezTempSim = TempSim.^(-1);
%time array for simulation
TimeSim = (TempSim-TempSim(1))/HeatRate;
%calculation of time and temperature step
TimeDiffSim = zeros(1,length(TimeSim)-1);
TempDiffSim = zeros(1,length(TempSim)-1);

for i = 2:length(TimeSim)
```

```
    TimeDiffSim(i-1) = TimeSim(i)-TimeSim(i-1);
    TempDiffSim(i-1) = TempSim(i)-TempSim(i-1);
end

TimeStepSim = mean(TimeDiffSim);
TempStepSim = mean(TempDiffSim);

%--------starting point and ending point of simulation--------
StartSim = round(1+length(TempSim)/(TempSim(end)-TempSim(1)) ...
    *(StartTemp-TempSim(1)));
EndSim = round(1+length(TempSim)/(TempSim(end)-TempSim(1)) ...
    *(EndTemp-TempSim(1)));
TempSimPeak = TempSim(StartSim:EndSim);

%--------simulation model with optimized parameters-------
%-----pre-definitions-----
CoverageKeinPlatz   = zeros(1,length(StartSim(1):EndSim(1)));
CoverageGenugPlatz   = zeros(1,length(StartSim(1):EndSim(1)));
CoverageBisschenPlatz   = zeros(1,length(StartSim(1):EndSim(1)));
CoverageFlach   = zeros(1,length(StartSim(1):EndSim(1)));
Rate1       = zeros(1,length(StartSim(1):EndSim(1)));
Rate2       = zeros(1,length(StartSim(1):EndSim(1)));
Rate3       = zeros(1,length(StartSim(1):EndSim(1)));
Rate4       = zeros(1,length(StartSim(1):EndSim(1)));
Rate5       = zeros(1,length(StartSim(1):EndSim(1)));
Rate6       = zeros(1,length(StartSim(1):EndSim(1)));
Rate       = zeros(1,length(StartSim(1):EndSim(1)));

OrderKeinPlatz  = paropt(1);
PreexpKeinPlatz = paropt(2);
EbindKeinPlatz  = paropt(3);
OrderBisschenPlatz  = paropt(4);
PreexpBisschenPlatz = paropt(5);
EbindBisschenPlatz  = paropt(6);
OrderGenugPlatz  = paropt(7);
PreexpGenugPlatz = paropt(8);
EbindGenugPlatz  = paropt(9);
FactorA = paropt(10);
FactorB = paropt(11);

%-----actual simulation-----
for k = 1 : length(StartSim(1):EndSim(1))
    %initial coverages of simulation and all subgroups;
    if k == 1
        CoverageKeinPlatz(1,k) = n0(1)+Excess;
        CoverageBisschenPlatz(1,k) = 0;
        CoverageGenugPlatz(1,k) = 0;
        CoverageFlach(1,k) = 0;

        %rates of the simulation;
        Rate1(1,k) = CoverageKeinPlatz(1,k)^OrderKeinPlatz...
            *TempSim(StartSim(1)+k-1)*PreexpKeinPlatz...
            *exp(-EbindKeinPlatz/(TempSim(StartSim(1)+k-1)));
        Rate2(1,k) = FactorA*Rate1(1,k);
        Rate3(1,k) = FactorB*Rate1(1,k);
        Rate4(1,k) = CoverageBisschenPlatz(1,k)^OrderBisschenPlatz...
            *TempSim(StartSim(1)+k-1)*PreexpBisschenPlatz...
            *exp(-EbindBisschenPlatz/(TempSim(StartSim(1)+k-1)));
        Rate5(1,k) = CoverageGenugPlatz(1,k)^OrderGenugPlatz...
            *TempSim(StartSim(1)+k-1)*PreexpGenugPlatz...
            *exp(-EbindGenugPlatz/(TempSim(StartSim(1)+k-1)));
        Rate6(1,k) = Rate5(1,k);

        Rate(1,k) = Rate6(1,k);
    else
```

```
        %coverages of the peak after initial step
        CoverageKeinPlatz(1,k) = CoverageKeinPlatz(1,k-1) ...
            -(Rate1(1,k-1)*TempStepSim/HeatRate)-(Rate2(1,k-1) ...
            *TempStepSim/HeatRate)-(Rate3(1,k-1) ...
            *TempStepSim/HeatRate);
        CoverageBisschenPlatz(1,k) = CoverageBisschenPlatz(1,k-1) ...
            +(Rate2(1,k-1)*TempStepSim/HeatRate)-(Rate4(1,k-1) ...
            *TempStepSim/HeatRate);
        CoverageGenugPlatz(1,k) = CoverageGenugPlatz(1,k-1) ...
            +(Rate3(1,k-1)*TempStepSim/HeatRate)+(Rate4(1,k-1) ...
            *TempStepSim/HeatRate)-(Rate5(1,k-1)*TempStepSim...
            /HeatRate);
        CoverageFlach(1,k) = CoverageFlach(1,k-1)+(Rate5(1,k-1) ...
            *TempStepSim/HeatRate);

        %constraints for coverages
        if CoverageKeinPlatz(1,k) < 0
            CoverageKeinPlatz(1,k) = 0;
        end
        if CoverageBisschenPlatz(1,k) < 0
            CoverageBisschenPlatz(1,k) = 0;
        end
        if CoverageGenugPlatz(1,k) < 0
            CoverageGenugPlatz(1,k) = 0;
        end
        if CoverageFlach(1,k) < 0
            CoverageFlach(1,k) = 0;
        end

        %rates of the peak after initial step
        Rate1(1,k) = CoverageKeinPlatz(1,k)^OrderKeinPlatz...
            *TempSim(StartSim(1)+k-1)*PreexpKeinPlatz...
            *exp(-EbindKeinPlatz/(TempSim(StartSim(1)+k-1)));
        Rate2(1,k) = FactorA*Rate1(1,k);
        Rate3(1,k) = FactorB*Rate1(1,k);
        Rate4(1,k) = CoverageBisschenPlatz(1,k)^OrderBisschenPlatz...
            *TempSim(StartSim(1)+k-1)*PreexpBisschenPlatz...
            *exp(-EbindBisschenPlatz/(TempSim(StartSim(1)+k-1)));
        Rate5(1,k) = CoverageGenugPlatz(1,k)^OrderGenugPlatz...
            *TempSim(StartSim(1)+k-1)*PreexpGenugPlatz...
            *exp(-EbindGenugPlatz/(TempSim(StartSim(1)+k-1)));
        Rate6(1,k) = Rate5(1,k);

        Rate(1,k) = Rate6(1,k);
    end
end

%area under the curves (experimental & simulated) for testing reasons
AreaData = sum(IntDataNormPeak)*TempStep/HeatRate;
AreaSim = sum(Rate)*TempStepSim/HeatRate;

%--------plotting of simulated coverages--------
figure;
plot(TempSim(StartSim(1):EndSim(1)),CoverageKeinPlatz, ...
    TempSim(StartSim(1):EndSim(1)),CoverageBisschenPlatz,...
    TempSim(StartSim(1):EndSim(1)),CoverageGenugPlatz, ...
    TempSim(StartSim(1):EndSim(1)),CoverageFlach)
h=legend('CoverageKeinPlatz', 'CoverageBisschenPlatz', ...
    'CoverageGenugPlatz', 'CoverageFlach');
set(h,'Location','best')
xlabel('Temperature [K]');
ylabel('Coverage [ML]');

%--------log plot of simulated rates--------
figure;
plot(RezTempData(Start(1):End(1)),IntDataNormPeak(Start(1):End(1)), ...
    RezTempSim(StartSim(1):EndSim(1)),Rate)
```

```
hold on
plot(RezTempSim(StartSim(1):EndSim(1)),Rate1)
plot(RezTempSim(StartSim(1):EndSim(1)),Rate2)
plot(RezTempSim(StartSim(1):EndSim(1)),Rate3)
plot(RezTempSim(StartSim(1):EndSim(1)),Rate4)
hold off
set(gca,'yscale','log');
set(gca,'XDir','Reverse');
xt=int16(xticks.^(-1));
set(gca,'xticklabel',xt)
axis([-inf inf 10e-6 inf]);
h=legend('Data','Rate','Rate1','Rate2','Rate3','Rate4');
set(h,'Location','best')
xlabel('Temperature [K]');
ylabel('Intensity [ML/s]');

%--------linear plot of simulated rates--------
f=figure;
plot(TempData(Start(1):End(1)),IntDataNormPeak(Start(1):End(1)), ...
    TempSim(StartSim(1):EndSim(1)),Rate)
hold on
% plot(RezTempSim(StartSim(1):EndSim(1)),Rate1)
% plot(RezTempSim(StartSim(1):EndSim(1)),Rate2)
% plot(RezTempSim(StartSim(1):EndSim(1)),Rate3)
% plot(RezTempSim(StartSim(1):EndSim(1)),Rate4)
hold off
axis([-inf inf 10e-6 inf]);
h=legend('Data','Rate','Rate1','Rate2','Rate3','Rate4');
set(h,'Location','best')
xlabel('Temperature [K]');
ylabel('Intensity [ML/s]');
%set(f,'Visible','Off');

%--------optimized parameters vs. initial parameters--------
%round optimized parameters
paropt_save = round(paropt,2);
initial_log = [initial(1) log(initial(2)) initial(3) initial(4) ...
    log(initial(5)) initial(6) initial(7) log(initial(8)) ...
    initial(9) initial(10) initial(11)];
paropt_log = [paropt(1) log(paropt(2)) paropt(3) paropt(4) ...
    log(paropt(5)) paropt(6) paropt(7) log(paropt(8)) ...
    paropt(9) paropt(10) paropt(11)];
compare = [initial_log;paropt_log;initial_log./paropt_log];

%--------result array for export to origin--------
origin_rate_exp = [TempData(Start:End)' IntDataNormPeak(Start:End)'];
origin_rate_sim = [TempSim(StartSim:EndSim)' Rate' Rate1' Rate2'...
    Rate3' Rate4'];
origin_coverage = [TempSim(StartSim:EndSim)' CoverageKeinPlatz'...
    CoverageBisschenPlatz' CoverageGenugPlatz' CoverageFlach'];

%--------objective function for optimization routine--------
function [J,coverageKeinPlatz,coverageBisschenPlatz,coverageGenugPlatz, ...
    coverageFlach, rate1,rate3,rate] = objective(par)

    global Start End HeatRate TempData IntDataNormPeak n0 TempStep Excess

    %--------pre-definitions--------
    lenPeak   = length(Start(1):End(1));
    beta      = HeatRate;
    temp      = TempData;
    intensity = IntDataNormPeak(1,Start(1):End(1));

    coverageKeinPlatz   = zeros(1,lenPeak);
    coverageGenugPlatz   = zeros(1,lenPeak);
    coverageBisschenPlatz   = zeros(1,lenPeak);
```

```
coverageFlach   = zeros(1,lenPeak);
rate1       = zeros(1,lenPeak);
rate2       = zeros(1,lenPeak);
rate3       = zeros(1,lenPeak);
rate4       = zeros(1,lenPeak);
rate5       = zeros(1,lenPeak);
rate6       = zeros(1,lenPeak);
rate       = zeros(1,lenPeak);

orderKeinPlatz  = par(1);
preexpKeinPlatz = par(2);
ebindKeinPlatz  = par(3);
orderBisschenPlatz  = par(4);
preexpBisschenPlatz = par(5);
ebindBisschenPlatz  = par(6);
orderGenugPlatz  = par(7);
preexpGenugPlatz = par(8);
ebindGenugPlatz  = par(9);
factorA = par(10);
factorB = par(11);

for k = 1 : lenPeak
    if k == 1
        %initial coverages
        coverageKeinPlatz(1,k) = n0(1)+Excess;
        coverageBisschenPlatz(1,k) = 0;
        coverageGenugPlatz(1,k) = 0;
        coverageFlach(1,k) = 0;

        %calculations of corresponding rates
        rate1(1,k) = coverageKeinPlatz(1,k)^orderKeinPlatz...
            *temp(Start(1)+k-1)*preexpKeinPlatz...
            *exp(-ebindKeinPlatz/(temp(Start(1)+k-1)));
        rate2(1,k) = factorA*rate1(1,k);
        rate3(1,k) = factorB*rate1(1,k);
        rate4(1,k) = coverageBisschenPlatz(1,k)^orderBisschenPlatz...
            *temp(Start(1)+k-1)*preexpBisschenPlatz...
            *exp(-ebindBisschenPlatz/(temp(Start(1)+k-1)));
        rate5(1,k) = coverageGenugPlatz(1,k)^orderGenugPlatz...
            *temp(Start(1)+k-1)*preexpGenugPlatz...
            *exp(-ebindGenugPlatz/(temp(Start(1)+k-1)));
        rate6(1,k) = rate5(1,k);

        rate(1,k) = rate6(1,k);

    else
        %coverages of the simulation after initial step
        coverageKeinPlatz(1,k) = coverageKeinPlatz(1,k-1) ...
            -(rate1(1,k-1)*TempStep/beta)-(rate2(1,k-1)*TempStep/beta) ...
            -(rate3(1,k-1)*TempStep/beta);
        coverageBisschenPlatz(1,k) = coverageBisschenPlatz(1,k-1) ...
            +(rate2(1,k-1)*TempStep/beta)-(rate4(1,k-1)*TempStep/beta);
        coverageGenugPlatz(1,k) = coverageGenugPlatz(1,k-1) ...
            +(rate3(1,k-1) *TempStep/beta)+(rate4(1,k-1)*TempStep/beta)...
            -(rate5(1,k-1)*TempStep/beta);
        coverageFlach(1,k) = coverageFlach(1,k-1)+(rate5(1,k-1) ...
            *TempStep/beta)-(rate6(1,k-1)*TempStep/beta);

        %constraints for coverages
        if coverageKeinPlatz(1,k) < 0
            coverageKeinPlatz(1,k) = 0;
        end
        if coverageBisschenPlatz(1,k) < 0
            coverageBisschenPlatz(1,k) = 0;
        end
        if coverageGenugPlatz(1,k) < 0
            coverageGenugPlatz(1,k) = 0;
```

```
            end
            if coverageFlach(1,k) < 0
                coverageFlach(1,k) = 0;
            end

            %rates of the simulation
            rate1(1,k) = coverageKeinPlatz(1,k)^orderKeinPlatz...
                *temp(Start(1)+k-1)*preexpKeinPlatz*exp(-ebindKeinPlatz...
                /(temp(Start(1)+k-1)));
            rate2(1,k) = factorA*rate1(1,k);
            rate3(1,k) = factorB*rate1(1,k);
            rate4(1,k) = coverageBisschenPlatz(1,k)^orderBisschenPlatz...
                *temp(Start(1)+k-1)*preexpBisschenPlatz...
                *exp(-ebindBisschenPlatz/(temp(Start(1)+k-1)));
            rate5(1,k) = coverageGenugPlatz(1,k)^orderGenugPlatz...
                *temp(Start(1)+k-1)*preexpGenugPlatz*exp(-ebindGenugPlatz...
                /(temp(Start(1)+k-1)));
            rate6(1,k) = rate5(1,k);

            rate(1,k) = rate6(1,k);
        end
    end

    %optimization criterion: least square optimization
    res(1) = sum((rate(1,:)-intensity(1,:)).^2);
    res = res./beta;
    J = sum(res);
End
```

## B.6 Simulated coverages and experimental integrated desorption rate of 2H-TPP and Ru-TPP

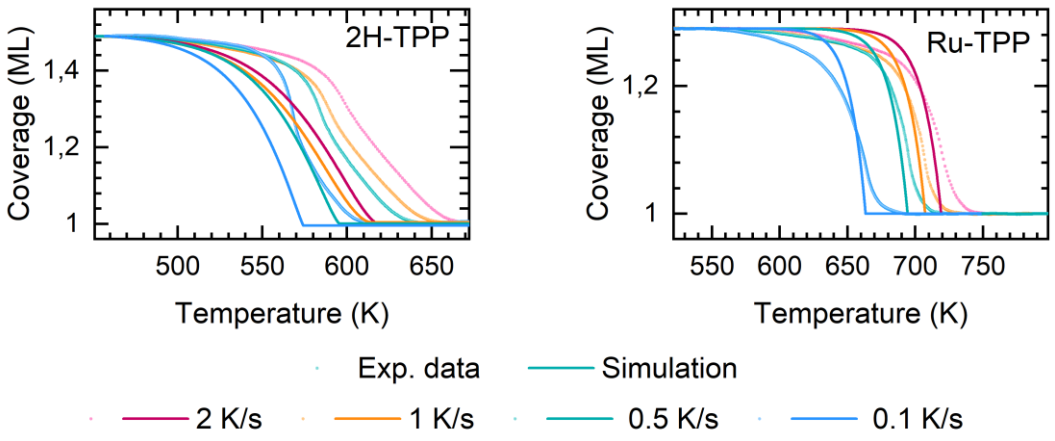


***Figure B.4*** *Experimental integrated desorption rates (scatter) and simulated coverages of desorbing molecules (line) of 2H-TPP and Ru-TPP for all heating rates. While a shift of about 20 K between experiment and simulation can be observed for 2H-TPP, the simulated and experimental coverages for Ru-TPP mostly differ in shape.*

# Bibliography


[1] C. B. Duke, *Proceedings of the National Academy of Sciences of the United States of America* **2003**, *100 (7)*, 3858 – 3864. DOI: 10.1073/pnas.0730358100.

[2] Binnig, Quate, Gerber, *Physical review letters* **1986**, *56 (9)*, 930 – 933. DOI: 10.1103/physrevlett.56.930.

[3] G. Binnig, H. Rohrer, C. Gerber, E. Weibel, *Appl. Phys. Lett.* **1982**, *40 (2)*, 178 – 180. DOI: 10.1063/1.92999.

[4] A. Biswas, I. S. Bayer, A. S. Biris, T. Wang, E. Dervishi, F. Faupel, *Advances in colloid and interface science* **2012**, *170 (1-2)*, 2 – 27. DOI: 10.1016/j.cis.2011.11.001.

[5] M. R. Wasielewski, *Chemical Reviews* **1992**, *92 (3)*, 435 – 461. DOI: 10.1021/cr00011a005.

[6] D. Gerster, J. Reichert, H. Bi, J. V. Barth, S. M. Kaniber, A. W. Holleitner, I. Visoly-Fisher, S. Sergani, I. Carmeli, *Nature nanotechnology* **2012**, *7 (10)*, 673 – 676. DOI: 10.1038/nnano.2012.165.

[7] S. Mathew, A. Yella, P. Gao, R. Humphry-Baker, B. F. E. Curchod, N. Ashari-Astani, I. Tavernelli, U. Rothlisberger, M. K. Nazeeruddin, M. Grätzel, *Nature Chem* **2014**, *6 (3)*, 242 – 247. DOI: 10.1038/nchem.1861.

[8] J. H. Burroughes, D. D. C. Bradley, A. R. Brown, R. N. Marks, K. Mackay, R. H. Friend, P. L. Burns, A. B. Holmes, *Nature* **1990**, *347 (6293)*, 539 – 541. DOI: 10.1038/347539a0.

[9] A. Endo, M. Ogasawara, A. Takahashi, D. Yokoyama, Y. Kato, C. Adachi, *Advanced materials (Deerfield Beach, Fla.)* **2009**, *21 (47)*, 4802 – 4806. DOI: 10.1002/adma.200900983.

[10] Y. Shirai, A. J. Osgood, Y. Zhao, K. F. Kelly, J. M. Tour, *Nano letters* **2005**, *5 (11)*, 2330 – 2334. DOI: 10.1021/nl051915k.

[11] T. Kudernac, N. Ruangsupapichat, M. Parschau, B. Maciá, N. Katsonis, S. R. Harutyunyan, K.-H. Ernst, B. L. Feringa, *Nature* **2011**, *479 (7372)*, 208 – 211. DOI: 10.1038/nature10587.

[12] G. A. Somorjai, Y. Li, *Proceedings of the National Academy of Sciences of the United States of America* **2011**, *108 (3)*, 917 – 924. DOI: 10.1073/pnas.1006669107.

[13] K. Zhou, Y. Li, *Angewandte Chemie (International ed. in English)* **2012**, *51 (3)*, 602 – 613. DOI: 10.1002/anie.201102619.

[14] K. Qadir, S. H. Joo, B. S. Mun, D. R. Butcher, J. R. Renzas, F. Aksoy, Z. Liu, G. A. Somorjai, J. Y. Park, *Nano letters* **2012**, *12 (11)*, 5761 – 5768. DOI: 10.1021/nl303072d.

[15] J. Liu, F. R. Lucci, M. Yang, S. Lee, M. D. Marcinkowski, A. J. Therrien, C. T. Williams, E. C. H. Sykes, M. Flytzani-Stephanopoulos, *J. Am. Chem. Soc.* **2016**, *138 (20)*, 6396 – 6399. DOI: 10.1021/jacs.6b03339.

[16] H.-J. Freund, *J. Am. Chem. Soc.* **2016**, *138 (29)*, 8985 – 8996. DOI: 10.1021/jacs.6b05565.

[17] M. D. Marcinkowski, M. T. Darby, J. Liu, J. M. Wimble, F. R. Lucci, S. Lee, A. Michaelides, M. Flytzani-Stephanopoulos, M. Stamatakis, E. C. H. Sykes, *Nature Chem* **2018**, *10 (3)*, 325 – 332. DOI: 10.1038/nchem.2915.

[18] R. Purrello, S. Gurrieri, R. Lauceri, *Coordination Chemistry Reviews* **1999**, *190-192*, 683 – 706. DOI: 10.1016/S0010-8545(99)00106-X.

[19] A. Schmoldt, H. F. Benthe, G. Haberland, *Biochemical pharmacology* **1975**, *24 (17)*, 1639 – 1641.

[20] H. Song, M. A. Reed, T. Lee, *Advanced materials (Deerfield Beach, Fla.)* **2011**, *23 (14)*, 1583 – 1608. DOI: 10.1002/adma.201004291.

[21] M. L. Perrin, E. Burzurí, H. S. J. van der Zant, *Chemical Society reviews* **2015**, *44 (4)*, 902 – 919. DOI: 10.1039/C4CS00231H.

[22] X. Li, Y. Wu, D. Steel, D. Gammon, T. H. Stievater, D. S. Katzer, D. Park, C. Piermarocchi, L. J. Sham, *Science* **2003**, *301 (5634)*, 809 – 811. DOI: 10.1126/science.1083800.

[23] B. M. Maune, M. G. Borselli, B. Huang, T. D. Ladd, P. W. Deelman, K. S. Holabird, A. A. Kiselev, I. Alvarado-Rodriguez, R. S. Ross, A. E. Schmitz, M. Sokolich, C. A. Watson, M. F. Gyure, A. T. Hunter, *Nature* **2012**, *481 (7381)*, 344 – 347. DOI: 10.1038/nature10707.

[24] S. A. Wolf, D. D. Awschalom, R. A. Buhrman, J. M. Daughton, S. von Molnár, M. L. Roukes, A. Y. Chtchelkanova, D. M. Treger, *Science* **2001**, *294 (5546)*, 1488 – 1495. DOI: 10.1126/science.1065389.

[25] D. D. Awschalom, M. E. Flatté, *Nature Phys* **2007**, *3 (3)*, 153 – 159. DOI: 10.1038/nphys551.

[26] L. Bogani, W. Wernsdorfer, *Nature materials* **2008**, *7 (3)*, 179 – 186. DOI: 10.1038/nmat2133.

[27] B. Kasemo, *Current Opinion in Solid State and Materials Science* **1998**, *3 (5)*, 451 – 459. DOI: 10.1016/S1359-0286(98)80006-5.

[28] D. G. Castner, B. D. Ratner, *Surface Science* **2002**, *500 (1-3)*, 28 – 60. DOI: 10.1016/S0039-6028(01)01587-4.

[29] J. V. Barth, G. Costantini, K. Kern, *Nature* **2005**, *437 (7059)*, 671 – 679. DOI: 10.1038/nature04166.

[30] T. Zambelli, Y. Boutayeb, F. Gayral, J. Lagoute, N. K. Girdhar, A. Gourdon, S. Gauthier, M.-J. Blanco, J.-C. Chambron, V. Heitz, J.-P. Sauvage, *Int. J. Nanosci.* **2004**, *03 (03)*, 331 – 341. DOI: 10.1142/s0219581x04002115.

[31] S. Banerjee, S. Mazumdar, *International journal of analytical chemistry* **2012**, *2012*, 282574. DOI: 10.1155/2012/282574.

[32] J. H. Gross, *Mass Spectrometry*, Springer International Publishing, Cham **2017**.

[33] M. Wilm, *Molecular & cellular proteomics MCP* **2011**, *10 (7)*, M111.009407. DOI: 10.1074/mcp.M111.009407.

[34] J. B. Fenn, M. Mann, C. K. Meng, S. F. Wong, C. M. Whitehouse, *Science (New York, N.Y.)* **1989**, *246 (4926)*, 64 – 71. DOI: 10.1126/science.2675315.

[35] J. B. Fenn, *Angewandte Chemie (International ed. in English)* **2003**, *42 (33)*, 3871 – 3894. DOI: 10.1002/anie.200300605.

[36] D. Z. Keifer, T. Motwani, C. M. Teschke, M. F. Jarrold, *Rapid communications in mass spectrometry RCM* **2016**, *30 (17)*, 1957 – 1962. DOI: 10.1002/rcm.7673.

[37] S. Dominguez-Medina, S. Fostner, M. Defoort, M. Sansa, A.-K. Stark, M. A. Halim, E. Vernhes, M. Gely, G. Jourdan, T. Alava, P. Boulanger, C. Masselon, S. Hentz, *Science* **2018**, *362 (6417)*, 918 – 922. DOI: 10.1126/science.aat6457.

[38] G. Verbeck, W. Hoffmann, B. Walton, *The Analyst* **2012**, *137 (19)*, 4393 – 4407. DOI: 10.1039/c2an35550g.

[39] S. Rauschenbach, M. Ternes, L. Harnau, K. Kern, *Annual review of analytical chemistry (Palo Alto, Calif.)* **2016**, *9 (1)*, 473 – 498. DOI: 10.1146/annurev-anchem-071015-041633.

[40] V. A. Mikhailov, T. H. Mize, J. L. P. Benesch, C. V. Robinson, *Analytical chemistry* **2014**, *86 (16)*, 8321 – 8328. DOI: 10.1021/ac5018327.

[41] V. Franchetti, B. H. Solka, W. E. Baitinger, J. W. Amy, R. G. Cooks, *International Journal of Mass Spectrometry and Ion Physics* **1977**, *23 (1)*, 29 – 35. DOI: 10.1016/0020-7381(77)80004-1.

[42] C. V. Robinson, *Proceedings of the National Academy of Sciences of the United States of America* **2019**, *116 (8)*, 2814 – 2820. DOI: 10.1073/pnas.1820450116.

[43] X. Wu, M. Delbianco, K. Anggara, T. Michnowicz, A. Pardo-Vargas, P. Bharate, S. Sen, M. Pristl, S. Rauschenbach, U. Schlickum, S. Abb, P. H. Seeberger, K. Kern, *Nature* **2020**, *582 (7812)*, 375 – 378. DOI: 10.1038/s41586-020-2362-1.

[44] V. Grill, J. Shen, C. Evans, R. G. Cooks, *Review of Scientific Instruments* **2001**, *72 (8)*, 3149 – 3179. DOI: 10.1063/1.1382641.

[45] S. Abb, N. Tarrat, J. Cortés, B. Andriyevsky, L. Harnau, J. C. Schön, S. Rauschenbach, K. Kern, *Angewandte Chemie (International ed. in English)* **2019**, *58 (25)*, 8336 – 8340. DOI: 10.1002/anie.201901340.

[46] Z. Ouyang, Z. Takáts, T. A. Blake, B. Gologan, A. J. Guymon, J. M. Wiseman, J. C. Oliver, V. J. Davisson, R. G. Cooks, *Science (New York, N.Y.)* **2003**, *301 (5638)*, 1351 – 1354. DOI: 10.1126/science.1088776.

[47] S. Rauschenbach, F. L. Stadler, E. Lunedei, N. Malinowski, S. Koltsov, G. Costantini, K. Kern, *Small (Weinheim an der Bergstrasse, Germany)* **2006**, *2 (4)*, 540 – 547. DOI: 10.1002/smll.200500479.

[48] C. Hamann, R. Woltmann, I.-P. Hong, N. Hauptmann, S. Karan, R. Berndt, *Review of Scientific Instruments* **2011**, *82 (3)*, 33903. DOI: 10.1063/1.3553010.

[49] Andreas Walz, Compact and versatile electrospray - controlled ion beam deposition with adjustable frequency RF ion guides and extended mass range, *Dissertation*, Technische Universität München **2020**.

[50] J. B. Taylor, I. Langmuir, *Phys. Rev.* **1933**, *44 (6)*, 423 – 458. DOI: 10.1103/PhysRev.44.423.

[51] Q. Li, B. Yang, H. Lin, N. Aghdassi, K. Miao, J. Zhang, H. Zhang, Y. Li, S. Duhm, J. Fan, L. Chi, *Journal of the American Chemical Society* **2016**, *138 (8)*, 2809 – 2814. DOI: 10.1021/jacs.5b13286.

[52] C. N. McEwen, B. S. Larsen, *International Journal of Mass Spectrometry* **2015**, *377*, 515 – 531. DOI: 10.1016/j.ijms.2014.07.018.

[53] M. L. Vestal, *Chemical Reviews* **2001**, *101 (2)*, 361 – 375. DOI: 10.1021/cr990104w.

[54] J. K. Eng, A. L. MCCormack, J. R. Yates, *Journal of the American Society for Mass Spectrometry*. DOI: 10.1021/jasms.8b00502.

[55] G. I. Taylor, *Proc. R. Soc. Lond. A* **1964**, *280 (1382)*, 383 – 397. DOI: 10.1098/rspa.1964.0151.

[56] M. Cloupeau, B. Prunet-Foch, *Journal of Electrostatics* **1990**, *25 (2)*, 165 – 184. DOI: 10.1016/0304-3886(90)90025-Q.

[57] A. Jaworek, A. Krupa, *Journal of Aerosol Science* **1999**, *30 (7)*, 873 – 893. DOI: 10.1016/S0021-8502(98)00787-3.

[58] I. Marginean, P. Nemes, A. Vertes, *Physical review. E, Statistical, nonlinear, and soft matter physics* **2007**, *76 (2 Pt 2)*, 26320. DOI: 10.1103/PhysRevE.76.026320.

[59] S. Verdoold, L.L.F. Agostinho, C. U. Yurteri, J.C.M. Marijnissen, *Journal of Aerosol Science* **2014**, *67*, 87 – 103. DOI: 10.1016/j.jaerosci.2013.09.008.

[60] J. Rosell-Llompart, J. Grifoll, I. G. Loscertales, *Journal of Aerosol Science* **2018**, *125*, 2 – 31. DOI: 10.1016/j.jaerosci.2018.04.008.

[61] M. Cloupeau, B. Prunet-Foch, *Journal of Electrostatics* **1989**, *22 (2)*, 135 – 159. DOI: 10.1016/0304-3886(89)90081-8.

[62] R. Juraschek, F. W. Röllgen, *International Journal of Mass Spectrometry* **1998**, *177 (1)*, 1 – 15. DOI: 10.1016/S1387-3806(98)14025-3.

[63] J. M. Grace, J.C.M. Marijnissen, *Journal of Aerosol Science* **1994**, *25 (6)*, 1005 – 1019. DOI: 10.1016/0021-8502(94)90198-8.

[64] J. F. de La Mora, *J. Fluid Mech.* **1992**, *243 (-1)*, 561. DOI: 10.1017/S0022112092002829.

[65] K. Tang, A. Gomez, *Physics of Fluids* **1994**, *6 (7)*, 2317 – 2332. DOI: 10.1063/1.868182.

[66] J. Rosell-Llompart, J. La Fernández de Mora, *Journal of Aerosol Science* **1994**, *25 (6)*, 1093 – 1119. DOI: 10.1016/0021-8502(94)90204-6.

[67] Tang, Gomez, *Journal of colloid and interface science* **1996**, *184 (2)*, 500 – 511. DOI: 10.1006/jcis.1996.0645.

[68] Rayleigh, *The London, Edinburgh, and Dublin Philosophical Magazine and Journal of Science* **1882**, *14 (87)*, 184 – 186. DOI: 10.1080/14786448208628425.

[69] Denis Duft, Tobias Achtzehn, Rene Müller, Bernd A. Huber, Thomas Leisner, *Nature* **2003**, *421 (6919)*, 128. DOI: 10.1038/421128a.

[70] V E Oberacker, W T Pinkston, H G W Kruse, *Rep. Prog. Phys.* **1999**, *48 (3)*, 327. DOI: 10.1088/0034-4885/48/3/002.

[71] L. Konermann, E. Ahadi, A. D. Rodriguez, S. Vahidi, *Analytical chemistry* **2013**, *85 (1)*, 2 – 9. DOI: 10.1021/ac302789c.

[72] G. van J. Berkel, *J. Anal. At. Spectrom.* **1998**, *13 (7)*, 603 – 607. DOI: 10.1039/A800373D.

[73] R. Abburi, S. Kalkhof, R. Oehme, A. Kiontke, C. Birkemeyer, *European journal of mass spectrometry (Chichester, England)* **2012**, *18 (3)*, 301 – 312. DOI: 10.1255/ejms.1187.

[74] E. Ahadi, L. Konermann, *Journal of the American Chemical Society* **2011**, *133 (24)*, 9354 – 9363. DOI: 10.1021/ja111492s.

[75] J. V. Iribarne, *The Journal of Chemical Physics* **1976**, *64 (6)*, 2287. DOI: 10.1063/1.432536.

[76] A. Gomez, K. Tang, *Physics of Fluids* **1994**, *6 (1)*, 404 – 414. DOI: 10.1063/1.868037.

[77] E. Ahadi, L. Konermann, *Journal of the American Chemical Society* **2010**, *132 (32)*, 11270 – 11277. DOI: 10.1021/ja1041989.

[78] P. Kebarle, U. H. Verkerk, *Mass spectrometry reviews* **2009**, *28 (6)*, 898 – 917. DOI: 10.1002/mas.20247.

[79] A. D. Rolland, J. S. Prell, *Trends in analytical chemistry TRAC* **2019**, *116*, 282 – 291. DOI: 10.1016/j.trac.2019.04.023.

[80] R. L. Baldwin, *Protein Science* **2000**, *9 (1)*, 207. DOI: 10.1110/ps.9.1.207.

[81] M. Dole, L. L. Mack, R. L. Hines, R. C. Mobley, L. D. Ferguson, M. B. Alice, *The Journal of Chemical Physics* **1968**, *49 (5)*, 2240 – 2249. DOI: 10.1063/1.1670391.

[82] A. T. Iavarone, E. R. Williams, *Journal of the American Chemical Society* **2003**, *125 (8)*, 2319 – 2327. DOI: 10.1021/ja021202t.

[83] C. J. Hogan, J. A. Carroll, H. W. Rohrs, P. Biswas, M. L. Gross, *Analytical chemistry* **2009**, *81 (1)*, 369 – 377. DOI: 10.1021/ac8016532.

[84] R. G. McAllister, H. Metwally, Y. Sun, L. Konermann, *Journal of the American Chemical Society* **2015**, *137 (39)*, 12667 – 12676. DOI: 10.1021/jacs.5b07913.

[85] E. Ahadi, L. Konermann, *The journal of physical chemistry. B* **2012**, *116 (1)*, 104 – 112. DOI: 10.1021/jp209344z.

[86] L. Konermann, A. D. Rodriguez, J. Liu, *Analytical chemistry* **2012**, *84 (15)*, 6798 – 6804. DOI: 10.1021/ac301298g.

[87] L. Konermann, S. Vahidi, M. A. Sowole, *Analytical chemistry* **2014**, *86 (1)*, 213 – 232. DOI: 10.1021/ac4039306.

[88] H. Busch, *Ann. Phys.* **1926**, *386 (25)*, 974 – 993. DOI: 10.1002/andp.19263862507.

[89] F. Gray, *Bell System Technical Journal* **1939**, *18 (1)*, 1 – 31. DOI: 10.1002/j.1538-7305.1939.tb00805.x.

[90] D. Gerlich, in *Advances in chemical physics*, Advances in Chemical Physics (Eds: C. Y. Ng, M. Bär), J. Wiley. New York **2007**.

[91] T. Kaposi, A Compact and Versatile Electrospray Ion Beam Deposition Setup: Advanced Sample Preparation for Experiments in Surface Science, *Dissertation*, Technische Universität München **2016**.

[92] W. Paul, H. Steinwedel, *Zeitschrift für Naturforschung A* **1953**, *8 (7)*. DOI: 10.1515/zna-1953-0710.

[93] W. Paul, M. Raether, *Z. Physik* **1955**, *140 (3)*, 262 – 273. DOI: 10.1007/BF01328923.

[94] P. H. Dawson, *Quadrupole Mass Spectrometry and Its Applications*, Elsevier Science, Burlington **1976**.

[95] P. H. Dawson, *Mass Spectrom. Rev.* **1986**, *5 (1)*, 1 – 37. DOI: 10.1002/mas.1280050102.

[96] D. J. Douglas, *Mass spectrometry reviews* **2009**, *28 (6)*, 937 – 960. DOI: 10.1002/mas.20249.

[97] J. A. Richards, R. M. Huey, J. Hiller, *International Journal of Mass Spectrometry and Ion Physics* **1973**, *12 (4)*, 317 – 339. DOI: 10.1016/0020-7381(73)80102-0.

[98] D. L. Shinholt, S. N. Anthony, A. W. Alexander, B. E. Draper, M. F. Jarrold, *The Review of scientific instruments* **2014**, *85 (11)*, 113109. DOI: 10.1063/1.4900627.

[99] G. F. Brabeck, P. T.A. Reilly, *International Journal of Mass Spectrometry* **2014**, *364*, 1 – 8. DOI: 10.1016/j.ijms.2014.03.008.

[100] G. E. Johnson, D. Gunaratne, J. Laskin, *Mass spectrometry reviews* **2016**, *35 (3)*, 439 – 479. DOI: 10.1002/mas.21451.

[101] S. Rauschenbach, R. Vogelgesang, N. Malinowski, J. W. Gerlach, M. Benyoucef, G. Costantini, Z. Deng, N. Thontasen, K. Kern, *ACS nano* **2009**, *3 (10)*, 2901 – 2910. DOI: 10.1021/nn900022p.

[102] G. Dubey, R. Urcuyo, S. Abb, G. Rinke, M. Burghard, S. Rauschenbach, K. Kern, *Journal of the American Chemical Society* **2014**, *136 (39)*, 13482 – 13485. DOI: 10.1021/ja5046499.

[103] S. A. Miller, *Science* **1997**, *275 (5305)*, 1447 – 1450. DOI: 10.1126/science.275.5305.1447.

[104] J. Shen, Y. H. Yim, B. Feng, V. Grill, C. Evans, R.G. Cooks, *International Journal of Mass Spectrometry* **1999**, *182-183*, 423 – 435. DOI: 10.1016/S1387-3806(98)14251-3.

[105] Bogdan Gologan, Zoltán Takáts, Jormarie Alvarez, Justin M. Wiseman, Nari Talaty, Zheng Ouyang, R. Graham Cooks, *J Am Soc Mass Spectrom* **2004**, *15 (12)*, 1874 – 1884. DOI: 10.1016/j.jasms.2004.09.005.

[106] J. Alvarez, J. H. Futrell, J. Laskin, *The journal of physical chemistry. A* **2006**, *110 (4)*, 1678 – 1687. DOI: 10.1021/jp0555044.

[107] O. Hadjar, J. H. Futrell, J. Laskin, *J. Phys. Chem. C* **2007**, *111 (49)*, 18220 – 18225. DOI: 10.1021/jp075293y.

[108] J. Laskin, P. Wang, O. Hadjar, *J. Phys. Chem. C* **2010**, *114 (12)*, 5305 – 5311. DOI: 10.1021/jp904384q.

[109] G. E. Johnson, T. Priest, J. Laskin, *ACS nano* **2012**, *6 (1)*, 573 – 582. DOI: 10.1021/nn2039565.

[110] G. E. Johnson, T. Priest, J. Laskin, *J. Phys. Chem. C* **2012**, *116 (47)*, 24977 – 24986. DOI: 10.1021/jp308795r.

[111] Z. Deng, N. Thontasen, N. Malinowski, G. Rinke, L. Harnau, S. Rauschenbach, K. Kern, *Nano letters* **2012**, *12 (5)*, 2452 – 2458. DOI: 10.1021/nl3005385.

[112] G. Rinke, S. Rauschenbach, S. Schrettl, T. N. Hoheisel, J. Blohm, R. Gutzler, F. Rosei, H. Frauenrath, K. Kern, *International Journal of Mass Spectrometry* **2015**, *377*, 228 – 234. DOI: 10.1016/j.ijms.2014.06.026.

[113] Sabine Abb, Ludger Harnau, Rico Gutzler, Stephan Rauschenbach, Klaus Kern, *Nat Commun* **2016**, *7 (1)*, 1 – 7. DOI: 10.1038/ncomms10335.

[114] Peng Wang, Omar Hadjar, Paul L. Gassman, Julia Laskin, *Phys. Chem. Chem. Phys.* **2008**, *10 (11)*, 1512 – 1522. DOI: 10.1039/B717617A.

[115] P. Wang, J. Laskin, *Angewandte Chemie (International ed. in English)* **2008**, *47 (35)*, 6678 – 6680. DOI: 10.1002/anie.200801366.

[116] Julia Laskin, Peng Wang, Omar Hadjar, *Phys. Chem. Chem. Phys.* **2008**, *10 (8)*, 1079 – 1090. DOI: 10.1039/B712710C.

[117] G. Binnig, H. Rohrer, *Phys. Bl.* **1983**, *39 (1)*, 16 – 17. DOI: 10.1002/phbl.19830390107.

[118] NobelPrize.org., *Nobel Media AB 2020.* **Fri. 2020.**

[119] M. Pörtner, Adsorption of phthalocyanine-complexes on hexagonal boron nitride templates, *Dissertation*, Technische Universität München **2020**.

[120] G. Gamow, *Z. Physik* **1928**, *51 (3-4)*, 204 – 212. DOI: 10.1007/BF01343196.

[121] J. Bardeen, *Phys. Rev. Lett.* **1961**, *6 (2)*, 57 – 59. DOI: 10.1103/PhysRevLett.6.57.

[122] Tersoff, Hamann, *Phys. Rev. B* **1985**, *31 (2)*, 805 – 813. DOI: 10.1103/physrevb.31.805.

[123] J. A. Stroscio, *Scanning tunneling microscopy*, Methods of experimental physics, Vol. 27, Acad. Press, Boston **1993**.

[124] C. J. Chen, *Introduction to Scanning Tunneling Microscopy*, Oxford University Press **2007**.

[125] J. Tersoff, D. R. Hamann, *Phys. Rev. Lett.* **1983**, *50 (25)*, 1998 – 2001. DOI: 10.1103/PhysRevLett.50.1998.

[126] Beer, *Ann. Phys.* **1852**, *162 (5)*, 78 – 88. DOI: 10.1002/andp.18521620505.

[127] *Lamberts Photometrie: Photometria, sive De mensura et gradibus luminus, colorum et umbrae (1760)* **1892**.

[128] D. A. Skoog, F. J. Holler, S. R. Crouch, *Principles of instrumental analysis*, 6th ed., Thomson Brooks/Cole, Belmont, Calif. **2007**.

[129] J. D. Watson, F. H. Crick, *Nature* **1953**, *171 (4356)*, 737 – 738. DOI: 10.1038/171737a0.

[130] J. Choi, T. Majima, *Chemical Society reviews* **2011**, *40 (12)*, 5893 – 5909. DOI: 10.1039/C1CS15153C.

[131] A. T. Phan, V. Kuryavyi, D. J. Patel, *Current opinion in structural biology* **2006**, *16 (3)*, 288 – 298. DOI: 10.1016/j.sbi.2006.05.011.

[132] S. Mondal, J. Bhat, J. Jana, M. Mukherjee, S. Chatterjee, *Molecular bioSystems* **2016**, *12 (1)*, 18 – 22. DOI: 10.1039/C5MB00611B.

[133] Kary B. Mullis, *Scientific American* **1990**, *262 (4)*, 56 – 65.

[134] *Molekulare Genetik*, 11th ed. (Eds: A. Nordheim, R. Knippers), Georg Thieme Verlag, Stuttgart, New York **2018**.

[135] S. B. Zimmerman, B. H. Pheiffer, *Proceedings of the National Academy of Sciences of the United States of America* **1979**, *76 (6)*, 2703 – 2707. DOI: 10.1073/pnas.76.6.2703.

[136] M. D. Hanwell, D. E. Curtis, D. C. Lonie, T. Vandermeersch, E. Zurek, G. R. Hutchison, *Journal of cheminformatics* **2012**, *4 (1)*, 17. DOI: 10.1186/1758-2946-4-17.

[137] A. Shivalingam, T. Brown, *Biochemical Society transactions* **2016**, *44 (3)*, 709 – 715. DOI: 10.1042/BST20160051.

[138] P. Heisig, *Pharmazie in unserer Zeit* **1997**, *26 (6)*, 322 – 323. DOI: 10.1002/pauz.19970260620.

[139] L. Pauling, R. B. Corey, *Proceedings of the National Academy of Sciences of the United States of America* **1951**, *37 (5)*, 241 – 250.

[140] B. N. Ames, D. T. Dubin, *J. Biol. Chem.* **1960**, *235 (3)*, 769 – 775. DOI: 10.1016/S0021-9258(19)67936-6.

[141] A. E. Pegg, P. P. McCann, *The American journal of physiology* **1982**, *243 (5)*, C212-21. DOI: 10.1152/ajpcell.1982.243.5.C212.

[142] C. W. Tabor, H. Tabor, *Microbiological Reviews* **1985**, *49 (1)*, 81 – 99.

[143] K. Igarashi, K. Kashiwagi, *Biochemical and biophysical research communications* **2000**, *271 (3)*, 559 – 564. DOI: 10.1006/bbrc.2000.2601.

[144] U. Bachrach, *Current protein & peptide science* **2005**, *6 (6)*, 559 – 566. DOI: 10.2174/138920305774933240.

[145] L. Zhang, H.-K. Lee, T. H. Pruess, H. S. White, G. Bulaj, *Journal of medicinal chemistry* **2009**, *52 (6)*, 1514 – 1517. DOI: 10.1021/jm801481y.

[146] TUM Phys. Dept. E20 ESI team, *ESI Machine Paper: manuscript in preparation*.

[147] R. Steinacher, Development of Soft Landing Instrumentation for SPM: Investigation Design and Implementation of Ion Guide, ESI Source, and the System Peripherals, Technische Universität München **2012**.

[148] Michael Weiss, Donald F Steiner, Louis H Philipson, in *Endotext [Internet]* (Eds: M. Weiss, D. F. Steiner, L. H. Philipson), MDText.com, Inc **2014**.

[149] A. H. Pekar, B. H. Frank, *Biochemistry* **1972**, *11 (22)*, 4013 – 4016. DOI: 10.1021/bi00772a001.

[150] A. K. Attri, C. Fernández, A. P. Minton, *Biophysical Chemistry* **2010**, *148 (1-3)*, 28 – 33. DOI: 10.1016/j.bpc.2010.02.002.

[151] E. J. Nettleton, P. Tito, M. Sunde, M. Bouchard, C. M. Dobson, C. V. Robinson, *Biophysical Journal* **2000**, *79 (2)*, 1053 – 1065. DOI: 10.1016/S0006-3495(00)76359-4.

[152] W Kadima, M Roy, R W Lee, N C Kaarsholm, M F Dunn, *J. Biol. Chem.* **1992**, *267 (13)*, 8963 – 8970.

[153] M. Lin, C. K. Larive, *Analytical biochemistry* **1995**, *229 (2)*, 214 – 220. DOI: 10.1006/abio.1995.1405.

[154] M. F. Dunn, *Biometals* **2005**, *18 (4)*, 295 – 303. DOI: 10.1007/s10534-005-3685-y.

[155] A. K. Attri, C. Fernández, A. P. Minton, *Biophysical Chemistry* **2010**, *148 (1-3)*, 23 – 27. DOI: 10.1016/j.bpc.2010.02.001.

[156] S. Rahuel-Clermont, C. A. French, N. C. Kaarsholm, M. F. Dunn, C. I. Chou, *Biochemistry* **1997**, *36 (19)*, 5837 – 5845. DOI: 10.1021/bi963038q.

[157] U. Derewenda, Z. Derewenda, G. G. Dodson, R. E. Hubbard, F. Korber, *Br Med Bull* **1989**, *45 (1)*, 4 – 18. DOI: 10.1093/oxfordjournals.bmb.a072320.

[158] W. Kadima, L. Ogendal, R. Bauer, N. Kaarsholm, K. Brodersen, J. F. Hansen, P. Porting, *Biopolymers* **1993**, *33 (11)*, 1643 – 1657. DOI: 10.1002/bip.360331103.

[159] A. Kumar, P. Venkatesu, *RSC Adv.* **2013**, *3 (2)*, 362 – 367. DOI: 10.1039/C2RA22277A.

[160] J. P. Reyes-Grajeda, *Recombinant Human Insulin* **2020**.

[161] G. Bonvin, S. Rudaz, J. Schappler, *Analytica chimica acta* **2014**, *813*, 97 – 105. DOI: 10.1016/j.aca.2013.12.043.

[162] R. B. Cole, *J. Mass Spectrom.* **2000**, *35 (7)*, 763 – 772. DOI: 10.1002/1096-9888(200007)35:7<763:AID-JMS16>3.0.CO;2-%23.

[163] G. Bouchoux, *Mass Spectrom. Rev.* **2012**, *31 (3)*, 391 – 435. DOI: 10.1002/mas.20349.

[164] I. A. Kaltashov, A. Mohimen, *Analytical chemistry* **2005**, *77 (16)*, 5370 – 5379. DOI: 10.1021/ac050511.

[165] A. Schmidt, M. Karas, T. Dülcks, *J Am Soc Mass Spectrom* **2003**, *14 (5)*, 492 – 500. DOI: 10.1016/S1044-0305(03)00128-4.

[166] M. Correia, M. T. Neves-Petersen, P. B. Jeppesen, S. Gregersen, S. B. Petersen, *PloS one* **2012**, *7 (12)*, e50733. DOI: 10.1371/journal.pone.0050733.

[167] D. Fabris, C. Fenselau, *Analytical chemistry* **1999**, *71 (2)*, 384 – 387. DOI: 10.1021/ac980753s.

[168] U. K. Boga Raja, S. Injeti, T. Culver, J. W. McCabe, L. A. Angel, *European journal of mass spectrometry (Chichester, England)* **2015**, *21 (6)*, 759 – 774. DOI: 10.1255/ejms.1396.

[169] T. A. Blake, Z. Ouyang, J. M. Wiseman, Z. Takáts, A. J. Guymon, S. Kothari, R. G. Cooks, *Analytical chemistry* **2004**, *76 (21)*, 6293 – 6305. DOI: 10.1021/ac048981b.

[170] K. D. D. Gunaratne, V. Prabhakaran, Y. M. Ibrahim, R. V. Norheim, G. E. Johnson, J. Laskin, *The Analyst* **2015**, *140 (9)*, 2957 – 2963. DOI: 10.1039/c5an00220f.

[171] A. C. Welinder, J. Zhang, D. B. Steensgaard, J. Ulstrup, *Phys. Chem. Chem. Phys.* **2010**, *12 (34)*, 9999 – 10011. DOI: 10.1039/C0CP01021A.

[172] D. Anthonii Lewenhoeck, *Philosophical Transactions (1665-1678)* **1677**, *12*, 1040 – 1046.

[173] H. Olle, *Physiology* **1986**, *1 (1)*, 12 – 15. DOI: 10.1152/physiologyonline.1986.1.1.12.

[174] D. Bancroft, L. D. Williams, A. Rich, M. Egli, *Biochemistry* **1994**, *33 (5)*, 1073 – 1086. DOI: 10.1021/bi00171a005.

[175] N. Korolev, A. P. Lyubartsev, A. Laaksonen, L. Nordenskiöld, *Biophysical Journal* **2002**, *82 (6)*, 2860 – 2875. DOI: 10.1016/S0006-3495(02)75628-2.

[176] B. G. Feuerstein, N. Pattabiraman, L. J. Marton, *Proceedings of the National Academy of Sciences of the United States of America* **1986**, *83 (16)*, 5948 – 5952. DOI: 10.1073/pnas.83.16.5948.

[177] D. D. La, J. N. Malegaonkar, M. A. Kobaisi, R. S. Bhosale, S. V. Bhosale, S. V. Bhosale, *New J. Chem.* **2018**, *42 (18)*, 15379 – 15386. DOI: 10.1039/C8NJ02636J.

[178] C. M. A. Gangemi, R. Randazzo, M. E. Fragalà, G. A. Tomaselli, F. P. Ballistreri, A. Pappalardo, R. M. Toscano, G. Trusso Sfrazzetto, R. Purrello, A. D'Urso, *New J. Chem.* **2015**, *39 (9)*, 6722 – 6725. DOI: 10.1039/c5nj01264c.

[179] K. Yasumoto, M. Yasumoto-Hirose, J. Yasumoto, R. Murata, S.-I. Sato, M. Baba, K. Mori-Yasumoto, M. Jimbo, Y. Oshima, T. Kusumi, S. Watabe, *Marine biotechnology (New York, N.Y.)* **2014**, *16 (4)*, 465 – 474. DOI: 10.1007/s10126-014-9566-z.

[180] P. M. Woster, in *Polyamine Cell Signaling* (Eds: J.-Y. Wang, R. A. Casero), Humana Press. Totowa, NJ **2006**.

[181] Q. Duez, H. Metwally, L. Konermann, *Analytical chemistry* **2018**, *90 (16)*, 9912 – 9920. DOI: 10.1021/acs.analchem.8b02115.

[182] S. Wickenburg, J. Lu, J. Lischner, H.-Z. Tsai, A. A. Omrani, A. Riss, C. Karrasch, A. Bradley, H. S. Jung, R. Khajeh, D. Wong, K. Watanabe, T. Taniguchi, A. Zettl, A. H. C. Neto, S. G. Louie, M. F. Crommie, *Nat Commun* **2016**, *7*, 13553. DOI: 10.1038/ncomms13553.

[183] Timur Skeini, Single Molecule Study of Beta-Carotene using Scanning Tunneling Microscope: (Up-close and Personal Investigation of Beta-Carotene), *Dissertation*, Ohio University **2010**.

[184] J. Lu, H.-Z. Tsai, A. N. Tatan, S. Wickenburg, A. A. Omrani, D. Wong, A. Riss, E. Piatti, K. Watanabe, T. Taniguchi, A. Zettl, V. M. Pereira, M. F. Crommie, *Nat Commun* **2019**, *10 (1)*, 477. DOI: 10.1038/s41467-019-08371-2.

[185] Atsushi Ikai, STM and AFM of bio/organic molecules and structures, *Dissertation*, Tokyo Institute of Technology **1996**.

[186] M. Tanigawa, T. Okada, *Analytica chimica acta* **1998**, *365 (1-3)*, 19 – 25. DOI: 10.1016/S0003-2670(97)00709-5.

[187] B. P. Singh, I. Saha, I. Nandi, M. J. Swamy, *Biochemical and biophysical research communications* **2017**, *493 (4)*, 1418 – 1424. DOI: 10.1016/j.bbrc.2017.09.148.

[188] C. Yanisch-Perron, J. Vieira, J. Messing, *Gene* **1985**, *33 (1)*, 103 – 119. DOI: 10.1016/0378-1119(85)90120-9.

[189] D. A. Benson, M. Cavanaugh, K. Clark, I. Karsch-Mizrachi, D. J. Lipman, J. Ostell, E. W. Sayers, *Nucleic acids research* **2013**, *41 (Database issue)*, D36-42. DOI: 10.1093/nar/gks1195.

[190] *Introduction to Biopolymer Physics* (Eds: J. R. C. van der Maarel), WORLD SCIENTIFIC **2007**.

[191] J. C. Schultz, C. A. Hack, W. H. Benner, *J Am Soc Mass Spectrom* **1998**, *9 (4)*, 305 – 313. DOI: 10.1016/S1044-0305(97)00290-0.

[192] ThermoFisher Scientific, *DNA and RNA Molecular Weights and Conversions*, https://www.thermofisher.com/de/de/home/references/ambion-tech-support/rna-tools-and-calculators/dna-and-rna-molecular-weights-and-conversions.html.

[193] NewEngland BioLabs Inc., *Topoisomerase I (E. coli)*, https://international.neb.com/products/m0301-topoisomerase-i-e-coli.

[194] NewEngland BioLabs Inc., *EcoRI-HF*, https://international.neb.com/products/r3101-ecori-hf.

[195] X. Cheng, D. G. Camp, Q. Wu, R. Bakhtiar, D. L. Springer, B. J. Morris, J. E. Bruce, G. A. Anderson, C. G. Edmonds, R. D. Smith, *Nucleic acids research* **1996**, *24 (11)*, 2183 – 2189. DOI: 10.1093/nar/24.11.2183.

[196] H. Lederer, R. P. May, J. K. Kjems, G. Baer, H. Heumann, *European journal of biochemistry* **1986**, *161 (1)*, 191 – 196. DOI: 10.1111/j.1432-1033.1986.tb10141.x.

[197] M. Adrian, B. ten Heggeler-Bordier, W. Wahli, A. Z. Stasiak, A. Stasiak, J. Dubochet, *The EMBO Journal* **1990**, *9 (13)*, 4551 – 4554. DOI: 10.1002/j.1460-2075.1990.tb07907.x.

[198] N. B. Vargaftik, B. N. Volkov, L. D. Voljak, *Journal of Physical and Chemical Reference Data* **1983**, *12 (3)*, 817 – 820. DOI: 10.1063/1.555688.

[199] R. Belda Maximino, *Physics and Chemistry of Liquids* **2009**, *47 (5)*, 475 – 486. DOI: 10.1080/00319100802241657.

[200] L. H. Pope, M. C. Davies, C. A. Laughton, C. J. Roberts, S. J. Tendler, P. M. Williams, *Journal of microscopy* **2000**, *199 (Pt 1)*, 68 – 78. DOI: 10.1046/j.1365-2818.2000.00703.x.

[201] A. Hüttig, *Illustration of the model*.

[202] H. Schlichting, *personal communication*.

[203] T. M. Nordlund, P. M. Hoffmann, *Quantitative understanding of biosystems: An introduction to biophysics*, Foundations of biochemistry and biophysics, CRC Press, Boca Raton **2019**.

[204] A. Hüttig, *personal communication*.

[205] R. G. Bhattacharyya, K. K. Nayak, A. N. Chakrabarty, *Inorganica Chimica Acta* **1988**, *153 (2)*, 79 – 86. DOI: 10.1016/S0020-1693(00)83863-3.

[206] D. Pang, A. R. Thierry, A. Dritschilo, *Frontiers in molecular biosciences* **2015**, *2*, 1. DOI: 10.3389/fmolb.2015.00001.

[207] C. Rivetti, M. Guthold, C. Bustamante, *Journal of molecular biology* **1996**, *264 (5)*, 919 – 932. DOI: 10.1006/jmbi.1996.0687.

[208] E. Shapir, L. Sagiv, N. Borovok, T. Molotski, A. B. Kotlyar, D. Porath, *J. Phys. Chem. B* **2008**, *112 (31)*, 9267 – 9269. DOI: 10.1021/jp803478f.

[209] M. J. Burkitt, in *Oxygen Radicals in Biological Systems Part D*, Vol. 234, Methods in Enzymology, Elsevier **1994**.

[210] B. G. Feuerstein, N. Pattabiraman, L. J. Marton, *Nucleic acids research* **1990**, *18 (5)*, 1271 – 1282. DOI: 10.1093/nar/18.5.1271.

[211] X. Fang, D. H. Reneker, *Journal of Macromolecular Science, Part B* **1997**, *36 (2)*, 169 – 173. DOI: 10.1080/00222349708220422.

[212] H. Tanaka, C. Hamai, T. Kanno, T. Kawai, *Surface Science* **1999**, *432 (3)*, L611-L616. DOI: 10.1016/S0039-6028(99)00623-8.

[213] R. Otero, M. Schöck, L. M. Molina, E. Laegsgaard, I. Stensgaard, B. Hammer, F. Besenbacher, *Angewandte Chemie (International ed. in English)* **2005**, *44 (15)*, 2270 – 2275. DOI: 10.1002/anie.200461586.

[214] R. Otero, W. Xu, M. Lukas, R. E. A. Kelly, E. Laegsgaard, I. Stensgaard, J. Kjems, L. N. Kantorovich, F. Besenbacher, *Angewandte Chemie (International ed. in English)* **2008**, *47 (50)*, 9673 – 9676. DOI: 10.1002/anie.200803333.

[215] S. Xu, M. Dong, E. Rauls, R. Otero, T. R. Linderoth, F. Besenbacher, *Nano letters* **2006**, *6 (7)*, 1434 – 1438. DOI: 10.1021/nl060563u.

[216] Q. Chen, D. J. Frankel, N. V. Richardson, *Langmuir the ACS journal of surfaces and colloids* **2002**, *18 (8)*, 3219 – 3225. DOI: 10.1021/la011722m.

[217] A. Ciesielski, M. El Garah, S. Masiero, P. Samorì, *Small (Weinheim an der Bergstrasse, Germany)* **2016**, *12 (1)*, 83 – 95. DOI: 10.1002/smll.201501017.

[218] A. C. Papageorgiou, S. Fischer, J. Reichert, K. Diller, F. Blobner, F. Klappenberger, F. Allegretti, A. P. Seitsonen, J. V. Barth, *ACS nano* **2012**, *6 (3)*, 2477 – 2486. DOI: 10.1021/nn204863p.

[219] B. Roelfs, E. Bunge, C. Schröter, T. Solomun, H. Meyer, R. J. Nichols, H. Baumgärtel, *J. Phys. Chem. B* **1997**, *101 (5)*, 754 – 765. DOI: 10.1021/jp961814y.

[220] P. Salvatore, R. R. Nazmutdinov, J. Ulstrup, J. Zhang, *The journal of physical chemistry. B* **2015**, *119 (7)*, 3123 – 3134. DOI: 10.1021/jp511909f.

[221] W. Xu, J.-G. Wang, M. F. Jacobsen, M. Mura, M. Yu, R. E. A. Kelly, Q.-Q. Meng, E. Laegsgaard, I. Stensgaard, T. R. Linderoth, J. Kjems, L. N. Kantorovich, K. V. Gothelf, F. Besenbacher, *Angewandte Chemie (International ed. in English)* **2010**, *49 (49)*, 9373 – 9377. DOI: 10.1002/anie.201003390.

[222] S. D. Fuerstenau, W. H. Benner, *Rapid communications in mass spectrometry RCM* **1995**, *9 (15)*, 1528 – 1538. DOI: 10.1002/rcm.1290091513.

[223] K. Terasaki, T. Yokoyama, *The journal of physical chemistry. B* **2019**, *123 (8)*, 1780 – 1783. DOI: 10.1021/acs.jpcb.8b12100.

[224] H. Tanaka, *J. Vac. Sci. Technol. B* **1997**, *15 (3)*, 602. DOI: 10.1116/1.589299.

[225] H. Tanaka, T. Kawai, *Surface Science* **2003**, *539 (1-3)*, L531-L536. DOI: 10.1016/S0039-6028(03)00794-5.

[226] Y. Yoshida, Y. Nojima, H. Tanaka, T. Kawai, *J. Vac. Sci. Technol. B* **2007**, *25 (1)*, 242. DOI: 10.1116/1.2431180.

[227] J. P. Toennies, *Appl. Phys.* **1974**, *3 (2)*, 91 – 114. DOI: 10.1007/BF00884407.

[228] G. A. Somorjai, S. B. Brumbach, *C R C Critical Reviews in Solid State Sciences* **1973**, *4 (1-4)*, 429 – 454. DOI: 10.1080/10408437308245837.

[229] F. O. Goodman, *Surface Science* **1971**, *26 (1)*, 327 – 362. DOI: 10.1016/0039-6028(71)90135-X.

[230] F. O. Goodman, *Dynamics of Gas-Surface Scattering*, Elsevier **2012**.

[231] J. A. Barker, D. J. Auerbach, *Surface Science Reports* **1984**, *4 (1-2)*, 1 – 99. DOI: 10.1016/0167-5729(84)90005-0.

[232] R. Frisch, O. Stern, *Z. Physik* **1933**, *84 (7-8)*, 430 – 442. DOI: 10.1007/bf01342223.

[233] John Edward Lennard-Jones, A. F. Devonshire, *Nature* **1936**, *137 (3478)*, 1069 – 1070. DOI: 10.1038/1371069a0.

[234] John Edward Lennard-Jones, A. F. Devonshire, *Proceedings of the Royal Society of London. Series A - Mathematical and Physical Sciences* **1937**, *158 (894)*, 242 – 252. DOI: 10.1098/rspa.1937.0017.

[235] R. I. Masel, R. P. Merrill, *Journal of Vacuum Science and Technology* **1998**, *14 (1)*, 333. DOI: 10.1116/1.569203.

[236] R. Gomer, Binh, V. T. (Ed.), *Surface Mobilities on Solid Materials: Fundamental Concepts and Applications*, NATO Advanced Science Institutes Series, Series B, Vol. 86, Springer, Boston, MA **1981**.

[237] J. Harris, *Phys. Scr.* **1987**, *36 (1)*, 156 – 165. DOI: 10.1088/0031-8949/36/1/026.

[238] I. Langmuir, *Chemical Reviews* **1930**, *6 (4)*, 451 – 479. DOI: 10.1021/cr60024a002.

[239] A. Cassuto, D. A. King, *Surface Science* **1981**, *102 (2-3)*, 388 – 404. DOI: 10.1016/0039-6028(81)90036-4.

[240] *Kinetics of Interface Reactions: Proceedings of a Workshop on Interface Phenomena, Campobello Island, Canada, September 24-27, 1986*, 1st ed., Springer Series in Surface Sciences, Vol. 8 (Eds: M. Grunze, H.-J. Kreuzer), Springer Berlin Heidelberg; Imprint: Springer, Berlin, Heidelberg **1987**.

[241] P. Kisliuk, *Journal of Physics and Chemistry of Solids* **1957**, *3 (1-2)*, 95 – 101. DOI: 10.1016/0022-3697(57)90054-9.

[242] P. Kisliuk, *Journal of Physics and Chemistry of Solids* **1958**, *5 (1-2)*, 78 – 84. DOI: 10.1016/0022-3697(58)90132-x.

[243] G. Ehrlich, *Journal of Applied Physics* **1961**, *32 (1)*, 4 – 15. DOI: 10.1063/1.1735956.

[244] H. J. Kreuzer, Z. W. Gortel, *Physisorption Kinetics*, Springer Science & Business Media **2012**.

[245] D. A. King, *Surface Science* **1975**, *47 (1)*, 384 – 402. DOI: 10.1016/0039-6028(75)90302-7.

[246] M. Polanyi, E. Wigner, *Zeitschrift für Physikalische Chemie* **1928**, *139A (1)*. DOI: 10.1515/zpch-1928-13930.

[247] R. E. Davis, *J. Phys. Chem.* **1959**, *63 (2)*, 308 – 309. DOI: 10.1021/j150572a046.

[248] H.Ibach, *Physics of surfaces and interfaces* **2006**.

[249] D. P. Woodruff, T. A. Delchar, *Modern techniques of surface science*, Cambridge solid state science series, Cambridge Univ. Press, Cambridge **1990**.

[250] P. Cavallotti, *Surface Science* **1979**, *83 (1)*, 325 – 334. DOI: 10.1016/0039-6028(79)90497-7.

[251] V. P. Zhdanov, *Surface Science* **1986**, *171 (2)*, L461-L463. DOI: 10.1016/0039-6028(86)91074-5.

[252] R. G. Jones, D. L. Perry, *Surface Science* **1979**, *82 (2)*, 540 – 548. DOI: 10.1016/0039-6028(79)90210-3.

[253] M. Vollmer, F. Träger, *Surface Science* **1987**, *187 (2-3)*, 445 – 462. DOI: 10.1016/S0039-6028(87)80067-5.

[254] H. J. Kreuzer, S. H. Payne, *Surface Science* **1988**, *200 (1)*, L433-L440. DOI: 10.1016/0039-6028(88)90420-7.

[255] S. H. Payne, H. J. Kreuzer, *Surface Science* **1988**, *205 (1-2)*, 153 – 176. DOI: 10.1016/0039-6028(88)90169-0.

[256] J. B. Miller, H. R. Siddiqui, S. M. Gates, J. N. Russell, J. T. Yates, J. C. Tully, M. J. Cardillo, *The Journal of Chemical Physics* **1987**, *87 (11)*, 6725 – 6732. DOI: 10.1063/1.453409.

[257] A. Wiengarten, J. A. Lloyd, K. Seufert, J. Reichert, W. Auwärter, R. Han, D. A. Duncan, F. Allegretti, S. Fischer, S. C. Oh, Ö. Sağlam, L. Jiang, S. Vijayaraghavan, D. Écija, A. C. Papageorgiou, J. V. Barth, *Chemistry (Weinheim an der Bergstrasse, Germany)* **2015**, *21 (35)*, 12285 – 12290. DOI: 10.1002/chem.201502001.

[258] S.Glasstone, K.J.Laidler, H.Eyring, *The theory of rate processes; the kinetics of chemical reactions, viscosity, diffusion and electrochemical phenomena* **1941**.

[259] K.J.Laidler, *Reaktionskinetik. 1 (1970). Homogene Gasreaktionen* **1970**.

[260] R.B.B. R.D.Levine, *Molecular reaction dynamics and chemical reactivity* **1987**.

[261] G. Comsa, R. David, K. D. Rendulic, *Phys. Rev. Lett.* **1977**, *38 (14)*, 775 – 778. DOI: 10.1103/PhysRevLett.38.775.

[262] K. D. Rendulic, A. Winkler, *The Journal of Chemical Physics* **1983**, *79 (10)*, 5151 – 5155. DOI: 10.1063/1.445641.

[263] H.P. Steinrück, *Das Prinzip der detaillierten Gleichgewichte im System H2/Nickel und Co/Nickel* **1985**.

[264] C. T. Rettner, E. K. Schweizer, C. B. Mullins, *The Journal of Chemical Physics* **1989**, *90 (7)*, 3800 – 3813. DOI: 10.1063/1.455838.

[265] D. L. Adams, *Surface Science* **1974**, *42 (1)*, 12 – 36. DOI: 10.1016/0039-6028(74)90003-X.

[266] J.A. Venables, M. Bienfait, *Surface Science* **1976**, *61 (2)*, 667 – 672. DOI: 10.1016/0039-6028(76)90076-5.

[267] G. Le Lay, M. Manneville, R. Kern, *Surface Science* **1977**, *65 (1)*, 261 – 276. DOI: 10.1016/0039-6028(77)90306-5.

[268] M. Bertucci, G. Le Lay, M. Manneville, R. Kern, *Surface Science* **1979**, *85 (2)*, 471 – 492. DOI: 10.1016/0039-6028(79)90266-8.

[269] U. Leuthusser, *Z Physik B* **1980**, *37 (1)*, 65 – 67. DOI: 10.1007/BF01325505.

[270] H. Pfnür, P. Feulner, H. A. Engelhardt, D. Menzel, *Chemical Physics Letters* **1978**, *59 (3)*, 481 – 486. DOI: 10.1016/0009-2614(78)85024-6.

[271] V. P. Zhdanov, *Surface Science Letters* **1981**, *102 (1)*, L35-L40. DOI: 10.1016/0167-2584(81)90570-3.

[272] V. P. Zhdanov, *Surface Science* **1981**, *111 (1)*, L662-L666. DOI: 10.1016/0039-6028(81)90465-9.

[273] V. P. Zhdanov, *Surface Science* **1983**, *133 (2-3)*, 469 – 483. DOI: 10.1016/0039-6028(83)90014-6.

[274] V. P. Zhdanov, *Surface Science* **1984**, *148 (2-3)*, L691-L693. DOI: 10.1016/0039-6028(84)90577-6.

[275] K. Nagai, A. Hirashima, *Surface Science Letters* **1986**, *171 (2)*, L464-L468. DOI: 10.1016/0167-2584(86)91131-X.

[276] Kreuzer, Chapman, March, *Physical review. A, General physics* **1988**, *37 (2)*, 582 – 586. DOI: 10.1103/physreva.37.582.

[277] Frisch, Hasslacher, Pomeau, *Physical review letters* **1986**, *56 (14)*, 1505 – 1508. DOI: 10.1103/PhysRevLett.56.1505.

[278] E G Thomas, *J. Phys. C: Solid State Phys.* **2001**, *9 (15)*, 2857. DOI: 10.1088/0022-3719/9/15/008.

[279] *Chemistry and Physics of Solid Surfaces V*, Springer Series in Chemical Physics, Vol. 35 (Eds: R. Vanselow, R. Howe), Springer Berlin Heidelberg, Berlin, Heidelberg, s.l. **1984**.

[280] M. A. Hove, S. Y. Tong, *The Structure of Surfaces*, Springer Series in Surface Sciences, Vol. 2, Springer, Berlin, Heidelberg **1985**.

[281] A. Natori, H. Ohtsubo, *Surface Science* **1986**, *171 (1)*, 13 – 44. DOI: 10.1016/0039-6028(86)90559-5.

[282] J. C. Tully, G. H. Gilmer, M. Shugard, *The Journal of Chemical Physics* **1979**, *71 (4)*, 1630 – 1642. DOI: 10.1063/1.438490.

[283] M. J. Bojan, W. A. Steele, *Surface Science* **1988**, *199 (3)*, L395-L402. DOI: 10.1016/0039-6028(88)90904-1.

[284] J. V. Barth, G. Costantini, K. Kern, in *Nanoscience and technology: A collection of reviews from Nature journals* (Eds: P. Rodgers), Macmillan Publishers Ltd. London, Singapore **2010**.

[285] M.G.L. R.L.Park, *Methods of Experimental Physics, Vol. 22* **1985**.

[286] P. A. Redhead, *Vacuum* **1962**, *12 (4)*, 203 – 211. DOI: 10.1016/0042-207X(62)90978-8.

[287] J. T. Yates, in *Solid State Physics: Surfaces*, Vol. 22, Methods in Experimental Physics, Elsevier **1985**.

[288] F. M. Lord, J. S. Kittelberger, *Surface Science* **1974**, *43 (1)*, 173 – 182. DOI: 10.1016/0039-6028(74)90226-X.

[289] C.-M. Chan, R. Aris, W. H. Weinberg, *Applications of Surface Science* **1978**, *1 (3)*, 360 – 376. DOI: 10.1016/0378-5963(78)90038-7.

[290] D. Edwards, *Surface Science* **1976**, *54 (1)*, 1 – 5. DOI: 10.1016/0039-6028(76)90082-0.

[291] J. C. Tracy, P. W. Palmberg, *Surface Science* **1969**, *14 (1)*, 274 – 277. DOI: 10.1016/0039-6028(69)90060-0.

[292] D. A. King, T. E. Madey, J. T. Yates, *The Journal of Chemical Physics* **1971**, *55 (7)*, 3236 – 3246. DOI: 10.1063/1.1676572.

[293] R. L. Gerlach, T. N. Rhodin, *Surface Science* **1970**, *19 (2)*, 403 – 426. DOI: 10.1016/0039-6028(70)90050-6.

[294] J. L. Falconer, R. J. Madix, *Surface Science* **1975**, *48 (2)*, 393 – 405. DOI: 10.1016/0039-6028(75)90414-8.

[295] E. Habenschaden, J. Küppers, *Surface Science Letters* **1984**, *138 (1)*, L147-L150. DOI: 10.1016/0167-2584(84)90346-3.

[296] W. L. Winterbottom, *Journal of Vacuum Science and Technology* **1972**, *9 (2)*, 936 – 941. DOI: 10.1116/1.1317830.

[297] W.L. Winterbottom, *Acta Metallurgica* **1967**, *15 (2)*, 303 – 310. DOI: 10.1016/0001-6160(67)90206-4.

[298] C. Pisani, G. Rabino, F. Ricca, *Surface Science* **1974**, *41 (1)*, 277 – 292. DOI: 10.1016/0039-6028(74)90309-4.

[299] A. M. de Jong, J. W. Niemantsverdriet, *Surface Science* **1990**, *233 (3)*, 355 – 365. DOI: 10.1016/0039-6028(90)90649-S.

[300] H. Schlichting, D. Menzel, *Surface Science* **1992**, *272 (1-3)*, 27 – 33. DOI: 10.1016/0039-6028(92)91418-B.

[301] H. J. Kreuzer, Z. Jun, S. H. Payne, W. Nichtl-Pecher, L. Hammer, K. Müller, *Surface Science* **1994**, *303 (1-2)*, 1 – 15. DOI: 10.1016/0039-6028(94)90614-9.

[302] J. F. Zhu, H. Ellmer, H. Malissa, T. Brandstetter, D. Semrad, P. Zeppenfeld, *Phys. Rev. B* **2003**, *68 (4)*, 456. DOI: 10.1103/PhysRevB.68.045406.

[303] L. K. Ono, B. R. Cuenya, *J. Phys. Chem. C* **2008**, *112 (47)*, 18543 – 18550. DOI: 10.1021/jp8065184.

[304] J. W. Evans, H. Pak, *Surface Science* **1988**, *199 (1-2)*, 28 – 42. DOI: 10.1016/0039-6028(88)90394-9.

[305] A. Einstein, *Ann. Phys.* **1905**, *322 (6)*, 132 – 148. DOI: 10.1002/andp.19053220607.

[306] J. Als-Nielsen, Des McMorrow, *Elements of modern X-ray physics*, 2nd ed., Wiley, Chichester **2011**.

[307] S. Hüfner, *Photoelectron Spectroscopy: Principles and Applications*, Advanced Texts in Physics, Springer, Berlin, Heidelberg **2003**.

[308] R. Romberg, S. P. Frigo, A. Ogurtsov, P. Feulner, D. Menzel, *Surface Science* **2000**, *451 (1-3)*, 116 – 123. DOI: 10.1016/S0039-6028(00)00016-9.

[309] P. S. Deimel, Bonding, Reactivity and Chemical Transformations of Adsorbed Organic and Metal-Organic Species, *Dissertation*, Technische Universität München **2019**.

[310] A. Gourdon, *Angewandte Chemie (International ed. in English)* **2008**, *47 (37)*, 6950 – 6953. DOI: 10.1002/anie.200802229.

[311] J. Méndez, M. F. López, J. A. Martín-Gago, *Chemical Society reviews* **2011**, *40 (9)*, 4578 – 4590. DOI: 10.1039/c0cs00161a.

[312] M. El Garah, J. M. MacLeod, F. Rosei, *Surface Science* **2013**, *613*, 6 – 14. DOI: 10.1016/j.susc.2013.03.015.

[313] J. Björk, F. Hanke, *Chemistry (Weinheim an der Bergstrasse, Germany)* **2014**, *20 (4)*, 928 – 934. DOI: 10.1002/chem.201303559.

[314] M. Lackinger, *Polym. Int.* **2015**, *64 (9)*, 1073 – 1078. DOI: 10.1002/pi.4943.

[315] L. Dong, P. N. Liu, N. Lin, *Accounts of chemical research* **2015**, *48 (10)*, 2765 – 2774. DOI: 10.1021/acs.accounts.5b00160.

[316] Q. Fan, J. M. Gottfried, J. Zhu, *Accounts of chemical research* **2015**, *48 (8)*, 2484 – 2494. DOI: 10.1021/acs.accounts.5b00168.

[317] P. A. Held, H. Fuchs, A. Studer, *Chemistry (Weinheim an der Bergstrasse, Germany)* **2017**, *23 (25)*, 5874 – 5892. DOI: 10.1002/chem.201604047.

[318] C. Steiner, J. Gebhardt, M. Ammon, Z. Yang, A. Heidenreich, N. Hammer, A. Görling, M. Kivala, S. Maier, *Nature communications* **2017**, *8*, 14765. DOI: 10.1038/ncomms14765.

[319] Z. Xiang, D. Cao, L. Dai, *Polym. Chem.* **2015**, *6 (11)*, 1896 – 1911. DOI: 10.1039/C4PY01383B.

[320] Q. Shen, H.-Y. Gao, H. Fuchs, *Nano Today* **2017**, *13*, 77 – 96. DOI: 10.1016/j.nantod.2017.02.007.

[321] L. Lafferentz, V. Eberhardt, C. Dri, C. Africh, G. Comelli, F. Esch, S. Hecht, L. Grill, *Nature Chem* **2012**, *4 (3)*, 215 – 220. DOI: 10.1038/nchem.1242.

[322] J. Eichhorn, D. Nieckarz, O. Ochs, D. Samanta, M. Schmittel, P. J. Szabelski, M. Lackinger, *ACS nano* **2014**, *8 (8)*, 7880 – 7889. DOI: 10.1021/nn501567p.

[323] A. Basagni, F. Sedona, C. A. Pignedoli, M. Cattelan, L. Nicolas, M. Casarin, M. Sambi, *Journal of the American Chemical Society* **2015**, *137 (5)*, 1802 – 1808. DOI: 10.1021/ja510292b.

[324] E. A. Lewis, M. D. Marcinkowski, C. J. Murphy, M. L. Liriano, A. J. Therrien, A. Pronschinske, E. C. H. Sykes, *Chemical communications (Cambridge, England)* **2017**, *53 (55)*, 7816 – 7819. DOI: 10.1039/c7cc02901b.

[325] M. Lackinger, *Chemical communications (Cambridge, England)* **2017**, *53 (56)*, 7872 – 7885. DOI: 10.1039/c7cc03402d.

[326] A. Basagni, L. Ferrighi, M. Cattelan, L. Nicolas, K. Handrup, L. Vaghi, A. Papagni, F. Sedona, C. Di Valentin, S. Agnoli, M. Sambi, *Chemical communications (Cambridge, England)* **2015**, *51 (63)*, 12593 – 12596. DOI: 10.1039/c5cc04317d.

[327] Q. Fan, C. Wang, L. Liu, Y. Han, J. Zhao, J. Zhu, J. Kuttner, G. Hilt, J. M. Gottfried, *J. Phys. Chem. C* **2014**, *118 (24)*, 13018 – 13025. DOI: 10.1021/jp5037475.

[328] M. Di Giovannantonio, M. Tomellini, J. Lipton-Duffin, G. Galeotti, M. Ebrahimi, A. Cossaro, A. Verdini, N. Kharche, V. Meunier, G. Vasseur, Y. Fagot-Revurat, D. F. Perepichka, F. Rosei, G. Contini, *Journal of the American Chemical Society* **2016**, *138 (51)*, 16696 – 16702. DOI: 10.1021/jacs.6b09728.

[329] N. A. A. Zwaneveld, R. Pawlak, M. Abel, D. Catalin, D. Gigmes, D. Bertin, L. Porte, *Journal of the American Chemical Society* **2008**, *130 (21)*, 6678 – 6679. DOI: 10.1021/ja800906f.

[330] C.-Z. Guan, D. Wang, L.-J. Wan, *Chemical communications (Cambridge, England)* **2012**, *48 (24)*, 2943 – 2945. DOI: 10.1039/c2cc16892h.

[331] S. Clair, M. Abel, L. Porte, *Chemical communications (Cambridge, England)* **2014**, *50 (68)*, 9627 – 9635. DOI: 10.1039/c4cc02678k.

[332] S. Weigelt, C. Busse, C. Bombis, M. M. Knudsen, K. V. Gothelf, T. Strunskus, C. Wöll, M. Dahlbom, B. Hammer, E. Laegsgaard, F. Besenbacher, T. R. Linderoth,

*Angewandte Chemie (International ed. in English)* **2007**, *46 (48)*, 9227 – 9230. DOI: 10.1002/anie.200702859.

[333] Y. Hu, N. Goodeal, Y. Chen, A. M. Ganose, R. G. Palgrave, H. Bronstein, M. O. Blunt, *Chemical communications (Cambridge, England)* **2016**, *52 (64)*, 9941 – 9944. DOI: 10.1039/c6cc03895f.

[334] F. Klappenberger, Y.-Q. Zhang, J. Björk, S. Klyatskaya, M. Ruben, J. V. Barth, *Accounts of chemical research* **2015**, *48 (7)*, 2140 – 2150. DOI: 10.1021/acs.accounts.5b00174.

[335] D. C. Dolinoy, D. Huang, R. L. Jirtle, *Proceedings of the National Academy of Sciences of the United States of America* **2007**, *104 (32)*, 13056 – 13061. DOI: 10.1073/pnas.0703739104.

[336] J. G. Bromer, Y. Zhou, M. B. Taylor, L. Doherty, H. S. Taylor, *FASEB journal official publication of the Federation of American Societies for Experimental Biology* **2010**, *24 (7)*, 2273 – 2280. DOI: 10.1096/fj.09-140533.

[337] J. E. Cooper, E. L. Kendig, S. M. Belcher, *Chemosphere* **2011**, *85 (6)*, 943 – 947. DOI: 10.1016/j.chemosphere.2011.06.060.

[338] A. L. Herbst, H. Ulfelder, D. C. Poskanzer, *The New England journal of medicine* **1971**, *284 (15)*, 878 – 881. DOI: 10.1056/NEJM197104222841604.

[339] J. Blatt, L. van Le, T. Weiner, S. Sailer, *Journal of Pediatric Hematology/Oncology* **2003**, *25 (8)*, 635.

[340] P. S. Deimel, K. Stoiber, L. Jiang, J. A. Lloyd, S. C. Oh, S. Fischer, Ö. Sağlam, H. Schlichting, A. C. Papageorgiou, J. V. Barth, F. Allegretti, J. Reichert, *J. Phys. Chem. C* **2019**, *123 (2)*, 1354 – 1361. DOI: 10.1021/acs.jpcc.8b11047.

[341] M. P. Seah, *Surf. Interface Anal.* **1989**, *14 (8)*, 488. DOI: 10.1002/sia.740140813.

[342] P. J. Barrie, *Physical chemistry chemical physics PCCP* **2012**, *14 (1)*, 318 – 326. DOI: 10.1039/c1cp22666e.

[343] P. J. Barrie, *Physical chemistry chemical physics PCCP* **2012**, *14 (1)*, 327 – 336. DOI: 10.1039/c1cp22667c.

[344] S. Fischer, A. C. Papageorgiou, J. A. Lloyd, S. C. Oh, K. Diller, F. Allegretti, F. Klappenberger, A. P. Seitsonen, J. Reichert, J. V. Barth, *ACS nano* **2014**, *8 (1)*, 207 – 215. DOI: 10.1021/nn4030493.

[345] Z. Tao, T. Wang, D. Wu, L. Feng, J. Huang, X. Wu, J. Zhu, *Chemical communications (Cambridge, England)* **2018**, *54 (51)*, 7010 – 7013. DOI: 10.1039/c8cc01719k.

[346] S. C. Oh, J. A. Lloyd, S. Fischer, Ö. Saglam, A. C. Papageorgiou, K. Diller, D. A. Duncan, F. Klappenberger, F. Allegretti, J. Reichert, J. V. Barth, *Chemical communications (Cambridge, England)* **2018**, *54 (88)*, 12495 – 12498. DOI: 10.1039/c8cc06632a.

[347] F. Bebensee, K. Svane, C. Bombis, F. Masini, S. Klyatskaya, F. Besenbacher, M. Ruben, B. Hammer, T. R. Linderoth, *Angewandte Chemie (International ed. in English)* **2014**, *53 (47)*, 12955 – 12959. DOI: 10.1002/anie.201406528.

[348] M. J. Jackman, K. L. Syres, D. J. H. Cant, S. J. O. Hardman, A. G. Thomas, *Langmuir the ACS journal of surfaces and colloids* **2014**, *30 (29)*, 8761 – 8769. DOI: 10.1021/la501357b.

[349] L. Smykalla, P. Shukrynau, C. Mende, H. Lang, M. Knupfer, M. Hietschold, *Chemical Physics* **2015**, *450-451*, 39 – 45. DOI: 10.1016/j.chemphys.2015.02.001.

[350] F. Bebensee, K. Svane, C. Bombis, F. Masini, S. Klyatskaya, F. Besenbacher, M. Ruben, B. Hammer, T. Linderoth, *Chemical communications (Cambridge, England)* **2013**, *49 (81)*, 9308 – 9310. DOI: 10.1039/c3cc45052j.

[351] D. Payer, A. Comisso, A. Dmitriev, T. Strunskus, N. Lin, C. Wöll, A. Devita, J. V. Barth, K. Kern, *Chemistry (Weinheim an der Bergstrasse, Germany)* **2007**, *13 (14)*, 3900 – 3906. DOI: 10.1002/chem.200601325.

[352] G. Heimel, S. Duhm, I. Salzmann, A. Gerlach, A. Strozecka, J. Niederhausen, C. Bürker, T. Hosokai, I. Fernandez-Torrente, G. Schulze, S. Winkler, A. Wilke, R. Schlesinger, J. Frisch, B. Bröker, A. Vollmer, B. Detlefs, J. Pflaum, S. Kera, K. J. Franke, N. Ueno, J. I. Pascual, F. Schreiber, N. Koch, *Nature chemistry* **2013**, *5 (3)*, 187 – 194. DOI: 10.1038/nchem.1572.

[353] G. Anger, A. Winkler, K. D. Rendulic, *Surface Science* **1989**, *220 (1)*, 1 – 17. DOI: 10.1016/0039-6028(89)90459-7.

[354] D. den Boer, M. Li, T. Habets, P. Iavicoli, A. E. Rowan, R. J. M. Nolte, S. Speller, D. B. Amabilino, S. de Feyter, J. A. A. W. Elemans, *Nature Chem* **2013**, *5 (7)*, 621 – 627. DOI: 10.1038/nchem.1667.

[355] S. BERNER, S. BIELA, G. LEDUNG, A. GOGOLL, J. BACKVALL, C. PUGLIA, S. OSCARSSON, *Journal of Catalysis* **2006**, *244 (1)*, 86 – 91. DOI: 10.1016/j.jcat.2006.08.017.

[356] B. Hulsken, R. van Hameren, J. W. Gerritsen, T. Khoury, P. Thordarson, M. J. Crossley, A. E. Rowan, R. J. M. Nolte, J. A. A. W. Elemans, S. Speller, *Nature nanotechnology* **2007**, *2 (5)*, 285 – 289. DOI: 10.1038/nnano.2007.106.

[357] S. Fahrendorf, N. Atodiresei, C. Besson, V. Caciuc, F. Matthes, S. Blügel, P. Kögerler, D. E. Bürgler, C. M. Schneider, *Nat Commun* **2013**, *4*, 2425. DOI: 10.1038/ncomms3425.

[358] J. M. Gottfried, *Surface Science Reports* **2015**, *70 (3)*, 259 – 379. DOI: 10.1016/j.surfrep.2015.04.001.

[359] W. Auwärter, D. Écija, F. Klappenberger, J. V. Barth, *Nature Chem* **2015**, *7 (2)*, 105 – 120. DOI: 10.1038/nchem.2159.

[360] H. Marbach, *Accounts of chemical research* **2015**, *48 (9)*, 2649 – 2658. DOI: 10.1021/acs.accounts.5b00243.

[361] W. Auwärter, A. Weber-Bargioni, S. Brink, A. Riemann, A. Schiffrin, M. Ruben, J. V. Barth, *Chemphyschem a European journal of chemical physics and physical chemistry* **2007**, *8 (2)*, 250 – 254. DOI: 10.1002/cphc.200600675.

[362] F. Buchner, V. Schwald, K. Comanici, H.-P. Steinrück, H. Marbach, *Chemphyschem a European journal of chemical physics and physical chemistry* **2007**, *8 (2)*, 241 – 243. DOI: 10.1002/cphc.200600698.

[363] K. Diller, A. C. Papageorgiou, F. Klappenberger, F. Allegretti, J. V. Barth, W. Auwärter, *Chemical Society reviews* **2016**, *45 (6)*, 1629 – 1656. DOI: 10.1039/C5CS00207A.

[364] R. González-Moreno, C. Sánchez-Sánchez, M. Trelka, R. Otero, A. Cossaro, A. Verdini, L. Floreano, M. Ruiz-Bermejo, A. García-Lekue, J. Á. Martín-Gago, C. Rogero, *J. Phys. Chem. C* **2011**, *115 (14)*, 6849 – 6854. DOI: 10.1021/jp200533a.

[365] K. Diller, F. Klappenberger, M. Marschall, K. Hermann, A. Nefedov, C. Wöll, J. V. Barth, *The Journal of Chemical Physics* **2012**, *136 (1)*, 14705. DOI: 10.1063/1.3674165.

[366] G. Di Santo, S. Blankenburg, C. Castellarin-Cudia, M. Fanetti, P. Borghetti, L. Sangaletti, L. Floreano, A. Verdini, E. Magnano, F. Bondino, C. A. Pignedoli, M.-T. Nguyen, R. Gaspari, D. Passerone, A. Goldoni, *Chemistry (Weinheim an der Bergstrasse, Germany)* **2011**, *17 (51)*, 14354 – 14359. DOI: 10.1002/chem.201102268.

[367] G. Di Santo, C. Sfiligoj, C. Castellarin-Cudia, A. Verdini, A. Cossaro, A. Morgante, L. Floreano, A. Goldoni, *Chemistry (Weinheim an der Bergstrasse, Germany)* **2012**, *18 (40)*, 12619 – 12623. DOI: 10.1002/chem.201201640.

[368] A. C. Papageorgiou, S. Fischer, S. C. Oh, O. Sağlam, J. Reichert, A. Wiengarten, K. Seufert, S. Vijayaraghavan, D. Ecija, W. Auwärter, F. Allegretti, R. G. Acres, K. C. Prince, K. Diller, F. Klappenberger, J. V. Barth, *ACS nano* **2013**, *7 (5)*, 4520 – 4526. DOI: 10.1021/nn401171z.

[369] C. Castellarin-Cudia, P. Borghetti, G. Di Santo, M. Fanetti, R. Larciprete, C. Cepek, P. Vilmercati, L. Sangaletti, A. Verdini, A. Cossaro, L. Floreano, A. Morgante, A. Goldoni, *Chemphyschem a European journal of chemical physics and physical chemistry* **2010**, *11 (10)*, 2248 – 2255. DOI: 10.1002/cphc.201000017.

[370] M. Röckert, M. Franke, Q. Tariq, S. Ditze, M. Stark, P. Uffinger, D. Wechsler, U. Singh, J. Xiao, H. Marbach, H.-P. Steinrück, O. Lytken, *Chemistry (Weinheim an der Bergstrasse, Germany)* **2014**, *20 (29)*, 8948 – 8953. DOI: 10.1002/chem.201402420.

[371] M. Röckert, M. Franke, Q. Tariq, D. Lungerich, N. Jux, M. Stark, A. Kaftan, S. Ditze, H. Marbach, M. Laurin, J. Libuda, H.-P. Steinrück, O. Lytken, *J. Phys. Chem. C* **2014**, *118 (46)*, 26729 – 26736. DOI: 10.1021/jp507303h.

[372] F. Buchner, I. Kellner, W. Hieringer, A. Görling, H.-P. Steinrück, H. Marbach, *Phys. Chem. Chem. Phys.* **2010**, *12 (40)*, 13082 – 13090. DOI: 10.1039/C004551A.

[373] C. Ruggieri, S. Rangan, R. A. Bartynski, E. Galoppini, *J. Phys. Chem. C* **2016**, *120 (14)*, 7575 – 7585. DOI: 10.1021/acs.jpcc.6b00159.

[374] P. Feulner, D. Menzel, *Journal of Vacuum Science and Technology* **1980**, *17 (2)*, 662 – 663. DOI: 10.1116/1.570537.

[375] S. P. Frigo, P. Feulner, B. Kassühlke, C. Keller, D. Menzel, *Phys. Rev. Lett.* **1998**, *80 (13)*, 2813 – 2816. DOI: 10.1103/PhysRevLett.80.2813.

[376] D. A. Duncan, P. S. Deimel, A. Wiengarten, R. Han, R. G. Acres, W. Auwärter, P. Feulner, A. C. Papageorgiou, F. Allegretti, J. V. Barth, *Chemical communications (Cambridge, England)* **2015**, *51 (46)*, 9483 – 9486. DOI: 10.1039/C5CC01639H.

[377] D. A. Duncan, P. S. Deimel, A. Wiengarten, M. Paszkiewicz, P. Casado Aguilar, R. G. Acres, F. Klappenberger, W. Auwärter, A. P. Seitsonen, J. V. Barth, F. Allegretti, *J. Phys. Chem. C* **2019**, *123 (51)*, 31011 – 31025. DOI: 10.1021/acs.jpcc.9b08661.

[378] H. Zaglmayr, T. Lackner, L. Sun, P. Zeppenfeld, *Synthetic Metals* **2017**, *228*, 64 – 69. DOI: 10.1016/j.synthmet.2017.03.015.

[379] K.E. Hermann, M.A. Van Hove, *LEEDpat*.

[380] P. Knecht, P. T. P. Ryan, D. A. Duncan, L. Jiang, J. Reichert, P. S. Deimel, F. Haag, J. T. Küchle, F. Allegretti, T.-L. Lee, M. Schwarz, M. Garnica, W. Auwärter, A. P. Seitsonen, J. V. Barth, A. C. Papageorgiou, *J. Phys. Chem. C* **2021**, *125 (5)*, 3215 – 3224. DOI: 10.1021/acs.jpcc.0c10418.

[381] A. Wiengarten, K. Seufert, W. Auwärter, D. Ecija, K. Diller, F. Allegretti, F. Bischoff, S. Fischer, D. A. Duncan, A. C. Papageorgiou, F. Klappenberger, R. G. Acres, T. H. Ngo, J. V. Barth, *J. Am. Chem. Soc.* **2014**, *136 (26)*, 9346 – 9354. DOI: 10.1021/ja501680n.

[382] J. W. Niemantsverdriet, *Spectroscopy in catalysis: An introduction*, 3rd ed., Wiley-VCH, Weinheim, Chichester **2010**.

[383] J. W. Niemantsverdriet, K. Markert, K. Wandelt, *Applied Surface Science* **1988**, *31 (2)*, 211 – 219. DOI: 10.1016/0169-4332(88)90062-1.

[384] H. Schlichting, *Illustration of the model based on joint discussions*.

[385] G. Rojas, X. Chen, C. Bravo, J.-H. Kim, J.-S. Kim, J. Xiao, P. A. Dowben, Y. Gao, X. C. Zeng, W. Choe, A. Enders, *J. Phys. Chem. C* **2010**, *114 (20)*, 9408 – 9415. DOI: 10.1021/jp1012957.

[386] M. Groenning, S. Frokjaer, B. Vestergaard, *Current protein & peptide science* **2009**, *10 (5)*, 509 – 528. DOI: 10.2174/138920309789352038.

[387] E. A. Kümmerle, E. Pomplun, *European biophysics journal EBJ* **2005**, *34 (1)*, 13 – 18. DOI: 10.1007/s00249-004-0431-2.

[388] William R. Bauer, F. H. C. Crick, James H. White, *Scientific American* **1980**, *243*, 118 – 133.

# Acknowledgements

Finally, I want to thank everybody who supported me during my PhD. The realization of this thesis would not have been possible without the help of many people, in particular:

**Prof. Dr. Johannes V. Barth**, for giving me the opportunity to work at his chair, for the proposition of the thesis and his guidance.

**Dr. Hartmut Schlichting** and **Dr. Annette Hüttig**, for supervision, discussions and ideas as well as support during experiments, programming and writing.

**Prof. Dr. Peter Feulner**, for knowing answers to almost every question and always having an open door – no matter whether the problem was technical or scientific.

**Dr. Andreas Walz**, for helping with MS measurements, building and repairing the ESI, all his support during my time at E20 – not to forget the 3D printing and the coffee breaks.

**Peter Deimel, Felix Haag** and **Dr. Francesco Allegretti**, for providing the TPD/XPS/LEED data, XPS/ LEED processing and analysis as well as all the discussions. **Dr. Joachim Reichert**, **Dr. Anthoula Papageorgiou** and **Peter Knecht**, for their support with the STM during measurements and maintenance.

**Reinhold Schneider**, for his support with electronic (and mechanical) problems, teaching me how to solder circuit boards. **Karl Eberle**, for his technical support and repairing not only with the vacuum chambers but also my bicycle tires. **Viktoria Blaschek**, for her help in administrative problems and for organising all the events.

The **workshop** of the physics department, for realizing the drafts of various components and being patient with all changes throughout the development process.

My long- and short-term **office colleagues**, for distractions, encouragement and support. I had a lot of fun with all of you.

The "**cooking group**" and the whole **E20 workgroup**, for many great lunch breaks and fun evenings with smoked/grilled and international food and beer; for the familiar working atmosphere, exciting discussions and the great time I had during my PhD.

My family, especially **Andreas Schmolke** and my parents **Petra** and **Wolfgang Stoiber** and **Reinhard Müller**, for their endless support during all these years, their encouragement and everything they did for me!